Support effects of metal oxides prepared by thermal decomposition on anode catalysts for direct ethanol fuel cells

by

© Hui Hang

A thesis submitted to the

School of Graduate Studies

in partial fulfillment of the requirements for the degree of

Doctor of Philosophy

Department of Chemistry

Memorial University of Newfoundland

April, 2022

St. John's Newfoundland

Abstract

Direct liquid fuel cells (DLFCs) are a candidate technology for sustainable power generation with high energy efficiency. Among renewable liquid fuels (e.g. ethanol, methanol and formic acid), bioethanol is the most attractive liquid fuel because of its low toxicity and high energy density. However, Pt anode catalysts for ethanol oxidation face problems, such as large overpotential (causing the decrease of fuel efficiency) and catalyst poisoning (leading to severe current decay). In order to improve catalyst performance, one strategy is to introduce metal oxide supports. Nevertheless, the support effects of metal oxides prepared by different methods could not be fairly evaluated and systematically compared due to a wide range of particle sizes and different structures. Therefore, a consistent method should be used for preparation of metal oxide-supported catalysts.

Thermal decomposition of M(acac)$_x$ complexes (acac = acetylecetonate) was investigated as a versatile method to rapidly prepare metal oxide supports (e.g. Ru oxide, Sn oxide, and mixed Ru-Sn oxides, Pb oxide, Mo oxide, Ga oxide, In oxide, V oxide, and Zr oxide) on Ti foil. Preformed Pt nanoparticles were drop coated onto the metal oxide supports, so that the morphology, size, and composition of the Pt were kept the same. Cyclic voltammetry was used to quickly investigate the influence of the metal oxide supports on catalytic activity of the Pt catalyst in ethanol oxidation. Charge transfer between metal oxide supports and the Pt (electronic/ligand effect) was analyzed using X-ray photoelectron spectroscopy. These metal-oxide supported catalysts were quickly prepared and screened on Ti electrodes for oxidation of ethanol.

The methodology of M(acac)$_x$ thermal decomposition was further applied to a carbon support with a high surface area, so that the prepared anode catalysts can be used in proton exchange membrane (PEM) cells for ethanol oxidation. Online detection of the amount of CO_2 produced from complete oxidation of ethanol in the PEM cell was developed using a non-dispersive infrared CO_2 sensor. Therefore, the influence of M(acac)$_x$ modification on the CO_2 yield could be evaluated. In addition, the enhancement of Pt-catalyzed oxidation of methanol and formic acid through modification with some M(acac)$_x$ was also investigated.

Dedication

To my wife, Yi Liu, for her understanding, encouragement, and constant support during my PhD program.

To my parents, for their support and encouragement in my life.

Acknowledgements

I would like to acknowledge my supervisor, Prof. Peter Pickup, for providing me the opportunity to study in his group. His patience, profound knowledge, encouragement, guidance, and support greatly promoted my progress and my interest in research. I am also grateful that his kindness and precious advice made my PhD life enjoyable.

I would like to deeply thank my supervisory committee members, Prof. Francesca Kerton and Prof. Jane Stockmann, for their valuable suggestions, support and the time they have dedicated throughout my PhD program. Thank you to all the faculty members at the Department of Chemistry who helped me through offering lectures, being examiners for my comprehensive exam and seminar, and providing assistance during my PhD program.

I would like to gratefully acknowledge the Department of Chemistry, School of Graduate Studies (SGS), Graduate Students' Union (GSU), Memorial University of Newfoundland, and Natural Science and Engineering Research Council of Canada for the services and financial support.

Thank you to Dr. Pickup's group and my friends for their encouragement and the fun we have had in the last four years.

My deepest appreciation to everyone who helped and encouraged me.

Table of contents

List of tables

List of figures

List of abbreviations

acac	Acetylacetonate
BLC	Basic lead carbonate
CFP	Carbon fiber paper
CNTs	Carbon nanotubes
CO	Carbon monoxide
CO_2	Carbon dioxide
DEFCs	Direct ethanol fuel cells
DEMS	Differential electrochemical mass spectroscopy
DHE	Dynamic hydrogen electrode
DLFCs	Direct liquid fuel cells
EASA	Electrochemically active surface area
EDX	Energy dispersive X-ray analysis
H_2O	Water
IR	Infrared
IRRAS	In situ infrared reflection-absorption spectroscopy
$M(acac)_x$	Metal acetylacetonate complexes

MEAs	Membrane electrode assemblies
MO_x	Metal oxides
MO_x/C	Metal oxide modified carbon supports
NDIR	Non-dispersive infrared
PEM	Proton exchange membrane
PEMFCs	Proton exchange membrane fuel cells
RHE	Reversible hydrogen electrode
SCE	Saturated calomel electrode
SEM	Scanning electron microscopy
TEM	Transmission electron microscopy
TGA	Thermogravimetric analysis
XAS	X-ray absorption spectroscopy
XPS	X-ray photoelectron spectroscopy
XRD	X-ray diffraction

List of symbols

a.u.	Arbitrary unit
A	Ampere
C	Coulomb
ca.	Approximately
η_{cell}	Efficiency
η_t	Theoretical energy efficiency
η_E	Voltage efficiency
η_F	Faradaic efficiency
e^-	Electron
e.g.	For example
E	Potential
E^o	Standard potential
eV	Electron volt
F	Faraday constant
G	Gibbs energy
H	Enthalpy

h	Hour
I	Current
i.e.	In other words
J	Current density
min	Minute
m/z	Mass to charge ratio
Λ	Wavelength
n_t	Total electron transfer number
n_{av}	Average electron transfer number
ϴ	Diffraction angle
Ω	Ohm
Q	Charge
ppm	Parts per million
s	Second
t	Time
V	Voltage (volts)
$\dot{V}$	Volumetric flow rate
vs.	Versus

Chapter 1

Introduction

1.1 Fuel cells

The overuse of fossil fuel has caused serious problems such as climate change and energy shortage. Therefore, there is an urgent need to replace fossil fuels with renewable energy. Currently, the main alternative energy sources are solar, wind and biomass energy.[1] However, it is not feasible to rely on only one renewable energy source for the entire replacement of fossil fuel. As renewable power sources that have been widely commercialized, both solar and wind power are easily affected by weather conditions.[2] The generation of electricity from solar power depends on the abundance of sunlight and cannot proceed at night. The effective utilization of wind energy is significantly related to wind velocity, which fluctuates throughout the year. Therefore, electricity might not be supplied continuously and steadily by using these energy sources. Theoretically, a controllable power source with high energy efficiency is complementary for building up a sustainable electricity system.[2]

A fuel cell is a type of powerful energy conversion device which converts chemical energy to electrical energy without fuel combustion. This technology is promising to continuously and controllably supply electricity by using renewable fuels. The concept of hydrogen fuel cells was first brought up by Sir William Robert Grove in the 19th century.[3-4] The basic structure of a typical fuel cell is composed of an anode, a cathode, and an electrolyte. At the beginning of the 20th century, fuel cells started to attract researchers' attention because of the increasing utilization of electricity. The first fully operational fuel cell was reported by Francis Thomas Bacon in 1959.[5] In the 1960s, a fuel cell was successfully applied in a space mission by NASA. After one century of exploration, various types of fuel cells have been developed, such as proton exchange membrane fuel cells, alkaline fuel cells, and solid oxide fuel cells. They differ from each other in electrolyte (e.g. polymer membrane, alkaline, and ceramic) and operation temperature (from ambient to 1000 °C).[5-6] They can be used for stationary or portable power generation.

1.1.1. Proton exchange membrane fuel cells (PEMFCs)

Among many types of fuel cells, PEMFCs have become the most attractive sustainable power sources due to their relatively low operation temperatures, high energy conversion efficiency, and fast start-up.[5-6] Although alkaline fuel cells also have these advantages, their stability is significantly influenced by carbon dioxide (CO_2) from the air, leading to a change in pH of the electrolyte and decrease of the fuel cell efficiency. Traditionally, combustion engines are used as power sources to convert chemical energy of fossil fuels to electricity (in power stations) or mechanical energy (in transportation) with low energy efficiency (typically 25-35%).[7-8] In comparison with internal combustion engines, PEMFCs have several outstanding benefits, including higher energy conversion efficiency (up to 65% using hydrogen fuel), lower harmful emissions and lower noise from mechanical movement.[9] Unlike other renewable but irregular-available power sources (e.g. solar, wind and water power generators), fuel cells are not affected by climate, sunlight, and geographic location, so it is possible to combine fuel cells with these renewable sources for continuous supply of power in stationary power stations. In transportation, the application of fuel cells in electrical vehicles as power generators has been of particular interest to researchers. It is a potential alternative to internal combustion engines in traditional vehicles, and therefore reduces the depletion of unrenewable fossil fuels and subsequent emission of greenhouse gases and poisonous substances. In comparison to batteries which is another potential alternative to conventional combustion engines, fuel cells have significantly higher energy density, much shorter energy-refill time, and longer recharge/refuel mileage.[10]

A PEMFC is composed of an anode, a cathode, and a proton exchange membrane (PEM) (Figure 1.1). The bipolar plates on each side have channels for the flow of fuel and oxygen or air. Both the anode and cathode contain catalysts and gas diffusion layers. They are easily set up in a membrane electrode assembly. Pt-based materials are the most commonly used catalysts in the anode and cathode. The electrochemical reactions in a PEMFC system involves oxidation of a fuel (e.g. hydrogen, methanol, ethanol) at the anode and oxygen reduction at the cathode. Atmospheric air can be directly used as the oxidant due to the tolerance of PEMFCs to CO_2.

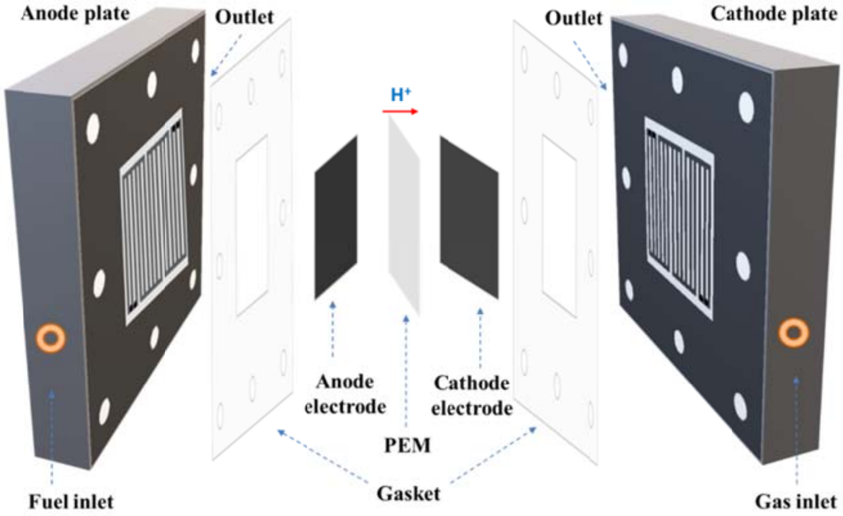

Figure 1.1. A scheme of a PEMFC.

Nowadays, hydrogen fuel cells are the most intensively developed PEMFCs. At the anode, hydrogen is oxidized into two protons by losing two electrons (Equation 1.1). PEMs are non-corrosive solid polymer films which conduct protons instead of acidic solution electrolytes.

Currently, the commonly used PEMs are perfluorosulfonic acid polymers (e.g. Nafion from DuPont). PEMs are normally composed of two phases: a continuous hydrophobic polymer frame and hydrophilic sulfonic groups.[11] The hydration of PEMs is essential for conducting protons since water (H_2O) participates in the dissociation of protons from sulfonic acid groups and their migration.[12] The protons are transferred through a PEM to the cathode through diffusion (in the form of H_3O^+ species) driven by electrochemical difference and concentration gradient, and hopping diffusion between proton carriers ($-SO_3H$ and H_3O^+ groups) in PEMs.[13] Since PEMs are not electrically conductive, the electrons migrate to the cathode through the electrical circuit and thereby produce electrical current. At the cathode, with protons and electrons, the reduction of oxygen generates water (Equation 1.2). The standard cell potential ($E°_{cathode} - E°_{anode}$) of a hydrogen fuel cell is 1.229 V.

$H_2 \rightarrow H^+ + 2\ e^-$ $E°_{anode} = 0.000\ V$ (Equation 1.1)

$O_2 + 4\ H^+ + 4\ e^- \rightarrow 2\ H_2O$ $E°_{cathode} = 1.229\ V$ (Equation 1.2)

The commercial applications of hydrogen-PEMFCs have been widely developed, such as electrical vehicles, ships, aircrafts, space exploration, power stations, portable power generators, and emergency back-up power supply.[14-20] In addition, when coupled with a CO_2 separation system, hydrogen-PEMFCs can simultaneously capture CO_2 from the air while supplying electricity.[21] However, there are two major challenges for extensive application of hydrogen-PEMFC equipment: bulk production of hydrogen from renewable sources and the security issue of flammable and explosive hydrogen highly compressed in storage and transportation.

The renewable liquid fuels (ethanol, methanol, and formic acid) can be produced from biomass (such as sugar-cane, corn, and woodchips),[22-25] or electrochemical CO_2 reduction using renewable electricity from solar and wind power.[26-28] These liquid fuels have higher volumetric energy density than hydrogen, and can be easily transported and stored using current gasoline systems with simple modification.[29] As hydrogen carriers, the liquid fuels can be directly fed into PEMFCs for electrochemical oxidization to generate electricity. These types of PEMFCs are called direct liquid fuel cells (DLFCs). As shown in Table 1.1, the theoretical efficiencies of the typical DLFCs are higher than that of hydrogen fuel cells (83%) under standard conditions (298.15 K and 101.325 kPa).[30] However, DLFCs are still under development, and improvement on their actual efficiency is needed for commercialization.

Table 1.1. A list of typical DLFCs and their operating temperatures, theoretical efficiencies (under standard conditions) and actual efficiencies.[10, 31]

Types	Operating temperature	Theoretical efficiency	Actual efficiency
Direct ethanol fuel cells	Ambient- 120 °C	97%	20-40%
Direct methanol fuel cells	Ambient- 110 °C	97%	35-60%
Direct formic acid fuel cells	30-60 °C	106%	30-50%

1.1.2. Direct ethanol fuel cells (DEFCs)

DEFCs are one of the most attractive PEMFCs for sustainable power production, since they can use bioethanol to generate electricity.[32] In comparison with methanol and formic acid, ethanol has much lower toxicity and higher energy density. It is massively produced from biomass fermentation for wide utilization as a blended component in gasoline.[33] Electricity is generated from DEFCs through ethanol electrooxidation, and the theoretical products from the use of DEFCs are only H_2O and CO_2. The CO_2 generated from DEFCs will be consumed by plant growth. In this carbon recycle, the net carbon emission can be zero. Theoretically, DEFCs are safe, environmentally benign, and have high theoretical energy-conversion efficiency. Various applications of DEFCs have been developed, such as power packs for charging laptops and mobile phones, the power generator for a wireless vacuum cleaner, and a bio-energy discovery kit.[34] A car prototype equipped with an ethanol fuel cell has been road tested.[35] In addition, DEFCs have been developed into a novel type of electrolysis cell for hydrogen production (without the supply of oxygen at the cathode).[36] Acetic acid, one of the main by-products of ethanol electrooxidation, is a food additive and valuable industrial chemical.[37]

The principle of a DEFC is shown in Figure 1.2. At the anode, oxidation of ethanol in water generates carbon dioxide, protons, and electrons at the surface of catalysts such as platinum nanoparticles (Equation 1.3). The electrons are transferred from the anode to the cathode resulting in electrical current. A PEM, which is usually a Nafion membrane with proton-conductivity and electrical insulation, is used as the electrolyte to separate the anode and cathode. The optimal operating temperature ranges between 60 °C and 80 °C. At the cathode, reduction of oxygen gas generates water under acidic conditions (Equation 1.4). The reactants at the anode (ethanol) and the cathode (oxygen gas from the air) can be continuously supplied from external sources. The diffusion layers of the anode and cathode are porous for the diffusion of fuel and air to the catalysts. Commonly, carbon fiber papers or fabrics are used to support the catalyst layers because of their good electrical conductivity and physical mechanical properties. The overall reaction of DEFCs is shown in Equation 1.5 for the complete oxidation of ethanol.

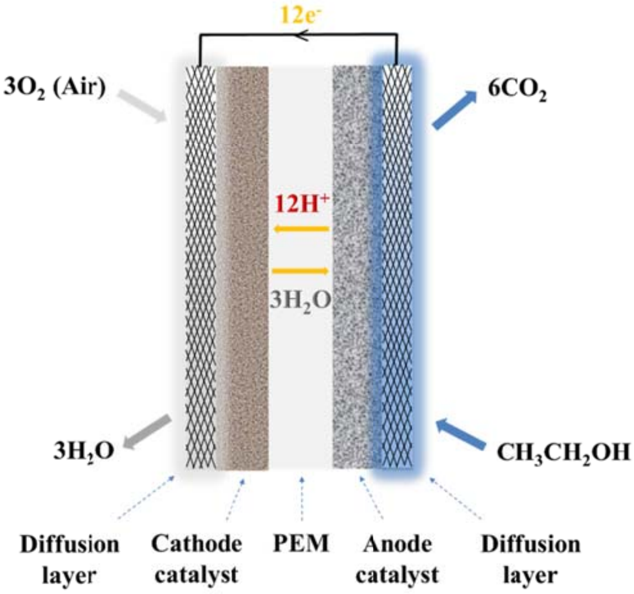

Figure 1.2. The principle of a direct ethanol fuel cell.

$CH_3CH_2OH + 3H_2O \rightarrow 2CO_2 + 12H^+ + 12e^-$ $E^{\circ}_{anode} = 0.085$ V (Equation 1.3)

$O_2 + 4 H^+ + 4 e^- \rightarrow 2 H_2O$ $E^{\circ}_{cathode} = 1.229$ V (Equation 1.4)

$CH_3CH_2OH + 3O_2 \rightarrow 2CO_2 + 3H_2O$ $E^{\circ}_{cell} = 1.144$ V (Equation 1.5)

The energy-conversion efficiency of DEFCs (η_{cell}) depends on the theoretical energy efficiency (η_t), voltage efficiency (η_E) and faradic efficiency (η_F) (Equation 1.6). The theoretical energy efficiency of DEFCs is 97% under standard conditions (298.15 K and 101.325 kPa), derived from Equation 1.7.[37] The voltage efficiency is determined by the cell potential (Equation 1.8), where E_{cell} represents the operating cell voltage, and $E^{\circ}_{cathode}$ and E°_{anode} are the reversible potentials of cathode and anode (Equation 1.4 and 1.5). In practice, the loss of voltage efficiency is mainly caused by increased overpotentials. Overpotential is the potential difference between the practical potential required for facilitating ethanol electrooxidation (or oxygen reduction) and the reversible potential. For Pt catalysts, a large activation overpotential is required for transferring electrons from ethanol oxidation, and can be decreased through optimizing electro-catalysts.[38] In addition, crossover overpotential is due to the crossover of ethanol (to the cathode) or oxygen (to the anode) resulting in a decrease in the operating cell voltage and loss of fuel. Instead of separated oxidation (anode) and reduction (cathode), the redox reaction of the crossed ethanol or oxygen directly reacts on the surface of catalysts without providing electrical current. The crossover could be diminished through exploring new polymer membranes and modification of PEMs.

For the complete oxidation of ethanol, the total number of electrons (n_t) transferred by each ethanol molecule is 12. However, currently the CO_2 selectivity of most anode catalysts is low, and the oxidation of ethanol is catalyzed to an incomplete extent, which results in the formation of acetic acid and acetaldehyde. The complete oxidation of ethanol to CO_2 has higher energy efficiency than the incomplete oxidations since more electrons are transferred from one ethanol molecule. The faradic efficiency (Equation 1.9) is influenced by the average of the electron transfer number (n_a), which can be calculated by measuring product distribution.

$$\eta_{cell} = \eta_t \times \eta_E \times \eta_F \qquad \text{(Equation 1.6)}$$

$$\eta_t = \frac{\Delta G^\circ}{\Delta H^\circ} \qquad \text{(Equation 1.7)}$$

$$\eta_E = \frac{E_{cell}}{E^\circ_{cathode} - E^\circ_{anode}} \qquad \text{(Equation 1.8)}$$

$$\eta_F = \frac{n_a}{n_t} \qquad \text{(Equation 1.9)}$$

1.2 Electrochemical oxidation of ethanol

1.2.1 Mechanism

Ethanol electro-oxidation is a complicated multiple-electron process involving various intermediates and products.[39] The mechanism of ethanol electro-oxidation has been investigated through online detection by differential electrochemical mass spectroscopy (DEMS) and in situ infrared reflection-absorption spectroscopy (IRRAS) techniques. IRRAS combines an infrared spectrometer with a spectroelectrochemical cell containing a CaF_2 window for infrared (IR) transmission.[40] It can provide insight on intermediates and the product distribution on electrode surfaces at different potentials. As a sensitive qualitative and quantitative analytical technique, DEMS combines an electrochemical cell with mass spectrometry for mechanistic study of electrochemical reactions. Through online detection of volatile intermediates and products (carbon dioxide and acetaldehyde), the DEMS analysis can provide information about the potentiodynamic electro-oxidation of ethanol.[41]

Analysis of product distributions has shown that the final products of ethanol electro-oxidation are mainly acetic acid, acetaldehyde and carbon dioxide (CO_2).[42] There are two main pathways for ethanol electro-oxidation (Figure 1.3). One pathway is partial oxidation of ethanol without C-C bond breaking, which leads to the formation of acetaldehyde by delivering two electrons (Equation 1.10) or acetic acid by delivering four electrons (Equation 1.11). Acetaldehyde can be further oxidized to acetic acid, which is the final product and difficult to be electro-oxidized.

$CH_3CH_2OH \rightarrow CH_3CHO + 2H^+ + 2e^-$ (Equation 1.10)

$CH_3CH_2OH + H_2O \rightarrow CH_3COOH + 4H^+ + 4e^-$ (Equation 1.11)

For the electrocatalytic oxidation of ethanol at Pt surfaces, an ethanol molecule needs to be adsorbed first through the oxidation of a α-hydrogen atom or hydrogen atoms of the hydroxyl group, and releases one proton and one electron (Equation 1.12 and 1.13).[39] Without C-C bond cleavage, the further oxidation of the initial species derived from ethanol adsorption leads to the formation of adsorbed Pt-$CHOCH_3$ species (Equation 1.14), which can be released from the Pt surface to generate aceteldehyde or further oxidized to acetic acid (Equation 1.16) with the aid of hydroxyl groups from water disassociation on the Pt surface (Equation 1.15).[43]

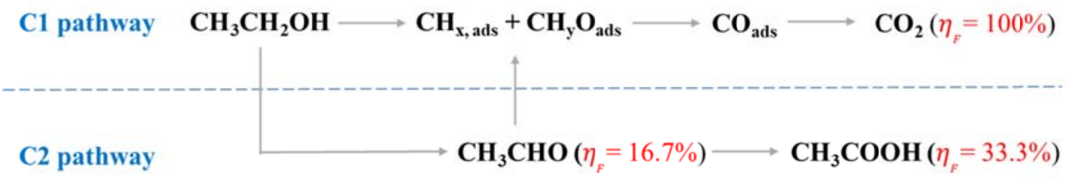

Figure 1.3. Proposed reaction pathways for electro-oxidation of ethanol on Pt electrodes.[42]

$CH_3CH_2OH + Pt \rightarrow Pt\text{-}OCH_2CH_3 + H^+ + e^-$ (Equation 1.12)

$CH_3CH_2OH + Pt \rightarrow Pt\text{-}CH(OH)CH_3 + H^+ + e^-$ (Equation 1.13)

$Pt\text{-}OCH_2CH_3$ or $Pt\text{-}CH(OH)CH_3 \rightarrow Pt\text{-}CHOCH_3 + H^+ + e^-$ (Equation 1.14)

$Pt + H_2O \rightarrow Pt\text{-}OH + H^+ + e^-$ (Equation 1.15)

$Pt\text{-}CHOCH_3 + Pt\text{-}OH \rightarrow 2Pt + CH_3COOH + H^+ + e^-$ (Equation 1.16)

The other pathway is complete oxidation of ethanol to carbon dioxide (Equation 1.3), which delivers twelve electrons. In this reaction, the C-C bond breaking of ethanol has to occur to produce adsorbed intermediates including $CH_{x,ads}$, and CH_yO_{ads} (Equation 1.17), which can be further oxidized to carbon monoxide (CO_{ads}) by releasing protons and electrons (Equation 1.18).[39] The further oxidation of CO_{ads} species to the final products (CO_2 and H_2O) proceeds with the hydroxyl groups on Pt surfaces (Equation 1.19), which is the limiting step at low potentials.[44] The Pt active sites are occupied by CO_{ads} due to its strong adsorption at Pt, and thereby unavailable for further reaction (i.e. catalyst poisoning). Therefore, the activity of a catalyst decreases with time. In addition, the complete oxidation of ethanol is inhibited due to CO_{ads} blocking, since multiple free and continuous Pt active sites (forming a cyclic adsorbate) are required for breaking C-C bonds.[45] Consequently, the selectivity of incomplete oxidation of ethanol to aceteldehyde and acetic acid is increased as fewer active sites are required for this pathway. The investigation of the mechanism of ethanol oxidation is essential for the rational design of electro-catalysts to achieve a high CO_2 selectivity in ethanol oxidation.

$$\text{Pt-OCH}_2\,\text{CH}_3 \text{ or Pt-CH(OH)CH}_3 \rightarrow \text{Pt-CH}_y\text{O} + \text{Pt-CH}_x + (5-x-y)\text{H}^+ + (5-x-y)\text{e}^- \qquad \text{(Equation 1.17)}$$

$$\text{Pt-CH}_y\text{O or Pt-CH}_x \rightarrow \text{Pt-CO} + (x \text{ or } y)\text{H}^+ + (x \text{ or } y)\text{e}^- \qquad \text{(Equation 1.18)}$$

$$\text{Pt-CO} + \text{Pt-OH} \rightarrow 2\text{Pt} + \text{CO}_2 + \text{H}^+ + \text{e}^- \qquad \text{(Equation 1.19)}$$

1.2.2 Catalysts

In order to solve the problems of catalyst poisoning and low energy conversion efficiency, a variety of binary and ternary anode catalysts have been investigated, such as PtM alloy catalysts (e.g. M = Ru, Ni, Sn, and Co) and metal oxide-supported catalysts.[46-47] PtRu has been most commonly used as an anode catalyst, and provides the best performance in DEFCs. However, it was reported that the n_{av} of PtRu in ethanol oxidation was low.[48] An on-line detection analysis of volatile products indicated that CO_2 selectivity of PtRu was lower than Pt.[49] The addition of Ru into the Pt catalyst promoted oxidation of intermediate aceteldehyde to acetic acid. In addition, PtSn is also a popular anode catalyst for ethanol electrooxidation.[47] Beyhan et al. prepared a PtSn/C catalyst by depositing PtSn nanoparticles on a carbon black support (C) (the symbol "/" in PtSn/C is used to make a distinction between different phases).[50] This catalyst gave higher current densities and a much lower onset potential, in comparison with Pt/C. PtSn/C catalysts with different atomic ratios (Pt:Sn = 3:1, 1:1, and 1:3) were investigated, and the PtSn(1:1)/C catalyst exhibited the highest current density for ethanol oxidation.[51] Moreover, the addition of Sn shifted the onset for CO oxidation to lower potentials compared to the Pt/C catalyst. However, online analysis of product distribution of ethanol oxidation by DEMS showed that the products were mainly acetic acid and acetaldehyde.[52] Although PtSn/C catalysts display higher catalytic activity than Pt catalysts for ethanol oxidation, mostly incomplete oxidation occurs with low energy conversion, instead of the complete oxidation of ethanol to CO_2 at low potential. For further improvement, many PtSnX trimetallic catalysts (e.g. PtSnPd/C, PtSnRh/C, PtSnNi/C, PtSnCo/C) were investigated.[47] Notably, the addition of Ni to PtSn provided the highest current densities for ethanol oxidation at low potentials, and adding Co resulted in the largest improvement in its catalytic activity at high potentials.

The combination of metal oxide supports with Pt alloy catalysts to form ternary catalysts provides a promising way to get optimum performance with both high CO_2 selectivity and high current density. Kowal et. al. reported that a ternary PtRh/SnO_2/C electrocatalyst selectively oxidized ethanol to CO_2 with high current efficiency.[53] The catalyst was prepared by depositing

PtRh nanoparticles on prefabricated carbon-supported Sn(IV) oxide nanoparticles. The combination of Pt and Rh lowered the barrier for the formation of the metal-CH_2CH_2O intermediate, of which the C–C bond can be effectively split for the further oxidation to CO_2. In addition, the presence of Rh was found to increase the electrochemical surface area of the PtRh alloy nanoparticles for hydrogen adsorption and desorption.[54] Consequently, the PtRh/SnO_2 provided faster kinetics of ethanol oxidation than the Pt, PtRh, and Pt/SnO_2 catalysts.

1.3 Catalyst support materials

The deposition of electrocatalyst particles (e.g. Pt nanoparticles) on support materials can greatly increase the electrochemically active surface area and reduce the aggregation of the catalyst. The performance of fuel cells is significantly affected by the properties of support materials. A high specific surface area of the support material is required to load a large amount of Pt nanoparticles. Moreover, the electrons generated from ethanol electro-oxidation need to be transferred to an electric circuit through the support material. High ohmic resistance of the support will lead to a loss of efficiency of a fuel cell. Therefore, an ideal catalyst support for fuel cells should satisfy the essential requirements including: high specific surface area (larger than 100 $m^2 g^{-1}$), high electrical conductivity, and high electrochemical stability.[55] In the past decades, carbon and non-carbon supports have been widely explored to improve the performance of catalysts in fuel cells.

1.3.1 Carbon supports

Carbon materials (e.g. carbon black, graphite, and carbon nanotubes) have been widely investigated as electrocatalyst supports due to their high specific surface area, good electrical conductivity, and high availability.[55] Carbon black mainly derives from agglomeration of spherical carbon nanoparticles with an amorphous structure, and a large quantity can be produced from pyrolysis of hydrocarbons (e.g. natural gas).[56-57] Graphite and carbon nanotubes (CNTs) have different structures derived from stacking and wrapping two-dimensional graphene respectively.[55] Among carbon materials, carbon black is most commonly used as the support for Pt nanoparticles for catalyst preparation due to good electrical conductivity, high specific surface area, and low cost. The specific surface area of Vulcan XC-72R carbon black (industrially produced by Cabot Corporation) is as high as 250 $m^2\ g^{-1}$.[58] For ethanol oxidation, higher peak currents were obtained on Vulcan XC-72R carbon black than a graphite support.[59]

1.3.2 Non-carbon supports

Due to the limitations (low utilization of catalysts and insufficient electrochemical stability) of carbon support materials, non-carbon supports were explored as alternatives to carbon materials to attain high durability and good performance of fuel cells, such as SiC, WO_3, SnO_2, TiO_2, and IrO_2.[55, 60-62] A SiC support was electrochemically inert at high potentials, which provided high resistance to corrosion in fuel cell applications. However, its low electrical conductivity diminishes the catalytic activity of Pt catalysts. Metal oxides have been widely studied as non-carbon catalyst supports. For instance, a WO_3-supported Pt catalyst was synthesized and applied as an anode electrocatalyst.[63] The WO_3-supported Pt catalyst exhibited higher stability than a carbon-supported Pt catalyst in an acidic medium, but lower catalytic activity towards methanol oxidation due to aggregation of Pt nanoparticles on the WO_3 support.[64]

SnO_2 is a kind of n-type semiconductor with much lower electrical conductivity (3.62×10^{-6} Ω^{-1} cm^{-1}) than carbon black (ca. 2.77 Ω^{-1} cm^{-1}).[58, 65] In the study by Takasaki et al., a nano-sized SnO_2 support strongly interacted with Pt nanoparticles and prevented catalyst aggregation, thus improving durability of the Pt catalyst.[66] After a voltage cycling test (60,000 cycles corresponding to a lifetime of twenty years with eight times of start-up/shut-down per day), the electrochemically active surface area of the Pt/SnO_2 was decreased slightly by 5.0%, in comparison to a drastic reduction by 80.3% for the Pt/C. This decrease mainly arose from the dissolution of Pt during the redox reaction, and the subsequent growth of Pt grains. Similar to SnO_2 support, both bulk TiO_2 and IrO_2 have higher ohmic resistance, which prevents delivery of electrons generated from the oxidation of fuels at Pt nanoparticles.[55] The low electrical conductivity of the metal oxide supports leads to low catalytic activity of the electrocatalysts.

Although metal oxides can be good proton conductors and have higher oxidation resistivity in comparison with carbon materials, they are generally not appropriate to be used as independent catalyst supports due to their low electrical conductivity. As another type of non-carbon support materials, metal supports such as titanium, silver, and gold are of interest to researchers because of their significantly higher electrical conductivity.[67-71]

Ti materials have been intensively investigated because of their advantages of non-toxicity, high electrical conductivity, good stability, and low production cost.[72] Their anticorrosion property is derived from a thin layer of naturally formed TiO_2 coated on the Ti surface. Ti wires, plates, and sponges have been explored for their potential to be applied as supports for electrocatalysts.[72-75] Among these Ti materials, the three-dimensional Ti sponges with porous structures are most appropriate to be applied as anode supports in fuel cells, since they are suitable for current collecting, electrolyte transport and gas diffusion. Furthermore, it is feasible to deposit metal or metal oxides particles on Ti sheets to study their catalytic performance in alcohol oxidation. $Pt_{(1-x)}(RuO_2)_x/Ti$ electrodes with different Pt-RuO_2 ratios were prepared through in-situ reactions of Pt and Ru precursors on Ti plates.[74] The optimum composition ($Pt_{0.5}(RuO_2)_{0.5}/Ti$) in ethanol oxidation was determined by cyclic voltammetry and chronoamperometry measurements. In terms of functionality, the Pt portion was responsible in catalyzing the electro-oxidation of ethanol. The RuO_2/Ti support did not show activity on ethanol oxidation, but had a significant effect on improving the catalytic activity of Pt. The onset of both CO and ethanol oxidation was negatively shifted towards low potentials, and lower current decay was observed in the chronoamperometry measurement.

1.3.3 Metal oxide/carbon hybrid supports (MO_x/C)

Hybrid supports combining carbon with metal oxides is another choice for supporting electrocatalysts and improving the performance of direct alcohol fuel cells (e.g. ethanol and methanol).[76] The addition of carbon to metal oxide supports can overcome the problems of low electrical conductivity and agglomeration of pure metal oxide supports. The deposition of the metal oxide layer on a carbon support can reduce direct contact between the carbon support and Pt catalyst, which reduces the corrosion of carbon caused by Pt-catalyzed oxidation at high potentials.[58] Meanwhile, the Pt nanoparticles can be stabilized by metal oxides. For instance, the modification of a Pt/C catalyst with RuO_2 significantly improved its stability during consecutive potential cycling (1000 cycles).[77] After the accelerated potential cycling test, the degradation of the electrochemically active surface area of the RuO_2 modified catalyst was less than that of the Pt/C catalyst, thereby allowing more electrocatalytic activity to be retained. This enhancement on catalyst stability was attributed to the solid acid nature of the intrinsically negatively charged RuO_2, which can restrict the diffusion of Pt^{n+} into the electrolyte. Similarly, a SnO_2/carbon nanotube composite-supported catalyst (Pt/SnO_2/CNTs) also demonstrated a higher stability than one without SnO_2 (Pt/CNTs).[78] Therefore, the modification of metal oxides on carbon supports effectively improves catalyst stability, through increasing the anti-corrosion ability of support materials and minimizing the dissolution and grain growth of Pt nanoparticles. Moreover, some metal oxide supports can work as co-catalysts to enhance the catalytic activity of Pt catalysts in electro-oxidation of ethanol, methanol, and CO.[79-80]

1.4 Metal oxide support effects

Recently, a variety of metal oxide supports have been investigated and showed co-catalytic effects on Pt-catalyzed electro-oxidation of ethanol, such as tin(IV) oxide (SnO_2), nickel(II) oxide (NiO), ruthenium(IV) oxide (RuO_2), titanium dioxide (TiO_2), molybdenum(VI) oxide (MoO_3), and iridium(IV) oxide (IrO_2).[81-86] In contrast to Pt/C catalysts, higher current densities were obtained by modification of the catalyst with metal oxides. Importantly, the introduction of metal oxide components to the catalysts was found to effectively diminish CO_{ads} poisoning, so that durability of the catalyst was improved. As examples, the support effects of RuO_2 and SnO_2 on Pt-catalyzed ethanol oxidation is discussed in the following sections.

1.4.1 Ruthenium oxide

The Ru in PtRu alloy catalysts was reported to intensively promote oxidation of the CO intermediates in methanol and ethanol oxidation. The co-catalytic effect can be explained by a bifunctional effect (Equations 1.20 and 1.21) and an electronic effect (which results in weakening the binding of CO at Pt).[87] Hydrous ruthenium oxide ($RuO_2 \cdot xH_2O$) was also found to play a similar role to Ru at the surface of PtRu.[88] Therefore, RuO_2 has been used in Pt-based catalysts to investigate how it influences electrocatalytic oxidation of ethanol and the intermediate CO_{ads}. Freitas et al. prepared $Pt_{(1-x)}(RuO_2)_x/Ti$ electrodes through thermal decomposition of Pt and Ru precursors on Ti plates at 400 °C.[74] For ethanol electro-oxidation, the performance of the electrodes prepared with different Pt-RuO_2 ratios was studied by linear sweep voltammetry. In Figure 1.4, the peaks below 1.2 V (*vs.* RHE) were mainly attributed to ethanol electro-oxidation. For $Pt_{(1-x)}(RuO_2)_x/Ti$ electrodes, the peak current density was increased with the Pt percentage. In addition, the RuO_2/Ti electrode without Pt showed no oxidation peak, which indicated Pt was the main active component to catalyze the oxidation of ethanol. However, the decrease of the percentage of RuO_2 resulted in the shift of the peak to more positive values. The region below 0.6 V (*vs.* RHE) exhibited the onset of ethanol electro-oxidation. In comparison with a Pt/Ti electrode, the addition of RuO_2 significantly increased the current density at the low potentials by more than 10 times for the $Pt_{(1-x)}(RuO_2)_x/Ti$ electrode with optimized molar ratio (Pt:RuO_2 = 1:1). The onset for ethanol electro-oxidation shifted from 0.6 to 0.4 V (*vs.* RHE). This suggests that a higher voltage efficiency can be obtained because of the lower overpotential for the $Pt_1(RuO_2)_1/Ti$.

$$Ru + H_2O \rightarrow Ru\text{-}OH + H^+ + e^- \qquad \text{(Equation 1.20)}$$

$$Ru\text{-}OH + Pt\text{-}CO \rightarrow Ru + Pt + CO_2 + H^+ \qquad \text{(Equation 1.21)}$$

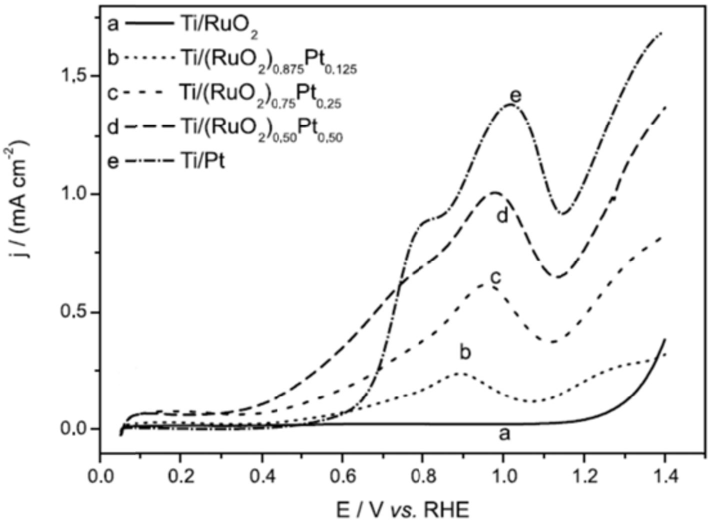

Figure 1.4. Linear sweep voltammograms obtained for electrooxidation of 0.5 M ethanol in 0.1 M $HClO_4$ on $Pt_{(1-x)}(RuO_2)_{(x)}/Ti$ electrodes. $\nu = 50$ mV s^{-1}, T = 25 °C.[74] (This article is published under an open access Creative Commons License.)

The influence of RuO_2 on Pt-catalyzed oxidation of the intermediate CO_{ads} was investigated, since CO oxidation is the limiting step of ethanol oxidation, especially at low potentials. Peng et al. studied the role of Ru components in CO electro-oxidation using carbon nanotubes (CNTs) as the support material.[89] Binary catalysts Pt/RuO_2/CNTs (Pt nanoparticles were on the outer layer), RuO_2/Pt/CNTs (the outer layer was RuO_2) and PtRu/CNTs were prepared as anode catalysts and compared with Pt/CNTs. Cyclic voltammetry analysis (two cycles) was performed on the four catalysts with pre-adsorbed CO (Figure 1.5). At Pt/CNTs, the electro-oxidation of CO_{ads} started at 0.58 V (*vs.* Ag/AgCl), and peaked at 0.70 V (*vs.* Ag/AgCl). There was no signal of CO oxidation below 0.58 V (*vs.* Ag/AgCl) for Pt/CNTs, but the other three catalysts containing Ru exhibited substantial activity for CO electro-oxidation. The potentials for the onset of electro-oxidation of

CO for the four catalysts increased in the order: Pt/RuO_2/CNTs < PtRu/CNTs < RuO_2/Pt/CNTs < Pt/CNTs. Therefore, the direct deposit of RuO_2 on the CNT support had the most significant effect on CO oxidation. The onset of CO oxidation for PtRu/CNTs was also shifted to a more negative potential in comparison with Pt/CNTs, which was attributed to the existence of hydrous ruthenium oxide ($RuO_2 \cdot xH_2O$) on the surface of a PtRu alloy catalyst.[88] In addition, the peak area of CO oxidation was proportional to the amount of oxidized CO and electrochemically active surface area. The largest peak area of Pt/RuO_2/CNTs indicated the largest utilization of Pt nanoparticles, since bare RuO_2 had no activity for CO oxidation. This arises from the improvement of Pt dispersion on RuO_2, which facilitated the formation of smaller sized Pt nanoparticles and the reduction of agglomeration of formed Pt nanoparticles. For RuO_2/Pt/CNTs, the decline of the electrochemically active surface was due to coverage of the Pt by the outer layer of RuO_2.

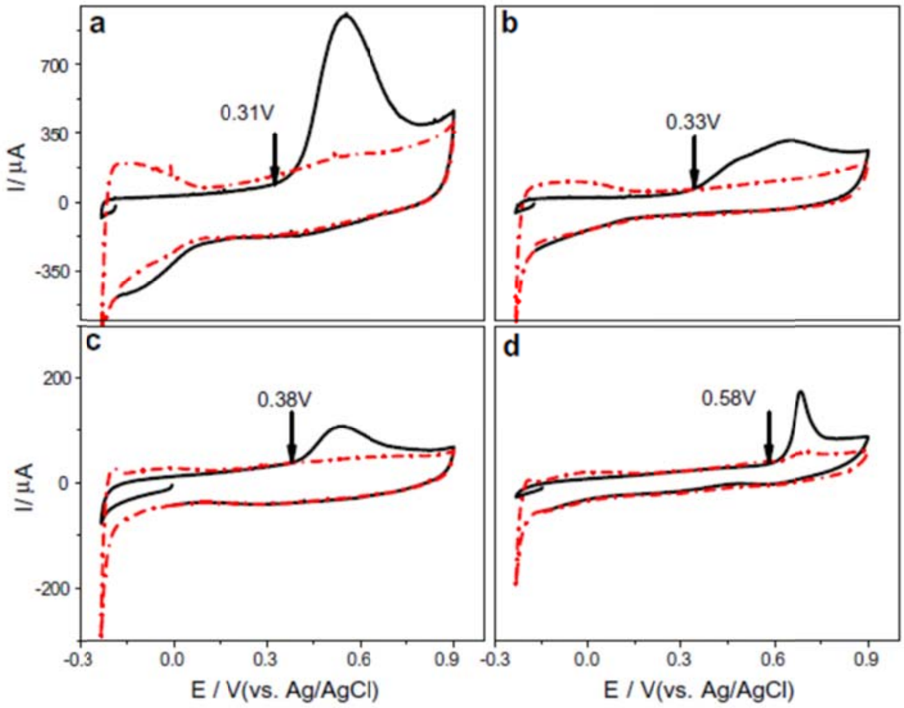

Figure 1.5. The cyclic voltammograms of pre-adsorption CO oxidation in 1 M $HClO_4$ solution for $Pt/RuO_2/CNTs$ (a), PtRu/CNTs (b), $RuO_2/Pt/CNTs$ (c) and Pt/CNTs (d) catalysts. The solid and dotted lines represent the 1st and the 2 nd cycle, respectively.[89] (Reproduced with permission of Elsevier. All rights reserved.)

The RuO_2 component added in Pt-based catalysts acts as a co-catalyst (a good water dissociator), an electrical conductor, and an anti-corrosion agent. In ethanol electro-oxidation at a Pt catalyst, the cleavage of the C-C bond of ethanol occurs at low potentials, but the further oxidation of the CO_{ads} intermediates needs the presence of Pt-OH that only forms at high potentials.[40] It was reported that the overpotential for RuO_2 to split a H_2O molecule was 0.21 V lower than Pt.[90] This implies that oxidants (e.g. hydroxyl species) are easier to be formed from water dissociation at RuO_2 than Pt. As described by the bifunctional mechanism (Equation 1.21), the hydroxyl species (Ru-OH) produced at lower potentials promotes the oxidation of intermediate CO_{ads} (Pt-CO).[87, 91] Therefore, anode catalysts containing RuO_2 can initiate the electro-oxidation of ethanol and CO at lower potentials than the bare Pt catalysts.

1.4.2 Tin oxide

Tin oxide supports have also been widely investigated and show great improvement on ethanol electro-oxidation.[40, 53, 76, 92-93] For example, Higuchi et al. studied the support effect of SnO_2 on a Pt catalyst for ethanol oxidation.[94] As shown in Figure 1.6, the linear sweep voltammograms showed that the SnO_2/C electrode without Pt had no activity on ethanol electro-oxidation. The distinct performance of Pt/SnO_2/C catalysts with different Pt:SnO_2 ratios implies that the SnO_2 support played an important role in ethanol electro-oxidation. The optimum ratio of Pt to Sn was 3:1. The catalyst containing less SnO_2 (Pt:SnO_2 = 9:1) had lower current density, and a similar voltammogram shape to the Pt/C. This was likely due to less contact occurring between Pt and SnO_2, as a result of insufficient SnO_2. However, the catalyst with more SnO_2 (Pt:SnO_2 = 1:3) resulted in an even lower oxidation current than Pt/C. The decrease of catalytic activity was attributed to the poor electronic conductivity of SnO_2. The poorer the conductivity of the catalyst, the larger the overpotential needed to perform ethanol oxidation. For the optimum catalyst, Pt/SnO_2/C (Pt:SnO_2 = 3:1), the addition of SnO_2 caused a large negative shift in the onset potential, from 0.40 to 0.20 V, in comparison with Pt/C. In addition, the current density for Pt/SnO_2(3:1)/C was significantly larger than the Pt/C in the range of 0.30-0.60 V (*vs.* RHE). The influence of SnO_2 on the onset potential and current density suggests that the SnO_2 support has a co-catalytic effect with the Pt catalyst for ethanol oxidation.[95-97]

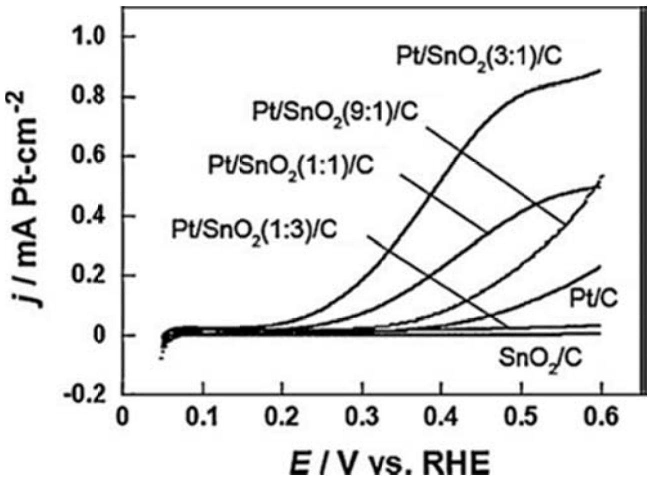

Figure 1.6. Linear sweep voltammograms for Pt/SnO$_2$(9:1)/C, Pt/SnO$_2$(3:1)/C, Pt/SnO$_2$(1:1)/C, Pt/SnO$_2$(1:3)/C, Pt/C, and SnO$_2$/C electrodes in Ar-saturated (1 M C_2H_5OH + 0.5 M H_2SO_4) solution at 30 °C. Sweep rate = 20 mV s^{-1}.[94] (Reproduced with permission of Elsevier. All rights reserved.)

The time dependence of the current density at 0.60 V (*vs.* RHE) for the Pt/SnO$_2$(3:1)/C and Pt/C is shown in Figure 1.7. The current decay was mainly caused by CO poisoning, which resulted in a loss of catalyst activity. Significantly, over a three-hour period, the current density for the Pt/SnO$_2$(3:1)/C decayed more slowly than that for the Pt/C. The improvement in the catalyst's tolerance to intermediate CO poisoning can be explained by the bifunctional and charge transfer mechanisms. The SnO$_2$ support promotes the removal of adsorbed CO from the Pt surface by providing OH species. In addition, charge transfer between Pt and SnO$_2$ makes Pt positively charged, which weakens the binding of Pt with intermediate CO.

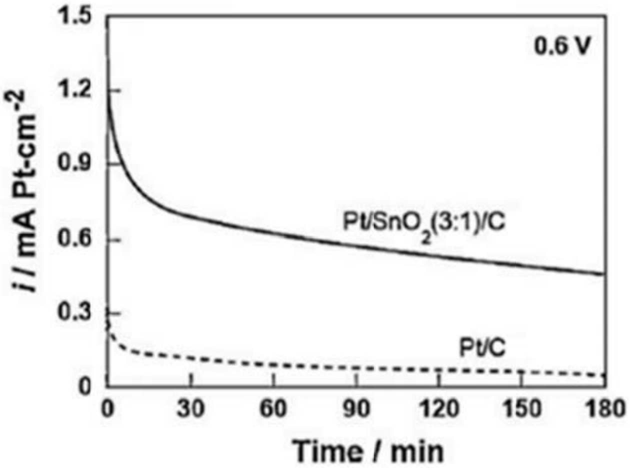

Figure 1.7. Time courses of current density at 0.60 V (*vs.* RHE) for Nafion-coated Pt/SnO_2(3:1)/C and Pt/C electrodes in Ar-saturated (1 M C_2H_5OH + 0.5 M H_2SO_4) solution at 30 ˚C.[94] (Reproduced with permission of Elsevier. All rights reserved.)

Since the intermediate CO can be strongly bonded to the Pt surface leading to a loss of its catalytic activity, it is essential to promote CO oxidation for the complete oxidation of ethanol. As presented in Figure 1.8, the CO stripping voltammograms of the Pt/SnO_2(3:1)/C and Pt/C exhibited significant enhancement in CO oxidation by the addition of SnO_2. The onset potential of CO oxidation for the Pt/SnO_2(3:1)/C negatively shifted to 0.25 V (*vs.* RHE), compared to 0.60 V (*vs.* RHE) of the Pt/C.[94] Distinctly, the Pt/SnO_2(3:1)/C showed two broad oxidation peaks at 0.45 and 0.83 V (*vs.* RHE). Specifically, the main oxidation peak at 0.83 V (*vs.* RHE) was assigned to the oxidation of strongly adsorbed CO on Pt, which negatively shifted in comparison with that of the Pt/C (0.90 V *vs.* RHE). It was proposed that the hydroxyl groups formed on SnO_2 at low potentials favor the oxidation of CO_{ads} on the Pt catalyst through the bifunctional mechanism.[98] The CO oxidation peak at 0.45 V (*vs.* RHE) was attributed to the electronic effect of Sn on CO oxidation. This effect was also observed for PtSn alloy catalyst.[99] The Sn has an electronic interaction with Pt, so that the bridge-bonded CO on the Pt surface can be oxidized at a lower potential due to its lower binding energy compared to the linearly-bonded CO.[99-100]

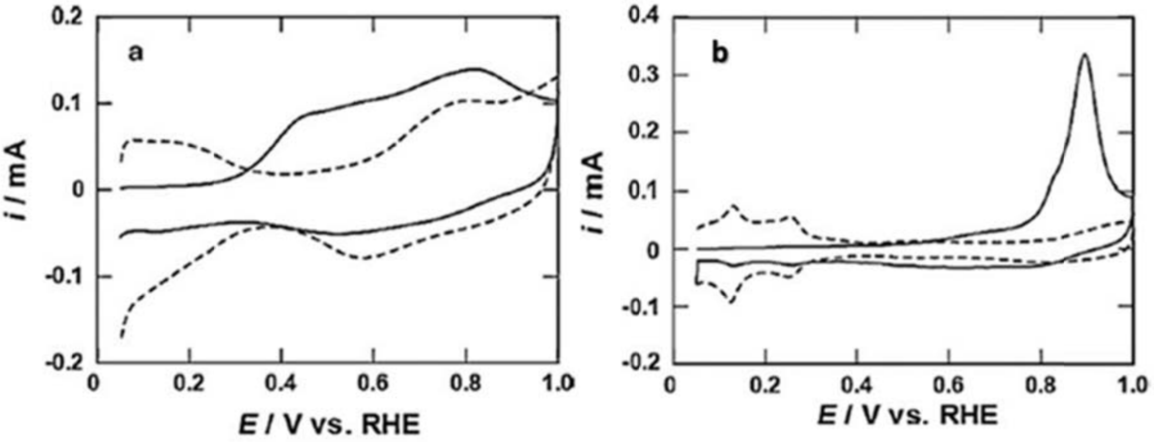

Figure 1.8. CO-stripping voltammograms (solid line) for Nafion-coated (a) Pt/SnO_2(3:1)/C and (b) Pt/C catalysts and the corresponding cyclic voltammograms (dash line) in 0.5M H_2SO_4 solution at 30 ˚C. Sweep rate = 50 mV s^{-1}.[94] (Reproduced with permission of Elsevier. All rights reserved.)

The product and intermediate analysis of ethanol oxidation on Pt/SnO_2/C has been investigated through in situ infrared reflection-absorption spectroscopy (IRRAS) and differential electrochemical mass spectrometry (DEMS). The IRRAS spectra of the Pt and Pt/SnO_2 showed chemical species on the electrode surfaces at different applied potentials for ethanol electro-oxidation (Figure 1.9 and Figure 1.10).[40] The potential was initially kept at −0.20 V (*vs.* Ag/AgCl) for 195 seconds in order to collect a background sample spectrum. Afterwards, the potential was stepped in a positive direction, and each potential was held for 180 seconds. After reaching 0.50 V (*vs.* Ag/AgCl), the potential was stepped backwards. In the range of 2500-2000 cm^{-1} (Figure

1.9), the bands at around 2050 cm^{-1} and 2343 cm^{-1} are respectively characteristic of the linear bond of adsorbed CO and the asymmetric stretching vibration of CO_2 on the electrodes. According to the IRRAS spectra of the Pt electrode, breaking of the C-C bond of ethanol occurred at low potential forming adsorbed CO. The intensity of CO increased with the potential from −0.20 to 0.20 V (*vs.* Ag/AgCl), and decreased from 0.20 to 0.50 V (*vs.* Ag/AgCl). Owing to the unavailability of forming oxidants for Pt electrode at low potential, the surface was poisoned by adsorbed CO leading to the limited CO_2 production. The further oxidation of intermediate CO to CO_2 started from 0.30 V (*vs.* Ag/AgCl). However, for the Pt/SnO_2 electrode, the complete oxidation of ethanol to CO_2 started at relatively lower potential (0.20 V *vs.* Ag/AgCl). In comparison with the Pt electrode, the lower intensity of CO and higher intensity of CO_2 at the Pt/SnO_2 electrode indicates SnO_2 promotes the oxidation of intermediate CO to CO_2. According to the change of the intensity of CO and CO_2 with potential, it can be concluded that the rate limiting step for ethanol oxidation was changed from the oxidation of CO (at lower potential) to C–C bond breaking (at higher potential). The main products of incomplete oxidation of ethanol are acetaldehyde and acetic acid. SnO_2 facilitates ethanol oxidation on Pt sites, but has no improvement in the selectivity of CO_2 production. As shown in Figure 1.10, in the range of 1350-850 cm^{-1}, the bands of 933 cm^{-1} and 1280 cm^{-1} were respectively attributed to acetaldehyde and acetic acid. The intensity of acetic acid at the Pt/SnO_2 electrode was higher than that at the Pt electrode. Therefore, the introduction of SnO_2 promotes not only the oxidation of intermediate CO of ethanol to CO_2, but also the incomplete oxidation of ethanol to acetic acid.

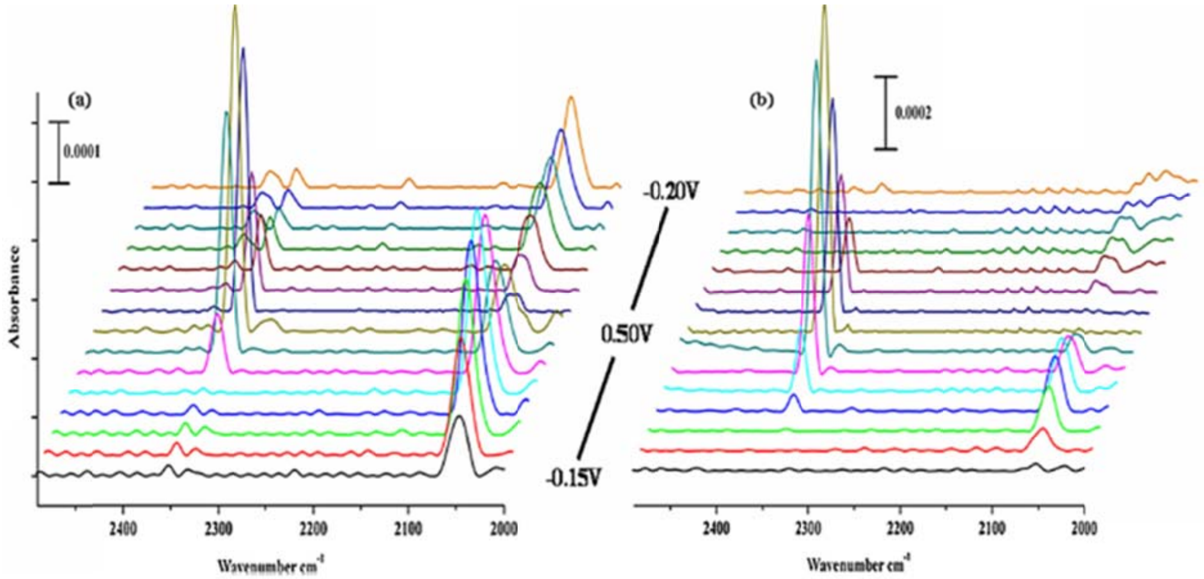

Figure 1.9. In situ IRRAS spectra in the range 2500-2000 cm^{-1} recorded during ethanol electro-oxidation in 0.5 M ethanol + 0.1 M $HClO_4$ solution: (a) a bare Pt electrode; (b) a Pt/SnO_2 electrode. The reference spectrum was taken at a potential of −0.20 V (*vs.* Ag/AgCl).[40] (Reproduced with permission of Elsevier. All rights reserved.)

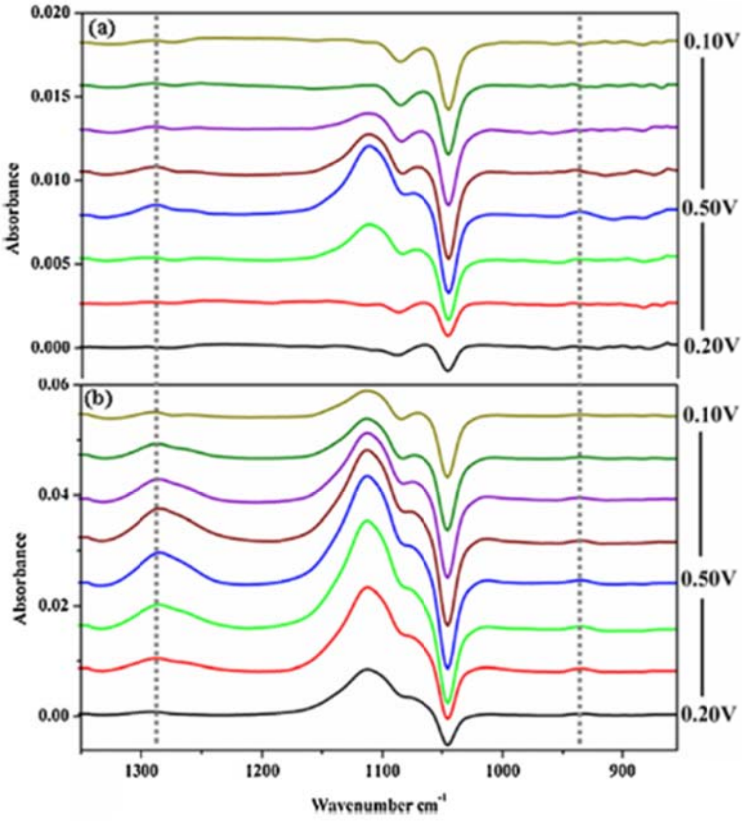

Figure 1.10. In situ IRRAS spectra in the range 1350-850 cm^{-1} recorded during ethanol electro-oxidation in 0.5 M ethanol + 0.1 M $HClO_4$ solution: (a) bare Pt electrode; (b) Pt/SnO_2 electrode. Reference spectrum was taken at a potential of −0.20 V.[40] (Reproduced with permission of Elsevier. All rights reserved.)

As a sensitive qualitative and quantitative analytical technique, DEMS combines an electrochemical cell with mass spectrometer for mechanistic study of electrochemical reactions. Through online detection of volatile intermediates and products, the potentiodynamic electro-oxidation of ethanol at SnO_2/Pt/graphene and Pt/graphene electrodes were investigated.[41] The DEMS measurement provided information about the reaction mechanism and catalyst performances. The faradaic current measured by cyclic voltammetry and the corresponding ion currents (charge) from CO_2 and acetaldehyde measured by DEMS are shown in Figure 1.11. Acetaldehyde can be measured by the mass signal (m/z = 29) of its fragment $[CHO]^+$. Both acetaldehyde and CO_2 give ion currents at the m/z = 44 mass signal. In order to exclude interference from acetaldehyde, the contribution of its interfering fragment $[CH_3CHO]^+$ at the ion current (m/z = 44) was subtracted from the total, to obtain the real CO_2 production. The ion current of $[CH_3CHO]^+$ corresponding to the ion current of $[CHO]^+$ for acetaldehyde, can be acquired by the experiment using pure acetaldehyde. The onset potentials for ethanol electro-oxidation at these two electrodes were both −0.30 V (*vs.* Hg/Hg_2SO_4). In comparison with the Pt/graphene electrode, the presence of SnO_2 negatively shifted the peak potential (the potential at which the current reaches a maxmium) from 0.30 to 0.20 V (*vs.* Hg/Hg_2SO_4). However, the onset potentials for CO_2 production at both electrodes were −0.10 V (*vs.* Hg/Hg_2SO_4), and their peak potentials were around 0.20 V (*vs.* Hg/Hg_2SO_4). Only at high potential, SnO_2/Pt/graphene electrode produced more CO_2 than the Pt/graphene electrode. Therefore, SnO_2 has no effect in decreasing the onset potential for CO_2 production in ethanol oxidation, but it promoted the removal of CO at high potential (Equation 1.22). This occurs because a higher potential is required for the oxidation of adsorbed CH_x, which is the main source of CO at the SnO_2/Pt/graphene electrode.[41] Based on the respective ion currents for acetaldehyde (Figure 1.11c), the addition of SnO_2 decreased the onset potential and peak potential for acetaldehyde production. The average yields of CO_2, acetaldehyde, and acetic acid were calculated based on DEMS data through calibration experiments. The product distributions at the SnO_2/Pt/graphene electrode showed less acetaldehyde, but more CO_2 and acetic acid than those at the Pt/graphene electrode, which agrees with the result of the IRRAS investigation. It suggests that the presence of the SnO_2 support does not improve CO_2 selectivity, but enhances the further oxidation of the intermediate acetaldehyde of ethanol oxidation to acetic acid (Equation 1.23).

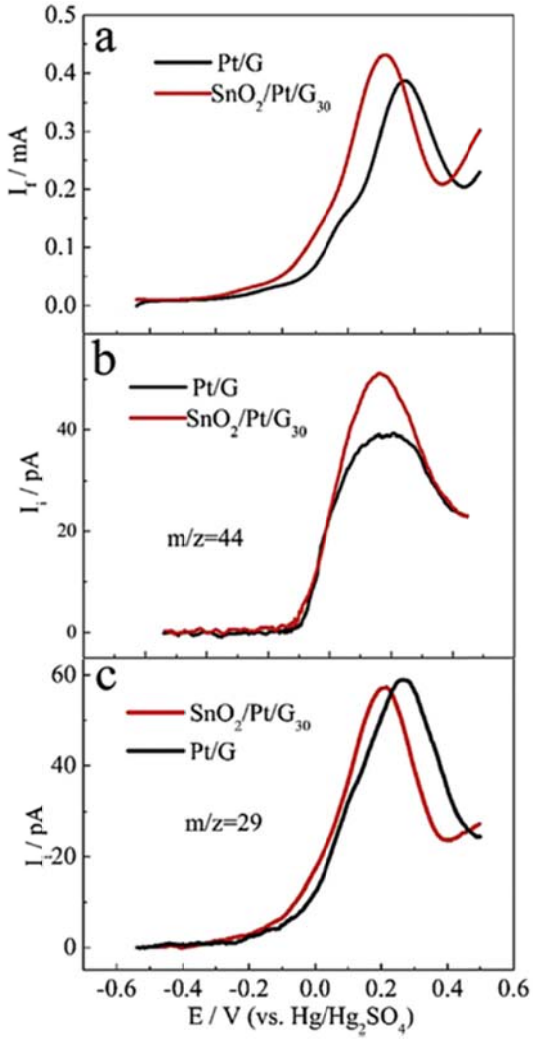

Figure 1.11. Simultaneously recorded voltammograms (a) and mass spectrometric voltammograms for *m/z* = 44 (CO_2) (b), *m/z* = 29 (acetaldehyde) (c) for ethanol oxidation on SnO_2/Pt/graphene and Pt/graphene catalysts (with same Pt contents) in 0.25 M ethanol + 0.5 M H_2SO_4 solution. Scan rate: 10 mV s^{-1}, room temperature.[41] (Reproduced with permission of Elsevier. All rights reserved.)

$Sn\text{-}OH + Pt\text{-}CO \rightarrow Sn + Pt + CO_2 + H^+$ (Equation 1.22)

$Sn\text{-}OH + Pt\text{-}CHOCH_3 \rightarrow Sn + Pt + CH_3COOH + H^+$ (Equation 1.23)

In conclusion, the use of a SnO_2 support provides abundant oxygenated groups (-OH), which promotes both the removal of CO from the Pt surface and the conversion of ethanol to acetic acid. The decrease of the onset potential of ethanol electro-oxidation resulted from the promotion of partial oxidation of ethanol to acetaldehyde with the SnO_2 support. The presence of SnO_2 had no effect on electro-catalytic splitting of the C–C bond in ethanol. In addition, SnO_2 symbiotically facilitated the removal of formed CO to enhance the current efficiency.

1.4.3 Mechanisms of metal oxide support effects

The oxidation of ethanol at Pt catalysts involves a number of elementary reactions, and includes the formation of various kinds of intermediates (e.g. CH_3CHO_{ads}, $CH_{x,ads}$, CH_yO_{ads}, and CO_{ads}). Some metal oxide supports have been confirmed to have a significant influence on electrocatalytic oxidation of ethanol and/or intermediates. This phenomenon derives from the interaction between Pt catalysts and metal oxide supports through co-catalytic (bifunctional mechanism and charge transfer mechanism), strain, and third-body effects.[81]

The co-catalytic effects of metal oxide supported Pt catalysts in ethanol electro-oxidation can be explained by bifunctional mechanism and charge transfer mechanism as illustrated in Figure 1.12.[81] The addition of metal oxides promotes the removal of the poisoning intermediate CO_{ads} at adjacent Pt with adsorbed hydroxyl species, which originate from the dissociative adsorption of water by metal oxides. The abundant hydroxyl species provided by metal oxides not only improve catalyst tolerance to CO poisoning, but also enhance the oxidation current through promoting CO_{ads} oxidation. The free Pt active sites released by CO_{ads} oxidation can adsorb further ethanol molecules for oxidation. Some metal oxides (e.g. RuO_2 and SnO_2) provide hydroxyl species at lower potentials than Pt, so that the onset of ethanol oxidation is shifted to lower potentials. Consequently, higher cell efficiency can be obtained through increase of the voltage efficiency. In addition, charge transfer by metal-support interaction can affect the catalytic activity of Pt catalysts.[101] When Pt and MO_x contact with each other, the charge tends to transfer from the one with lower electronegativity to the one with higher electronegativity due to their electronegativity difference. The second metal atom can affect the energy level of Pt, which changes the adsorption energy of the reactant, intermediates, and products during the electrocatalytic reaction. X-ray absorption spectroscopy (XAS) and X-ray photoelectron spectroscopy (XPS) are the common technologies used to investigate electronic structure of a sample through measuring the X-ray absorption coefficient and binding energy, respectively.[81, 101-103] The electronegativity change of an analyte can be determined according to the difference in absorption coefficients and binding energies. Figure 1.13 demonstrates the similar influence of MO_x supports on the integrated XAS intensity of Pt catalysts related to the current of ethanol oxidation.[82] The strong binding of CO_{ads} at Pt occurs through electron donation from CO σ to Pt and back donation from Pt to CO π^*. The higher intensity of XAS absorption indicated higher vacancy of the Pt 5d band, which resulted in weakening of the binding of CO_{ads} to Pt by weakening the back donation from Pt to CO π^*.[82, 104] This leads to an increase of the reaction kinetics of CO_{ads} oxidation. Moreover, the electronic effect of metal oxides (e.g. Ru oxide and Sn oxide) on Pt can increase water activation and Pt-OH strength, which promotes the formation of Pt-OH and CO_{ads} oxidation.[105] However, the electronic effect of the Pt-support interaction is not only influenced by the nature of a support, but also the preparation method of a catalyst and the particle sizes of Pt.[106-107] The bifunctional effect was reported to result in a more significant improvement on CO oxidation than the electronic effect for a RuO_2-supported Pt catalyst.[108]

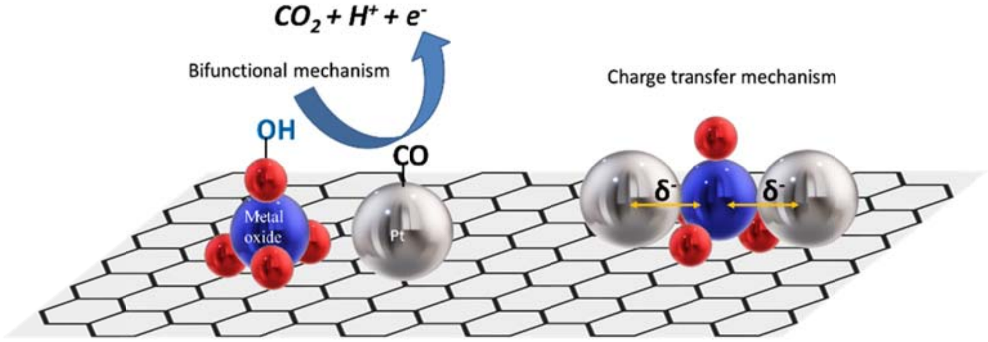

Figure 1.12. Mechanisms of metal oxide effects.[81]

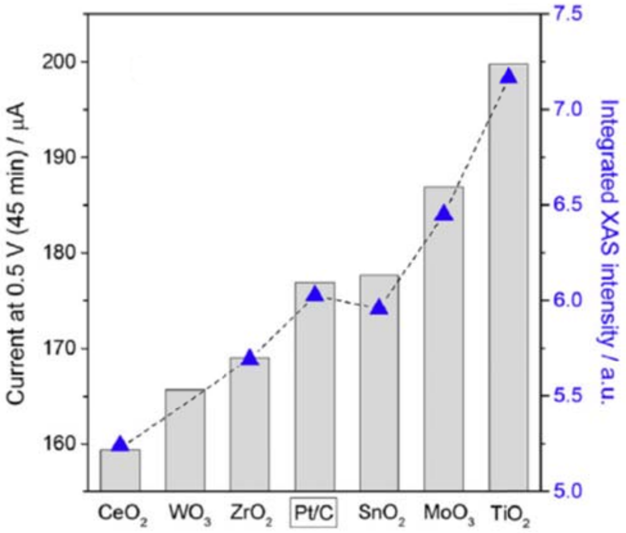

Figure 1.13. Plot of the integrated intensities of X-ray absorption (Pt L_3 signals) overlaid with the ethanol oxidation currents (in basic medium) taken after 45 min polarization at 0.50 V (*vs.* RHE) for Pt/C, $Pt/CeO_2/C$, $Pt/ZrO_2/C$, $Pt/SnO_2/C$, $Pt/MoO_3/C$, and $Pt/TiO_2/C$ catalysts.[82] (Reproduced with permission of Elsevier. All rights reserved.)

The presence of a second metal component in a Pt catalyst (e.g. PtM or Pt/MO_x) can improve the electro-oxidation of ethanol, methanol, and especially formic acid through a third body effect.[109-112] The third body effect originates from inactive adatoms at the Pt surface, which can enhance oxidation current by blocking the formation of poisoning species CO_{ads} and increase the desorption of intermediates. For ethanol electro-oxidation, the third body effect normally results in decrease of CO_2 selectivity.[112-113] The blockage of active sites by adatoms inhibits the cleavage of the C-C bond of ethanol due to lack of several adjacent Pt atoms, but promotes its oxidation to acetaldehyde and acetic acid since fewer Pt atoms are required.[114-115]

A change of lattice strain of Pt-based catalysts can affect their catalytic activity, through a strain effect.[116] Due to the addition of adatoms or different support materials in synthesis, compressive or expansive strain of Pt-Pt bonds results in an increase or decrease of *d*-orbital overlap, which modifies the electronic structure of the Pt catalysts (shift of *d*-band center position).[117-122] A Pt catalyst can be expansively strained when prepared on a substrate with larger lattice (e.g. Au), and compressively strained on a substrate with smaller lattice (e.g. Rh). A catalyst with an expansive strain was reported to have increased activity for the oxidation of ethanol and methanol, but the one with compressive strain had decreased activity.[123]

1.5 Thermal decomposition of metal acetylacetonate complexes for preparation of metal oxide supports

The traditional preparation of metal oxides (precipitation and hydrothermal methods) are time-consuming, and require corrosive reagents and high calcination temperature of above 300 °C.[76] In addition, the prepared metal oxides have inconsistent shapes (sphere and nanosheet) and particle sizes (several to hundreds of nm), which influences the activity of catalysts. Recently, thermal decomposition of metal acetylacetonate complexes (M(acac)$_x$) (Equation 1.24) has been confirmed as a versatile method for preparing metal oxides (e.g. ruthenium oxide) and complex metal oxides (e.g. indium tin oxide).[124-127] A variety of metal oxides can be synthesized at low temperatures (< 300 ˚C) by isothermal decomposition of M(acac)$_x$, such as In, Mo, Ru, and Ga oxides.[128-132]

$$M(acac)_x \rightarrow MO_x + \text{volatiles} \qquad \text{(Equation 1.24)}$$

In the ambient atmosphere, thermal decomposition of M(acac)$_x$ can proceed through three types of reactions related with temperature: (a) ligand exchange with hydroxyl groups on a substrate surface (e.g. silica) at a low temperature (Equation 1.25); (b) proton-assisted thermolysis between 150 and 300 ˚C (Equation 1.26); (c) oxidative decomposition of the remaining ligands to produce small organic fragments (e.g., acetone), water and CO_2 at above 300 ˚C (Equation 1.24).[133] The properties of support materials (e.g. silica and alumina) have a significant influence on the decomposition temperature and the structure of the MO_x produced.[124, 133] For example, thermal decomposition of M(acac)$_x$ (M = Mn, Ni, and Fe) on a TiO_2 support can occur at lower temperatures in comparison with the pure precursors without TiO_2.[134] Moreover, the MO_x particles (Ni, Co, Mn, and Fe oxides) formed on TiO_2 were amorphous nanoparticles (below 5 nm), which was different from the crystalline MO_x particles produced via thermal decomposition of pure M(acac)$_x$ without TiO_2 support. The structure difference was attributed to the strong electronic communication of MO_x-TiO_2, which restricted the mobility of surface-bounded metallic species, thereby prevented the formation of a crystalline lattice on TiO_2. The support effect on the structure of produced MO_x was also found in thermal decomposition of

$Mn(acac)_3$ and $VO(acac)_2$ on alumina supports.[135-136] A catalyst or co-catalyst with an amorphous structure usually exhibits higher catalytic activity than that with a crystalline structure because of a larger number of active sites.[137-143]

$$\text{Si-OH} + \text{M(acac)}_x \rightarrow \text{Si-O-M(acac)}_{(x-1)} + \text{Hacac} \qquad \text{(Equation 1.25)}$$

$$\text{M(acac)}_x + \text{H}_2\text{O} \rightarrow \text{HO-M(acac)}_{(x-1)} + \text{Hacac} \qquad \text{(Equation 1.26)}$$

1.6 Thesis objectives

The overall goal of this thesis was to systematically investigate the support effect of metal oxides on Pt-catalyzed ethanol oxidation, which would lead to a good understanding towards development of more efficient and cost-effective ethanol fuel cells. The following objectives were pursued in order to achieve this. The first objective of this thesis was to develop a consistent and quick methodology for preparation of various metal oxides and their mixtures with similar structures and particle sizes. The metal oxide support should be synthesized at a relatively low temperature to obtain a highly active amorphous structure (see section 1.5). In addition, the preparation process would avoid introducing the impurities of other cations (e.g. Na^+) and anions (e.g. Cl^-) to exclude their interferences. In Chapter 3, electrodes were prepared by in-situ deposition of catalysts on bulk Ti supports, which avoids separation of catalysts with a centrifuge or by filtration as well as preparation of catalyst ink, thereby being a less time-consuming method for screening catalysts. A consistent and quick methodology of $M(acac)_x$ thermal decomposition was developed to prepare two metal oxides (Ru oxide and Sn oxide) and their mixtures (Ru+Sn oxide) on Ti foil. A certain amount of preformed Pt nanoparticles was assembled on the metal oxide supports by drop coating, so that the interference of strain effect can be almost excluded.

The support effects (bifunctional and charge transfer effects) of the metal oxides on Pt-catalyzed ethanol oxidation were systematically evaluated and compared through cyclic voltammetry. Furthermore, the influence of Ru/Sn atomic ratio on ethanol oxidation was investigated by adjusting the ratio of $Ru(acac)_3$ to $Sn(acac)_2$ during the preparation of Ru+Sn oxide supports.

The second objective of this thesis was to apply the methodology of $M(acac)_x$ thermal decomposition to a carbon support for the preparation of fuel/electrolysis cell anodes to study their performance in ethanol oxidation. In Chapter 4, a carbon support with high surface area was used as the substrate to replace the Ti foil for metal oxide preparation by $M(acac)_x$ thermal decomposition. Therefore, the prepared catalysts could be loaded on carbon fiber paper and assembled in an electrolysis cell for the investigation of their catalytic activity for ethanol oxidation. Anode catalysts were synthesized by self-assembly of Pt nanoparticles evenly on the carbon supports modified with metal oxides (Ru oxide/C, Sn oxide/C, and Ru+Sn oxide/C). The electrochemical performance of the prepared catalysts was investigated by cyclic voltammetry and chronoamperometry. Afterwards, the optimal catalyst (Pt/Ru+Sn oxide/C) was further applied to an electrolysis cell as the anode for ethanol oxidation.

The third objective of this thesis was to develop a methodology for online detection of the amount of CO_2 produced from complete oxidation of ethanol in an electrolysis cell. This methodology could be used to investigate the effect of $M(acac)_x$ modification on CO_2 selectivity. In Chapter 5, $Pb(acac)_2$ modified Ti and carbon electrodes were prepared to investigate their support effects on Pt-catalyzed ethanol oxidation. Thermal decomposition of $Pb(acac)_2$ produced Pb oxide on a Ti foil, but basic lead carbonate (BLC) on a carbon support. The electrochemical properties of Pt/Pb oxide/Ti and Pt/BLC/C on ethanol oxidation were studied through cyclic voltammetry and chronoamperometry. For Pt/BLC/C catalysts, the Pb/Pt atomic ratio had a significant influence on their catalytic activity for ethanol oxidation. Moreover, the stability of the Pt/BLC/C catalyst (Pb:Pt = 0.22) was studied to explain the current decay in chronoamperometry measurements. The Pt/BLC/C catalyst was used as the anode in a 9-anode electrolysis cell for further study of its performance for ethanol oxidation. A methodology of online CO_2 detection was developed to measure the amount of CO_2 produced from complete oxidation of ethanol. The influence of $Pb(acac)_2$ modification on CO_2 selectivity was investigated for better understanding the mechanism of its enhancement on ethanol oxidation.

The final objective of this thesis was to expand the investigation of the support effects of metal oxides prepared by $M(acac)_x$ thermal decomposition. In Chapter 6, screening of catalysts for ethanol oxidation was performed among various metal oxide supported Pt catalysts. Some other metal oxide supports (Mo oxide, Mo+Sn oxide, Ga oxide, In oxide, V oxide, and Zr oxide) were quickly synthesized by $M(acac)_x$ thermal decomposition on Ti foils. The support effects of these metal oxides on Pt catalysts for ethanol oxidation were investigated by electrochemical measurements.

1.7 References

1. Al-Shetwi, A. Q.; Hannan, M.; Jern, K. P.; Mansur, M.; Mahlia, T., Grid-connected renewable energy sources: Review of the recent integration requirements and control methods. *Journal of Cleaner Production,* **2020**, *253*, 119831.

2. Deng, X.; Lv, T., Power system planning with increasing variable renewable energy: A review of optimization models. *Journal of Cleaner Production,* **2020**, *246*, 118962.

3. Andújar, J. M.; Segura, F., Fuel cells: History and updating. A walk along two centuries. *Renewable and Sustainable Energy Reviews,* **2009**, *13* (9), 2309-2322.

4. Grimes, P. In *Historical pathways for fuel cells. The new electric century*, Fifteenth Annual Battery Conference on Applications and Advances (Cat. No. 00TH8490), IEEE: 2000; pp 41-45.

5. Sharaf, O. Z.; Orhan, M. F., An overview of fuel cell technology: Fundamentals and applications. *Renewable and Sustainable Energy Reviews,* **2014**, *32*, 810-853.

6. Lucia, U., Overview on fuel cells. *Renewable and Sustainable Energy Reviews,* **2014**, *30*, 164-169.

7. Bezdek, R. H.; Wendling, R. M., Economic, environmental, and job impacts of increased efficiency in existing coal-fired power plants. *Journal of Fusion Energy,* **2013**, *32* (2), 215-220.

8. Howey, D. A.; Martinez-Botas, R.; Cussons, B.; Lytton, L., Comparative measurements of the energy consumption of 51 electric, hybrid and internal combustion engine vehicles. *Transportation Research Part D: Transport and Environment,* **2011**, *16* (6), 459-464.

9. Liu, X.; Reddi, K.; Elgowainy, A.; Lohse-Busch, H.; Wang, M.; Rustagi, N., Comparison of well-to-wheels energy use and emissions of a hydrogen fuel cell electric vehicle relative to a conventional gasoline-powered internal combustion engine vehicle. *International Journal of Hydrogen Energy,* **2020**, *45* (1), 972-983.

10. Wilberforce, T.; Alaswad, A.; Palumbo, A.; Dassisti, M.; Olabi, A.-G., Advances in stationary and portable fuel cell applications. *International Journal of Hydrogen Energy,* **2016**, *41* (37), 16509-16522.

11. Gierke, T. D.; Hsu, W. Y., The Cluster-Network Model of Ion Clustering in Perfluorosulfonated Membranes. In *Perfluorinated Ionomer Membranes*, Eisenberg, A.; Yeager, H. L., Eds. ACS Publications: 1982; Vol. 180, pp 283-307.

12. Yang, C.; Costamagna, P.; Srinivasan, S.; Benziger, J.; Bocarsly, A. B., Approaches and technical challenges to high temperature operation of proton exchange membrane fuel cells. *Journal of Power Sources,* **2001**, *103* (1), 1-9.

13. Peighambardoust, S. J.; Rowshanzamir, S.; Amjadi, M., Review of the proton exchange membranes for fuel cell applications. *International Journal of Hydrogen Energy,* **2010**, *35* (17), 9349-9384.

14. Ma, S.; Lin, M.; Lin, T.-E.; Lan, T.; Liao, X.; Maréchal, F.; Yang, Y.; Dong, C.; Wang, L., Fuel cell-battery hybrid systems for mobility and off-grid applications: A review. *Renewable and Sustainable Energy Reviews,* **2021**, *135*, 110119.

15. Wang, Y.; Chen, K. S.; Mishler, J.; Cho, S. C.; Adroher, X. C., A review of polymer electrolyte membrane fuel cells: Technology, applications, and needs on fundamental research. *Applied Energy,* **2011**, *88* (4), 981-1007.

16. Hua, T.; Ahluwalia, R.; Eudy, L.; Singer, G.; Jermer, B.; Asselin-Miller, N.; Wessel, S.; Patterson, T.; Marcinkoski, J., Status of hydrogen fuel cell electric buses worldwide. *Journal of Power Sources,* **2014**, *269*, 975-993.

17. Giacoppo, G.; Hovland, S.; Barbera, O., 2 kW Modular PEM fuel cell stack for space applications: Development and test for operation under relevant conditions. *Applied Energy,* **2019**, *242*, 1683-1696.

18. Olabi, A.; Wilberforce, T.; Abdelkareem, M. A., Fuel cell application in the automotive industry and future perspective. *Energy,* **2021**, *214*, 118955.

19. Ma, Z.; Eichman, J.; Kurtz, J., Fuel cell backup power system for grid service and microgrid in telecommunication applications. *Journal of Energy Resources Technology,* **2019**, *141* (6).

20. Bethoux, O., Hydrogen fuel cell road vehicles: State of the art and perspectives. *Energies,* **2020**, *13* (21), 5843.

21. Abdelkareem, M. A.; Lootah, M. A.; Sayed, E. T.; Wilberforce, T.; Alawadhi, H.; Yousef, B. A.; Olabi, A., Fuel cells for carbon capture applications. *Science of The Total Environment,* **2021**, *769*, 144243.

22. Badwal, S.; Giddey, S.; Kulkarni, A.; Goel, J.; Basu, S., Direct ethanol fuel cells for transport and stationary applications-A comprehensive review. *Applied Energy,* **2015**, *145*, 80-103.

23. Gautam, P.; Upadhyay, S.; Dubey, S., Bio-methanol as a renewable fuel from waste biomass: Current trends and future perspective. *Fuel,* **2020**, *273*, 117783.

24. Preuster, P.; Albert, J., Biogenic formic acid as a green hydrogen carrier. *Energy Technology,* **2018**, *6* (3), 501-509.

25. Liu, X.; Li, S.; Liu, Y.; Cao, Y., Formic acid: A versatile renewable reagent for green and sustainable chemical synthesis. *Chinese Journal of Catalysis,* **2015**, *36* (9), 1461-1475.

26. Karapinar, D.; Creissen, C. E.; Rivera de la Cruz, J. G.; Schreiber, M. W.; Fontecave, M., Electrochemical CO_2 reduction to ethanol with copper-based catalysts. *ACS Energy Letters,* **2021**, *6* (2), 694-706.

27. Bos, M.; Kersten, S.; Brilman, D., Wind power to methanol: Renewable methanol production using electricity, electrolysis of water and CO_2 air capture. *Applied Energy,* **2020**, *264*, 114672.

28. Ma, Z.; Legrand, U.; Pahija, E.; Tavares, J. R.; Boffito, D. C., From CO_2 to formic acid fuel cells. *Industrial & Engineering Chemistry Research,* **2020**, *60* (2), 803-815.

29. Friedl, J.; Stimming, U., Model catalyst studies on hydrogen and ethanol oxidation for fuel cells. *Electrochimica Acta,* **2013**, *101*, 41-58.

30. Nacef, M.; Affoune, A., Comparison between direct small molecular weight alcohols fuel cells' and hydrogen fuel cell's parameters at low and high temperature. Thermodynamic study. *International Journal of Hydrogen Energy,* **2011**, *36* (6), 4208-4219.

31. Demirci, U. B., Direct liquid-feed fuel cells: Thermodynamic and environmental concerns. *Journal of Power Sources,* **2007**, *169* (2), 239-246.

32. Kamarudin, M. Z. F.; Kamarudin, S. K.; Masdar, M. S.; Daud, W. R. W., Direct ethanol fuel cells. *International Journal of Hydrogen Energy,* **2013**, *38* (22), 9438-9453.

33. Hoa, L. Q.; Vestergaard, M. C.; Tamiya, E., Carbon-based nanomaterials in biomass-based fuel-fed fuel cells. *Sensors,* **2017**, *17* (11), 2587.

34. Shaari, N.; Kamarudin, S. K.; Bahru, R.; Osman, S. H.; Ishak, N. A. I. M., Progress and challenges: Review for direct liquid fuel cell. *International Journal of Energy Research,* **2021**, *45* (5), 6644-6688.

35. Ong, B.; Kamarudin, S. K.; Basri, S., Direct liquid fuel cells: A review. *International Journal of Hydrogen Energy,* **2017**, *42* (15), 10142-10157.

36. Zakaria, K.; Thimmappa, R.; Mamlouk, M.; Scott, K., Hydrogen generation by alcohol reforming in a tandem cell consisting of a coupled fuel cell and electrolyser. *International Journal of Hydrogen Energy,* **2020**, *45* (15), 8107-8117.

37. An, L.; Zhao, T.; Li, Y., Carbon-neutral sustainable energy technology: Direct ethanol fuel cells. *Renewable and Sustainable Energy Reviews,* **2015**, *50*, 1462-1468.

38. Dresch, M. A.; Matos, B. R.; Godoi, D. R. M.; Linardi, M.; Fonseca, F. C.; Villullas, H. d. l. M.; Santiago, E. I., Advancing direct ethanol fuel cell operation at intermediate temperature by combining Nafion-hybrid electrolyte and well-alloyed PtSn/C electrocatalyst. *International Journal of Hydrogen Energy,* **2021**, *46* (24), 13252-13264.

39. Moghaddam, R. B.; Pickup, P. G., Support effects on the oxidation of ethanol at Pt nanoparticles. *Electrochimica Acta,* **2012**, *65*, 210-215.

40. Magee, J. W.; Zhou, W.-P.; White, M. G., Promotion of Pt surfaces for ethanol electro-oxidation by the addition of small SnO_2 nanoparticles: Activity and mechanism. *Applied Catalysis B: Environmental,* **2014**, *152*, 397-402.

41. Qu, Y.; Li, C.; Wang, L.; Gao, Y.; Rao, J.; Yin, G., Mild synthesis of layer-by-layer SnO_2 nanosheet/Pt/graphene composites as catalysts for ethanol electro-oxidation. *International Journal of Hydrogen Energy,* **2016**, *41* (32), 14036-14046.

42. Wang, Y.; Zou, S.; Cai, W.-B., Recent advances on electro-oxidation of ethanol on Pt-and Pd-based catalysts: From reaction mechanisms to catalytic materials. *Catalysts,* **2015**, *5* (3), 1507-1534.

43. Léger, J.-M.; Rousseau, S.; Coutanceau, C.; Hahn, F.; Lamy, C., How bimetallic electrocatalysts does work for reactions involved in fuel cells?: Example of ethanol oxidation and comparison to methanol. *Electrochimica Acta,* **2005**, *50* (25-26), 5118-5125.

44. Vigier, F.; Coutanceau, C.; Hahn, F.; Belgsir, E.; Lamy, C., On the mechanism of ethanol electro-oxidation on Pt and PtSn catalysts: electrochemical and in situ IR reflectance spectroscopy studies. *Journal of Electroanalytical Chemistry,* **2004**, *563* (1), 81-89.

45. Lima, F.; Gonzalez, E., Ethanol electro-oxidation on carbon-supported Pt–Ru, Pt–Rh and Pt–Ru–Rh nanoparticles. *Electrochimica Acta,* **2008**, *53* (6), 2963-2971.

46. Antolini, E., Catalysts for direct ethanol fuel cells. *Journal of Power Sources,* **2007**, *170* (1), 1-12.

47. Akhairi, M.; Kamarudin, S., Catalysts in direct ethanol fuel cell (DEFC): An overview. *International Journal of Hydrogen Energy,* **2016**, *41* (7), 4214-4228.

48. Brueckner, T. M.; Pickup, P. G., Kinetics and stoichiometry of methanol and ethanol oxidation in multi-anode proton exchange membrane cells. *Journal of The Electrochemical Society,* **2017**, *164* (12), F1172.

49. Wnuk, P.; Lewera, A., On-line analysis of ethanol electrochemical oxidation process in a low-temperature direct ethanol fuel cell. *Electrochimica Acta,* **2020**, *330*, 135256.

50. Beyhan, S.; Coutanceau, C.; Léger, J.-M.; Napporn, T. W.; Kadırgan, F., Promising anode candidates for direct ethanol fuel cell: Carbon supported PtSn-based trimetallic catalysts prepared by Bönnemann method. *International Journal of Hydrogen Energy,* **2013**, *38* (16), 6830-6841.

51. Rizo, R.; Sebastián, D.; Lázaro, M. J.; Pastor, E., On the design of Pt-Sn efficient catalyst for carbon monoxide and ethanol oxidation in acid and alkaline media. *Applied Catalysis B: Environmental,* **2017**, *200*, 246-254.

52. Mostafa, E.; Ilsley, R.; Attard, G.; Baltruschat, H., Quantitative DEMS study of ethanol oxidation: Effect of surface structure and Sn surface modification. *Physical Chemistry Chemical Physics,* **2012**, *14* (46), 16115-16129.

53. Kowal, A.; Li, M.; Shao, M.; Sasaki, K.; Vukmirovic, M.; Zhang, J.; Marinkovic, N.; Liu, P.; Frenkel, A.; Adzic, R., Ternary Pt/Rh/SnO_2 electrocatalysts for oxidizing ethanol to CO_2. *Nature Materials,* **2009**, *8* (4), 325-330.

54. Soares, L. A.; Morais, C.; Napporn, T. W.; Kokoh, K. B.; Olivi, P., Beneficial effects of rhodium and tin oxide on carbon supported platinum catalysts for ethanol electrooxidation. *Journal of Power Sources,* **2016**, *315*, 47-55.

55. Samad, S.; Loh, K. S.; Wong, W. Y.; Lee, T. K.; Sunarso, J.; Chong, S. T.; Daud, W. R. W., Carbon and non-carbon support materials for platinum-based catalysts in fuel cells. *International Journal of Hydrogen Energy,* **2018**, *43* (16), 7823-7854.

56. Antolini, E., Carbon supports for low-temperature fuel cell catalysts. *Applied Catalysis B: Environmental,* **2009**, *88* (1-2), 1-24.

57. Jäger, C.; Henning, T.; Schlögl, R.; Spillecke, O., Spectral properties of carbon black. *Journal of Non-Crystalline Solids,* **1999**, *258* (1-3), 161-179.

58. Pérez-Rodríguez, S.; Pastor, E.; Lázaro, M., Electrochemical behavior of the carbon black Vulcan XC-72R: Influence of the surface chemistry. *International Journal of Hydrogen Energy,* **2018**, *43* (16), 7911-7922.

59. Dong, L.; Gari, R. R. S.; Li, Z.; Craig, M. M.; Hou, S., Graphene-supported platinum and platinum–ruthenium nanoparticles with high electrocatalytic activity for methanol and ethanol oxidation. *Carbon,* **2010**, *48* (3), 781-787.

60. Khotseng, L.; Bangisa, A.; Modibedi, R. M.; Linkov, V., Electrochemical evaluation of Pt-based binary catalysts on various supports for the direct methanol fuel cell. *Electrocatalysis,* **2016**, *7* (1), 1-12.

61. Nguyen, S. T.; Lee, J.-M.; Yang, Y.; Wang, X., Excellent durability of substoichiometric titanium oxide as a catalyst support for Pd in alkaline direct ethanol fuel cells. *Industrial & Engineering Chemistry Research,* **2012**, *51* (30), 9966-9972.

62. Liang, Y.; Cui, Z.; Zhu, S.; Liu, Y.; Yang, X., Silver nanoparticles supported on TiO_2 nanotubes as active catalysts for ethanol oxidation. *Journal of Catalysis,* **2011**, *278* (2), 276-287.

63. Chhina, H.; Campbell, S.; Kesler, O., Ex situ evaluation of tungsten oxide as a catalyst support for PEMFCs. *Journal of The Electrochemical Society,* **2007**, *154* (6), B533.

64. Rajesh, B.; Karthik, V.; Karthikeyan, S.; Thampi, K. R.; Bonard, J.-M.; Viswanathan, B., Pt-WO_3 supported on carbon nanotubes as possible anodes for direct methanol fuel cells. *Fuel,* **2002**, *81* (17), 2177-2190.

65. Bahadur, J.; Ghahremani, A. H.; Martin, B.; Druffel, T.; Sunkara, M. K.; Pal, K., Solution processed Mo doped SnO_2 as an effective ETL in the fabrication of low temperature planer perovskite solar cell under ambient conditions. *Organic Electronics*, **2019**, 67, 159-167.

66. Takasaki, F.; Matsuie, S.; Takabatake, Y.; Noda, Z.; Hayashi, A.; Shiratori, Y.; Ito, K.; Sasaki, K., Carbon-free Pt electrocatalysts supported on SnO_2 for polymer electrolyte fuel cells: Electrocatalytic activity and durability. *Journal of The Electrochemical Society,* **2011**, *158* (10), B1270.

67. Zambrano, J.; Min, B., Comparison on efficiency of electrochemical phenol oxidation in two different supporting electrolytes (NaCl and Na_2SO_4) using Pt/Ti electrode. *Environmental Technology & Innovation,* **2019**, *15*, 100382.

68. Zhang, Y.; Qi, Y.; Yin, Z.; Wang, H.; He, B.; Liang, X.; Li, J.; Li, Z., Nano-V_2O_5/Ti porous membrane electrode with enhanced electrochemical activity for the high-efficiency oxidation of cyclohexane. *Green Chemistry,* **2018**, *20* (17), 3944-3953.

69. Tavella, F.; Ampelli, C.; Leonardi, S. G.; Neri, G., Photo-electrochemical sensing of dopamine by a novel porous TiO_2 array-modified screen-printed Ti electrode. *Sensors,* **2018**, *18* (10), 3566.

70. Zhang, Y.; Xu, S.; Xiao, X.; Liu, Y.; Qian, Y.; Li, Y., Single gold nanowire electrodes and single Pt@ Au nanowire electrodes: Electrochemistry and applications. *Chemical Communications,* **2017**, *53* (19), 2850-2853.

71. Wang, D.; Hua, H.; Liu, Y.; Tang, H.; Li, Y., Single Ag nanowire electrodes and single Pt@ Ag nanowire electrodes: Fabrication, electrocatalysis, and surface-enhanced raman scattering applications. *Analytical Chemistry,* **2019**, *91* (7), 4291-4295.

72. Yuan, G.; Wang, L.; Zhang, X.; Luque, R.; Wang, Q., Electrochemical valorization of carboxylates in aqueous solution for the production of biofuels, fine chemicals, and hydrogen. *Green Chemistry,* **2020**, *22* (2), 525-531.

73. Han, J.; Yang, L.; Yang, L.; Jiang, W.; Luo, X.; Luo, S., PtRu nanoalloys loaded on graphene and TiO_2 nanotubes co-modified Ti wire as an active and stable methanol oxidation electrocatalyst. *International Journal of Hydrogen Energy,* **2018**, *43* (15), 7338-7346.

74. Freitas, R. G.; Marchesi, L. F. Q.; Forim, M. R.; Bulhões, L. O.; Pereira, E. C.; Santos, M. C.; Oliveira, R. T., Ethanol electrooxidation using Ti/(RuO_2)(x) Pt (1-x) electrodes prepared by the polymeric precursor method. *Journal of the Brazilian Chemical Society,* **2011**, *22* (9), 1709-1717.

75. Chang, L.; Chen, B.; Qiao, H.; Huang, H.; Guo, Z.; He, Y.; Xu, R.; Xionghui, X., Study of the effects of pretreatment processing on the properties of metal oxide coatings on Ti-based sheet. *Journal of The Electrochemical Society,* **2021**, *168* (3), 033501.

76. Kuriganova, A.; Leontyeva, D.; Ivanov, S.; Bund, A.; Smirnova, N., Electrochemical dispersion technique for preparation of hybrid MO x-C supports and Pt/MO_x-C electrocatalysts for low-temperature fuel cells. *Journal of Applied Electrochemistry,* **2016**, *46* (12), 1245-1260.

77. Saida, T.; Sugimoto, W.; Takasu, Y., Enhanced activity and stability of Pt/C fuel cell anodes by the modification with ruthenium-oxide nanosheets. *Electrochimica Acta,* **2010**, *55* (3), 857-864.

78. Li, J. J.; Wang, J. S.; Guo, X.; Zhao, J. H.; Song, C. Y.; Wang, L. C., Improving the stability and ethanol electro-oxidation activity of Pt catalysts by selectively anchoring Pt particles on carbon-nanotubes-supported-SnO_2. *Fuel Cells,* **2012**, *12* (5), 898-903.

79. Zhang, Z.; Liu, J.; Gu, J.; Su, L.; Cheng, L., An overview of metal oxide materials as electrocatalysts and supports for polymer electrolyte fuel cells. *Energy & Environmental Science,* **2014**, *7* (8), 2535-2558.

80. Hua, H.; Hu, C.; Zhao, Z.; Liu, H.; Xie, X.; Xi, Y., Pt nanoparticles supported on submicrometer-sized TiO_2 spheres for effective methanol and ethanol oxidation. *Electrochimica Acta,* **2013**, *105*, 130-136.

81. Alvarenga, G.; Villullas, H., Transition metal oxides in the electrocatalytic oxidation of methanol and ethanol on noble metal nanoparticles. *Current Opinion in Electrochemistry,* **2017**, *4* (1), 39-44.

82. Godoi, D. R.; Villullas, H. M.; Zhu, F.-C.; Jiang, Y.-X.; Sun, S.-G.; Guo, J.; Sun, L.; Chen, R., A comparative investigation of metal-support interactions on the catalytic activity of Pt nanoparticles for ethanol oxidation in alkaline medium. *Journal of Power Sources,* **2016**, *311*, 81-90.

83. Tabet-Aoul, A.; Saidani, F.; Rochefort, D.; Mohamedi, M., Pulsed laser synthesis of SnO_2-Pt nano-thin films onto carbon nanotubes and their electrocatalytic activity towards ethanol oxidation. *International Journal of Electrochemical Science,* **2011**, *6* (12), 6385-6397.

84. Hasan, M.; Newcomb, S. B.; Razeeb, K. M., Porous core/shell Ni@ NiO/Pt hybrid nanowire arrays as a high efficient electrocatalyst for alkaline direct ethanol fuel cells. *Journal of The Electrochemical Society,* **2012**, *159* (7), F203.

85. De, A.; Datta, J.; Haldar, I.; Biswas, M., Catalytic intervention of MoO_3 toward ethanol oxidation on PtPd nanoparticles decorated MoO_3-polypyrrole composite support. *ACS Applied Materials & Interfaces,* **2016**, *8* (42), 28574-28584.

86. Miecznikowski, K., Enhancement of activity of PtRh nanoparticles towards oxidation of ethanol through modification with molybdenum oxide or tungsten oxide. *Journal of Solid State Electrochemistry,* **2012**, *16* (8), 2723-2731.

87. Tian, M.; Shi, S.; Shen, Y.; Yin, H., PtRu alloy nanoparticles supported on nanoporous gold as an efficient anode catalyst for direct methanol fuel cell. *Electrochimica Acta,* **2019**, *293*, 390-398.

88. Rolison, D. R.; Hagans, P. L.; Swider, K. E.; Long, J. W., Role of hydrous ruthenium oxide in Pt-Ru direct methanol fuel cell anode electrocatalysts: The importance of mixed electron/proton conductivity. *Langmuir,* **1999**, *15* (3), 774-779.

89. Peng, F.; Zhou, C.; Wang, H.; Yu, H.; Liang, J.; Yang, J., The role of RuO_2 in the electrocatalytic oxidation of methanol for direct methanol fuel cell. *Catalysis Communications,* **2009**, *10* (5), 533-537.

90. Kong, X.; Xu, K.; Zhang, C.; Dai, J.; Norooz Oliaee, S.; Li, L.; Zeng, X.; Wu, C.; Peng, Z., Free-standing two-dimensional Ru nanosheets with high activity toward water splitting. *ACS Catalysis,* **2016**, *6* (3), 1487-1492.

91. Lee, M. J.; Kang, J. S.; Kang, Y. S.; Chung, D. Y.; Shin, H.; Ahn, C.-Y.; Park, S.; Kim, M.-J.; Kim, S.; Lee, K.-S., Understanding the bifunctional effect for removal of CO poisoning: Blend of a platinum nanocatalyst and hydrous ruthenium oxide as a model system. *ACS Catalysis,* **2016**, *6* (4), 2398-2407.

92. Wang, X.; Hu, X.; Huang, J.; Zhang, W.; Ji, W.; Hui, Y.; Yao, X., Electrospinning synthesis of porous carbon fiber supported Pt-SnO_2 anode catalyst for direct ethanol fuel cell. *Solid State Sciences,* **2019**, *94*, 64-69.

93. Du, W.; Yang, G.; Wong, E.; Deskins, N. A.; Frenkel, A. I.; Su, D.; Teng, X., Platinum-tin oxide core-shell catalysts for efficient electro-oxidation of ethanol. *Journal of the American Chemical Society,* **2014**, *136* (31), 10862-10865.

94. Higuchi, E.; Miyata, K.; Takase, T.; Inoue, H., Ethanol oxidation reaction activity of highly dispersed Pt/SnO_2 double nanoparticles on carbon black. *Journal of Power Sources,* **2011**, *196* (4), 1730-1737.

95. Baranova, E. A.; Tavasoli, A.; Amir, T., Particle size effect of unsupported Pt/SnO_x nanoparticles for ethanol electro-oxidation. *Electrocatalysis,* **2011**, *2* (2), 89-95.

96. Hsu, R. S.; Higgins, D.; Chen, Z., Tin-oxide-coated single-walled carbon nanotube bundles supporting platinum electrocatalysts for direct ethanol fuel cells. *Nanotechnology,* **2010**, *21* (16), 165705.

97. Santos, A. L.; Profeti, D.; Olivi, P., Electrooxidation of methanol on Pt microparticles dispersed on SnO_2 thin films. *Electrochimica Acta,* **2005**, *50* (13), 2615-2621.

98. Huang, H.; Hayes, E. T. C.; Gianolio, D.; Cibin, G.; Hage, F. S.; Ramasse, Q. M.; Russell, A. E., Role of SnO_2 in the bifunctional mechanism of CO oxidation at Pt-SnO_2 electrocatalysts. *ChemElectroChem,* **2021**, *8* (13), 2572-2582.

99. Lim, D.-H.; Choi, D.-H.; Lee, W.-D.; Park, D.-R.; Lee, H.-I., The effect of Sn addition on a Pt/C electrocatalyst synthesized by borohydride reduction and hydrothermal treatment for a low-temperature fuel cell. *Electrochemical and Solid State Letters,* **2007**, *10* (5), B87.

100. Greeley, J.; Nørskov, J. K.; Mavrikakis, M., Electronic structure and catalysis on metal surfaces. *Annual Review of Physical Chemistry,* **2002**, *53* (1), 319-348.

101. Monyoncho, E. A.; Ntais, S.; Brazeau, N.; Wu, J. J.; Sun, C. L.; Baranova, E. A., Role of the metal ‐ oxide support in the catalytic activity of Pd nanoparticles for ethanol electrooxidation in alkaline media. *ChemElectroChem,* **2016**, *3* (2), 218-227.

102. Venturini, S. I.; Antolini, E.; Perez, J., Effect of CeO_2 presence on the electronic structure and the activity for ethanol oxidation of carbon supported Pt. *Catalysts,* **2021**, *11* (5), 579.

103. Anniyev, T.; Ogasawara, H.; Ljungberg, M. P.; Wikfeldt, K. T.; MacNaughton, J. B.; Näslund, L.-Å.; Bergmann, U.; Koh, S.; Strasser, P.; Pettersson, L. G. M., Complementarity between high-energy photoelectron and L-edge spectroscopy for probing the electronic structure of 5d transition metal catalysts. *Physical Chemistry Chemical Physics,* **2010**, *12* (21), 5694-5700.

104. Hammer, B.; Morikawa, Y.; Nørskov, J. K., CO chemisorption at metal surfaces and overlayers. *Physical Review Letters,* **1996**, *76* (12), 2141.

105. Melke, J.; Schoekel, A.; Dixon, D.; Cremers, C.; Ramaker, D. E.; Roth, C., Ethanol oxidation on carbon-supported Pt, PtRu, and PtSn catalysts studied by operando X-ray absorption spectroscopy. *The Journal of Physical Chemistry C,* **2010**, *114* (13), 5914-5925.

106. Ciapina, E. G.; Santos, S. F.; Gonzalez, E. R., The electro-oxidation of carbon monoxide and ethanol on supported Pt nanoparticles: The influence of the support and catalyst microstructure. *Journal of Solid State Electrochemistry,* **2013**, *17* (7), 1831-1842.

107. Liu, L.; Corma, A., Metal catalysts for heterogeneous catalysis: From single atoms to nanoclusters and nanoparticles. *Chemical Reviews,* **2018**, *118* (10), 4981-5079.

108. Lu, C.; Rice, C.; Masel, R.; Babu, P.; Waszczuk, P.; Kim, H.; Oldfield, E.; Wieckowski, A., UHV, electrochemical NMR, and electrochemical studies of platinum/ruthenium fuel cell catalysts. *The Journal of Physical Chemistry B,* **2002**, *106* (37), 9581-9589.

109. Figueiredo, M. C.; Sorsa, O.; Doan, N.; Pohjalainen, E.; Hildebrand, H.; Schmuki, P.; Wilson, B. P.; Kallio, T., Direct alcohol fuel cells: Increasing platinum performance by modification with sp-group metals. *Journal of Power Sources,* **2015**, *275*, 341-350.

110. Rutkowska, I. A.; Wadas, A.; Kulesza, P. J., Enhancement of oxidative electrocatalytic properties of platinum nanoparticles by supporting onto mixed WO_3/ZrO_2 matrix. *Applied Surface Science,* **2016**, *388*, 616-623.

111. Liu, Y.-T.; Yuan, Q.-B.; Duan, D.-H.; Zhang, Z.-L.; Hao, X.-G.; Wei, G.-Q.; Liu, S.-B., Electrochemical activity and stability of core-shell Fe_2O_3/Pt nanoparticles for methanol oxidation. *Journal of Power Sources,* **2013**, *243*, 622-629.

112. Figueiredo, M. C.; Santasalo-Aarnio, A.; Vidal-Iglesias, F. J.; Solla-Gullón, J.; Feliu, J. M.; Kontturi, K.; Kallio, T., Tailoring properties of platinum supported catalysts by irreversible adsorbed adatoms toward ethanol oxidation for direct ethanol fuel cells. *Applied Catalysis B: Environmental,* **2013**, *140*, 378-385.

113. Altarawneh, R. M.; Brueckner, T. M.; Chen, B.; Pickup, P. G., Product distributions and efficiencies for ethanol oxidation at PtNi octahedra. *Journal of Power Sources,* **2018**, *400*, 369-376.

114. Sheng, T.; Qiu, C.; Lin, X.; Lin, W.-F.; Sun, S.-G., Insights into ethanol electro-oxidation over solvated Pt (100): Origin of selectivity and kinetics revealed by DFT. *Applied Surface Science,* **2020**, *533*, 147505.

115. Figueiredo, M. C.; Arán-Ais, R. M.; Feliu, J. M.; Kontturi, K.; Kallio, T., Pt catalysts modified with Bi: Enhancement of the catalytic activity for alcohol oxidation in alkaline media. *Journal of Catalysis,* **2014**, *312*, 78-86.

116. Kim, D.-S.; Kim, C.; Kim, J.-K.; Kim, J.-H.; Chun, H.-H.; Lee, H.; Kim, Y.-T., Enhanced electrocatalytic performance due to anomalous compressive strain and superior electron retention properties of highly porous Pt nanoparticles. *Journal of Catalysis,* **2012**, *291*, 69-78.

117. Frenkel, A. I.; Small, M. W.; Smith, J. G.; Nuzzo, R. G.; Kvashnina, K. O.; Tromp, M., An in situ study of bond strains in 1 nm Pt catalysts and their sensitivities to cluster-support and cluster-adsorbate interactions. *The Journal of Physical Chemistry C,* **2013**, *117* (44), 23286-23294.

118. Wang, H.; Liu, Z.; Ji, S.; Wang, K.; Zhou, T.; Wang, R., Ethanol oxidation activity and structure of carbon-supported Pt-modified PdSn-SnO_2 influenced by different stabilizers. *Electrochimica Acta,* **2013**, *108*, 833-840.

119. Marinkovic, N. S.; Li, M.; Adzic, R. R., Pt-based catalysts for electrochemical oxidation of ethanol. *Topics in Current Chemistry,* **2019**, *377*, 11.

120. Kitchin, J. R.; Nørskov, J. K.; Barteau, M. A.; Chen, J. G., Modification of the surface electronic and chemical properties of Pt (111) by subsurface 3d transition metals. *The Journal of Chemical Physics,* **2004**, *120* (21), 10240-10246.

121. Yao, Y.; Hu, S.; Chen, W.; Huang, Z.-Q.; Wei, W.; Yao, T.; Liu, R.; Zang, K.; Wang, X.; Wu, G., Engineering the electronic structure of single atom Ru sites via compressive strain boosts acidic water oxidation electrocatalysis. *Nature Catalysis,* **2019**, *2* (4), 304-313.

122. Strasser, P.; Koh, S.; Anniyev, T.; Greeley, J.; More, K.; Yu, C.; Liu, Z.; Kaya, S.; Nordlund, D.; Ogasawara, H., Lattice-strain control of the activity in dealloyed core-shell fuel cell catalysts. *Nature Chemistry,* **2010**, *2* (6), 454-460.

123. Li, M.; Liu, P.; Adzic, R. R., Platinum monolayer electrocatalysts for anodic oxidation of alcohols. *The Journal of Physical Chemistry Letters,* **2012**, *3* (23), 3480-3485.

124. Plyuto, Y. V.; Babich, I. V.; Sharanda, L. F.; De Wit, A. M.; Mol, J. C., Thermolysis of Ru $(acac)_3$ supported on silica and alumina. *Thermochimica Acta,* **1999**, *335* (1-2), 87-91.

125. Miyazaki, H.; Matsui, H.; Nagano, T.; Karuppuchamy, S.; Ito, S.; Yoshihara, M., Synthesis and electronic behaviors of TiO_2/carbon clusters/Cr_2O_3 composite materials. *Applied Surface Science,* **2008**, *254* (22), 7365-7369.

126. Matsui, H.; Saito, Y.; Karuppuchamy, S.; Yoshihara, M., The electronic behaviors of TiO_2/MnO_2/carbon clusters composite materials obtained by the calcination of a TiO $(acac)_2$/Mn $(acac)_3$/epoxy resin complex. *Current Applied Physics,* **2009**, *9* (6), 1203-1209.

127. Szkutnik, P. D.; Rapenne, L.; Roussel, H.; Lachaud, C.; Lahootun, V.; Weiss, F.; Jiménez, C., Influence of precursor nature on the thermal growth of tin-indium oxide layers by MOCVD. *Surface and Coatings Technology,* **2013**, *230*, 305-311.

128. Mahfouz, R. M.; Al-Ahmari, S.; Al-Fawaz, A.; Al-Othman, Z.; Warad, I. K.; Siddiqui, M. R. H., Kinetic analysis for non-isothermal decomposition of unirradiated and γ-irradiated indium acetyl acetonate. *Materials Research,* **2011**, *14* (1), 7-10.

129. Ganchev, M.; Sendova-Vassileva, M.; Popkirov, G.; Vitanov, P. In *Thermal treatment of solution-processed nano-sized thin films of molybdenum oxide*, Journal of Physics: Conference Series, IOP Publishing: 2016; p 012011.

130. Mahfouz, R. M.; Siddiqui, M. R. H.; Al-Ahmari, S. A.; Alkayali, W. Z., Kinetic analysis of thermal decomposition of unirradiated and γ-irradiated tris(acetylacetonato)-ruthenium(III) [Ru $(acac)_3$]. *Progress in Reaction Kinetics and Mechanism,* **2007**, *32* (1), 1-27.

131. Musić, S.; Popović, S.; Maljković, M.; Furić, K.; Gajović, A., Formation of RuO_2 and Ru by thermal decomposition of ruthenium(III)-acetylacetonate. *Journal of Materials Science Letters,* **2002**, *21* (14), 1131-1134.

132. Mahfouz, R. M.; Al-Khamis, K. M.; Siddiqui, M. R. H.; Al-Hokbany, N. S.; Warad, I.; Al-Andis, N. M., Kinetic studies of isothermal decomposition of unirradiated and γ-irradiated gallium acetylacetonate: New route for synthesis of gallium oxide nanoparticles. *Progress in Reaction Kinetics and Mechanism,* **2012**, *37* (3), 249-262.

133. Van Der Voort, P.; White, M. G.; Vansant, E. F., Thermal decomposition of $VO(acac)_2$ deposited on the surfaces of silica and alumina. *Langmuir,* **1998**, *14* (1), 106-112.

134. Schubert, J. S.; Popovic, J.; Haselmann, G. M.; Nandan, S. P.; Wang, J.; Giesriegl, A.; Cherevan, A. S.; Eder, D., Immobilization of Co, Mn, Ni and Fe oxide co-catalysts on TiO_2 for photocatalytic water splitting reactions. *Journal of Materials Chemistry A,* **2019**, *7* (31), 18568-18579.

135. Babich, I. V.; Davydenko, L. A.; Sharanda, L. F.; Plyuto, Y. V.; Makkee, M.; Moulijn, J. A., Oxidative thermolysis of $Mn(acac)_3$ on the surface of γ-alumina support. *Thermochimica Acta,* **2007**, *456* (2), 145-151.

136. Baltes, M.; Collart, O.; Van Der Voort, P.; Vansant, E., Synthesis of supported transition metal oxide catalysts by the designed deposition of acetylacetonate complexes. *Langmuir,* **1999**, *15* (18), 5841-5845.

137. Duan, Y.; Yu, Z. Y.; Hu, S. J.; Zheng, X. S.; Zhang, C. T.; Ding, H. H.; Hu, B. C.; Fu, Q. Q.; Yu, Z. L.; Zheng, X., Scaled‐up synthesis of amorphous NiFeMo oxides and their rapid

surface reconstruction for superior oxygen evolution catalysis. *Angewandte Chemie,* **2019**, *131* (44), 15919-15924.

138. Wachs, I. E., Recent conceptual advances in the catalysis science of mixed metal oxide catalytic materials. *Catalysis Today,* **2005**, *100* (1-2), 79-94.

139. Indra, A.; Menezes, P. W.; Sahraie, N. R.; Bergmann, A.; Das, C.; Tallarida, M.; Schmeißer, D.; Strasser, P.; Driess, M., Unification of catalytic water oxidation and oxygen reduction reactions: Amorphous beat crystalline cobalt iron oxides. *Journal of the American Chemical Society,* **2014**, *136* (50), 17530-17536.

140. Cai, W.; Chen, R.; Yang, H.; Tao, H. B.; Wang, H.-Y.; Gao, J.; Liu, W.; Liu, S.; Hung, S.-F.; Liu, B., Amorphous versus crystalline in water oxidation catalysis: A case study of NiFe alloy. *Nano letters,* **2020**, *20* (6), 4278-4285.

141. Zhang, C.; Fagan, R. D.; Smith, R. D.; Moore, S. A.; Berlinguette, C. P.; Trudel, S., Mapping the performance of amorphous ternary metal oxide water oxidation catalysts containing aluminium. *Journal of Materials Chemistry A,* **2015**, *3* (2), 756-761.

142. Kuai, L.; Geng, J.; Chen, C.; Kan, E.; Liu, Y.; Wang, Q.; Geng, B., A reliable aerosol ‐ spray ‐ assisted approach to produce and optimize amorphous metal oxide catalysts for electrochemical water splitting. *Angewandte Chemie International Edition,* **2014**, *53* (29), 7547-7551.

143. Zhang, C.; Trudel, S.; Berlinguette, C. P., Water oxidation catalysis: Survey of amorphous binary metal oxide films containing lanthanum and late 3d transition metals. *European Journal of Inorganic Chemistry,* **2014**, *2014* (4), 660-664.

Chapter 2

Experimental

2.1 Chemicals and materials

The following chemicals and materials were used as received: ruthenium(III) acetylacetonate (Ru(acac)$_3$, Sigma-Aldrich), tin(II) acetylacetonate (Sn(acac)$_2$, Sigma-Aldrich), lead(II) acetylacetonate (Pb(acac)$_2$, Sigma-Aldrich), indium(III) acetylacetonate (In(acac)$_3$, Sigma-Aldrich), bis(acetylacetonato) dioxomolybdenum(VI) (MoO$_2$(acac)$_2$, Sigma-Aldrich), gallium(III) acetylacetonate (Ga(acac)$_3$, Sigma-Aldrich), vanadyl acetylacetonate (VO(acac)$_2$, Sigma-Aldrich), zirconium(IV) acetylacetonate (Zr(acac)$_4$, Sigma-Aldrich), dihydrogen hexachloroplatinate(IV) hexahydrate ($H_2PtCl_6 \cdot 6H_2O$, Pressure Chemical Co.), sodium citrate (Sigma-Aldrich), sodium borohydride ($NaBH_4$, BDH Chemicals), methanol (ACP Chemicals), anhydrous ethanol (Commercial Alcohols Inc.), 1-propanol (Sigma-Aldrich), 2-propanol (Caledon), formic acid (Sigma-Aldrich), sulphuric acid (Fisher Scientific), hydrogen peroxide (30%, ACP Chemicals Inc.), Nafion solution (5%, DuPont), titanium foil (0.25 mm thick, Sigma Aldrich), titanium foil (0.025 mm thick, Sigma Aldrich), carbon black (C, Vulcan XC-72, Cabot), carbon fibre paper (CFP, Toray^{TM}), and HiSPEC 13100 70% Pt on advanced carbon (Alfa Aesar). Distilled-deionized water was used throughout. High purity nitrogen (Praxair Canada Inc.) was used in electrochemical measurements.

Before using, the pre-treatment of commercial proton exchange membranes was performed as follows:[1] square pieces (ca. 4.5 × 4.5 cm) cut from as-received Nafion™ 117 membranes were heated in 3% H_2O_2 (aq) at 80 °C with stirring for 1 h, followed by rinse and immersion in distilled water for 15 min at ambient temperature. Afterwards, the membranes were heated in 1 M H_2SO_4 (aq) at 80 °C with stirring for 1 h. Finally, the membranes were heated in deionized water at 80°C with stirring for 3 h, then rinsed and stored in deionized water.

2.2 Preparation of electrodes and membrane electrode assemblies (MEAs)

Ti electrodes (3.0 × 0.5 cm) were prepared by cutting a Ti foil (0.25 mm thick), and the catalysts were deposited at the end of the electrode (area: 0.5 × 0.5 cm). Carbon black/carbon fiber paper (C/CFP) electrodes were prepared by the spray painting method. Firstly, a square piece of CFP (ca. 10 × 10 cm) was cut from the as-received CFP. Then, a carbon black suspension (10 mg mL^{-1} in 2-propanol) was sprayed onto the piece of the CFP using a Paasche VL airbrush with a nitrogen (N_2) source. A piece of CFP coated with a 1 mg cm^{-2} carbon black support layer was obtained, which was then cut into C/CFP discs (diameter Ø = 0.5 cm) as the electrodes.

Catalyst inks were prepared by using a mixture of water (50 μL), 2-propanol (75 μL) and 1-propanol (75 μL), to disperse 4.0 mg of the catalyst by sonication for 3 h. Each ink (ca. 5-15 μL) was painted onto a 0.24 cm^2 disc of C/CFP to give a Pt loading of 0.30 mg cm^{-2} or 0.10 mg cm^{-2}. All electrodes were dried at ambient temperature overnight before use.

In order to prepare MEAs, anodes were firstly prepared by depositing catalysts on C/CFP discs (0.24 cm^2) with a target Pt loading of 1 mg cm^{-2} for each electrode, followed by dropping Nafion solution on the top to give a target loading of 20 wt%. The electrodes were dried in a fume hood overnight. The 5 cm^2 cathode consisted of 4 mg cm^{-2} Pt black loaded onto wet-proofed Toray^{TM} CFP (TGP-H-090). Nine anodes and a cathode were pressed onto each side of a treated Nafion^{TM} 117 membrane with a pressure of 1.5 MPa during assembly of the cell, at ambient temperature.[2]

2.3 Electrochemical measurements

In a three-electrode cell, electrochemical measurements in aqueous H_2SO_4 solutions were conducted at ambient temperature with a BioLogic SP-50 Potentiostat operated with EC-Lab software. A piece of Ti foil or C/CFP loaded with an anode catalyst was used as the working electrode, while a saturated calomel electrode (SCE) and a platinum wire acted as the reference and counter electrode, respectively. All measurements were made under a nitrogen (N_2) atmosphere following purging with N_2 for 15 min.

In a nine-anode proton exchange membrane (PEM) cell, polarization curves were measured with a MSTAT multi-channel potentiostat (Arbin Instruments). As shown in Figure 2.1, the cell was operated in a crossover mode with 0.1 M ethanol solution pumped into the cathode by a NE-300 New Era Pump Systems syringe pump, while N_2 was purged into the anode at a flow rate of 10 mL min^{-1} to avoid interference from oxygen.[1] Ethanol was transferred from the cathode to the anode by diffusion across the PEM. The reaction at the cathode was $2H^+ + e^- \rightarrow H_2$, so that the cathode can be treated as a pseudo reference electrode (dynamic hydrogen electrode).[3] The cell was maintained at 80 °C by a 60 W Watlow heating plate with a Digi Sense temperature controller. Steady-state currents were recorded from 0.9 V to 0 V in 0.05 V, 3 min steps. The average currents over the last 2 min are reported.

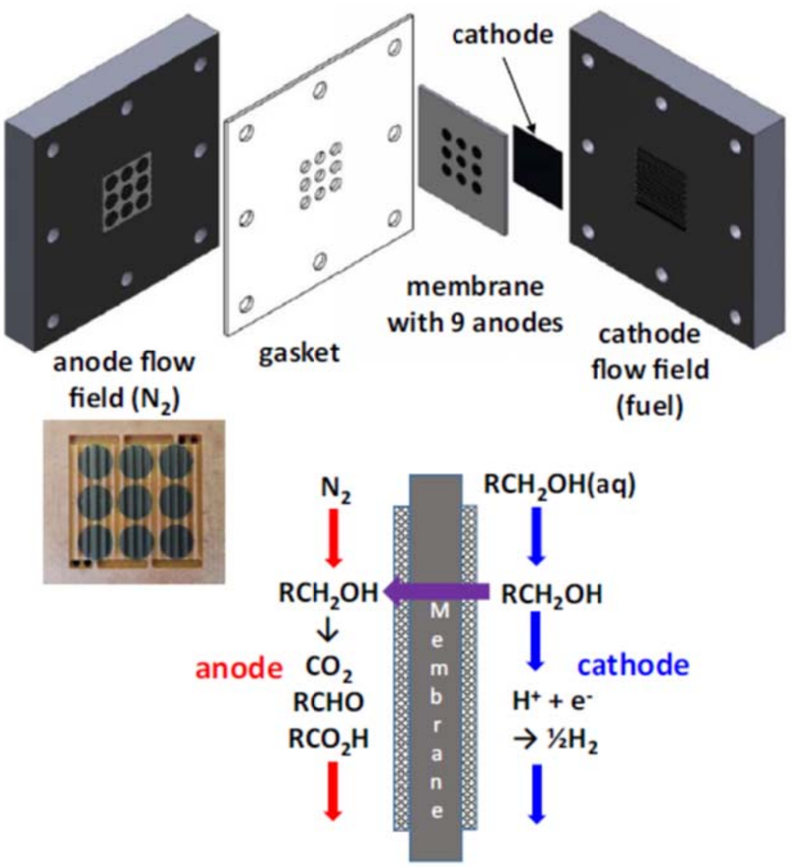

Figure 2.1. Schematic diagram of the nine-anode PEM cell (top) and the crossover mode of operation (bottom). R = H or CH_3.[1] (This article is published under an open access Creative Commons License.)

2.4 Non-dispersive infrared (NDIR) carbon dioxide detector

A commercial NDIR CO_2 sensor (Telaire T6615 Series) operated with eCO2View software was used for online monitoring of the concentration of CO_2 produced from the PEM cell, as shown in Figure 2.2. The gaseous products were flushed into the sample chamber of the sensor by the N_2 flow (50 mL min^{-1}). The IR light from an infrared lamp is transmitted through the sample chamber and an optical filter to allow the selected wavelength to reach the infrared detector.[4] With the NDIR CO_2 detector, the concentration of CO_2 was selectively detected by measuring CO_2 absorption under the infrared light of a specific wavelength (commonly used wavelength: 4.26 μm).[4]

Figure 2.2. The NDIR CO_2 sensor.

2.5 Catalyst characterization techniques

2.5.1 Thermogravimetric analysis (TGA)

TGA is an analytical technique to characterize materials by measuring the mass of a sample as a function of temperature. The TGA experiments were carried out with a TA instruments Q500 thermogravimetric analyzer, and the data were processed using the Thermal Advantage software. The sample was loaded on a TGA platinum sample pan. The operating conditions of a conventional ramp method were set with a heating rate of 20 °C min^{-1}, a temperature range from ambient temperature to 800 °C, and a gas condition of air. Carbon was burned at ca. 600 °C, and Ru oxide, Sn oxide and Pt were solid-state and thermally stable over the operating temperature range. Therefore, the total percentage of metal loading of the prepared MO_x/C supports and Pt/MO_x/C catalysts can be easily obtained by TGA analysis. In addition, the decomposition of $Ru(acac)_3$, $Sn(acac)_3$, and $Pb(acac)_2$ on a carbon black support was analyzed under non-isothermal and isothermal (keeping a temperature for a certain time) conditions.

The analysis of $Pb(acac)_2$ decomposition was conducted by Dr. Jianbin Lin at the Centre for Chemical Analysis, Research and Training (C-CART), Memorial University of Newfoundland.

2.5.2 X-ray diffraction (XRD)

In order to identify crystalline components and estimate particles sizes of the synthesized support materials and catalysts, XRD measurements were carried out on a Rigaku Ultima IV X-ray diffractometer using a copper x-ray source at a power of 40 kV and 44 mA (Cu Kα radiation, $\lambda = 1.5418$ Å) and a scintillation counter detector. The X-ray powder diffraction was conducted from 20 to 90 degrees, at a scan rate of 1.0 degrees per minute. This work was performed by Dr. Wanda Aylward at Core Research Equipment and Instrument Training (CREAIT), Memorial University of Newfoundland.

2.5.3 Transmission electron microscopy (TEM)

TEM was used for morphology and particle size analysis. It can provide extremely high-resolution images by transmitting the electron beam through a thin layer sample. For preparation of the TEM samples, the catalysts were well dispersed in deionized water by sonication. A drop of each sample solution was applied onto a TEM grid, which was allowed to dry overnight. The

TEM analysis was conducted on a A Tecnai Spirit scanning transmission electron microscope by Dr. Stephanie Tucker at Faculty of Medicine, Memorial University of Newfoundland.

2.5.4 Scanning electron microscopy (SEM) with energy dispersive X-ray analysis (EDX)

SEM is another type of electron microscopy which can provide surface morphology. High-resolution images are obtained from the secondary or backscattered electron signals by applying focused scanning electron beams to a sample surface. When SEM is coupled with an EDX system, the energies and intensities of the emitted X-rays can be measured by an EDX analyzer, thus providing element distribution and semi-quantitative information.

The sample on a Ti electrode was directly applied for SEM and EDX analysis. For analysis of the catalysts with C supports, about 2 mg of each catalyst powder was dispersed in 200 μL of deionized water by sonication for 3 h. Afterwards, the sample solution was applied to an adhesive carbon tab on a specimen stub. The SEM-EDX analysis was carried out using a Model FEI Quanta 400 scanning electron microscope equipped with a Bruker 4th generation XFlash SDD X-ray detector. This work was performed by Dr. David Grant and Dylan Goudie at CREAIT, Memorial University of Newfoundland.

2.5.5 X-ray photoelectron spectroscopy (XPS)

XPS is one of the most widely used surface analytical techniques, which bombards X-ray photons to the surface of a sample and measures the kinetic energies of emission electrons by a high-resolution electron spectrometer. It can be used for sensitive surface analysis with only a few nanometers in depth, and provides sample information including atomic compositions, oxidation states, species, and binding constants. The binding energy is determined by the photoelectric effect Equation 2.1:[5]

$$BE = hv - (KE + \phi) \qquad \text{(Equation 2.1)}$$

Where hv is the energy of injected X-ray photons (h: Planck's constant; v: the frequency of a photon), KE is the resulting kinetic energy of the ejected electrons, ϕ is the work function for instrumental correction, and BE is the binding energy of the electron in the orbital concerned, which is characteristic of a specific electron orbital in a specific atom. A change in oxidation state or chemical bonding will lead to a change in the binding energy, which is referred to as a chemical shift.[6] This allows to provide the information about oxidation states and species of an element.

XPS analyses of the samples were performed using a VG Microtech MultiLab ESCA 2000 X-ray Photoelectron Spectrometer by Andrew George at the Clean Technologies Research Institute (CTRI), Dalhousie University.

2.6 References

1. Brueckner, T. M.; Pickup, P. G., Kinetics and stoichiometry of methanol and ethanol oxidation in multi-anode proton exchange membrane cells. *Journal of The Electrochemical Society,* **2017**, *164* (12), F1172.

2. Altarawneh, R. M.; Majidi, P.; Pickup, P. G., Determination of the efficiency of ethanol oxidation in a proton exchange membrane electrolysis cell. *Journal of Power Sources,* **2017**, *351*, 106-114.

3. Nogueira, J. A.; Varela, H., Direct liquid fuel cells - the Influence of temperature and dynamic instabilities. *Energy & Fuels,* **2020**, *34* (10), 12995-13009.

4. Gibson, D.; MacGregor, C., A novel solid state non-dispersive infrared CO_2 gas sensor compatible with wireless and portable deployment. *Sensors,* **2013**, *13* (6), 7079-7103.

5. Lefebvre, J.; Galli, F.; Bianchi, C. L.; Patience, G. S.; Boffito, D. C., Experimental methods in chemical engineering: X-ray photoelectron spectroscopy - XPS. *The Canadian Journal of Chemical Engineering,* **2019**, *97* (10), 2588-2593.

6. Greczynski, G.; Hultman, L., X-ray photoelectron spectroscopy: Towards reliable binding energy referencing. *Progress in Materials Science,* **2020**, *107*, 100591.

Chapter 3

Ethanol oxidation at Pt nanoparticles supported on titanium modified by thermal decomposition of tin and ruthenium acetylacetonate complexes

This chapter has been published in part in:

H. Hang; P. G. Pickup, Ethanol oxidation at Pt nanoparticles supported on titanium modified by thermal decomposition of tin and ruthenium acetylacetonate complexes. Journal of The Electrochemical Society, 2021, 168(10), 106503.

H. Hang; P. G. Pickup, Pt/metal oxide/Ti and Pt/metal oxide/carbon composite films for ethanol oxidation. ECS Transactions, 2020, 97(7), 837.

The principal author (Hui Hang) contributed to all aspects of the project as the main researcher including: literature review, designing some of the experiments, performing all of the experiments, collecting, analyzing, presenting the data, and writing parts of the published manuscripts.

The corresponding author (Prof. Peter G. Pickup) was the principal investigator. He proposed the initial experiments, oversaw all aspects of the project, and contributed to several aspects of the project including: experimental design, data analysis, writing and revision of the manuscripts, submission to the journals, and supervision of the principal author (Hui Hang).

3.1 Introduction

Titanium has been one of the most important support materials for electrocatalysis since the development of Dimensionally Stable Anodes for the chlor-alkali industry.[1] It is also important in water electrolysis,[2-3] fuel cells,[4-6] and waste water treatment.[7-8] The use of Ti in fuel cells has focussed primarily on bipolar plates, gas diffusion media, and microporous layers,[4-5] and there has also been interest in its use as a catalyst support. Ti mesh coated with Pt and Pt alloy catalysts has been used as anodes for direct methanol fuel cells,[9] and in direct borohydride fuel cells.[10]

Electrocatalysis of fuel cell reactions has been reported for various Ti supported catalysts. Nanoporous networks of Pt, PtRu, PtIr, PtPb, and PtPd grown hydrothermally on Ti plates were reported for CO, methanol and formic acid oxidation.[11] PtIr/Ti provided the highest activity for methanol oxidation, while PtPb/Ti was superior for formic acid. Multilayered Pt/Ir/Pt films on Ti also provided high activities for methanol oxidation,[12] and a $Pt_{64}Ir_{33}Ru_3$/Ti electrode provided high activities for oxygen reduction, and the oxidation of formic acid and methanol.[13] Pt/Ti and Pt/$BaTiO_3$/Ti electrodes, prepared on Ti foil, have been used for oxidation of methanol and ethanol under both acidic and basic conditions.[14] Pd/Ti[15] and PtNi/Ti[16] have been reported for methanol oxidation, and Pd/Ti,[17] PdRu/Ti,[17] and PtNi/Ti[16] were used for ethanol oxidation, under basic conditions. Recently, Pt/Nb-SnO_2/Ti and Pt/Nb-SnO_2/Ti electrodes were shown to provide high activities for methanol oxidation.[18]

Alloying of Pt with Ti has also been shown to be effective for increasing activity for fuel cell reactions. PtTi alloy nanoparticles have shown higher activities for oxygen reduction, and improved CO tolerance for hydrogen oxidation.[19] Pt_3Ti has been shown to exhibit a lower affinity for CO adsorption and higher oxidation current densities for both formic acid and methanol than Pt or PtRu.[20] Ordered PtTi nanoparticles have shown improved durability over Pt for oxygen reduction in polymer electrolyte membrane (PEM) fuel cells.[21]

The purpose of the work reported here was to explore the use of metal oxide modified Ti foil supports for ethanol oxidation. Ti offers a number of potential advantages over carbon in the fabrication of electrodes for fundament studies and for use in direct ethanol fuel cells, including beneficial support effects, stability at elevated temperatures, and durability. Controlling support effects is particularly important in ethanol oxidation because it allows the activity of Pt based catalysts to be increased with better retention of efficiency for the complete oxidation to CO_2, than alloys.[22-23] Here we have employed thermal decomposition of $Ru(acac)_3$ and $Sn(acac)_2$ complexes (acac = acetylacetonate) to modify Ti foil in order to modulate support effects.[24] The resulting Ru oxide, Sn oxide, and mixed oxide coatings improve the activities of adsorbed Pt nanoparticles for ethanol oxidation.

3.2 Experimental

3.2.1 Materials

A colloidal solution of 5 nm Pt nanoparticles (0.48 mg mL^{-1} Pt) was prepared as previously described.[25]

3.2.2 Electrode preparation

Working electrodes were prepared by deposition of each catalyst on a strip of Ti foil. First, a Ru oxide and/or Sn oxide layer was prepared by applying 1.25 μL of 0.02 M $Ru(acac)_3$ (in methanol), $Sn(acac)_2$ (in 2-propanol) or their mixture onto a ca. 0.5 × 0.5 cm area of a Ti strip

(250 μm) (i.e. 1.0×10^{-7} mol cm^{-2} of complex), allowing it to dry, and then heating it on a hot plate in air, at 150 °C for 1 h and then 180 °C for 1 h. After cooling to ambient temperature, the oxide deposits were washed with ethanol, 0.1 M H_2SO_4 and deionized water and dried at 70 °C. Then 5.0 μL of the Pt nanoparticle solution (ca. 10 μg cm^{-2} Pt) was evenly drop-coated onto the oxide deposit and allowed to dry.

3.3 Results and discussion

3.3.1 Characterization of the metal oxide layers

Figure 3.1 shows an SEM image of Ru-Sn oxide on Ti foil, where it can be seen that a relatively uniform film had been produced, and an X-ray spectrum (EDX), which shows the presence of both Ru and Sn. However, the measured mole ratio of Sn:Ru was ca. 14:1, which is much higher than the 1:1 $Ru(acac)_3$:$Sn(acac)_2$ ratio used to prepare the sample. This difference can be attributed to sublimation of most of the $Ru(acac)_3$ before it decomposed.[26] Based on the quantities of the $Ru(acac)_3$ and $Sn(acac)_2$ precursors, and the measured Sn:Ru ratio, a compact SnO_2+RuO_2 would be ca. 11 nm thick. For comparision, the layer of Pt nanoparticles applied for the electrochemical studies was ca. 5 nm, representing approximately one monolayer of close packed particles. SEM, TEM and AFM images of Pt nanoparticle prepared in the same way, and with the same average diameter have been previously published.[25]

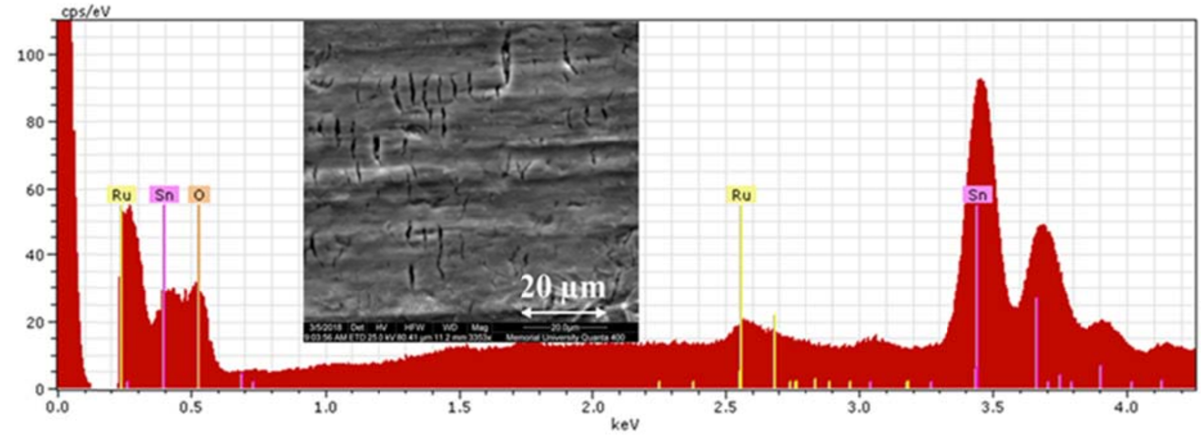

Figure 3.1. X-ray emission spectrum and SEM image (inset) of a Ti foil modified by thermal decomposition of a 1:1 mixture of Ru(acac)$_3$ and Sn(acac)$_2$.

For XRD, a thinner Ti foil (25 µm thick, 1 × 1 cm) and a higher loading of M(acac)$_n$ (2.0×10^{-6} mol cm^{-2}), than used to prepare electrodes, was required to observe peaks for the metal oxides. Figure 3.2 shows XRD data for 25 µm Ti foil (a) and samples that had been coated with Ru(acac)$_3$ (b), Sn(acac)$_2$ (c), and a mixture of Ru(acac)$_3$ and Sn(acac)$_2$ (d), and heated in air to 150 °C, 180 °C, then 250 °C each for 1 h. All of the patterns are dominated by the peaks for the α-Ti substrate. No new peaks were produced by the residue from Ru(acac)$_3$ decomposition, while Sn(acac)$_2$ produced new broad peaks at ca. 27°, 34° and 54° that are characteristic of SnO$_2$.[27] Similar XRD patterns have been reported for Sn oxide layers on silicon prepared by pulsed laser deposition.[28] Very weak, broad peaks were seen at similar positions when a mixture of Ru(acac)$_3$ and Sn(acac)$_2$ was used, but it is not possible to distinguish between the presence of SnO$_2$, RuO$_2$ or a mixed oxide because their peaks are at similar positions.[27]

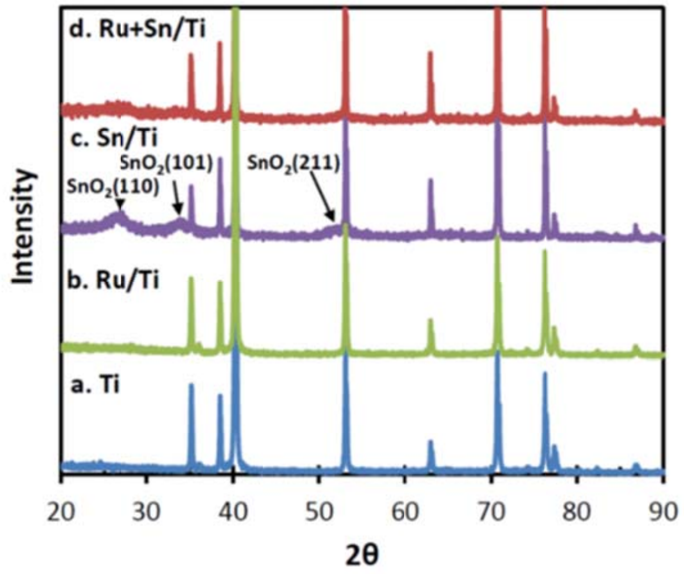

Figure 3.2. X-ray diffraction patterns for Ti foil (a) and Ti foil coated by thermal decomposition of Ru(acac)$_3$ (b), Sn(acac)$_2$ (c), and a mixture of Ru(acac)$_3$ and Sn(acac)$_2$ (d).

Figure 3.3 shows XPS spectra of Ti foil, and samples that had been coated with Sn(acac)$_2$ (b), Ru(acac)$_3$ (c), and a mixture of Ru(acac)$_3$ and Sn(acac)$_2$ (d), and heated in air to 150 °C, 180 °C, then 250 °C each for 1 h. Following decomposition of Sn(acac)$_2$ on the Ti surface, the XPS spectrum was dominated by Sn 3d$_{5/2}$ and Sn 3d$_{3/2}$ peaks, at 486.65 eV and 495.09 eV respectively. These binding energies (BE) are characteristic of SnO$_2$. The O 1s peak is also consistent with the presence of SnO$_2$, as well as adventitious –OH groups.[29] Hereafter, samples prepared with just Sn(acac)$_2$ will be referred to as SnO$_2$/Ti.

Similarly, decomposition of Ru(acac)$_3$ produced a spectrum that was dominated by Ru (3d, 3p, and 3s) and O 1s peaks, indicative of primarily RuO$_2$ (hereafter referred to as RuO$_2$/Ti).[30] Decomposition of a mixture of Ru(acac)$_3$ and Sn(acac)$_2$ produced a spectrum dominated by SnO$_2$, with only a small shoulder at 281.44 eV characteristic of RuO_2. This is consistent with the EDX data, and inference that a large fraction of the $Ru(acac)_3$ sublimed before it could be converted to RuO_2. Addition of Ru to the SnO_2, decreased the Sn $3d_{5/2}$ and Sn $3d_{5/2}$ binding energies slightly, to 486.55 eV (0.10 eV lower) and 494.96 eV (0.13 eV lower) respectively. In view of the high Sn:Ru ratio, and very minor effect of the Ru on the Sn XPS peaks, samples prepared with both $Ru(acac)_3$ and $Sn(acac)_3$ will be referred to as Ru-doped SnO_2/Ti.

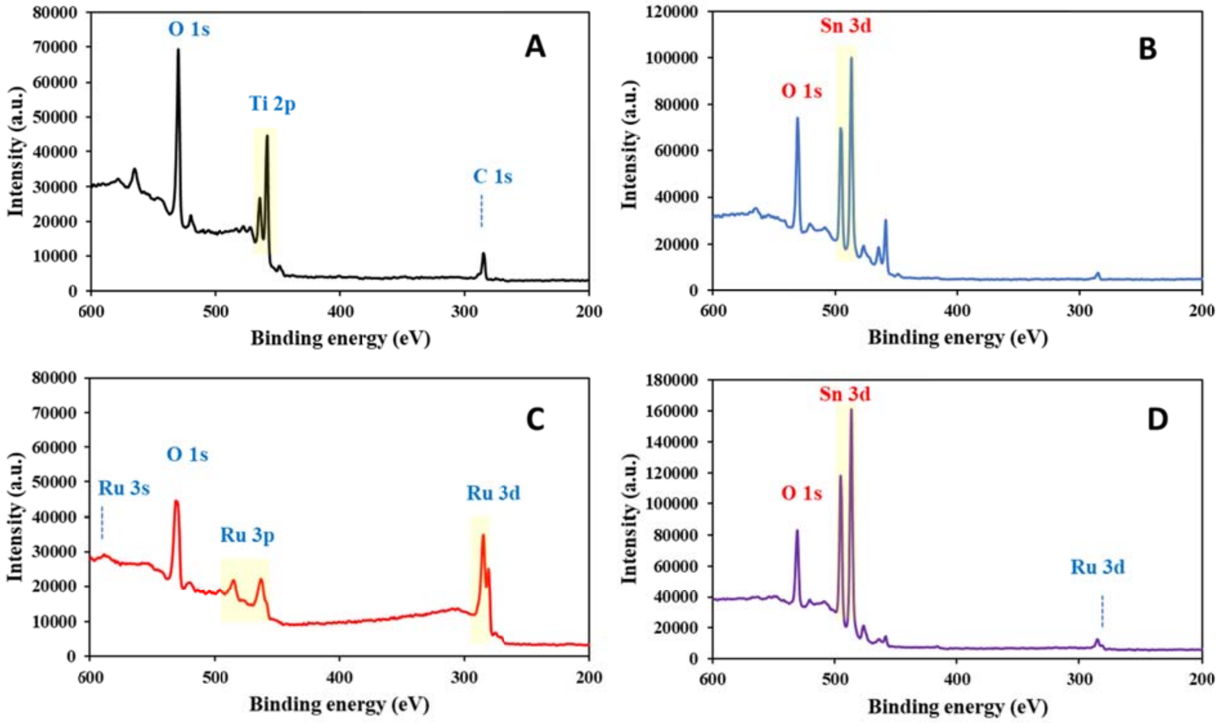

Figure 3.3. X-ray photoelectron spectra for Ti foil (A) and Ti foil coated by thermal decomposition of $Sn(acac)_2$ (B), $Ru(acac)_3$ (C), and a mixture of $Ru(acac)_3$ and $Sn(acac)_2$ (D).

Closer inspection of the Ru 3d and O 1s regions of the spectra (Figure 3.4) reveals a range of Ru oxidation states and significant differences between the SnO_2/Ti and Ru-doped SnO_2/Ti samples. Deconvolution of the overlapping Ru 3d and C 1s peaks for RuO_2/Ti indicates that the RuO_2 layer was amorphous (a-RuO_2; Ru $3d_{5/2}$ BE = 280.76 eV) with incipient crystallinity indicated by a component at 282.53 eV.[30] A larger component with a lower BE of 280.13 eV indicates the presence of a lower oxidation state, presumably Ru(III). In contrast, the Ru $3d_{5/2}$ region of the Ru-doped SnO_2/Ti spectrum shows predominantly the presence of amorphous Ru(IV) at 281.44 eV, which is consistent with the assumption that Ru was incorporated into the SnO_2 lattice.[31] However, there is also a clear lower binding energy shoulder (280.11 eV), indicating the presence of a lower Ru oxidation state. Donation of electron density from this state to Sn(IV) is presumably responsible for the small decrease in the Sn 3d binding energy for Ru-doped SnO_2/Ti relative to SnO_2/Ti in Figure 3.3.

SnO_2/Ti and Ru-doped SnO_2/Ti gave similar O 1s spectra (Figure 3.4) with a main oxide (O^{2-}) peak at 530.27 eV and 530.42 eV, respectively, and a shoulder at higher binding energy due to adsorbed water. In contrast, two distinct peaks were observed for RuO_2/Ti, with a shoulder at ca. 533.5 eV. The peaks at 529.47 eV and 531.47 eV are consistent with values of 529.4 eV 530.8 eV, respectively, reported for O^{2-} and OH^- in amorphous hydrous RuO_2 that has been heated to 175 or 200 °C, while the shoulder is due to H_2O (reported at 532.4 eV).[30]

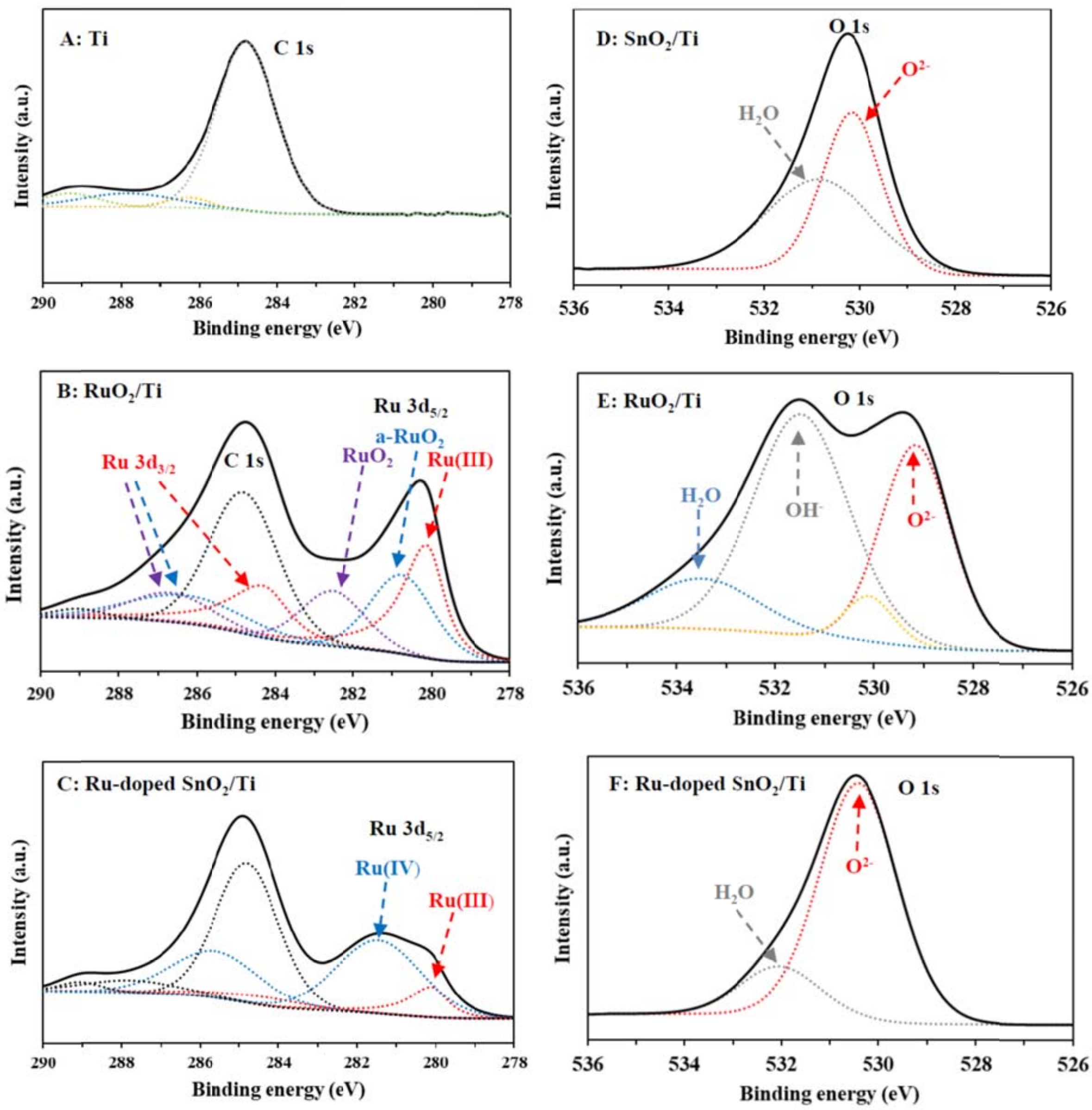

Figure 3.4. Ru 3d and O 1s regions of selected spectra from Figure 3.3.

3.3.2 Ethanol oxidation

Evaluation of the effects of the oxide layers on ethanol oxidation at Pt nanoparticles was performed by cyclic voltammetry at ambient temperature in a conventional cell with a liquid electrolyte (H_2SO_4(aq)), using catalyst layers prepared on Ti foil. Preformed Pt nanoparticles were simply drop-coated onto the oxide layer that had been prepared on a Ti strip. Prior to ethanol oxidation measurement, the electrochemically active areas of the Pt nanoparticles were determined by cyclic voltammetry, as illustrated in Figure 3.5. The presence of the oxide layers did not change the voltammogram significantly relative to Pt nanoparticles deposited directly onto the Ti substrate (Pt/Ti). Electrochemically active Pt areas, determined from the area under the H-desorption peaks (−0.2 to +0.15 V) were 0.28, 0.25, 0.29, 0.33 cm^2 for Pt/Ti, Pt/RuO_2/Ti, Pt/SnO_2/Ti and Pt/Ru-doped SnO_2/Ti, respectively. The slightly higher values, if significant, can be attributed to the higher surface areas presented by the rougher oxide layers (Figure 3.1), relative to the Ti substrate.

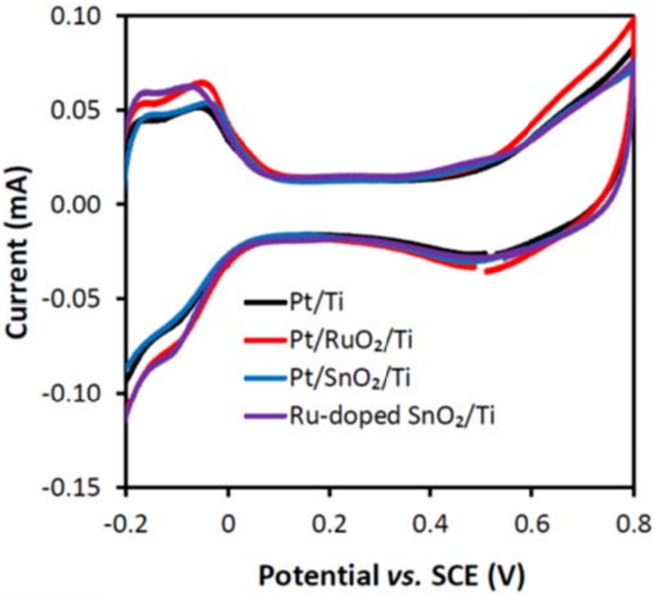

Figure 3.5. Cyclic voltammograms (100 mV s^{-1}) of Pt/Ti, Pt/RuO_2/Ti, Pt/SnO_2/Ti and Pt/Ru-doped SnO_2/Ti electrodes in 0.1 M H_2SO_4(aq).

Figure 3.6 shows voltammograms for ethanol oxidation at Pt/RuO_2/Ti, Pt/SnO_2/Ti and Pt/Ru-doped SnO_2/Ti electrodes. They show large enhancements in the electrocatalytic activity of the Pt when any of the oxides were present, with Ru-doped SnO_2 providing the highest peak current and earliest onset of ethanol oxidation. SnO_2 gave an early onset of ethanol oxidation, but the peak current was low, presumably due to its low conductivity. RuO_2 has high conductivity, but only shifted the onset by about 50 mV relative to Pt/Ti. Clearly, the presence of both SnO_2 and RuO_2 is necessary to obtain optimum performance, and there is a strong synergistic effect. Even a small amount of Ru (Sn:Ru mole ratio of ca. 14 for the sample in Figure 3.6) causes as large increase in activity relative to SnO_2 alone.

Similar results to those in Figure 3.6 have been reported for Ru and Sn oxides on glassy carbon substrates,[25] although the enhancements reported here are much greater, and the electrodes were more stable to potential cycling. In addition, the synthesis of the oxides by thermal decomposition is much more versatile and can be readily applied to high surface area substrates,[26] scaled-up and ultimately automated.

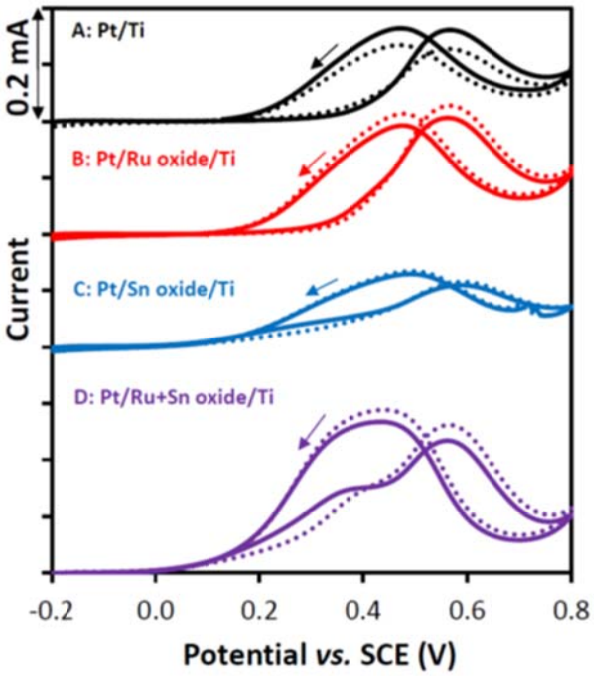

Figure 3.6. Cyclic voltammograms (10 mV s^{-1}; 2nd cycle dotted) of catalyst coated Ti electrodes (2.4 μg Pt) in 0.2 M ethanol + 0.1 M H_2SO_4.

The preparation of mixed Ru-Sn oxide layers by simply mixing the precursor $M(acac)_n$ solutions allows rapid assessment of the effects of the Ru:Sn ratio on the catalytic activity of the Pt nanoparticles. Figure 3.7 shows currents at 0.1 V and 0.3 V during linear sweep voltammetry *vs.* the mol% of $Sn(acac)_2$ in the precursor solution. These plots show a very strong synergistic effect between Ru and Sn in the oxide layer, with a peak at 33% Sn. This precursor composition provided the highest activity at all potentials. The optimum Sn:Ru ratio of the resulting oxide layer can be estimated to be ca. 7:1, based on the assumption that the fraction of $Ru(acac)_3$ lost by sublimation was the same as for the 50% Sn sample analysed by EDX (Figure 3.1).

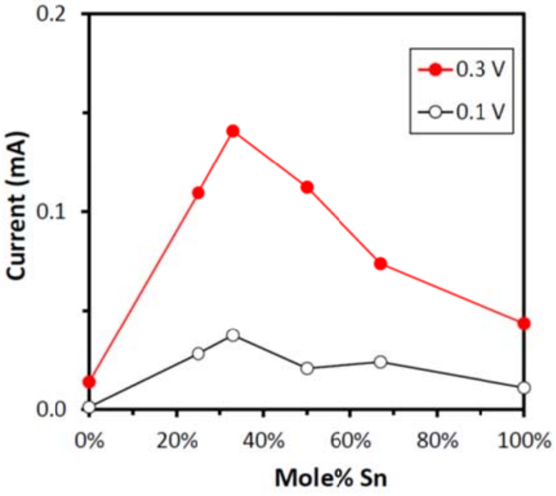

Figure 3.7. Currents at 0.1 V (○) and 0.3 V (●) during the first anodic scan *vs.* the mole% of $Sn(acac)_2$ in the oxide precursor solution, for oxidation of 0.2 M ethanol + 0.1 M H_2SO_4 at Pt/Ru+Sn oxide/Ti electrodes.

It is crucial here to note that the increases in electrocatalytic activity of Pt nanoparticles have been achieved without altering their composition. Although alloying Pt with Ru and/or Sn can also increase activities substantially, the presence of these elements at the catalyst surface greatly inhibits selectivity for the complete oxidation of ethanol to CO_2, resulting in low faradaic efficiency.[32] The use of oxide supports allows activity to be increased with better retention of efficiency.[22-23]

3.3.3 Mechanisms

The roles of Ru oxide and Sn oxide in promoting ethanol oxidation at Pt nanoparticles have previously been attributed to the oxidation of adsorbed CO (CO_{ads}) by surface Ru-OH groups (bifunctional/Langmuir–Hinshelwood mechanism), and the electronic (ligand) effect of Sn oxide.[25] These differing roles can explain the synergistic effect that is seen clearly in Figure 3.6

and Figure 3.7. The strong dependence of the activity on the Ru:Sn ratio shows that these effects, and their balance, can be tuned to optimize performance, and also provides a test of the validity of this mechanistic model.

Firstly, it is instructive to re-examine the model based on the current understanding of the role of Sn oxide in promoting electrocatalysis at Pt. Crooks and coworkers have reported a computational and experimental study of the electronic effect of SnO_x ($x = 1.9$ or 2.0) supports on Au nanoparticles, in which it was shown by XPS that electron transfer from the oxide to Au promoted oxygen reduction.[33] Density functional theory (DFT) calculations indicated that oxygen vacancies were responsible for the electronic effect, which was found to be localized at specific Au atoms that were next to oxygen vacancies. A similar catalytic effect on oxygen reduction, and charge transfer (from Sn to Pt), has been reported for Nb and Sb doped tin oxide decorated with Pt nanoparticles.[34] Adzic and coworkers demonstrated that promotion of methanol oxidation at Pt by SnO_2 nanoparticles was correlated with the strength of Sn-OH bonding, suggesting a bifunctional role of Sn-OH in releasing CO_{ads}.[35] However, the observation of a lower binding energy Sn 3d peak in the XPS of the most active sample indicates that electron transfer from Sn(II) to Pt could also be responsible for the increased activity.

In order to probe the electronic effect of the Ru-doped SnO_2 employed in this work, XPS was used to measure the Pt binding energies of Pt nanoparticles drop coated onto Ru-doped SnO_2/Ti. Figure 3.8 compares the Pt 4d and Pt 4f regions for a Pt/Ru-doped SnO_2/Ti electrode and Pt nanoparticles coated directly onto the Ti substrate (deconvoluted Pt 4 f spectra are shown in Figure 3.9). It can be seen that the presence of Ru-doped SnO_2 caused a significant decrease in the Pt $4d_{5/2}$ binding energy, from 314.9 eV to 314.1 eV, indicating that there was electron transfer from the oxide layer to the Pt nanoparticles. This effect is presumably enhanced by the presence of Ru(III) in the SnO_2 lattice, which donates electron density to Sn(IV) (Figure 3.3).

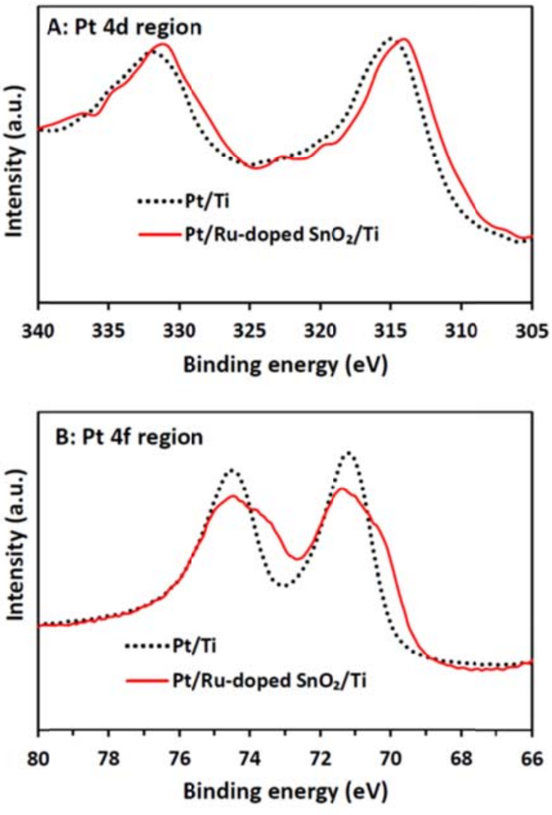

Figure 3.8. Pt 4d (A) and 4f (B) regions of XPS spectra of Pt nanoparticles on unmodified Ti (Pt/Ti) and Ru-doped SnO_2/Ti (Pt/Ru-doped SnO_2/Ti)

The Pt 4f region of the XPS (Figure 3.8B), which is more sensitive to surface species, shows the presence of two distinct oxidation states for the Pt/Ru-doped SnO_2/Ti, that can be assigned to the bulk Pt(0) at 70.1 eV for Pt $4f_{7/2}$ and Pt-OH at 71.7 eV. In contrast, a single Pt(0) peak at 71.0 eV is seen for the Pt/Ti sample. This indicates that electron transfer from Ru-doped SnO_2 makes the Pt nanoparticles more susceptible to surface oxidation.

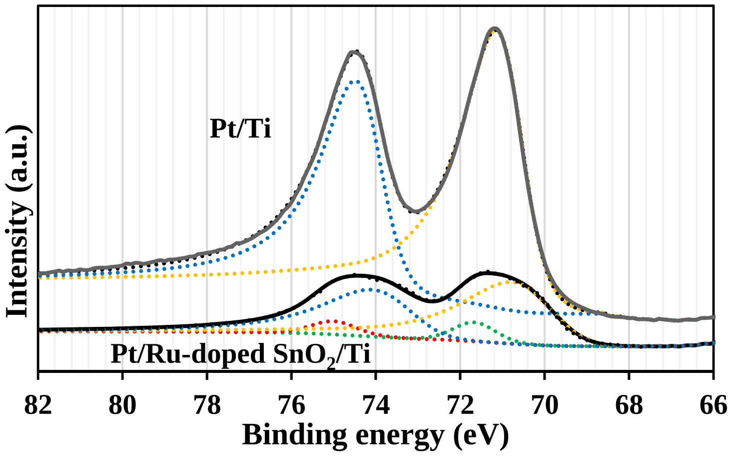

Figure 3.9. Deconvoluted Pt 4f regions of the XPS spectra for Pt nanoparticles on unmodified Ti (Pt/Ti) and Ru-doped SnO_2/Ti (Pt/Ru-doped SnO_2/Ti). The peaks for Pt/Ti were fitted (black dotted line) with a single Pt(0) state (blue and yellow) while Pt(0) and Pt(II) (hydroxide) (red and green) were required for Pt/Ru-doped SnO_2/Ti. The fitted backgrounds are omitted for clarity.

These observations are consistent with the previous reports discussed above, and indicate that both ligand and bifunctional effects can play a role in improving the activities of Pt/Ru-doped SnO_2/Ti electrodes. Both effects can promote the oxidation of CO_{ads}, while the electronic effect also influences the adsorption strength of ethanol.[36] The voltammetric responses in Figure 3.6 provide a clear differentiation of the differing effects of the Ru and Sn component of the oxide supports. The primary effect of SnO_2 is a substantial decrease in the onset potential for ethanol oxidation, which can be attributed primarily to its electronic effect. In contrast, RuO_2 mainly causes an increase in peak current, which can be attributed to its bifunctional effect. The variation of the balance of these effects with the level of Ru doping in the mixed oxides is a plausible explanation for the dependence on the Sn:Ru ratio, although further work is required to fully quantify this.

3.4 Conclusions

Thermal decomposition of Ru(acac)$_3$ and Sn(acac)$_2$ metal acetylacetonate complexes on Ti is a convenient and effective method for preparing mixed Sn + Ru oxide (Ru-doped SnO$_2$) supports for electrocatalysis. Drop coating these supports with preformed pure Pt nanoparticles ensures that the support does not influence their size, shape, or composition, and therefore allows unambiguous comparison of supports with different Sn:Ru ratios. XPS measurements suggest that both ligand and bifunctional effects are involved in the promoting effect of Ru-doped SnO$_2$ on ethanol oxidation, and that the optimum performance obtained by using 33 mole% of Sn(acac)$_2$ in the oxide precursor solution occurs when these effects are balanced. The methodology employed here is very versatile, and can be applied to other electrode materials (e.g. high surface area carbon), and oxides (e.g. Pb, In, Mo).[24]

3.5 References

1. Karlsson, R. K.; Cornell, A., Selectivity between oxygen and chlorine evolution in the chlor-alkali and chlorate processes. *Chemical Reviews,* **2016**, *116* (5), 2982-3028.

2. Katsounaros, I.; Cherevko, S.; Zeradjanin, A. R.; Mayrhofer, K. J., Oxygen electrochemistry as a cornerstone for sustainable energy conversion. *Angewandte Chemie International Edition,* **2014**, *53* (1), 102-121.

3. Bühler, M.; Hegge, F.; Holzapfel, P.; Bierling, M.; Suermann, M.; Vierrath, S.; Thiele, S., Optimization of anodic porous transport electrodes for proton exchange membrane water electrolyzers. *Journal of Materials Chemistry A,* **2019**, *7* (47), 26984-26995.

4. Omrani, R.; Shabani, B., Review of gas diffusion layer for proton exchange membrane-based technologies with a focus on unitised regenerative fuel cells. *International Journal of Hydrogen Energy,* **2019**, *44* (7), 3834-3860.

5. Ozden, A.; Shahgaldi, S.; Li, X.; Hamdullahpur, F., A review of gas diffusion layers for proton exchange membrane fuel cells - With a focus on characteristics, characterization techniques, materials and designs. *Progress in Energy and Combustion Science,* **2019**, *74*, 50-102.

6. Baudler, A.; Schmidt, I.; Langner, M.; Greiner, A.; Schröder, U., Does it have to be carbon? Metal anodes in microbial fuel cells and related bioelectrochemical systems. *Energy & Environmental Science,* **2015**, *8* (7), 2048-2055.

7. Rao, A. N. S.; Venkatarangaiah, V. T., Metal oxide-coated anodes in wastewater treatment. *Environmental Science and Pollution Research,* **2014**, *21* (5), 3197-3217.

8. Garcia-Segura, S.; Ocon, J. D.; Chong, M. N., Electrochemical oxidation remediation of real wastewater effluents - a review. *Process Safety and Environmental Protection,* **2018**, *113*, 48-67.

9. Chetty, R.; Scott, K.; Kundu, S.; Muhler, M., Optimization of mesh-based anodes for direct methanol fuel cells. *Journal of Electrochemical Energy Conversion and Storage,* **2010**, *7* (3), 031011.

10. Abahussain, A. A.; de Leon, C. P.; Walsh, F. C., Mass-transfer measurements at porous 3D Pt-Ir/Ti electrodes in a direct borohydride fuel cell. *Journal of The Electrochemical Society,* **2018**, *165* (3), F198.

11. Wang, J.; Holt-Hindle, P.; MacDonald, D.; Thomas, D. F.; Chen, A., Synthesis and electrochemical study of Pt-based nanoporous materials. *Electrochimica Acta,* **2008**, *53* (23), 6944-6952.

12. Zulke, A. A.; Matos, R.; Pereira, E. C., Metallic multilayered films electrodeposited over titanium as catalysts for methanol electro-oxidation. *Electrochimica Acta,* **2013**, *105*, 578-583.

13. Yi, Q.; Li, L.; Yu, W.; Zhou, Z.; Liu, X.; Xu, G., Hydrothermal synthesis of titanium-supported PtIrRu/Ti electrode and its electrocatalytic activity. *Journal of Alloys and Compounds,* **2008**, *466* (1-2), 52-58.

14. Hu, C.; He, X.; Xia, C., Pt hierarchical structure catalysts on $BaTiO_3$/Ti electrode for methanol and ethanol electrooxidations. *Journal of Power Sources,* **2010**, *195* (6), 1594-1598.

15. Chikoidze, E.; Rogers, D. J.; Teherani, F. H.; Rubio, C.; Sauthier, G.; Von Bardeleben, H. J.; Tchelidze, T.; Ton-That, C.; Fellous, A.; Bove, P., Puzzling robust 2D metallic conductivity in undoped β-Ga_2O_3 thin films. *Materials Today Physics,* **2019**, *8*, 10-17.

16. Tamašauskaitė-Tamašiūnaitė, L.; Balčiūnaitė, A.; Vaiciukevičienė, A.; Selskis, A.; Pakštas, V., Investigation of nanostructured platinum-nickel supported on the titanium surface as electrocatalysts for alkaline fuel cells. *Journal of Power Sources,* **2012**, *208*, 242-247.

17. Yi, Q.; Niu, F.; Song, L.; Liu, X.; Nie, H., Electrochemical activity of novel titanium-supported porous binary Pd-Ru particles for ethanol oxidation in alkaline media. *Electroanalysis,* **2011**, *23* (9), 2232-2240.

18. Merati, Z.; Parsa, J. B., Enhancement of the catalytic activity of Pt nanoparticles toward methanol electro-oxidation using doped-SnO_2 supporting materials. *Applied Surface Science,* **2018**, *435*, 535-542.

19. Kawasoe, Y.; Tanaka, S.; Kuroki, T.; Kusaba, H.; Ito, K.; Teraoka, Y.; Sasaki, K., Preparation and electrochemical activities of Pt–Ti alloy PEFC electrocatalysts. *Journal of The Electrochemical Society,* **2007**, *154* (9), B969.

20. Abe, H.; Matsumoto, F.; Alden, L. R.; Warren, S. C.; Abruña, H. D.; DiSalvo, F. J., Electrocatalytic performance of fuel oxidation by Pt_3Ti nanoparticles. *Journal of the American Chemical Society,* **2008**, *130* (16), 5452-5458.

21. Park, H.-Y.; Jeon, T.-Y.; Lee, K.-S.; Yoo, S. J.; Sung, Y.-E.; Jang, J. H., Carbon-supported ordered Pt-Ti alloy nanoparticles as durable oxygen reduction reaction electrocatalyst for polymer electrolyte membrane fuel cells. *Journal of Electrochemical Science and Technology,* **2016**, *7* (4), 269-276.

22. James, D. D.; Moghaddam, R. B.; Chen, B.; Pickup, P. G., Ruthenium-tin oxide/carbon supported platinum catalysts for electrochemical oxidation of ethanol in direct ethanol fuel cells. *Journal of The Electrochemical Society,* **2018**, *165* (3), F215.

23. Chen, B.; Brueckner, T. M.; Altarawneh, R. M.; Pickup, P. G., Composition dependence of ethanol oxidation at ruthenium-tin oxide/carbon supported platinum catalysts. *Journal of The Electrochemical Society,* **2018**, *165* (15), J3019.

24. Hang, H.; Pickup, P. G., Pt/metal oxide/Ti and Pt/metal oxide/carbon composite films for ethanol oxidation. *ECS Transactions,* **2020**, *97* (7), 837.

25. Moghaddam, R. B.; Pickup, P. G., Support effects on the oxidation of ethanol at Pt nanoparticles. *Electrochimica Acta,* **2012**, *65*, 210-215.

26. Hang, H.; Altarawneh, R. M.; Brueckner, T. M.; Pickup, P. G., Pt/Ru-Sn oxide/carbon catalysts for ethanol oxidation. *Journal of The Electrochemical Society,* **2020**, *167* (5), 054518.

27. Lee, J.-M.; Han, S.-B.; Lee, Y.-W.; Song, Y.-J.; Kim, J.-Y.; Park, K.-W., RuO_2-SnO_2 nanocomposite electrodes for methanol electrooxidation. *Journal of Alloys and Compounds,* **2010**, *506* (1), 57-62.

28. Vasil'eva, M. S.; Rudnev, V. S.; Zabudskaya, N. E., Plasma-electrochemical formation of Sn-containing oxide layers on titanium. *Protection of Metals and Physical Chemistry of Surfaces,* **2018**, *54* (6), 1157-1164.

29. Jadhav, H.; Suryawanshi, S.; More, M.; Sinha, S., Pulsed laser deposition of tin oxide thin films for field emission studies. *Applied Surface Science,* **2017**, *419*, 764-769.

30. Foelske, A.; Barbieri, O.; Hahn, M.; Kötz, R., An X-ray photoelectron spectroscopy study of hydrous ruthenium oxide powders with various water contents for supercapacitors. *Electrochemical and Solid State Letters,* **2006**, *9* (6), A268.

31. Gaudet, J.; Tavares, A. C.; Trasatti, S.; Guay, D., Physicochemical characterization of mixed RuO_2-SnO_2 solid solutions. *Chemistry of Materials,* **2005**, *17* (6), 1570-1579.

32. Altarawneh, R. M.; Pickup, P. G., Product distributions and efficiencies for ethanol oxidation in a proton exchange membrane electrolysis cell. *Journal of The Electrochemical Society,* **2017**, *164* (7), F861.

33. Ostojic, N.; Duan, Z.; Galyamova, A.; Henkelman, G.; Crooks, R. M., Electrocatalytic study of the oxygen reduction reaction at gold nanoparticles in the absence and presence of interactions with SnO_x supports. *Journal of the American Chemical Society,* **2018**, *140* (42), 13775-13785.

34. Jiménez-Morales, I.; Cavaliere, S.; Jones, D.; Rozière, J., Strong metal-support interaction improves activity and stability of Pt electrocatalysts on doped metal oxides. *Physical Chemistry Chemical Physics,* **2018**, *20* (13), 8765-8772.

35. Zhou, W.-P.; An, W.; Su, D.; Palomino, R.; Liu, P.; White, M. G.; Adzic, R. R., Electrooxidation of methanol at SnO_x-Pt interface: A tunable activity of tin oxide nanoparticles. *The Journal of Physical Chemistry Letters,* **2012**, *3* (22), 3286-3290.

36. El Sawy, E. N.; Brueckner, T. M.; Pickup, P. G., Electrochemical oxidation of methanol and ethanol at Rh@Pt and Ru@Pt catalysts. *Journal of The Electrochemical Society,* **2020**, *167* (10), 106507.

Chapter 4

Pt/Ru-Sn oxide/carbon catalysts for ethanol oxidation

This chapter has been published as:

H. Hang; R. M. Altarawneh; T. M. Brueckner; P. G. Pickup, Pt/Ru–Sn oxide/carbon catalysts for ethanol oxidation. Journal of The Electrochemical Society, 2020, 167(5), 054518.

Some modifications were made to the original paper for inclusion as a chapter in this thesis (e.g. the style of the references). The supporting information was incorporated into this chapter.

The principal author (Hui Hang) was the main researcher and contributed to all aspects of the project including: literature review, designing some of the experiments, performing 92% of the experiments, collecting, analyzing, presenting the data, and writing parts of the manuscript. R. M. Altarawneh and T. M. Brueckner contributed to the testing of the catalysts in the PEM cell.

The corresponding author (Prof. Peter G. Pickup) proposed the initial experiments, oversaw all aspects of the project, and contributed to several aspects of the project including: experimental design, data analysis, writing and revision of the manuscript, submission to the journal, and supervision of the principal author (Hui Hang).

4.1 Introduction

Efficient electrochemical oxidation of ethanol is a prerequisite for the development of direct ethanol fuel cells (DEFC) as a competitive technology for sustainable power generation.[1-2] In theory, DEFC are safe, environmentally benign, and have an energy-conversion efficiency of 97%. However, their high anode overpotentials, and the incomplete oxidation of ethanol to acetic acid and acetaldehyde, present major challenges to their implementation. To address these problems, a wide variety of binary and ternary anode catalysts have been investigated, and there have been considerable improvements in the electrochemical performances of DEFC.[3-4] Consequently, the remaining major challenge is to decrease the production of by-products to manageable levels. In this context, metal oxide supports appear to offer significant potential in combination with alloys such as PtRh and PtNi that provide increased selectivity for the complete oxidation of ethanol to carbon dioxide.[3-4]

The use of oxide supported Pt catalysts in polymer electrolyte membrane fuel cells (PEMFC) has been recently reviewed.[5] Mo, W, and Ti oxide have been widely used in cathode catalysts for oxygen reduction, while Sn oxide has most commonly been used in anodes for methanol and ethanol oxidation. Incorporation of Sn oxide into Pt based catalysts for ethanol oxidation can increase both activities and selectivities for the complete oxidation to CO_2.[6-8] Mixed oxides of Sn with Sb [9-11] and Ru [12-14] have also been employed.

Pt nanoparticle catalysts supported on co-deposited Sn and Ru oxides on carbon black showed enhanced activity for ethanol oxidation, while largely maintaining the selectivity of Pt/C.[13-14] However, the oxide deposition method involving the reaction of $KRuO_4$ and $SnCl_4$ with carbon black is difficult to control,[14] making it difficult to optimize the Sn to Ru ratio. Here we describe a new method for deposition of mixed Ru+Sn oxides on carbon black, based on the thermal decomposition of the metal acetylacetonate complexes (Ru(acac)$_3$ and Sn(acac)$_2$), and the development of Pt/Ru-Sn oxide/C catalysts for ethanol oxidation. The use of acetylacetonate complexes allows oxides to be produced at lower temperatures than for the conventional method using chlorides,[15] and so is more compatible with the use of carbon substrates.

4.2 Experimental

4.2.1 Materials

A colloidal solution of Pt nanoparticles (0.48 mg mL^{-1} Pt) was prepared as previously described.[16] The average particle diameter was determined to be 4.9 nm by X-ray diffraction.

4.2.2 Synthesis and characterization

Thermogravimetric (TGA) measurements were performed using a TA Instruments Q500 TGA, under an air atmosphere. For investigation of the thermal decompostion of Ru(acac)$_3$ and Sn(acac)$_2$ complexes on Vulcan XC-72 carbon black (C), a certain volume of Ru(acac)$_3$ (0.02 M in methanol) and/or Sn(acac)$_2$ (0.02 M in 2-propanol) was mixed thoroughly with C through sonication for 3 h. Following drying overnight in a fume hood, decompostion of the samples was analyzed by increasing the temperature up to 800 °C at 20 °C/min. In some cases the temperature was halted at selected values to investigate isothermal behaviour. Bulk Ru+Sn oxide/C samples were also analyzed by TGA in order to determine their metal oxide loading.

A Model FEI Quanta 400 scanning electron microscope with an energy dispersive X-ray detector (SEM/EDX) and Rigaku Ultima IV X-ray diffractometer (XRD) were used to characterize the oxide layers. Bulk samples of oxide coated C were prepared for these measurements as follows. A mixture of C (9.3 mg) and $Ru(acac)_3$ (1.167 mL, 0.02 M in methanol), or 0.02 M $Sn(acac)_2$ in 2-propanol (0.734 mL) + 0.02 M $Ru(acac)_3$ in methanol (0.584 mL), was allowed to dry and then heated in air, on a hot plate at 250 °C for 1 h. After being cooled, the product was washed with ethanol, 0.1 M H_2SO_4 and deionized water. These materials were dispersed in 2-propanol to prepare layers for characterization by XRD and SEM/EDX.

Bulk samples of oxide-coated C ($Ru_xSn_yO_2/C$) used for preparation of catalysts were prepared as follows. C (100 mg) was dispersed well by sonication for 3 h in a mixture of $Ru(acac)_3$ (0.02 M in methanol) and $Sn(acac)_2$ (0.02 M in 2-propanol). The loading of M(acac) on carbon black was maintained at 0.004 mol g^{-1}, while the ratio of Ru to Sn was varied. After drying at ambient temperature overnight, the mixture was heated in air, on a hot plate at 150 °C for 1 h, and then 180 °C for 2 h. This dual-temperature program was selected in order to minimize loss of Ru while also producing Sn oxide. The product was washed with 2-propanol, methanol and deionized water, and dried in an oven at 100 °C for 6 h. The oxide loading was determined by TGA and the Ru:Sn ratio (x and y in the oxide formulae) was determined by EDX.

$Pt/Ru_xSn_yO_2/C$ catalysts were prepared by absorbing Pt nanoparticles onto the oxide-coated C support materials. In order to prepare 23% $Pt/Ru_{0.67}Sn_{0.33}O_2/C$, for example, 58.5 mg of $Ru_{0.67}Sn_{0.33}O_2/C$ was dispersed in the required volume of Pt nanoparticle solution by 3 h of sonication, allowed to settle overnight, and collected by filtration. Following washing three times with deionized water, the catalyst was dried at 80 °C for 6 h. A 23% Pt/C catalyst was prepared similarly by using unmodified C. The compositions and characteristics of the $Pt/Ru_xSn_yO_2/C$

catalysts are summarized in Table 4.1. A Tecnai Spirit scanning transmission electron microscope was used to obtain TEM images.

4.2.3 Electrochemical measurements

Working electrodes were prepared as follows. Carbon fibre paper was coated with a carbon black support layer (C/CFP; 1 mg cm^{-2}) by spraying a C suspension (10 mg mL^{-1} in 2-propanol) onto CFP (10 × 10 cm). Catalyst inks were prepared by added water (50 μL), 2-propanol (75 μL) and 1-propanol (75 μL), to disperse 4.0 mg of the catalyst and sonication for 3 h. Each ink (ca. 5-15 μL) was painted onto a 0.24 cm^2 disc of C/CFP to give a Pt loading of 0.30 mg cm^{-2}. All electrodes were dried at ambient temperature overnight before use.

Voltammetric and chronoamperometric measurements were carried out using a Bio-Logic SP-50 Potentiostat/Galvanostat operated with EC-Lab software. A saturated calomel electrode (SCE) and a platinum wire were used as the reference and counter electrodes. Nitrogen was used to purge the electrolyte solution prior to all measurements, and to maintain an inert atmosphere during measurements.

A nine-anode polymer electrolyte membrane (PEM) electrolysis cell,[17] operated at 80 °C and controlled with a MSTAT multi-channel potentiostat from Arbin Instruments, was used to evaluate one catalyst for use in DEFC. Electrodes for this cell were prepared as follows. At 100 °C, a mixture of 5.5 mL Ru(acac)$_3$ (3.5 mM) and 5.5 mL Sn(acac)$_2$ (3.5 mM) in methanol was slowly and evenly drop-coated on C/CFP (25 cm^2). The temperature was maintained at 100 °C for 2 h, followed by 150 °C for 2 h and 180 °C for 0.5 h. After cooling to ambient temperature, the oxide/C layer was washed with ethanol and allowed to dry. Discs (0.24 cm^2) cut from this oxide modified substrate, were drop coated with the Pt nanoparticle solution at 70 °C, to provide a Pt loading of 1.0 mg cm^{-2}, allowed to dry for 5 min, and then washed with 0.1 M H_2SO_4 and deionized water. Nafion solution (22 μL) was then drop-coated onto each electrode at 60 °C and allowed to dry for 10 min.

The PEM cell was operated in crossover mode with a 0.1 M ethanol solution pumped through the cathode flow field at 0.5 mL min^{-1} while the anode flow field was purged with 30 mL min^{-1} N_2 gas to prevent interference from oxygen.[17] Under these conditions, the flux of ethanol to the anode is controlled by its diffusion rate through the membrane and the cathode acts as a dynamic hydrogen electrode. Polarization curves were recorded by applying each potential for 3 min and averaging the current over the final 2 min.

4.3 Results and discussion

4.3.1 Thermal decomposition of $Ru(acac)_3$ and $Sn(acac)_2$ on Vulcan XC-72 carbon black

As shown in Figure 4.1, $Ru(acac)_3$ started to decompose on the surface of carbon black at ca. 150 °C, which is in agreement with a previous report,[18] and was essentially complete at 245 °C. The resulting Ru oxide catalyzed the combustion of the carbon support, shifting the peak in the combustion rate from 750 °C to 590 °C. The residue of 5.9% RuO_2 represents a yield of 58.5% (ca. 50% after correction for the residual mass from the carbon support), indicating that ca. 50% of the mass loss from 150 to 245 °C was due to sublimation of $Ru(acac)_3$.

Decomposition of $Sn(acac)_2$ on carbon black (Figure 4.1) also began at ca. 150 °C, but was much slower than for $Ru(acac)_3$. Two mass-loss steps were observed with similar changes in mass. The loss of mass between 150 and 400 °C can be attribited primarily to loss of one of the acetylacetonate ligands (8.1% of the initial mass), while loss of the second ligand occurred at ca. 400-500 °C, overlapping with the onset of combustion of the carbon support. The residue mass of 14.0% at 800 °C is slightly higher than the amount of SnO_2 (12.3%) that should have been formed, which can be attributed in part to the residual mass of impurities in the carbon support (ca. 1%).

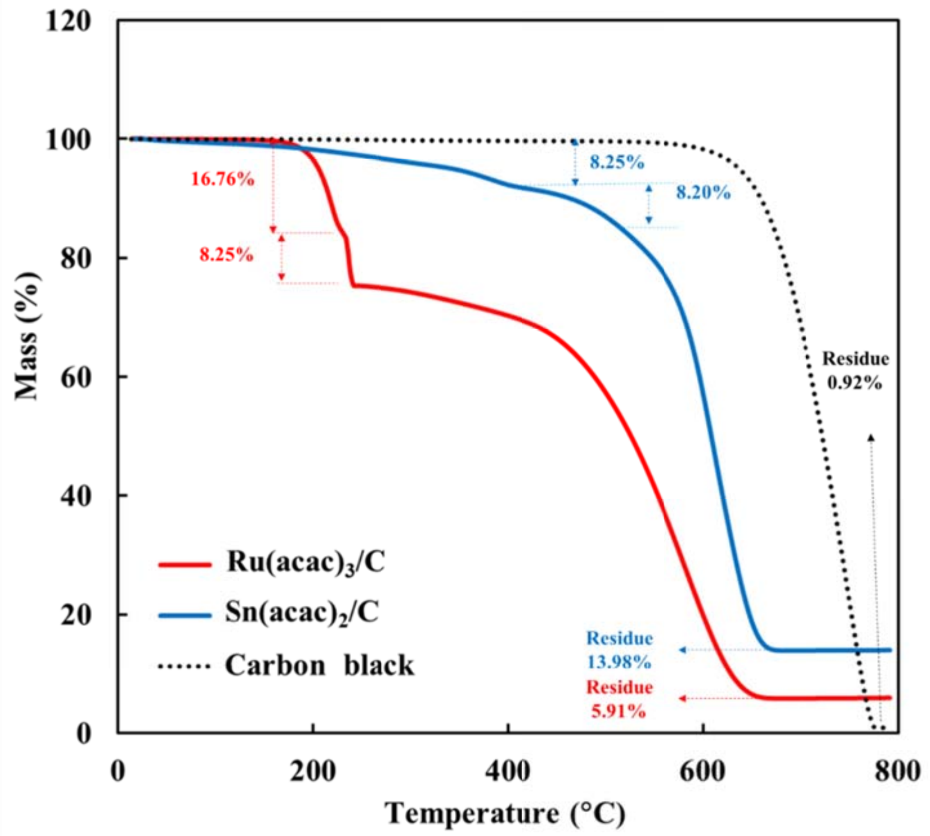

Figure 4.1. TGA plots for decomposition of $Ru(acac)_3$ and $Sn(acac)_2$ on Vulcan XC-72 carbon black.

Additional experiments with 30 min periods of isothermal decomposition were used to guide the selection of temperatures for the preparation of bulk samples of oxide coated carbon black

(Figure 4.2). The initial pause in the temperature ramp at 180 °C resulted in almost complete decomposition/sublimation of $Ru(acac)_3$ (21.7% mass loss), followed by only a 2.7% mass loss at 230 °C for 30 min. In contrast there was only a 2.3% loss of mass for $Sn(acac)_2$ at 180 °C, indicating that there was loss of the first ligand, but unlikely to be significant formation of SnO_2. Following 30 min at 350 °C the total mass loss (12.7%) was close to the calculated value of 13.6% for decomposition to SnO_2. It should be noted that SnO_2 can be deposited from $Sn(acac)_2$ by chemical vapour deposition at temperatures above 100 °C.[19]

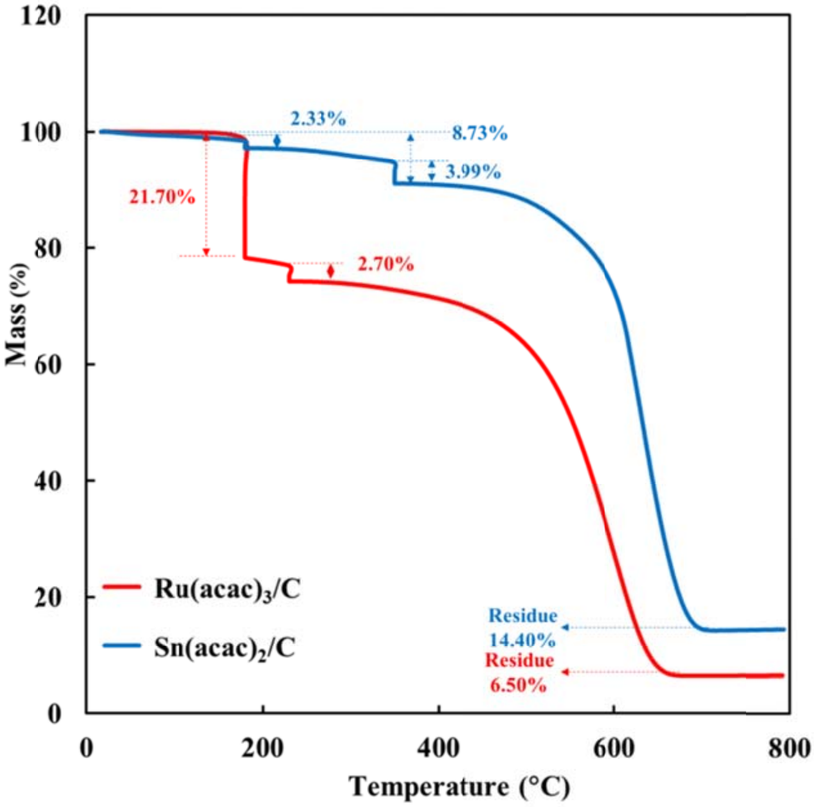

Figure 4.2. TGA plots for the decomposition of $Ru(acac)_3$ and $Sn(acac)_2$ on Vulcan XC-72 carbon black with 30 min isothermal periods at 180 °C, and 230 °C for $Ru(acac)_3$ or 350 °C for $Sn(acac)_2$.

The co-decomposition of $Ru(acac)_3$ and $Sn(acac)_2$ on carbon black (Figure 4.3) was quite different from decomposition of the individual components. By 260 °C, there had been a ca. 10% loss of mass, corresponding to decomposition/sublimation of most of the $Ru(acac)_3$, which was followed by a sharp 6.3% mass loss at ca. 265 °C corresponding to decomposition of the $Sn(acac)_2$ (theoretically 6.8%). The residual mass of 9.7% was close to the theoretical mass of 11.2%. Cleary, the decomposition of $Sn(acac)_2$ was catalysed by the RuO_2, and the sublimation of $Ru(acac)_3$ was suppressed by the presence of $Sn(acac)_2$. Although the co-decomposition has been described here as step-wise, these observations indicate that it is concerted to some extent, and that there is likely to be some mixing of the Ru and Sn oxides, particularly during isothermal decomposition at lower temperatures.

TGA of a Ru+Sn oxide/C composite prepared using a maximum temperature of 180 °C is shown in Figure 4.3. The Ru+Sn oxide strongly catalysed combustion of the carbon support, which occurred in two distinct stages at ca. 350 °C and 400 °C, *vs.* 750 °C for the carbon support alone (Figure 4.1). This suggests that the Ru and Sn oxides were not fully mixed. The residual mass of 33.7% from the Ru+Sn oxide/C composite was close to the expected value of 35.7%, indicating that sublimation of $Ru(acac)_3$ has only a small influence on the composition of mixed oxides prepared at 180 °C.

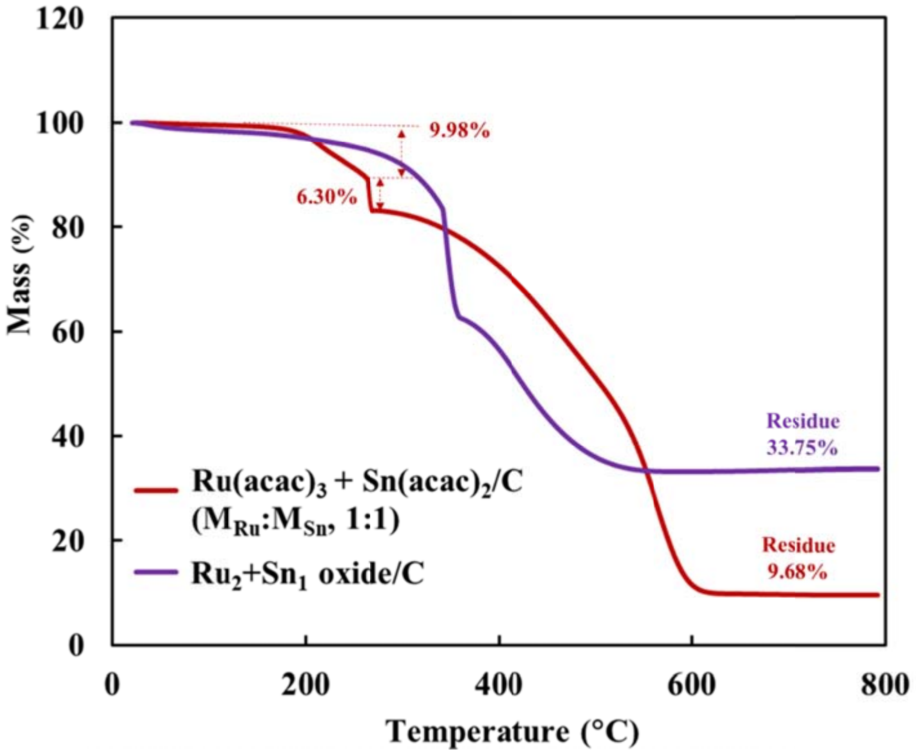

Figure 4.3. TGA plot for decomposition of a mixture of $Ru(acac)_3$ and $Sn(acac)_2$ on Vulcan XC-72 carbon black (0.55 mmol $Ru(acac)_3$ + 0.55 mmol $Sn(acac)_2$ per g of C), and a Ru+Sn oxide/C composite prepared with target Ru:Sn ratio of 2:1 and an oxide loading of 35.7%.

4.3.2 Characterization of the metal oxides and catalysts

Figure 4.4 shows an X-ray spectrum for Ru+Sn oxide on C, which shows the presence of both Ru and Sn in an approximately 1:1 molar ratio. XRD (Figure 4.5) confirmed that oxides had been formed. When $Ru(acac)_3$ alone was used, the peak positions were close to the standard values for RuO_2, while the mixed oxide showed sharp RuO_2 peaks with broad shoulders corresponding to SnO_2. The mixed oxide must therefore have consisted of a mixture of RuO_2 crystallites and a less ordered mixed Ru-Sn oxide.[20] The dominant RuO_2 peaks with SnO_2

shoulders are consistent with the TGA, which shows that RuO_2 would begin forming first to produce RuO_2 rich cores with SnO_2 rich shells.

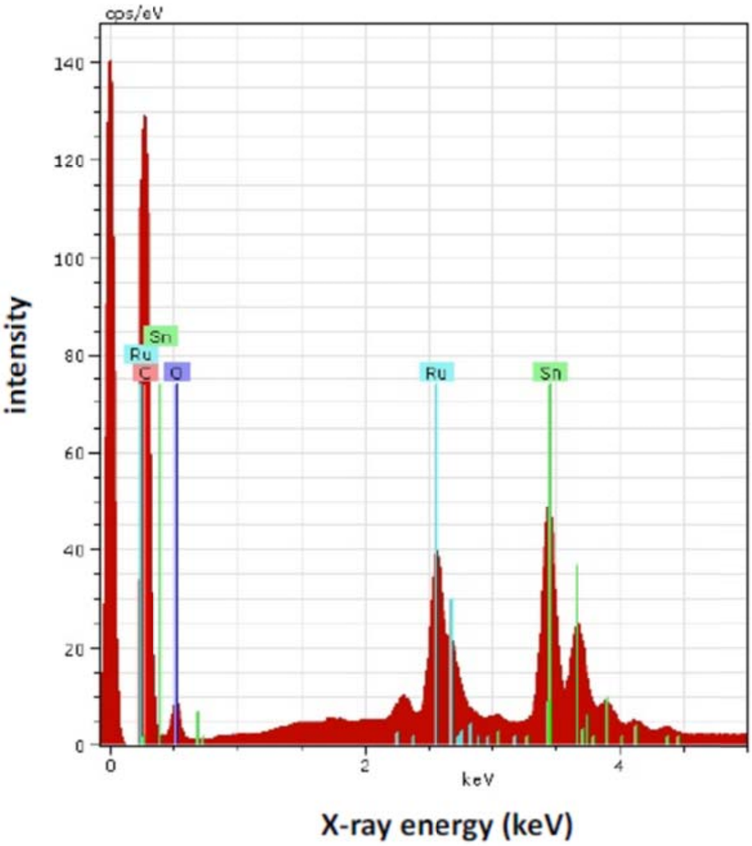

Figure 4.4. X-ray emission spectrum (EDX) of Ru+Sn oxide on carbon black. The target Ru:Sn ratio was 1:1.

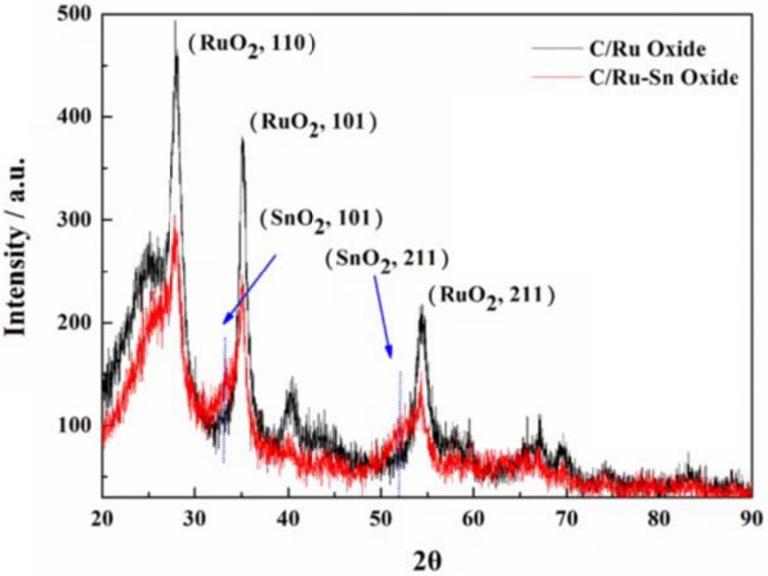

Figure 4.5. X-ray diffraction patterns for Ru oxide/C and Ru+Sn oxide/C composites.

Figure 4.6 shows a TEM image of the Pt/$Ru_{0.55}Sn_{0.45}O_2$/C catalyst. The morphology, consisting of linked 20-50 nm particles, is characteristic of the carbon support. Well dispersed Pt particles (ca. 5 nm dark spots) can also be clearly seen. However, there are no clear features that can be attributed to the Ru+Sn oxide, indicating that it consisted of very small particles (< 5 nm) and was well distributed over the carbon support. The Pt particle diameter is consistent with the size (4.9 nm) determined by XRD and the narrow size distribution consistently produced by the synthesis method.[16, 21] TEM images of the Pt/$Ru_{0.38}Sn_{0.62}O_2$/C and Pt/$Ru_{0.67}Sn_{0.33}O_2$/C, as indicated in Figure 4.7 and Figure 4.8, show similar features and particle sizes.

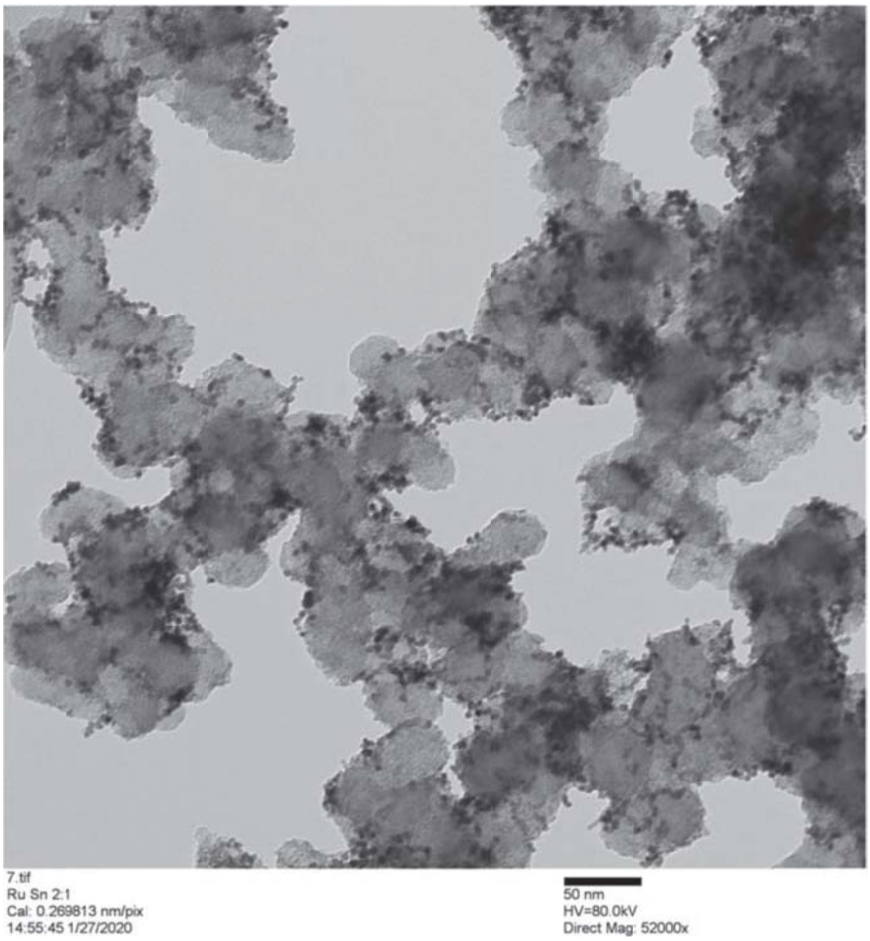

Figure 4.6. TEM image of the Pt/$Ru_{0.55}Sn_{0.45}O_2$/C catalyst. The scale bar is 50 nm.

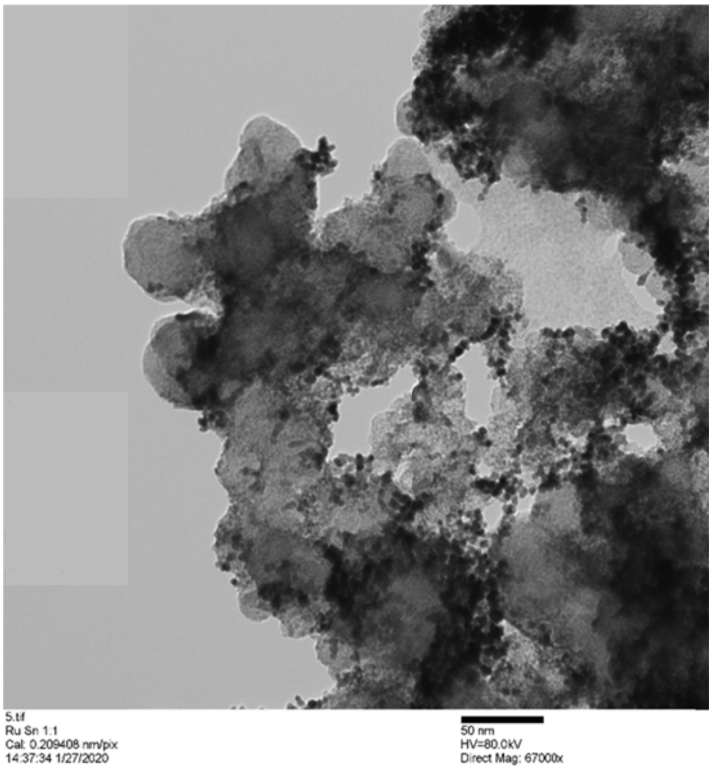

Figure 4.7. TEM image of the Pt/$Ru_{0.38}Sn_{0.62}O_2$/C catalyst. The scale bar is 50 nm.

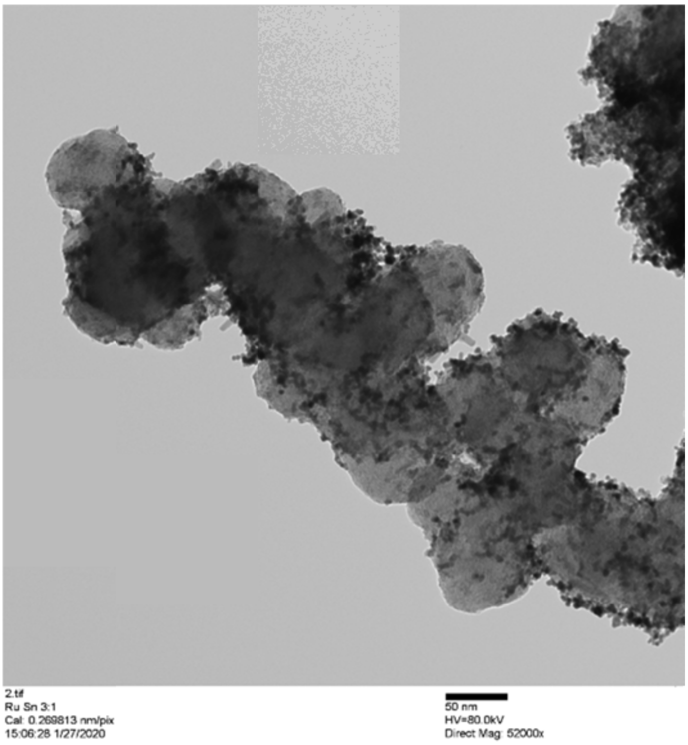

Figure 4.8. TEM image of the Pt/$Ru_{0.67}Sn_{0.33}O_2$/C catalyst. The scale bar is 50 nm.

Table 4.1. Compositions of the catalysts employed in this work.

Name	Target Ru:Sn atomic ratio	Measured Ru:Sn atomic ratio	Ru (mass%)	Sn (mass%)	Pt (mass%)
Pt/$Ru_{0.38}Sn_{0.62}O_2$/C	1:1	38:62	9.0 %	17.4 %	22.5 %
Pt/$Ru_{0.55}Sn_{0.45}O_2$/C	2:1	55:45	14.1 %	13.6 %	22.5 %
Pt/$Ru_{0.63}Sn_{0.37}O_2$/C	3:1	63:37	15.9 %	10.9 %	24.7 %

Figure 4.9 shows cyclic voltammograms in 0.5 M H_2SO_4(aq) of electrodes prepared with the Pt/C, Pt/$Ru_{0.55}Sn_{0.45}O_2$/C, and commercial 70% Pt/C catalysts. The voltammogram for the Pt/C catalyst is very similar to that for the commercial 70% Pt/C catalyst, indicating high

electrochemical utilization of the Pt nanoparticles. The slightly lower charges in the hydrogen adsorption and desorption regions can be attributed to the larger Pt particle size (4.9 *vs.* 3.6 nm). Charges in the hydrogen region are similar for the Pt/Ru-Sn oxide/C and Pt/C catalysts, but the Pt/Ru-Sn oxide/C catalyst gave much higher charging currents at potentials above ca. 0 V due to the pseudo-capacitance of the oxide support. The broad capacitive region from 0 to 0.8 V is characteristic of hydrous RuO_2.[14]

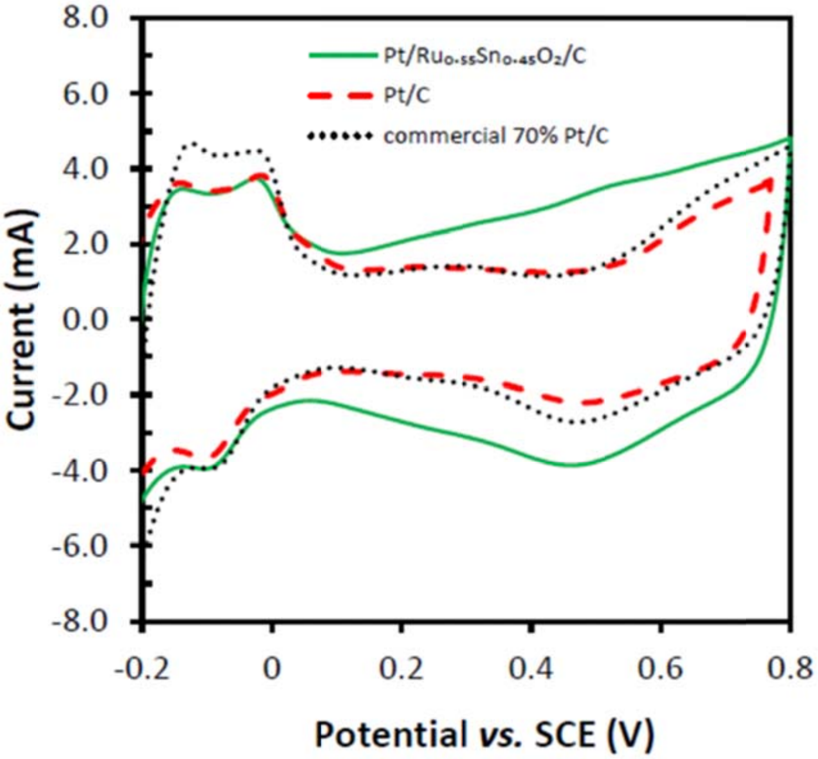

Figure 4.9. Cyclic voltammograms (100 mV s^{-1}) of Pt/C, $Pt/Ru_{0.55}Sn_{0.45}O_2/C$, and 70% Pt/C electrodes in 0.5 M H_2SO_4(aq).

4.3.3 Ethanol oxidation

Initial evaluation of the effects of the oxide layers on ethanol oxidation at Pt nanoparticles was performed by cyclic voltammetry at ambient temperature in a conventional cell with a 0.5 M H_2SO_4(aq) electrolyte. Figure 4.10 compares 1st cycle voltammograms at Pt/C, Pt/$Ru_{0.55}Sn_{0.45}O_2$/C, and 70% Pt/C electrodes. The results for the two Pt/C electrodes were very similar, with the commercial catalyst producing slightly higher currents due to the smaller Pt particle size. In contrast, the Pt/$Ru_{0.55}Sn_{0.45}O_2$/C catalyst produced much higher currents at low potentials (0.1 to 0.5 V) on the forward scan, and decreased the peak potential slightly. There was a similar shift in the peak potential on the reverse scan, and slightly higher currents at low potentials. The more pronounced effect of the Ru-Sn oxide coating at low potentials on the forward scan indicates that it mitigates the effects of adsorbed CO produced as an intermediate in ethanol oxidation, by providing -OH sites for its oxidation and/or via an electronic (charge-transfer) effect.[16] At higher potentials, CO is rapidly oxidized by Pt-OH, resulting in the peak at ca. 0.65 V. On the reverse scan, reduction of the Pt-OH layer produces a CO-free Pt surface that is more active for ethanol oxidation.[22]

Similar results to those in Figure 4.10 have been reported for Ru and Sn oxides on glassy carbon substrates,[16] and for Pt/Ru-Sn oxide/C catalysts with Ru-Sn oxide layers prepared by reaction of the carbon surface with $KRuO_4$ and $SnCl_4$.[14] This therefore validates the thermal decomposition of $Ru(acac)_3$ and $Sn(acac)_2$ as an alternative and potentially valuable method to produce Ru-Sn oxide/C supports for fuel-cell catalysts.

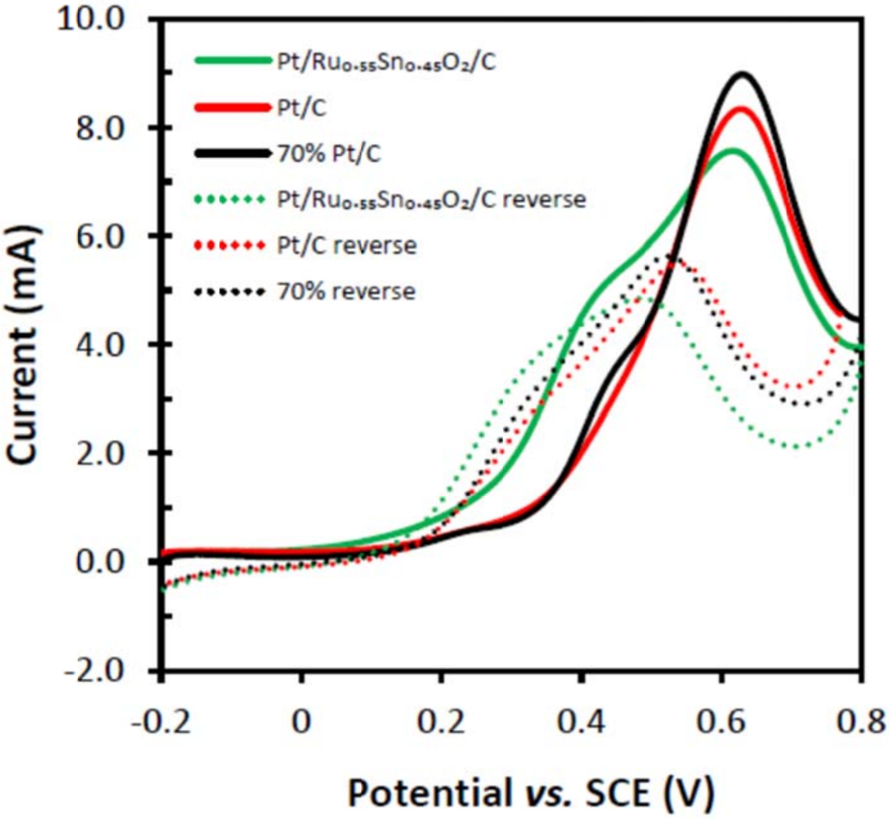

Figure 4.10. Cyclic voltammograms (10 mV s^{-1}) for oxidation of 0.2 M ethanol in 0.5 M H_2SO_4 at Pt/C, Pt/$Ru_{0.55}Sn_{0.45}O_2$/C, and 70% Pt/C electrodes. Dotted lines show the reverse scans.

Pt/RuO_2/C and Pt/SnO_2/C catalysts, prepared by using $Ru(acac)_3$ or $Sn(acac)_2$ alone to prepare the support, also showed some improvements in activity for ethanol oxidation over Pt/C (Figure 4.11). However, increases in performance were much larger when mixed $Ru_xSn_yO_2$ oxides were used. The synergy between Ru and Sn in mixed oxide supports has been attributed to the coupling of the high conductivity and strong bifunctional effect of RuO_2 with the strong electronic (ligand) effect of SnO_2.[14, 16]

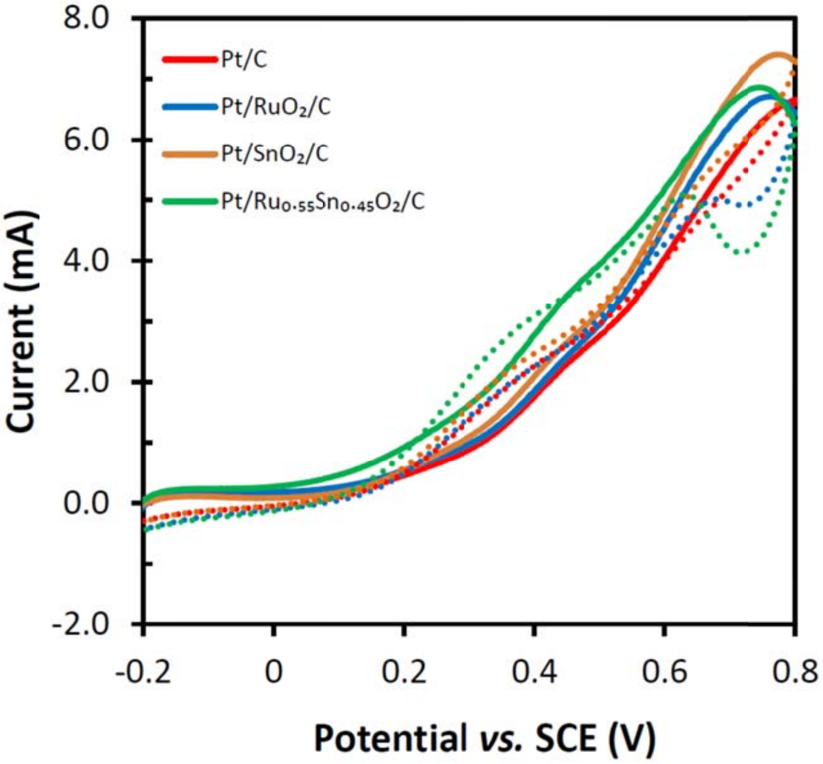

Figure 4.11. Cyclic voltammograms (10 mV s^{-1}) for oxidation of 0.2 M ethanol in 0.1 M H_2SO_4 at Pt/C, Pt/RuO_2/C, Pt/SnO_2/C, and Pt/$Ru_{0.55}Sn_{0.45}O_2$/C electrodes. Dotted lines show the reverse scans. Note that H_2SO_4 concentration was lower than for the voltammetry reported in the manuscript, and that the peak potentials are higher due to the increase solution resistance.

4.3.4 Effect of Ru:Sn ratio

Figure 4.12 shows voltammograms for ethanol oxidation at Pt/Ru-Sn oxide/C catalysts prepared with three different Ru to Sn ratios (the targeted and measured ratios are provided in Table 4.1). It can be seen that over the range investigated, changing the Ru to Sn had only a minor influence on ethanol oxidation. The intermediate composition (Pt/$Ru_{0.55}Sn_{0.45}O_2$/C), prepared with a 2:1 $Ru(acac)_3$:$Sn(acac)_2$ ratio provided somewhat higher currents than the others at potentials between 0.3 and 0.5 V on both the 1st and 2nd forward scan, and between 0.4 and 0.2 V on the reverse scan. This suggests that the optimum Ru:Sn ratio in the oxide support is close to 1:1.

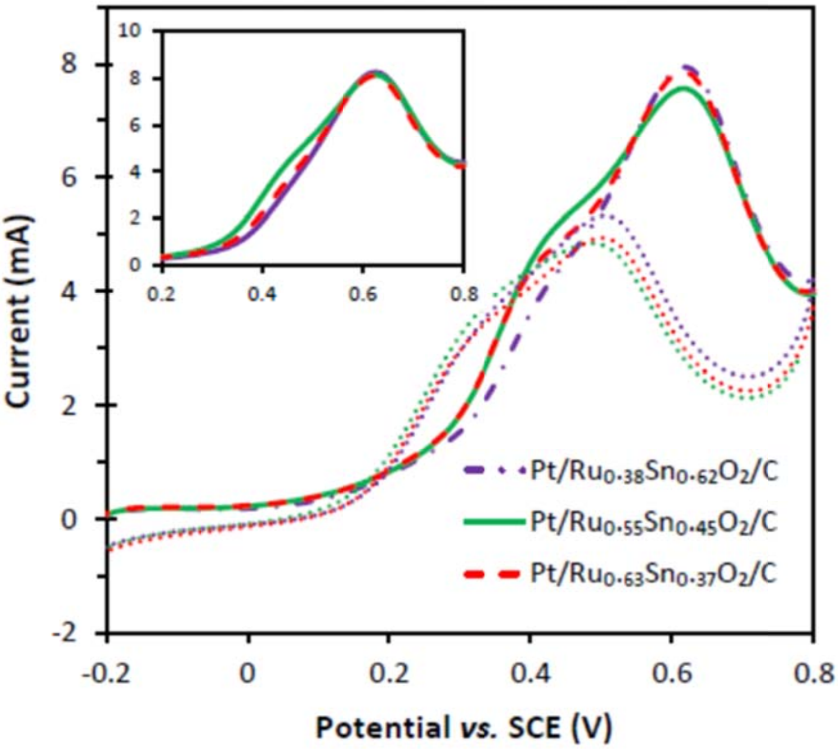

Figure 4.12. Cyclic voltammograms (10 mV s^{-1}) for oxidation of 0.2 M ethanol in 0.5 M H_2SO_4 at $Pt/Ru_{0.38}Sn_{0.62}O_2/C$, $Pt/Ru_{0.55}Sn_{0.45}O_2/C$, and $Pt/Ru_{0.67}Sn_{0.33}O_2/C$ electrodes. Dotted lines show the reverse scans and the inset shows the 2nd forward scans.

Chronoamperometry measurements (Figure 4.13) showed large enhancements in the electrocatalytic activity of the Pt at low potentials when Ru-Sn oxide was present. The optimum composition varied with potential, with the $Pt/Ru_{0.55}Sn_{0.45}O_2/C$ catalyst providing the highest currents up to 0.2 V and the $Pt/Ru_{0.63}Sn_{0.37}O_2/C$ catalyst providing the highest currents at 0.3-0.5

V. All of the catalysts, including the commercial Pt/C catalyst provided quite stable currents at 0.2 V, but showed increasingly rapid decays at higher potentials. Increasing the Ru content of the oxide increased stability at potentials above 0.3 V.

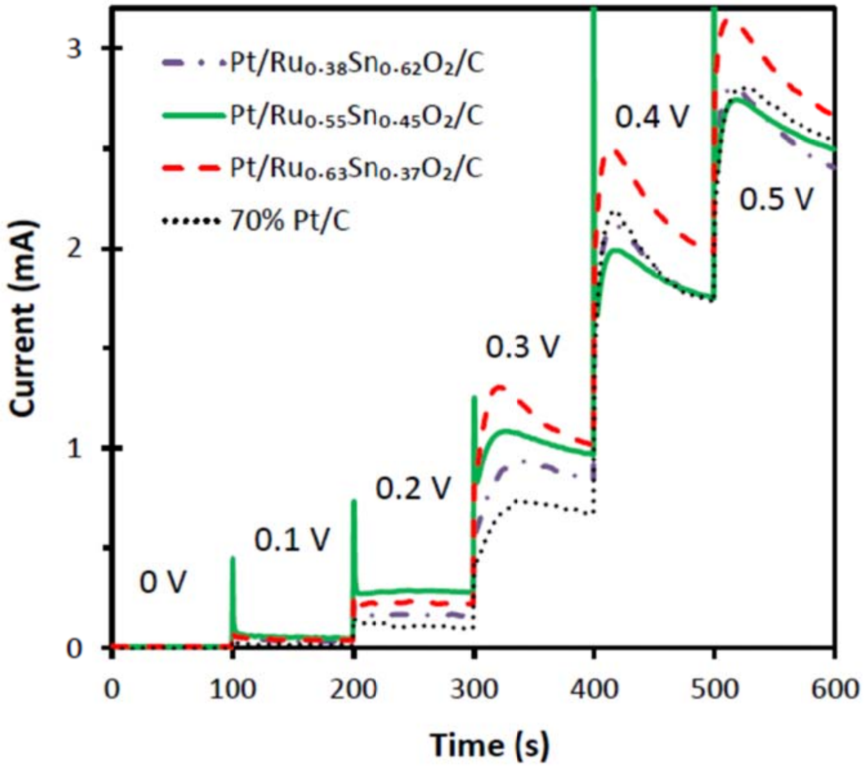

Figure 4.13. Current *vs.* time during a series of potential steps for oxidation of 0.2 M ethanol in 0.5 M H_2SO_4 at $Pt/Ru_{0.38}Sn_{0.62}O_2/C$, $Pt/Ru_{0.55}Sn_{0.45}O_2/C$, and $Pt/Ru_{0.67}Sn_{0.33}O_2/C$, and 70% Pt/C electrodes.

Longer term experiments showed pronounced differences, however. Figure 4.14 shows data over 1 h periods for the Pt/C and $Pt/Ru_{0.63}Sn_{0.37}O_2/C$ catalysts at 0.2 V and 0.3 V. The first data set in each case was obtained with a pristine electrode initially at open circuit, with different electrodes employed at each potential. The 2nd data set in each case was obtained on the same electrode following a step to 0.7 V for 5 s to remove adsorbates; primarily CO.

It can be seen from the 1st data sets in Figure 4.14 that the Pt/$Ru_{0.63}Sn_{0.37}O_2$/C catalyst initially produced much higher currents than Pt/C at both potentials. At 0.2 V the current at the Pt/$Ru_{0.63}Sn_{0.37}O_2$/C electrode was still slightly higher after 1 h, but the effect of the Pt-Ru oxide had decreased greatly. Following adsorbate stripping at 0.7 V, both electrodes showed higher currents than in the 1st data set, indicating that they had been activated. However, there were not significant differences between the two electrodes, indicating that the effect of the Pt-Ru oxide had been irreversibly lost. At 0.3 V, the decay in activity of the Pt/$Ru_{0.63}Sn_{0.37}O_2$/C catalyst was much more pronounced, falling below that of the Pt/C catalyst after ca. 30 min. Following adsorbate stripping at 0.7 V, the Pt/C electrode produced higher currents than the Pt/$Ru_{0.63}Sn_{0.37}O_2$/C catalyst, again indicating that the effect of the Pt-Ru oxide had been irreversibly lost.

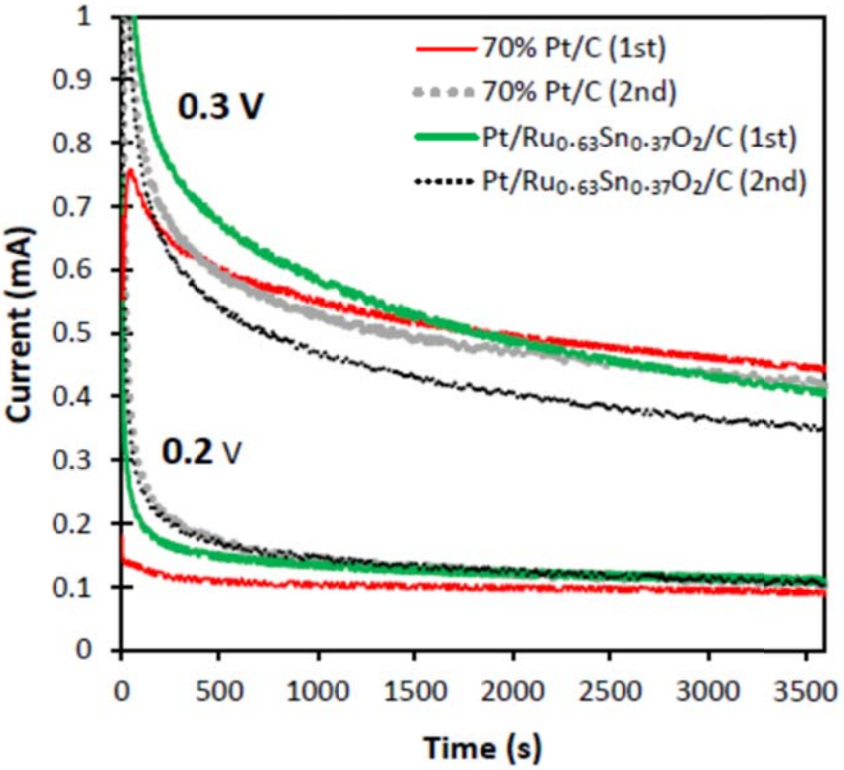

Figure 4.14. Current *vs.* time for oxidation of 0.2 M ethanol in 0.5 M H_2SO_4 at 0.2 V and 0.3 V at $Pt/Ru_{0.67}Sn_{0.33}O_2/C$ and 70% Pt/C electrodes. The 1st data set is for a step from the open circuit potential for a pristine electrode. The 2nd data set is for the same electrode following a step to 0.7 V for 5s.

The limited stability of Pt/Ru+Sn oxide/C catalysts in H_2SO_4(aq) has been reported previously, and is assumed to be due to dissolution of the oxide.[14, 16] However, much better stability has been observed in PEM fuel [13] and electrolysis [14] cells at 80 °C.

4.3.5 Ethanol electrolysis at 80 °C in a PEM cell

Figure 4.15 shows steady state currents *vs.* potential polarization curve for Pt/$Ru_{0.55}Sn_{0.45}O_2$/C/CPF (1.0 mg Pt cm^{-2}) electrodes at 80 °C in the PEM cell. High currents were maintained during the 1 h conditioning period and data collection, indicating good durability of the catalyst under these conditions. At low potentials, the Pt/$Ru_{0.55}Sn_{0.45}O_2$/C catalyst provided much higher currents in the PEM cell than a commercial 20% Pt/C catalyst with a higher Pt loading (2.0 mg Pt cm^{-2}) operating under the same conditions. The higher currents for the 20% Pt/C electrodes at higher potentials were presumably due partly to the higher Pt loading employed and partly to difficulty in controlling the drop coating method used to prepare the Pt/$Ru_{0.55}Sn_{0.45}O_2$/C/CFP electrodes. Preparation of Pt/$Ru_xSn_yO_2$/C/CFP electrodes by spraying the precursor metal acetylacetonate and Pt nanoparticle solution onto C/CFP should be more effective, and will facilitate optimization of compositions, decompositions temperatures, and loadings. These preliminary results clearly demonstrate the potential of synthesis of oxide supported catalysts directly onto DEFC electrodes.

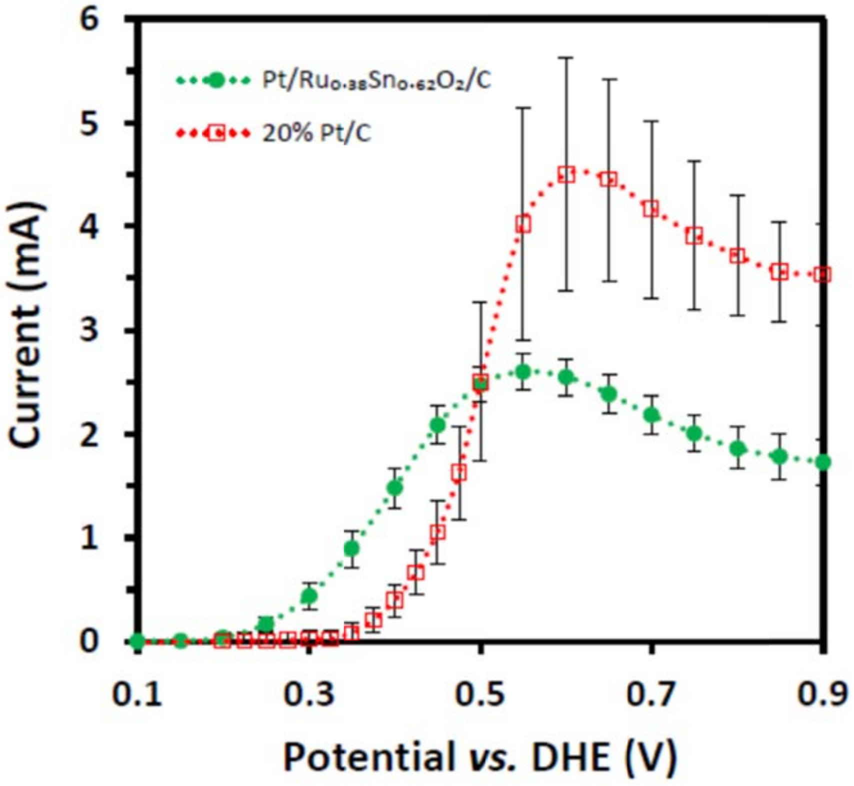

Figure 4.15. Polarization curves for ethanol oxidation (0.1 M) at Pt/$Ru_{0.55}Sn_{0.45}O_2$/C (1.0 mg Pt cm^{-2}) and 20% Pt/C (2.0 mg Pt cm^{-2}) anodes in a nine-anode PEM electrolysis cell at 80 °C. Averages and standard deviations are shown for 3 electrodes of each type.

4.4 Conclusions

Thermal decomposition of $Ru(acac)_3$ and $Sn(acac)_2$ on Vulcan XC-72 carbon black produces mixed oxide composite supports that substantially increase the activity of Pt nanoparticles for ethanol oxidation. The activity of the catalysts was not strongly dependent on the Ru:Sn ratio, but increasing the Ru content increased stability in H_2SO_4(aq). Although the stability of the oxide coating was poor at high potentials in H_2SO_4(aq), much better durability was obtained in a PEM cell at 80 °C.

Electrodes for PEM electrolysis and fuel (DEFC) cells can be fabricated by coating a carbon fibre paper backing layer consecutively with carbon black, $Ru(acac)_3$ + $Sn(acac)_2$, and Pt nanoparticles, with appropriate thermal processing. A low Pt loading anode with high activity at low potentials was prepared in this way. This methodology is well suited for rapid preparation and screening of libraries of oxide supported catalysts to optimize activity and durability under fuel cell conditions. It can be used to produce a wide variety of oxide supports and offers simple control of the catalyst composition.

4.5 References

1. An, L.; Zhao, T. S.; Li, Y. S., Carbon-neutral sustainable energy technology: Direct ethanol fuel cells. *Renewable and Sustainable Energy Reviews,* **2015**, *50*, 1462-1468.

2. Ong, B. C.; Kamarudin, S. K.; Basri, S., Direct liquid fuel cells: A review. *International Journal of Hydrogen Energy,* **2017**, *42* (15), 10142-10157.

3. Akhairi, M. A. F.; Kamarudin, S. K., Catalysts in direct ethanol fuel cell (DEFC): An overview. *International Journal of Hydrogen Energy,* **2016**, *41* (7), 4214-4228.

4. Antolini, E., Pt-Ni and Pt-M-Ni (M = Ru, Sn) anode catalysts for low-temperature acidic direct alcohol fuel cells: A review. *Energies,* **2017**, *10* (1), 42.

5. Elezovic, N. R.; Radmilovic, V. R.; Krstajic, N. V., Platinum nanocatalysts on metal oxide based supports for low temperature fuel cell applications. *RCS Advances,* **2016**, *6* (8), 6788-6801.

6. Mann, J.; Yao, N.; Bocarsly, A. B., Characterization and analysis of new catalysts for a direct ethanol fuel cell. *Langmuir,* **2006**, *22*, 10432-10436.

7. Kowal, A.; Li, M.; Shao, M.; Sasaki, K.; Vukmirovic, M. B.; Zhang, J.; Marinkovic, N. S.; Liu, P.; Frenkel, A. I.; Adzic, R. R., Ternary Pt/Rh/SnO_2 electrocatalysts for oxidizing ethanol to CO_2. *Nature Materials,* **2009**, *8*, 325-330.

8. Zhang, Z. Q.; Wu, Q.; Mao, K.; Chen, Y. G.; Du, L. Y.; Bu, Y. F.; Zhuo, O.; Yang, L. J.; Wang, X. Z.; Hu, Z., Efficient ternary synergism of platinum/tin oxide/nitrogen-doped

carbon leading to high-performance ethanol oxidation. *ACS Catalysis,* **2018**, *8* (9), 8477-8483.

9. Kim, Y. S.; Jang, H. S.; Kim, W. B., An efficient composite hybrid catalyst fashioned from Pt nanoparticles and Sb-doped SnO_2 nanowires for alcohol electro-oxidation. *Journal of Materials Chemistry,* **2010**, *20*, 7859–7863.

10. Neto, A. O.; Brandalise, M.; Dias, R. R.; Ayoub, J. M. S.; Silva, A. C.; Penteado, J. C.; Linardi, M.; Spinace, E. V., The performance of Pt nanoparticles supported on $Sb_2O.SnO_2$, on carbon and on physical mixtures of $Sb_2O_5.SnO_2$ and carbon for ethanol electro-oxidation. *International Journal of Hydrogen Energy,* **2010**, *35*, 9177-9181.

11. Neto, E. S. V.; Gomes, M. A.; Salazar-Banda, G. R.; Eguiluz, K. I. B., Pt and Pt-Rh nanowires supported on carbon and SnO_2:Sb nanoparticles for ethanol electrochemical oxidation in acidic media. *International Journal of Hydrogen Energy,* **2018**, *43* (1), 178-188.

12. Krstajic, M. N.; Obradovic, M. D.; Babic, B. M.; Radmilovic, V. R.; Lacnjevac, U. C.; Krstajic, N. V.; Gojkovic, S. L., Electrochemical oxidation of methanol on $Pt/(Ru_xSn_{1-x})O_2$ nanocatalyst. *Journal of the Serbian Chemical Society,* **2013**, *78* (11), 1703-1716.

13. James, D. D.; Moghaddam, R. B.; Chen, B. Y.; Pickup, P. G., Ruthenium-tin oxide/carbon supported platinum catalysts for electrochemical oxidation of ethanol in direct ethanol fuel cells. *Journal of The Electrochemical Society,* **2018**, *165* (3), F215.

14. Chen, B. Y.; Brueckner, T. M.; Altarawneh, R. M.; Pickup, P. G., Composition dependence of ethanol oxidation at ruthenium-tin oxide/carbon supported platinum catalysts. *Journal of The Electrochemical Society,* **2018**, *165* (15), J3019.

15. Wang, X.; Deng, F. Y.; Tang, Z. Z.; Wu, B.; Tang, D.; Lin, W., The nature of phase separation in a Ru-Sn-O ternary oxide electrocatalyst. *Physical Chemistry Chemical Physics,* **2013**, *15* (11), 3977-3984.

16. Moghaddam, R. B.; Pickup, P. G., Support effects on the oxidation of ethanol at Pt nanoparticles. *Electrochimica Acta,* **2012**, *65*, 210-215.

17. Brueckner, T. M.; Pickup, P. G., Kinetics and stoichiometry of methanol and ethanol oxidation in multi-anode proton exchange membrane cells. *Journal of The Electrochemical Society,* **2017**, *64* (12), F1172.

18. Mahfouz, R. M.; Siddiqui, A. R. H.; Al-Ahmari, S. A.; Alkayali, W. Z., Kinetic analysis of thermal decomposition of unirradiated and gamma-irradiated tris(acetylacetonato)-ruthenium(III) [Ru(acac)$_3$]. *Progress in Reaction Kinetics and Mechanism,* **2007**, *32* (1), 1-27.

19. Maruyama, T.; Ikuta, Y., Tin dioxide thin-films prepared by chemical vapor-deposition from tin(II) acetylacetonate. *Solar Energy Materials and Solar Cells,* **1992**, *28* (3), 209-215.

20. Lee, J. M.; Han, S. B.; Lee, Y. W.; Song, Y. J.; Kim, J. Y.; Park, K. W., RuO_2-SnO_2 nanocomposite electrodes for methanol electrooxidation. *Journal of Alloys and Compounds,* **2010**, *506*, 57-62.

21. Yang, J.; Lee, J. Y.; Too, H. P., Size effect in thiol and amine binding to small Pt nanoparticles. *Analytica Chimica Acta,* **2006**, *571*, 206-210.

22. Zhao, Y. Z.; Li, X. M.; Schechter, J. M.; Yang, Y. A., Revisiting the oxidation peak in the cathodic scan of the cyclic voltammogram of alcohol oxidation on noble metal electrodes. *RSC Advances,* **2016**, *6* (7), 5384-5390.

Chapter 5

Modification of carbon black and titanium by thermal decomposition of lead acetylacetonate to improve activities for ethanol and formic oxidation at supported Pt catalysts

Aspects of this chapter (ca. 50% of its content) have been published in the paper below:

H. Hang; P. G. Pickup, Modification of carbon black by thermal decomposition of lead acetylacetonate to improve activities for ethanol oxidation at supported Pt catalysts. ECS Transactions, 2020, 97(7), 929.

The principal author (Hui Hang) as the main researcher contributed to all aspects of the project including: literature review, designing some of the experiments, performing all of the experiments, analyzing and presenting the data, and writing the first draft of the manuscript.

The corresponding author (Prof. Peter G. Pickup) proposed the initial experiments, oversaw all aspects of the project, and contributed to several aspects of the project including: experimental design, data analysis, revision of the draft manuscript, submission to the journal, and supervision of the principal author (Hui Hang).

The raw data is provided in Appendix A.

5.1 Introduction

Direct liquid fuel cells (DLFCs) are a type of promising energy-conversion device with high theoretical efficiency. In comparison with hydrogen, liquid biofuels (e.g. ethanol and formic acid) have outstanding advantages in volumetric energy density, transportation, storage, and safety.[1-3] Ethanol is produced on a large scale from biomass as bioethanol, while formic acid can be sustainably generated from CO_2 electroreduction using renewable electricity.[4-6] With the aim of superseding internal combustion engines for transportation and electricity generation, the tremendous potential of DLFCs has attracted the interest of numerous researchers. However, the performance of DLFCs still needs further improvement for commercialization. Optimization of anode catalysts for DLFCs is important for improving their current density and fuel efficiency.

Aiming to improve the performance of pure platinum (Pt) anode catalysts for DLFCs, many other metallic components have been introduced into the catalysts (e.g. binary alloy catalysts and metal oxide-supported catalysts). PtPb alloy catalysts initially attracted researchers' attention because of their remarkable performance for formic acid oxidation.[7] The presence of Pb greatly promoted the direct oxidation of formic acid to carbon dioxide (CO_2) by dehydrogenation at low potentials, which was explained by a third body effect.[8] PtPb was also found to enhance the current density in methanol oxidation, and the addition of Pb to the Pt catalyst led to a lower charge-transfer resistance.[9]

Lead oxides are active for the oxidation of small organic compounds. PbO has been used as an ethanol sensor material.[10] As a strong oxidant, PbO_2 was used to electrochemically oxidize organic pollutants.[11] Significantly, a lead oxide supported anode catalyst (Pt/PbO_x) was reported to have a similar effect as PtPb on formic acid oxidation.[12] Under basic conditions, PbO_2 modification of a commercial Pt catalyst improved its performance through providing a higher catalytic activity and durability for ethanol oxidation.[13] However, the behavior of Pt/PbO for ethanol oxidation under acidic conditions has not been reported.

Among a variety of commercial catalysts, carbon black is the common support material due to its advantages in electrical conductivity, specific surface area, bulk production, and cost. Thermal decomposition of $M(acac)_x$ complexes (acac = acetylacetonate) has been reported as a versatile method to rapidly prepare metal oxide supports on high surface area carbon electrode materials for electrocatalysis of ethanol oxidation.[14] Due to its strong corrosion resistance and electrical conductivity, titanium in various forms (e.g. felt, mesh, and foam) has been applied as electrodes for methanol electrooxidation, water electrolysis in polymer electrolyte membrane electrolysis cells, and photoelectrocatalytic degradation of organic contaminant.[15-18] It is an excellent candidate for supporting catalysts in fuel cells.

In this work, high surface area carbon black and titanium were modified by thermal decomposition of lead acetylacetonate ($Pb(acac)_2$), and used as supports for Pt catalysts to investigate the effect on oxidation of ethanol and formic acid. $Pb_3(CO_3)_2(OH)_2$ (basic lead carbonate, BLC) and PbO were respectively produced on carbon black and titanium supports by $Pb(acac)_2$ thermal decomposition. Pt nanoparticles were prepared separately and adsorbed onto the modified supports. Large enhancement in ethanol oxidation was observed at both Pt/BLC/C and Pt/PbO/Ti electrodes in cyclic voltametric measurements. Moreover, the presence of BLC greatly enhanced the activity of the Pt nanoparticles for formic acid oxidation at low potentials. For Pt/PbO/Ti, charge transfer between Pt and the PbO support was investigated by X-ray photoelectron spectroscopy. The stability of Pt/BLC/C was also investigated, and the catalyst was applied as the anode catalyst in a proton exchange membrane (PEM) electrolysis cell to investigate its performance and CO_2 selectivity for use in direct ethanol fuel cells. A Pt/BLC/C catalyst exhibited the potential to be used in direct formic acid fuel cells and direct ethanol fuel cells.

5.2 Experimental

5.2.1 Synthesis of Pt/BLC/C catalysts

The modified carbon black support materials (BLC/C) used for preparation of catalysts were prepared as follows. Carbon black (100 mg) was dispersed well by sonication for 3 h in a solution of lead acetylacetonate ($Pb(acac)_2$) (0.005 M in methanol). The loading of $Pb(acac)_2$ on the carbon black was adjusted by changing the volume of $Pb(acac)_2$ solution. After drying at ambient temperature overnight, the mixture was heated in air on a hot plate at 150 °C for 1 h and then 250 °C for 2 h. The product was washed with methanol and deionized water, and dried in an oven at 100 °C for 6 h.

Pt/BLC/C catalysts with similar Pt percentages were prepared by adsorbing the same amount of Pt nanoparticles onto the modified carbon black support materials. A colloidal solution of 5 nm Pt nanoparticles (0.48 mg mL^{-1} Pt) was prepared as previously described.[19] 58.5 mg of the modified carbon black support material was dispersed in 36.3 mL of the Pt nanoparticle solution by 3 h of sonication, allowed to settle overnight, and collected by filtration. The catalyst was washed three times with deionized water, followed by drying at 80 °C for 6 h. A Pt/C catalyst was prepared similarly by using unmodified carbon black for comparison on catalytic activity.

5.2.2 Preparation of Pt/PbO/Ti electrodes

Ti based working electrodes were prepared by synthesis of each catalyst on a strip of Ti foil (250 μm thick). PbO modification of a Ti electrode was performed by applying 5.0 μL of 0.005 M $Pb(acac)_2$ in methanol onto a ca. 0.5 × 0.5 cm area of a Ti strip, allowing it to dry, and heating it on a hot plate in air at 150 °C for 1 h and then 180 °C for 1 h. After cooling to the ambient temperature, the oxide deposit was washed with ethanol, 0.1 M H_2SO_4 and deionized water and heated at 70 °C until completely dry. A Pt/PbO/Ti electrode was prepared by evenly drop coating 5.0 μL of the Pt nanoparticle solution (ca. 0.01 mg cm^{-2} of Pt) onto the oxide deposit and allowed to dry. A Pt/Ti electrode was prepared by coating same amount of Pt nanoparticles on a strip of Ti foil without PbO modification.

5.2.3 Characterization

Thermal decomposition behavior of $Pb(acac)_2$ complex with and without carbon black support were investigated by thermogravimetric (TGA) measurement using a TA Instruments Q500 TGA. The materials produced by $Pb(acac)_2$ thermal decomposition on Ti and carbon black were identified by X-ray diffraction (XRD) using a Model Rigaku Ultima IV X-ray diffractometer. To characterize the product layer on a Ti support with XRD, the sample was prepared on a thinner Ti foil (25 μm thick, 1 × 1 cm) with a higher loading of $Pb(acac)_2$ (2×10^{-6} moles cm^{-2}), and heated on a hot plate at 150 °C, 180 °C each for 1 h. Through XRD measurement, the average crystallite sizes (shown in Table 5.1) of Pt nanoparticles for Pt/C and

Pt/BLC/C catalysts were evaluated using Scherrer's equation ($D = 0.9\lambda/\beta \cos \theta$), where the wavelength λ is 0.15406 nm, β is the full width at half maximum intensity of the peak, and θ is diffraction peak.[20] The Pt percentages and Pt:Pb ratios of prepared Pt/BLC/C catalysts were characterized by a FEI Quanta 400 scanning electron microscope with an energy dispersive X-ray detector (SEM/EDX), and are shown in Table 5.2. A VG Microtech MultiLab ESCA 2000 X-ray Photoelectron Spectrometer (XPS) was used to characterize Pt/PbO/Ti for investigating possibility of charge transfer between Pt and PbO. The XPS measurements were carried out by Andrew George, at Dalhousie University (the Clean Technologies Research Institute). The XPS samples were prepared as follows: the solution containing 0.002 mmol $Pb(acac)_2$ was dropping coated on a thin Ti foil (25 μm thick, 1 × 1cm). After drying in a fume hood, they were heated on a hot plate at 150 °C and then 180 °C, each for 1 h. Finally, Pt/PbO/Ti and Pt/Ti samples were prepared by drop coating 20 μL of Pt nanoparticle solution on the Ti foils (1 × 1cm) with and without $Pb(acac)_2$ modification, then dried at 70 °C.

5.2.4 Electrochemical measurements

Working electrodes of carbon black supported catalysts were prepared as follows. Carbon fiber paper (10 × 10 cm) was coated with carbon black as a support layer (1 mg cm^{-2}) by spraying with a carbon black suspension (10 mg mL^{-1} in 2-propanol). Catalyst inks, prepared by dispersing 4.0 mg of catalyst in water (50 μL), 2-propanol (75 μL) and 1-propanol (75 μL) by sonication for 3 h, were painted onto 0.24 cm^2 discs of carbon black/carbon fiber paper (C/CFP) to give Pt loadings of 0.30 mg cm^{-2}. All electrodes were dried at ambient temperature overnight before use. Voltammetric and chronoamperometric measurements were carried out using a Bio-Logic SP-50 Potentiostat/Galvanostat operated with EC-Lab software. A saturated calomel electrode (SCE) and a platinum wire were used as the reference and counter electrodes. Nitrogen was used to purge the electrolyte solution prior to all measurements and maintain an inert atmosphere during measurements.

A nine-anode PEM electrolysis cell controlled with a MSTAT multichannel potentiostat (Arbin Instruments) was used to investigate the performance of a Pt/BLC/C catalyst for ethanol oxidation at 80 °C.[21] This cell contains nine separated anodes, so it can be used to evaluate and compare different catalysts simultaneously. Working electrodes were prepared by painting a certain volume of catalyst ink onto a 0.24 cm^2 disc of C/CFP to give a Pt loading of 1.0 mg cm^{-2}. Afterwards, 6 μL of Nafion solution was drop coated on the top of each electrode. For each catalyst, three working electrodes were prepared, and dried in a fume hood at ambient temperature overnight before use. In crossover mode of the PEM cell, a 0.1 M ethanol solution was pumped through the cathode at 0.5 mL min^{-1}, and N_2 gas was purged to the anode with 10 mL min^{-1} flow to prevent interference from oxygen.[21] At the anode, the flux of ethanol to the working electrodes is controlled by its diffusion rate through the membrane. The cathode was assembled with a Pt black electrode, which also acted as a dynamic hydrogen electrode. Polarization curves were recorded by applying each potential for 3 min and averaging the current over the final 2 min.

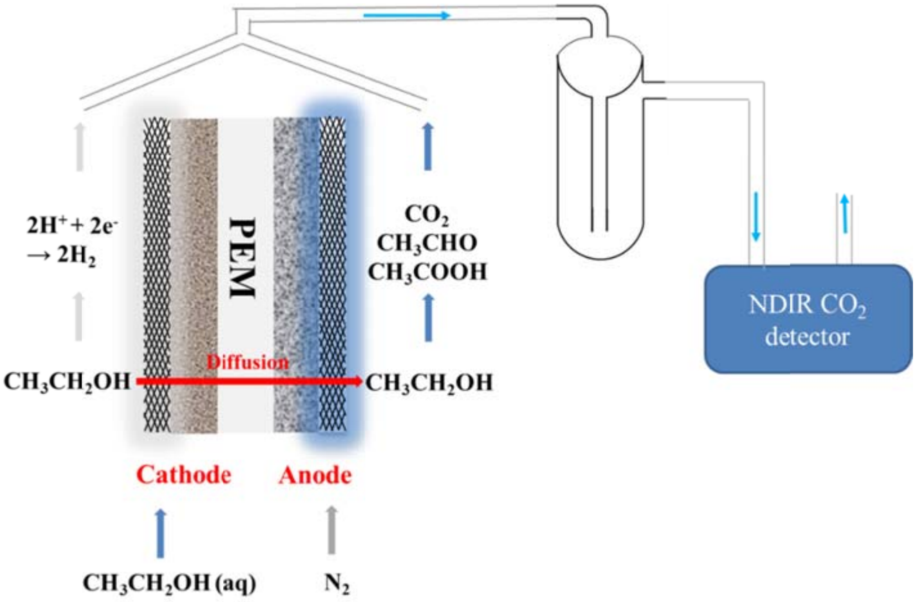

Figure 5.1. Scheme of the set-up for measuring CO_2 generated from the PEM cell (one of the nine anodes and part of the cathode are shown as an example) with a non-dispersive infrared (NDIR) CO_2 detector.

For in situ monitoring of produced CO_2, a non-dispersive infrared (NDIR) CO_2 detector was connected to the PEM cell as shown in Figure 5.1. For each catalyst, three electrodes were measured simultaneously. The products from both the anode and cathode were collected and passed through liquid collection glassware, so the CO_2 concentration in the gaseous exhaust could be measured by a commercial Telaire 6615 CO_2 detector and recorded by eCO2View software. The flow rate of N_2 was controlled at 50 mL min^{-1} due to the requirement of the sensor. According to previous research of our group, the CO_2 yield for methanol oxidation under these conditions was close to 100%.[22] In this experiment, calibration of the CO_2 detector was performed by online measuring of the CO_2 concentration of the outlet gases from oxidization of

0.1 M methanol (0.2 mL min^{-1}) at various potentials. The theoretical concentration of produced CO_2 was calculated using Equation 5.1.

$$Theoretical\ CO_2\ concentration\ (ppm)=\frac{(\frac{It}{nF})\times 10^6}{\frac{\dot{V}t}{V_m}+(\frac{It}{nF})} \qquad \text{(Equation 5.1)}$$

Where I is sum of currents of three electrodes for the same catalyst (A), n is the number of electrons transferred for forming a CO_2 molecule, F is the faraday constant (96500 A s mol^{-1}), $\dot{V}$ is the volumetric flow rate of nitrogen in L s^{-1}, V_m is molar volume of any gas in L mol^{-1}, and t is the time length (s). The oxidation current and CO_2 concentration reading (ppm) were allowed to stabilize, and their averages over the last 60 s were used for calculation. As shown in Figure 5.2, the CO_2 calibration curve has a good linearity ($R^2 = 0.9981$), and its slope (1.0266) close to one indicates that the NDIR CO_2 detector can accurately measure CO_2 concentration of the products from the PEM cell.[22] For ethanol oxidation, the CO_2 yield was measured for 0.1 M ethanol (0.2 mL min^{-1}) oxidized at 0.5 V (*vs.* DHE), with N_2 flow of 50 mL min^{-1}. The CO_2 concentration was calculated with the CO_2 calibration curve. The CO_2 yield of ethanol oxidation was calculated using Equation 5.2.

$$Faradaic\ CO_2\ yield=\frac{experimental\ concentration\ of\ CO_2}{theoretical\ concentration\ of\ CO_2} \qquad \text{(Equation 5.2)}$$

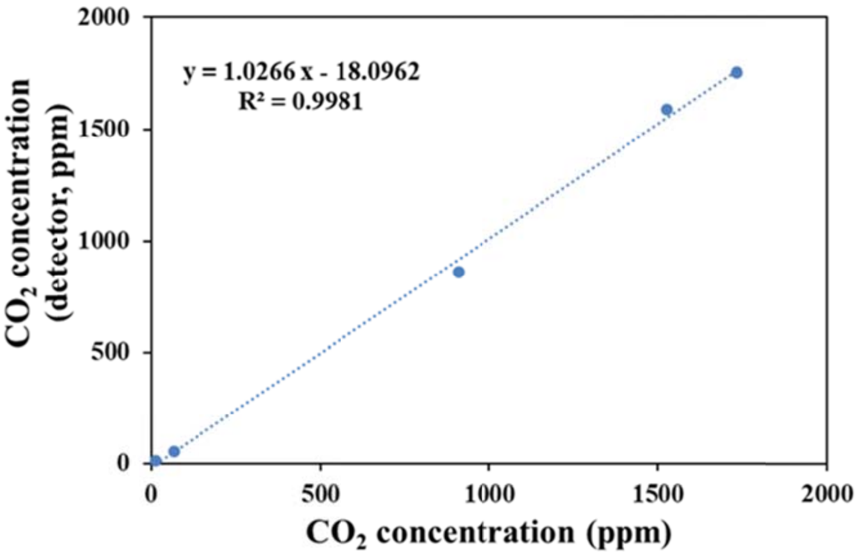

Figure 5.2. Calibration curve of the CO_2 detector with CO_2 produced from oxidation of methanol (0.1 M) in the PEM cell, at 80 °C.

5.3 Results and discussion

5.3.1 Thermal decomposition of $Pb(acac)_2$ on Vulcan XC-72 carbon black

The behavior of $Pb(acac)_2$ thermal decomposition on a carbon black support is shown in Figure 5.3. In the region of 150-300 °C, $Pb(acac)_2$ slowly decomposed to $Pb_3(CO_3)_2(OH)_2$, which was identified by XRD analysis of the product from isothermal decomposition of $Pb(acac)_2$ at 250 °C (Figure 5.4). It had a mass loss of 10.29%, which is in good agreement with the theoretical value of 10.45%. At above 300 °C, the conversion of $Pb_3(CO_3)_2(OH)_2$ to $Pb(CO_3)\cdot xPbO$ occurred.[23] In addition, oxidation of carbon was catalyzed by the Pb components, which resulted in a lower temperature (ca. 450 °C) for carbon combustion in comparison with ca. 750 °C for pure carbon black. PbO can be obtained by further decomposition of the Pb component at above 400 °C.[24] However, the residue of $Pb(acac)_2$ thermal decomposition at above

450 °C on the carbon black support was not pure PbO. The percentage of the residue (20.75%) was higher than the theoretical value of PbO (15.88%). This can probably be attributed to the formation of a PbO/C composite with a structure of the carbon black covered with a PbO shell.[25] Both PbO/C composite and BLC/C anode materials can provide high gravimetric capacity and stable long-term cycling in Li-ion batteries.[26-27]

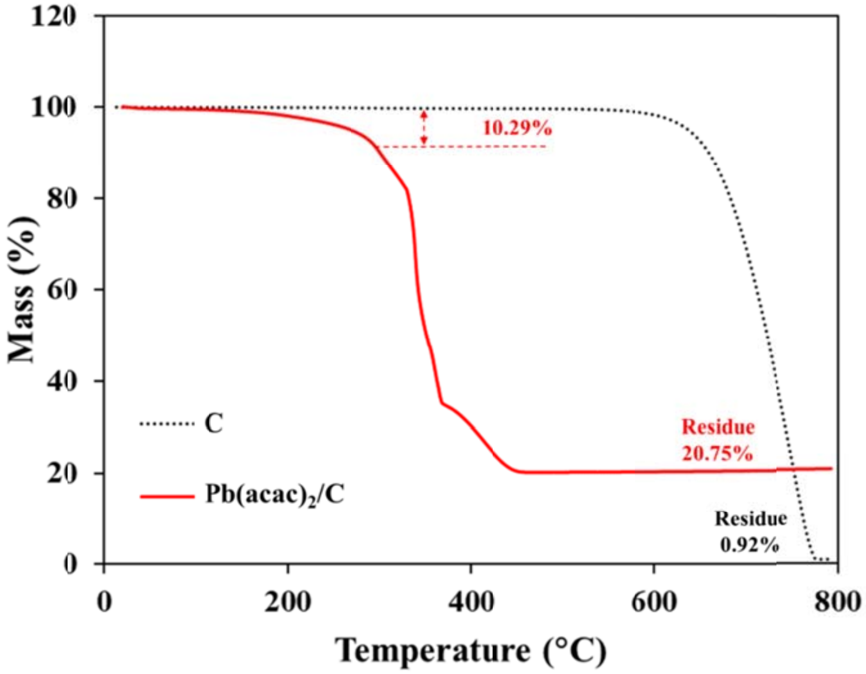

Figure 5.3. TGA plots for decomposition of C and C/Pb(acac)$_2$ (0.1 mmol/100 mg carbon black) with elevated temperature to 800.00 °C by 20.00 °C/min.

5.3.2 Characterization of the prepared support materials and catalysts

As shown in Figure 5.4, in comparison with carbon black, the XRD pattern of the Pb(acac)$_2$-modified carbon black support materials was dominated by the characteristic peaks of $Pb_3(CO_3)_2(OH)_2$ (basic lead carbonate (BLC), or hydrocerussite).[28] Although small peaks are also observed for PbO, we refer to the Pb containing product as BLC for simplicity. XRD data for a Ti foil and a Ti foil modified by $Pb(acac)_2$ thermal decomposition are presented in Figure 5.5. Besides the characteristics peaks of α-Ti for the Ti foil, the new peaks of the sample modified with $Pb(acac)_2$ can be assigned to orthorhombic lead oxide (β-PbO).[29-31] Normally, β-PbO can be synthesized by heating α-PbO at about 490 °C.[32] The $Pb(acac)_2$ thermal decomposition on a Ti support provides a low-temperature route to β-PbO.

It is interesting that the product from $Pb(acac)_2$ thermal decomposition was significantly influenced by the support material with BLC on carbon black and β-PbO on the Ti support. Support materials have a strong effect on the behavior of thermal decomposition of $M(acac)_x$ complexes and the nature of products (e.g. composition and structure, and particle size). Schubert et al. reported that the addition of a TiO_2 support can significantly lower the temperature for thermal decomposition of $M(acac)_x$ (M = Mn, Fe, and Co), in comparison with pure $M(acac)_x$.[33] In contrast to crystalline MO_x produced from thermal decomposition of these pure $M(acac)_x$, amorphous and small MO_x nanoparticles (less than 5 nm) were formed on the TiO_2 substrate. The difference could arise from active electronic communication between the TiO_2 support and the MO_x products, which prohibited the mobility of the metallic species on the surface to crystals. In addition, the oxidation states of formed metallic species on the TiO_2 support could be distinct from the ones produced with pure precursors. The major product was FeO on the TiO_2 support, whereas Fe_2O_3 was produced from thermal decomposition of pure $Fe(acac)_3$.

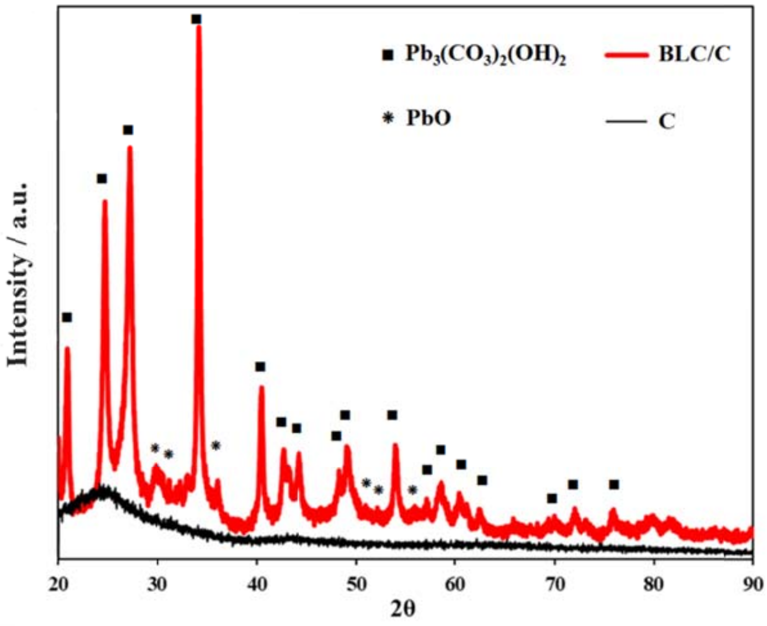

Figure 5.4. XRD patterns of carbon black modified by thermal decomposition of $Pb(acac)_2$ and unmodified carbon black.

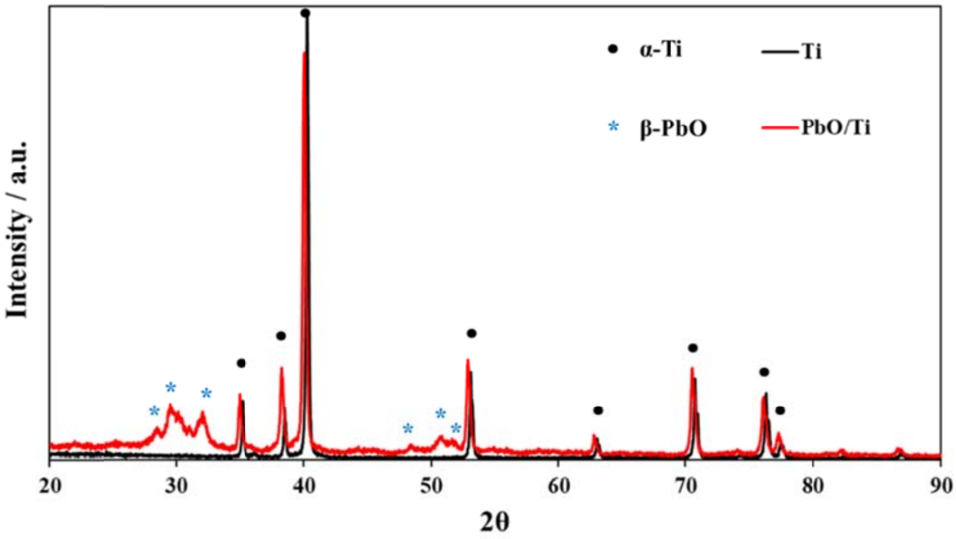

Figure 5.5. X-ray diffraction patterns for Ti foils with and without modification by thermal decomposition of $Pb(acac)_2$.

X-ray emission spectra of the catalysts (Figure 5.6) show similar Pt intensity for the three catalysts, while the Pb intensity increased with the Pb(acac)$_2$ to carbon ratio employed in the synthesis. This indicates that these catalysts were successfully prepared with similar Pt loadings and increasing Pb:Pt ratios. We denote the catalysts as Pt/BLC(*x*)/C, where *x* is the atomic ratio of Pb to Pt. Pt loadings (mass%) and Pb:Pt ratios determined from the EDX spectra are shown in Table 5.1. The Pt particle diameters of the Pt/C and Pt/BLC(*x*)/C catalysts were determined by XRD, and the values are shown in Table 5.2. This indicates the prepared Pt nanoparticles had similar particle sizes of around 5 nm, and their distribution on different supports did not change their sizes with this preparation method.

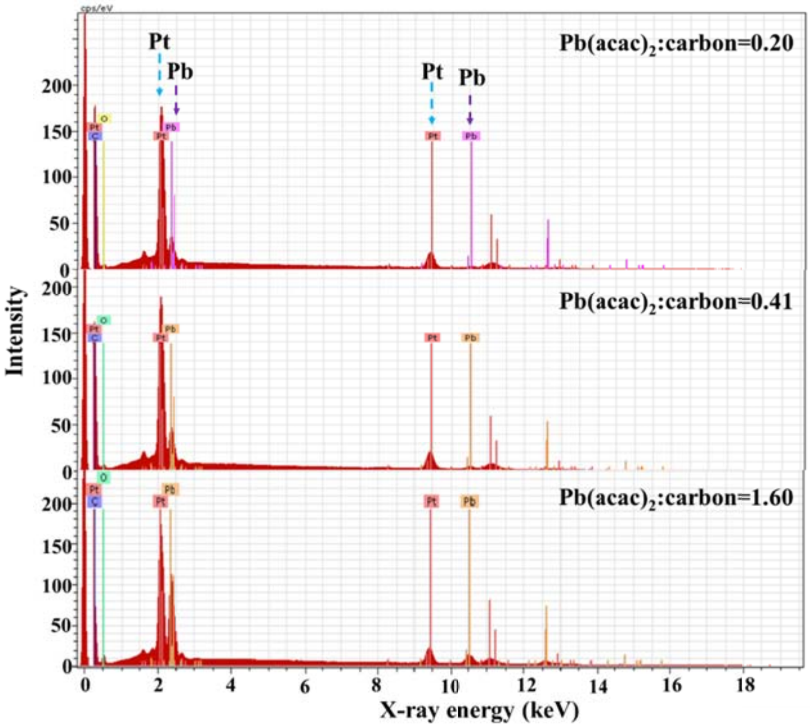

Figure 5.6. X-ray emission spectra (EDX) of Pt/BLC/C catalysts prepared with Pb(acac)$_2$ to carbon mass ratios of 0.20, 0.41, and 1.60.

Table 5.1. Compositions of the catalysts employed in this work.

Name	Target Pb:Pt atomic ratio	Measured Pb:Pt atomic ratio	Pb (mass%)	Pt (mass%)
24% Pt/BLC(0.14)/C	0.29	0.14	3.6%	24%
26% Pt/BLC(0.22)/C	0.52	0.22	6.1%	26%
26% Pt/BLC(0.80)/C	1.28	0.80	22%	26%
25% Pt/C	—	—	—	25%

Table 5.2. Average Pt particle sizes of the catalysts measured by XRD.

Name	Average diameter of Pt nanoparticles (nm)
Pt/C	4.9
Pt/BLC(0.14)/C	4.7
Pt/BLC(0.22)/C	4.7
Pt/BLC(0.80)/C	4.9

As shown in Figure 5.7, the voltammogram of the Pt/C catalyst prepared by adsorbing Pt nanoparticles onto unmodified carbon black is similar to that of the commercial 70% Pt/C catalyst, with similar hydrogen adsorption/desorption peaks between −0.20 and 0 V. With the same Pt loadings (0.3 mg $\mathrm{cm^{-1}}$) of the prepared Pt/C and the commercial 70% Pt/C electrodes, their difference in electrochemically active surface area arises from the different particle sizes as reported previously.[14] In contrast, Pt/BLC(0.80)/C shows almost complete suppression of the hydrogen adsorption and desorption peaks, probably due to coverage of the surface, and prominent oxidation and reduction peaks at ca. 0.30 V presumably resulting from a $\mathrm{Pb^0/Pb^{2+}}$ couple.[34] It suggests that $\mathrm{Pb^0}$ was adsorbed on the surface of the Pt nanoparticles. In addition, the redox reaction of Pb species needs Pt as a catalyst, since no reduction or oxidation peak was observed in the voltammogram of the BLC/C (Figure 5.8). With the increase of Pb:Pt ratio, the redox peaks (in the region between ca. 0.20 and 0.60 V) of the Pb components increased and shifted to low potentials, while the hydrogen adsorption and desorption peaks (between −0.20 and 0 V) decreased. The inverse correlation between BLC loading and hydrogen adsorption/desorption peaks confirms that the suppression of the hydrogen peaks was caused by the Pb component. In Figure 5.9, suppression of the hydrogen adsorption/desorption peaks is also observed at the Pt/PbO/Ti electrode. However, the suppression did not occur in previously reported work when a Pb component was enclosed with Pt atoms forming a Pb@Pt core-shell catalyst.[35]

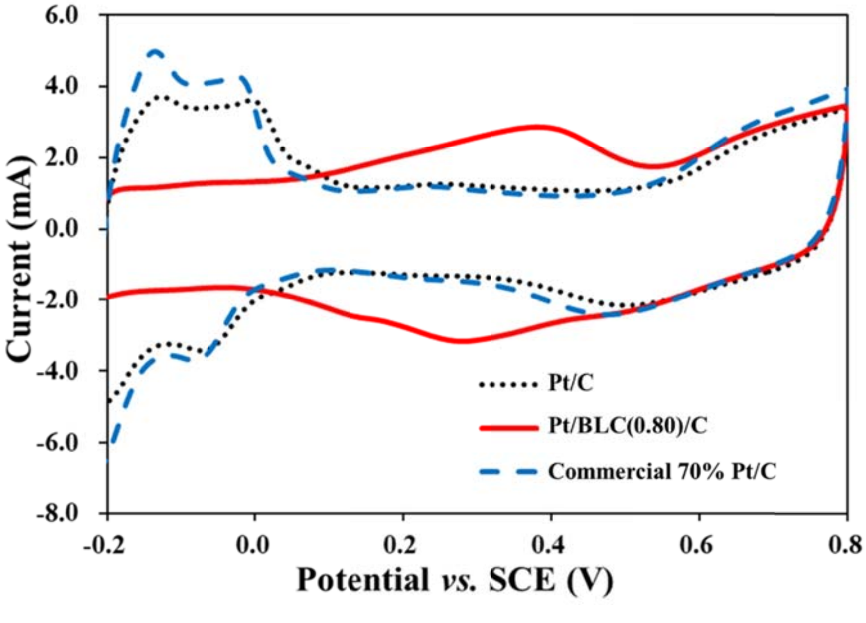

Figure 5.7. Cyclic voltammograms (100 mV s^{-1}) of Pt/C, Pt/BLC(0.80)/C, and 70% Pt/C electrodes (Pt loading: 0.30 mg cm^{-2}) in 0.5 M H_2SO_4(aq).

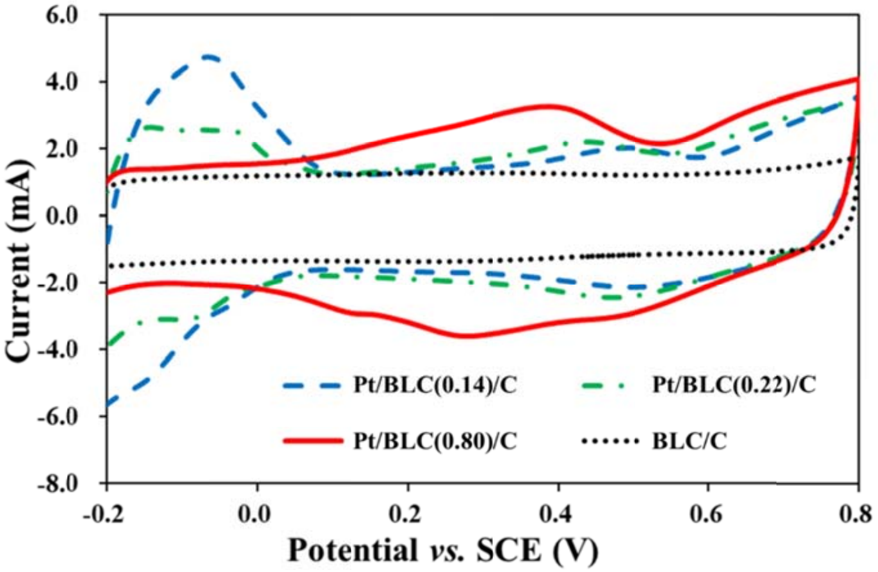

Figure 5.8. Cyclic voltammograms (100 mV s^{-1}) of Pt/BLC(0.14)/C, Pt/BLC(0.22)/C, Pt/BLC(0.80)/C and BLC/C electrodes (Pt loading: 0.30 mg cm^{-2}) in 0.5 M H_2SO_4(aq).

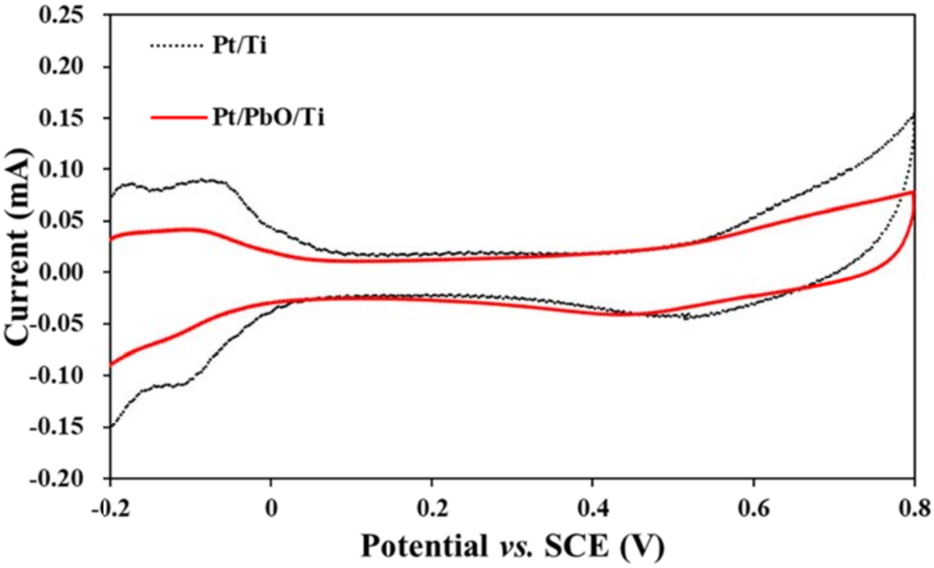

Figure 5.9. Cyclic voltammograms (100 mV s^{-1}) of Pt/Ti and Pt/PbO/Ti electrodes (Pt loading: 0.01 mg cm^{-2}) in 0.1 M H_2SO_4(aq).

5.3.3 Ethanol oxidation

In Figure 5.10, linear sweep voltammograms are compared for Pt/PbO/Ti and Pt/Ti electrodes (Pt loading: 10 μg cm^{-2} on 0.25 cm^2 of Ti) in 0.1 M H_2SO_4(aq) containing 0.2 M ethanol. In comparison with Pt/Ti, the modification of PbO greatly enhanced Pt-catalyzed ethanol oxidation. Notably, the oxidation peak shifted to a lower potential from 0.55 V to 0.52 V, and the peak current increased from 0.44 mA to 0.60 mA. Presumably, the presence of PbO can lower the potential for oxidizing the intermediate CO, and favor CO oxidation by providing more hydroxide groups (-OH) from water dissociation. The introduction of a Pb component to a Pt catalyst was reported to promote CO oxidation with a lower peak potential, and CO tolerance of the catalyst was improved because of repulsion between Pb and CO.[36] Chronoamperometry measurements were performed in 0.1 M H_2SO_4(aq) containing 0.2 M ethanol, and the current was measured over 100 s periods at each potential after cleaning the catalyst surface at 0.70 V for 5 s. As shown in Figure 5.11, higher oxidation currents at the Pt/PbO/Ti electrode were maintained at 0.40 and 0.50 V in contrast to the Pt/Ti electrode. However, sharp current decays were observed over the first 20 s for Pt/PbO/Ti at 0.20 and 0.30 V.

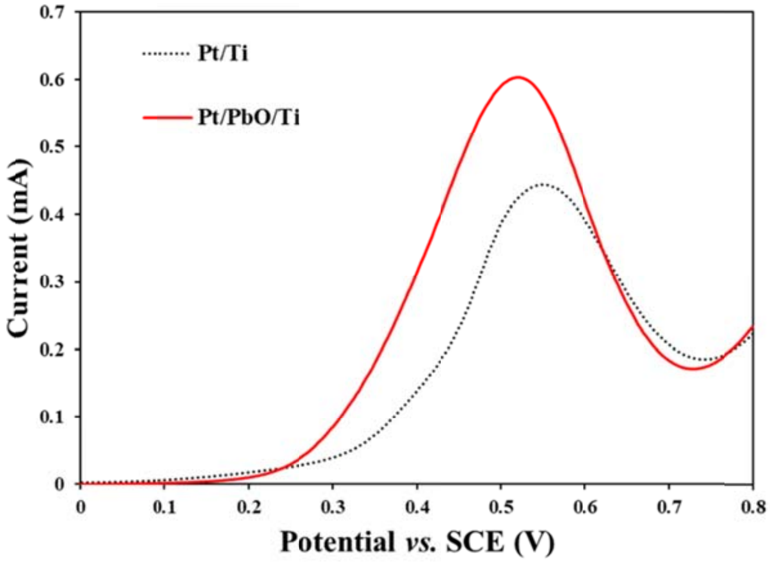

Figure 5.10. Linear sweep voltammograms (10 mV s^{-1}) for oxidation of 0.2 M ethanol + 0.1 M H_2SO_4(aq) at Pt/Ti and Pt/PbO/Ti electrodes (Pt loading: 0.01 mg cm^{-2}).

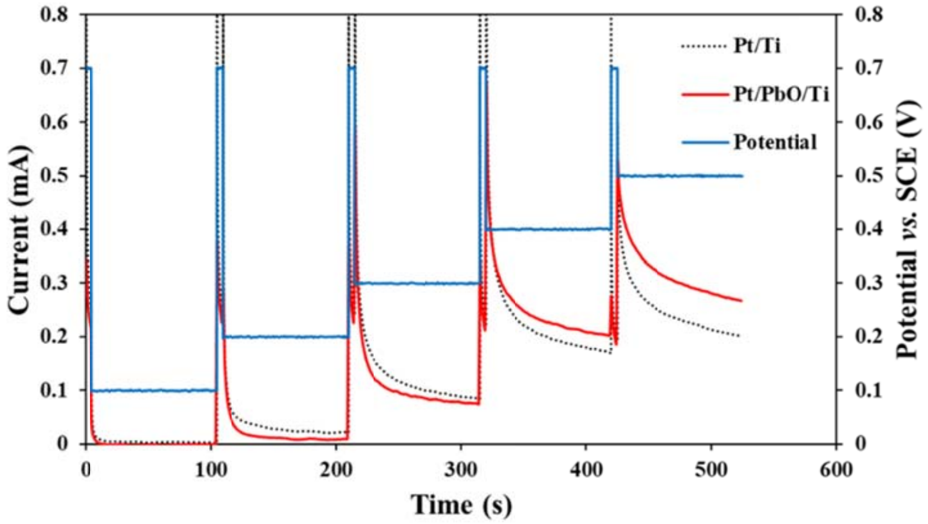

Figure 5.11. Chronoamperometry measurements for oxidation of 0.2 M ethanol + 0.1 M H_2SO_4(aq) at Pt/Ti and Pt/PbO/Ti electrodes (Pt loading: 0.01 mg cm^{-2}) were made consecutively over 100 s periods at each potential, after cleaning catalyst surface at 0.70 V for 5 s.

Carbon fiber paper disc electrodes coated with Pt/C, Pt/BLC(0.80)/C and commercial 70% Pt/C catalysts (Pt loading: 0.3 mg cm^{-2} on 0.24 cm^2 of C/CFP) were used to evaluate the effects of the BLC support on ethanol oxidation at Pt nanoparticles. As shown in Figure 5.12, the outstanding performance of the Pt/BLC(0.80)/C catalyst indicates that the BLC support can play an important role in ethanol oxidation. The addition of BLC led to a large negative shift in the onset potential from ca. 0.40 to 0.25 V, in comparison with Pt/C. The peak oxidation current for Pt/BLC(0.80)/C was also significantly higher than for Pt/C. The influence of BLC on the onset potential and current density suggests that the BLC support had a co-catalytic effect with the Pt catalyst for ethanol oxidation. Importantly, the Pt/BLC(0.80)/C catalyst even had better performance in ethanol oxidation than the high-performance commercial 70% Pt/C catalyst. In the second cycle (Figure 5.12 inset), the peak current slightly increased for the Pt/BLC(0.80)/C catalyst, but decreased for the Pt/C and commercial 70% Pt/C catalysts, suggesting better tolerance of Pt/BLC(0.80)/C to CO poisoning. The addition of $Pb_3(CO_3)_2(OH)_2$ can promote ethanol oxidation through providing OH species from itself and electrochemical dissociation of water, which facilitates the removal of the poisoning intermediate (adsorbed CO) by completing its further oxidation to CO_2. In Figure 5.13, chronoamperometry measurements show that depositing BLC on the carbon support greatly enhanced the activity of Pt for ethanol oxidation at short times (< 10 s). Notably, the current at 0.50 V for Pt/BLC(0.80)/C was even higher than for the commercial 70% Pt/C. While the current at 0.30 and 0.40 V decayed rapidly for the Pt/BLC(0.80)/C electrode, it was more stable at 0.50 V. The reason for current decay is discussed in section 5.3.4.

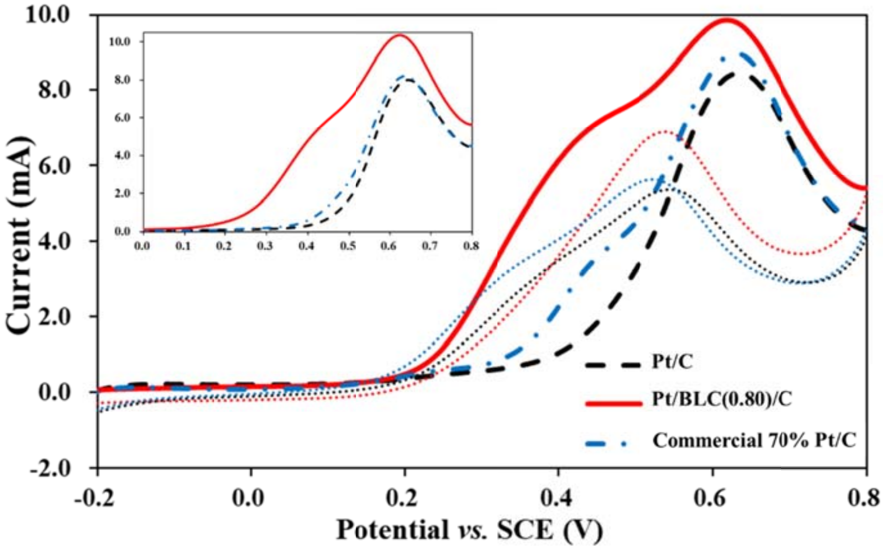

Figure 5.12. Cyclic voltammograms (10 mV s^{-1}) for oxidation of 0.2 M ethanol in 0.5 M H_2SO_4(aq) at Pt/C, Pt/BLC(0.80)/C, and commercial 70% Pt/C electrodes with a Pt loading of 0.30 mg cm^{-2} (the first cycle). Dotted lines show the reverse scans and the inset shows the 2nd forward scans.

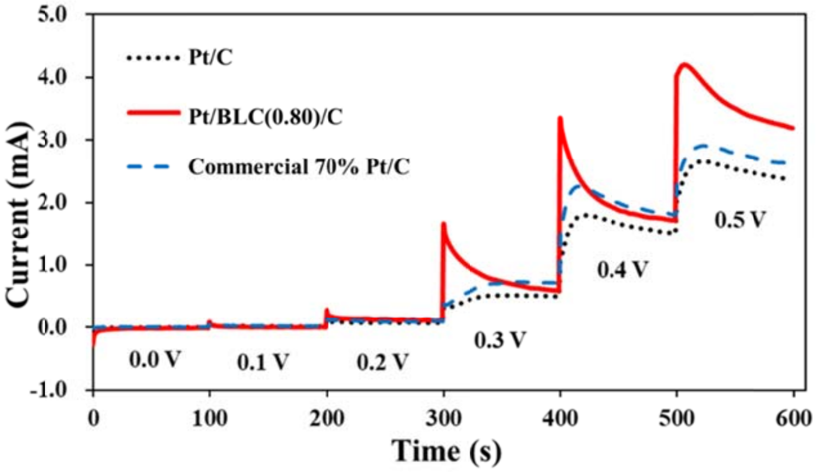

Figure 5.13. Current *vs.* time during a series of potential steps for oxidation of 0.2 M ethanol in 0.5 M H_2SO_4(aq) at Pt/ C, Pt/BLC(0.80)/C and 70% Pt/C electrodes (Pt loading: 0.30 mg cm^{-2}).

In order to investigate the effect of Pb loading on catalytic activity, Pt/BLC/C catalysts with different Pb to Pt ratios (0.14, 0.22, and 0.80) were prepared, with the Pt loading constant at ca. 25 mass%. In Figure 5.14, the cyclic voltammograms show that the amount of BLC loaded on the carbon support had a significant effect on the current for ethanol oxidation. The current increased at all potentials as the Pb:Pt ratio was increased. This confirms that the BLC support played an important role as a co-catalyst in ethanol oxidation. As exhibited in Figure 5.15, the chronoamperometry measurements indicate that current decay was affected by Pb:Pt ratio, and the optimum Pb:Pt ratio varied with different potentials. Large enhancements were observed at 0.50 V as the Pb:Pt ratio was increased, with Pt/BLC(0.80)/C providing the largest current. However, the Pt/BLC(0.22)/C catalyst gave higher and more stable currents than Pt/BLC(0.14)/C and Pt/BLC(0.80)/C catalysts at 0.20, 0.30, and 0.40 V. In this region, the catalyst performance was improved with the slight increase of Pb:Pt ratio from 0.14 to 0.22, but severe current decay was observed for the catalyst with the highest Pb:Pt ratio (0.80). The fast current decay was presumably caused by its poor stability due to the composition change of BLC between 0.20 and 0.40 V, which was coincidental with the region of current decay.

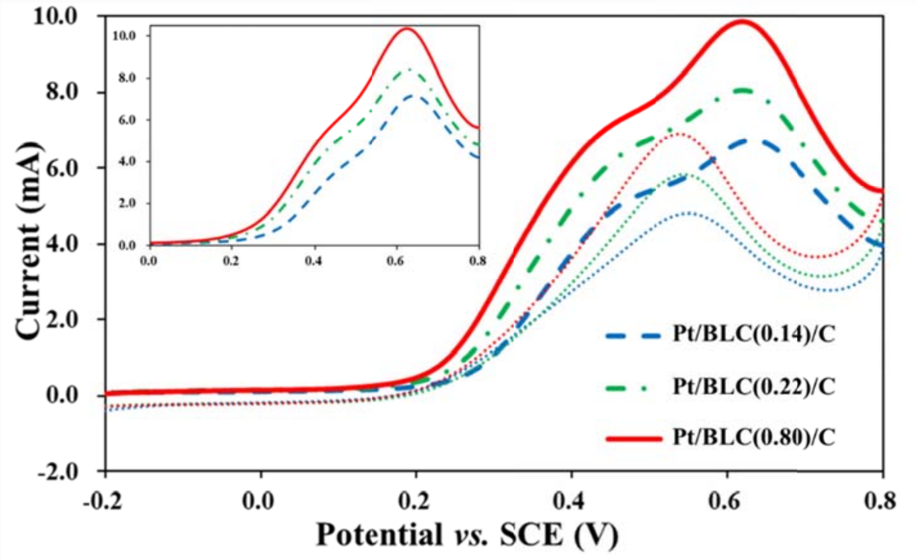

Figure 5.14. Cyclic voltammograms (10 mV s^{-1}) for oxidation of 0.2 M ethanol in 0.5 M H_2SO_4(aq) at Pt/BLC(0.14)/C, Pt/BLC(0.22)/C and Pt/BLC(0.80)/C electrodes (Pt loading: 0.30 mg cm^{-2}). Dotted lines show the reverse scans and the inset shows the 2nd forward scans.

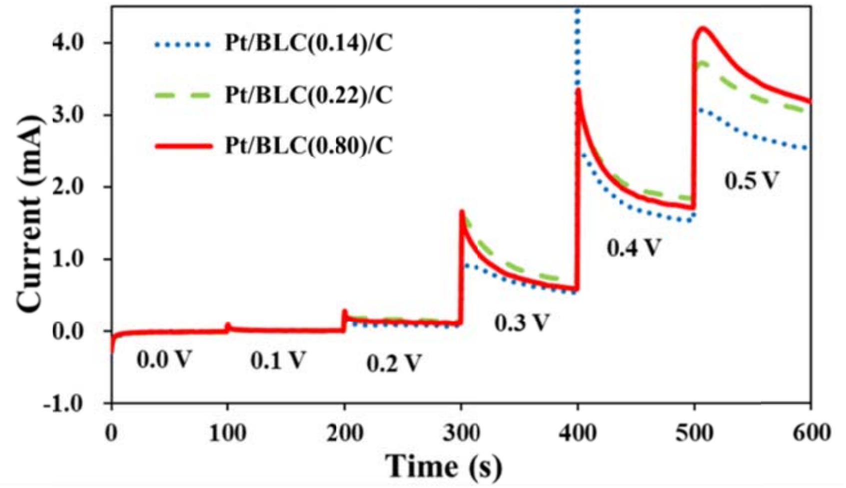

Figure 5.15. Current vs time during a series of potential steps for oxidation of 0.2 M ethanol in 0.5 M H_2SO_4(aq) at Pt/BLC(0.14)/C, Pt/BLC(0.22)/C and Pt/BLC(0.80)/C electrodes (Pt loading: 0.30 mg cm^{-2}).

5.3.4 Stability investigation

To investigate catalyst stability and the reason for current decay in chronoamperometry measurement, two Pt/BLC(0.22)/C electrodes (1.0 × 1.0 cm) with and without performing cyclic voltammetry in H_2SO_4(aq) were analyzed by XRD. The XRD patterns are shown in Figure 5.16. The characteristic peaks of Pt are centered at 40.0°, 46.6°, 68.0°, and 81.7°, and the peaks situated at 26.4° and 54.5° are assigned to CFP.[37-38] The small peaks (20.9°, 23.9°, 27.7°, 29.7°, 32.4°, 33.2°, 43.8°, and 44.7°) that appeared after running cyclic voltammetry in 0.5 M H_2SO_4(aq) are attributed to $PbSO_4$.[39] This indicates that BLC is unstable during cycling, and can form a $PbSO_4$ precipitate on the catalyst surface in H_2SO_4(aq). Coverage of Pt active area by the $PbSO_4$ precipitate probably led to the fast current decays in chronoamperometry measurements at 0.20, 0.30, and 0.40 V. In addition, suppression of the hydrogen adsorption/desorption peaks was also observed at PtPb and PdPb catalysts in 0.5 M KOH(aq).[40] There is a likelihood that Pb^0 produced from the reduction of BLC covered the Pt active area (between −0.20 and 0.10 V) and resulted in blocking of hydrogen adsorption. Then, oxidation of Pb in H_2SO_4(aq) would form $PbSO_4$ between 0.20 and 0.40 V.

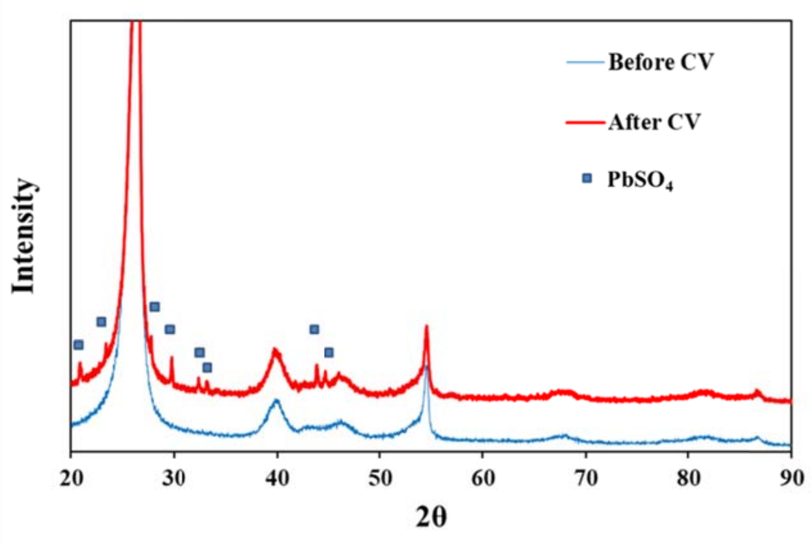

Figure 5.16. XRD patterns of a Pt/BLC(0.22)/C electrode before and after performing cyclic voltammetry measurement in 0.5 M H_2SO_4(aq).

5.3.5 Ethanol electrolysis at 80 °C in a PEM cell

Aiming to evaluate the performance of Pt/BLC/C catalyst for DEFCs, a nine-anode cell assembled with Pt/C and Pt/BLC(0.22)/C anodes (Pt loading: 1.0 mg cm^{-2} on 0.24 cm^2 of C/CFP) was fed with an aqueous solution of 0.1 M ethanol and operated at 80 °C. Figure 5.17 shows polarization curves plotted as steady-state currents and the reproducibility at various potentials. The average currents at the Pt/BLC(0.22)/C electrodes were ca. 30% higher than those at the Pt/C electrodes at high potentials, while they had similar oxidation currents at low potentials. The faradaic yields of CO_2 were determined using a NDIR CO_2 detector and are reported in Table 5.3. The faradaic CO_2 yield at Pt/C was 86 %, which is close to the value measured by Rao et. al using online differential electrochemical mass spectrometry.[41] Pt/BLC(0.22)/C had a lower CO_2 yield in comparison with Pt/C. This indicates that providing OH species has no improvement on selectivity for breaking the C-C bond of ethanol. The OH species brought by BLC enhanced ethanol oxidation due to a bifunctional effect in oxidizing the CO intermediate, and assisted in lowering the energy barrier for the oxidation of adsorbed CH_2CHOH species oxidized to acetic acid.[42-43]

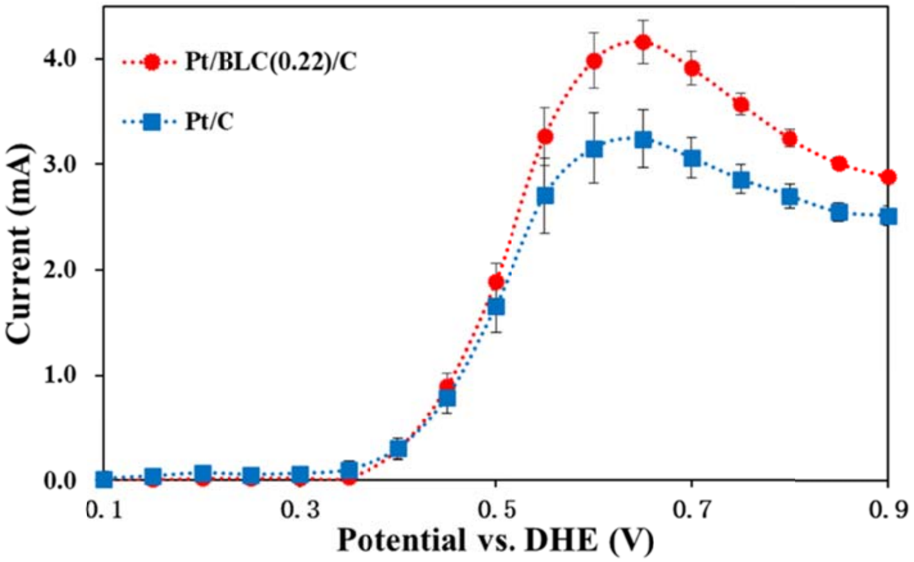

Figure 5.17. Polarization curves for 0.1 M ethanol oxidation at Pt/C and Pt/BLC(0.22)/C anodes (Pt loading: 1.0 mg cm^{-2} on 0.24 cm^{-2} of C/CFP) in a nine-anode PEM electrolysis cell at 80 °C. Averages and standard deviations of the oxidation currents are obtained from three electrodes for each catalyst.

Table 5.3. Calculated faradaic yields of CO_2 from NDIR CO_2 measurements on the exhaust from both the anode and cathode of a PEM cell operated at 80 °C with 0.1 M ethanol solution.

Anode catalyst	Pt loading (mg cm^{-2})	Faradaic CO_2 yield
26% Pt/BLC(0.22)/C	1.0	61%
25% Pt/C	1.0	86%

5.3.6 Formic acid oxidation

The performance of Pt/BLC(0.22)/C electrodes with a low Pt loading (0.1 mg cm^{-2} on 0.24 cm^2 of C/CFP) was studied by cyclic voltammetry in the oxidation of 0.2 M formic acid. As shown in Figure 5.18, the linear sweep voltammograms indicate that Pt/BLC(0.22)/C had a much lower oxidation peak potential (0.25 V) than Pt/C (0.62 V), suggesting two different reaction mechanisms (direct and indirect pathways). Dehydrogenation (Equation 5.3) of formic acid mainly proceeded at 0.25 V for Pt/BLC(0.22)/C, which directly generated CO_2 without forming CO intermediates (CO_{ads}). Pt/C primarily carried out indirect oxidation of formic acid at 0.62 V (Equation 5.4, 5.5, and 5.6). CO intermediates produced from dehydration of formic acid were further oxidized to CO_2 as hydroxide species formed at Pt at high potentials. The selective oxidation of formic acid by the direct pathway for Pt/BLC(0.22)/C can be explained by a third body effect.[44] At low potentials, Pb^{2+} was reduced to Pb^0, and covered on Pt surface, resulting in a decrease in the hydrogen peaks. The Pb at the Pt surface would cause the formation of isolated single Pt atoms, so that dehydration of formic acid, which could not occur without two adjacent Pt atoms, is suppressed. Instead, dehydrogenation of formic acid proceeded at the isolated Pt atoms.

Direct pathway: $HCOOH \rightarrow CO_2 + H^+ + 2e^-$ (Equation 5.3)

Indirect pathway: $HCOOH + Pt \rightarrow Pt\text{-}CO + H_2O$ (Equation 5.4)

$Pt + H_2O \rightarrow Pt\text{-}OH + H^+ + e^-$ (Equation 5.5)

$Pt\text{-}CO + Pt\text{-}OH \rightarrow 2Pt + CO_2 + H^+ + 2e^-$ (Equation 5.6)

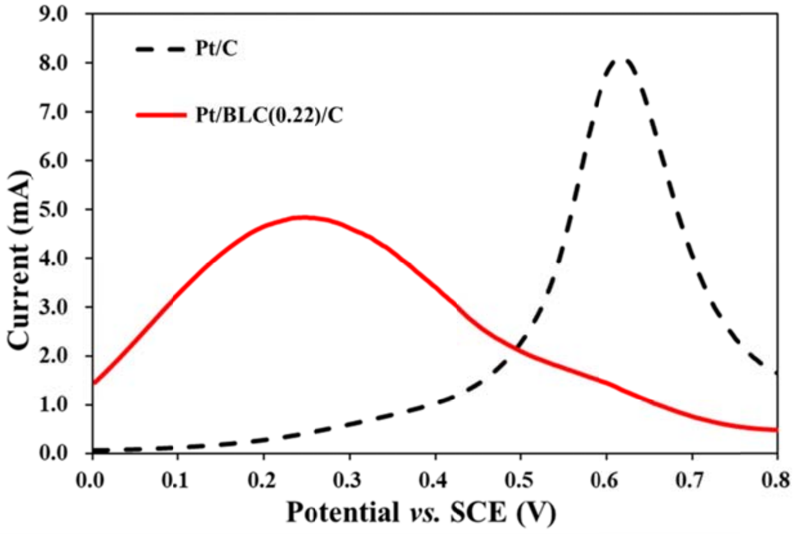

Figure 5.18. Linear sweep voltammograms (10 mV s^{-1}) for oxidation of 0.2 M formic acid in 0.5 M H_2SO_4(aq) at Pt/C and Pt/BLC(0.22)/C electrodes (Pt loading: 0.10 mg cm^{-2}).

The durability of the catalysts was studied by chronoamperometry. As shown in Figure 5.19, the results further confirmed the outstanding performance of Pt/BLC(0.22)/C on formic acid oxidation. At Pt/BLC(0.22)/C, the oxidation currents were 70 times higher than at Pt/C at 0 V, and 40 times higher at 0.10 V. This means the introduction of a small amount of BLC can tremendously enhance fuel efficiency and power output. Moreover, stable currents were maintained with time at 0 and 0.10 V, since catalyst poisoning by CO_{ads} was avoided under the direct pathway. At 0.20, 0.30, and 0.40 V, fast current decays for Pt/BLC(0.22)/C were observed, which may have been due to blocking of the active Pt sites by $PbSO_4$ precipitation.

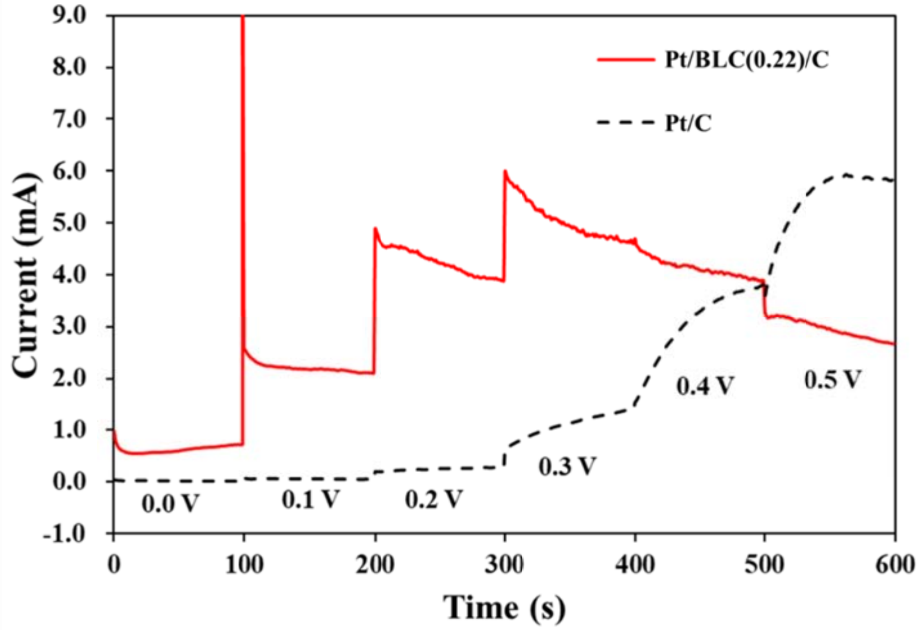

Figure 5.19. Current vs time during a series of potential steps for oxidation of 0.2 M formic acid in 0.5 M H_2SO_4(aq) at Pt/C and Pt/BLC(0.22)/C electrodes (Pt loading: 0.10 mg cm^{-2}).

5.3.7 Mechanistic investigation

In order to understand the enhancement on ethanol oxidation by the PbO support (in Figure 5.10), XPS measurements were performed on Pt/Ti and Pt/PbO/Ti to examine the charge transfer between Pt and the PbO support. Figure 5.20A and B show the Pt 4f region of the XPS spectra and the fitting curves for Pt/Ti and Pt/PbO/Ti. For Pt/Ti, the binding energies of 74.3 and 71.1 eV were assigned to Pt $4f_{5/2}$ and Pt $4f_{7/2}$ of metallic Pt, respectively.[45] In the Pt 4f XPS spectrum of Pt/PbO/Ti, the peaks centered at 71.4 and 74.6 eV correspond to the Pt $4f_{7/2}$ and Pt $4f_{5/2}$ of metallic Pt. Their fitting curves indicate that metallic Pt was prepared and deposited onto the Ti and PbO/Ti supports, and no Pt^{2+} was detected. In Figure 5.20C, the comparison of their XPS spectra indicates that the addition of PbO did have a slight effect on the binding energy of Pt with a slight positive shift (0.3 eV). The charge transferred from Pt to the PbO support can weaken CO adsorption at Pt.[46] In addition, metal oxide supports usually provide abundant OH species at low potentials, which can promote oxidation of the poisoning intermediate CO_{ad}. In comparison with Pt/Ti, the better performance of Pt/PbO/Ti on ethanol oxidation was probably due to a bifunctional effect and a charge transfer effect brought by PbO.[42]

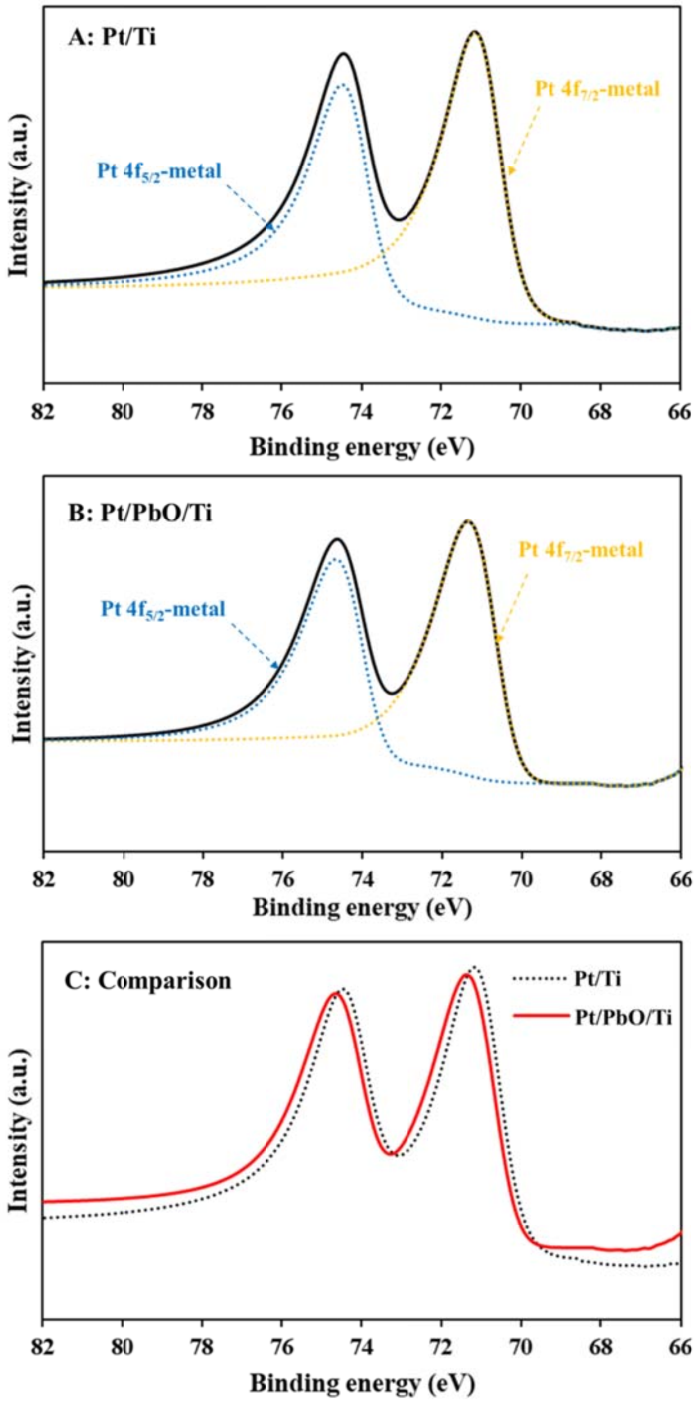

Figure 5.20. XPS spectra (Pt 4f region) and fitting curves (dotted lines) of Pt nanoparticles on Ti (A) and PbO/Ti (B); and their comparison (C).

5.4 Conclusions

Thermal decomposition of $Pb(acac)_2$ can be used to rapidly prepare BLC-containing catalysts on a carbon support and PbO supported catalysts on a Ti support. The presence of BLC significantly increased the activity of Pt nanoparticles in oxidation of ethanol and formic acid, presumably resulting from the combination of a third body effect and a bifunctional effect. These effects were more pronounced and persistent in cyclic voltammetry than in chronoamperometry. Nevertheless, the fast current decays in chronoamperometry measurements are due to a change of the Pb-containing layer to $PbSO_4$, which can not be formed in the PEM cell. In formic acid oxidation, the addition of BLC selectively promoted the direct oxidation of formic acid to CO_2. Pt/BLC(0.22)/C provided stable and 70 times higher oxidation current than Pt/C at 0 V. The bifunctional and charge transfer effects are responsible for the electrocatalytic improvement of Pt/PbO/Ti catalysts in ethanol oxidation.

5.5 References

1. Badwal, S. P. S.; Giddey, S.; Kulkarni, A.; Goel, J.; Basu, S., Direct ethanol fuel cells for transport and stationary applications - A comprehensive review. *Applied Energy,* **2015**, *145*, 80-103.

2. Zhou, Y.; Zhu, X.; Zhang, B.; Ye, D.-D.; Chen, R.; Liao, Q., High performance formic acid fuel cell benefits from Pd-PdO catalyst supported by ordered mesoporous carbon. *International Journal of Hydrogen Energy,* **2020**, *45* (53), 29235-29245.

3. Mardini, N.; Bicer, Y., Direct synthesis of formic acid as hydrogen carrier from CO_2 for cleaner power generation through direct formic acid fuel cell. *International Journal of Hydrogen Energy,* **2021**, *46* (24), 13050-13060.

4. Chen, X.; Liu, Y.; Wu, J., Sustainable production of formic acid from biomass and carbon dioxide. *Molecular Catalysis,* **2020**, *483*, 110716.

5. Ma, Z.; Legrand, U.; Pahija, E.; Tavares, J. R.; Boffito, D. C., From CO_2 to formic acid fuel cells. *Industrial & Engineering Chemistry Research,* **2020**, *60* (2), 803-815.

6. Rumayor, M.; Dominguez-Ramos, A.; Irabien, A., Formic Acid manufacture: Carbon dioxide utilization alternatives. *Applied Sciences,* **2018**, *8* (6), 914.

7. Uhm, S.; Chung, S. T.; Lee, J., Activity of Pt anode catalyst modified by underpotential deposited Pb in a direct formic acid fuel cell. *Electrochemistry Communications,* **2007**, *9* (8), 2027-2031.

8. Shen, T.; Chen, S.; Zeng, R.; Gong, M.; Zhao, T.; Lu, Y.; Liu, X.; Xiao, D.; Yang, Y.; Hu, J., Tailoring the antipoisoning performance of Pd for formic acid electrooxidation via an ordered PdBi intermetallic. *ACS Catalysis,* **2020**, *10* (17), 9977-9985.

9. Liu, Z.; Guo, B.; Tay, S. W.; Hong, L.; Zhang, X., Physical and electrochemical characterizations of PtPb/C catalyst prepared by pyrolysis of platinum(II) and lead(II) acetylacetonate. *Journal of Power Sources,* **2008**, *184* (1), 16-22.

10. Hyun, S. K.; Sun, G.-J.; Lee, J. K.; Lee, C.; Lee, W. I.; Kim, H. W., Ethanol gas sensing using a networked PbO-decorated SnO_2 nanowires. *Thin Solid Films,* **2017**, *637*, 21-26.

11. De Moura, D. C.; Quiroz, M. A.; Da Silva, D. R.; Salazar, R.; Martínez-Huitle, C. A., Electrochemical degradation of Acid Blue 113 dye using TiO_2-nanotubes decorated with PbO_2 as anode. *Environmental Nanotechnology, Monitoring & Management,* **2016**, *5*, 13-20.

12. Buzzo, G. S.; Niquirilo, R. V.; Suffredini, H. B., Active Pt-PbO_x/C anodes to promote the formic acid oxidation in presence of sulfuric acid. *Journal of the Brazilian Chemical Society,* **2010**, *21* (1), 185-190.

13. Yang, W.-H.; Zhang, Q.-H.; Wang, H.-H.; Zhou, Z.-Y.; Sun, S.-G., Preparation and utilization of a sub-5 nm PbO_2 colloid as an excellent co-catalyst for Pt-based catalysts toward ethanol electro-oxidation. *New Journal of Chemistry,* **2017**, *41* (20), 12123-12130.

14. Hang, H.; Altarawneh, R. M.; Brueckner, T. M.; Pickup, P. G., Pt/Ru-Sn Oxide/Carbon catalysts for ethanol oxidation. *Journal of The Electrochemical Society,* **2020**, *167* (5), 054518.

15. Arenas, L.; De León, C. P.; Walsh, F. C., Three-dimensional porous metal electrodes: Fabrication, characterisation and use. *Current Opinion in Electrochemistry,* **2019**, *16*, 1-9.

16. Liu, C.; Carmo, M.; Bender, G.; Everwand, A.; Lickert, T.; Young, J. L.; Smolinka, T.; Stolten, D.; Lehnert, W., Performance enhancement of PEM electrolyzers through iridium-coated titanium porous transport layers. *Electrochemistry Communications,* **2018**, *97*, 96-99.

17. Wang, Y.; Wei, Z.; Gao, B.; Qi, X.; Li, L.; Zhang, Q.; Xia, M., The electrochemical oxidation of methanol on a Pt/TNTs/Ti electrode enhanced by illumination. *Journal of Power Sources,* **2011**, *196* (3), 1132-1135.

18. Zhang, A.; Zhou, M.; Liu, L.; Wang, W.; Jiao, Y.; Zhou, Q., A novel photoelectrocatalytic system for organic contaminant degradation on a TiO_2 nanotube (TNT)/Ti electrode. *Electrochimica Acta,* **2010**, *55* (18), 5091-5099.

19. Moghaddam, R. B.; Pickup, P. G., Support effects on the oxidation of ethanol at Pt nanoparticles. *Electrochimica Acta,* **2012**, *65*, 210-215.

20. Byun, M. Y.; Lee, M. S., Effect of carboxylate stabilizers on the performance of Pt/C catalysts for furfural hydrogenation. *Journal of Environmental Chemical Engineering,* **2021**, 106293.

21. Brueckner, T. M.; Pickup, P. G., Kinetics and stoichiometry of methanol and ethanol oxidation in multi-anode proton exchange membrane cells. *Journal of The Electrochemical Society,* **2017**, *164* (12), F1172.

22. James, D. D.; Pickup, P. G., Measurement of carbon dioxide yields for ethanol oxidation by operation of a direct ethanol fuel cell in crossover mode. *Electrochimica Acta,* **2012**, *78*, 274-278.

23. Yamaguchi, J.; Sawada, Y.; Sakurai, O.; Uematsu, K.; Nobuyasu, M.; Kato, M., Thermal decomposition of hydrocerussite ($2PbCO_3 \cdot Pb\ (OH)_2$) in carbon dioxide atmosphere (0-50 atm). *Thermochimica Acta,* **1980**, *37* (1), 79-88.

24. Li, S.; Yang, W.; Chen, M.; Gao, J.; Kang, J.; Qi, Y., Preparation of PbO nanoparticles by microwave irradiation and their application to Pb(II)-selective electrode based on cellulose acetate. *Materials Chemistry and Physics,* **2005**, *90* (2-3), 262-269.

25. Pan, Q.; Wang, Z.; Liu, J.; Yin, G.; Gu, M., PbO@C core-shell nanocomposites as an anode material of lithium-ion batteries. *Electrochemistry Communications,* **2009**, *11* (4), 917-920.

26. Weeks, J. A.; Zuiker, M. J.; Srinivasan, H. S.; Sun, H.-H.; Burrow, J. N.; Beccar, P.; Heller, A.; Mullins, C. B., A stable lead(II) oxide-carbon composite anode candidate for secondary lithium batteries. *Journal of The Electrochemical Society,* **2020**, *167* (6), 060509.

27. Zhang, Y.; Feng, C.; Zhang, Y.; Wu, H.; Liu, T., Synthesis and electrochemical performance of $Pb_3(OH)_2(CO_3)_2$/C anode material for lithium-ion battery application. *Ionics,* **2020**, 1-7.

28. Bu, L.; Zhang, N.; Guo, S.; Zhang, X.; Li, J.; Yao, J.; Wu, T.; Lu, G.; Ma, J.-Y.; Su, D., Biaxially strained PtPb/Pt core/shell nanoplate boosts oxygen reduction catalysis. *Science,* **2016**, *354* (6318), 1410-1414.

29. Wang, Y.; Xie, Y.; Li, W.; Wang, Z.; Giammar, D. E., Formation of lead(IV) oxides from lead(II) compounds. *Environmental Science & Technology,* **2010**, *44* (23), 8950-8956.

30. Ng, S. H.; Wang, J.; Konstantinov, K.; Wexler, D.; Chen, J.; Liu, H.-K., Spray pyrolyzed PbO-carbon nanocomposites as anode for lithium-ion batteries. *Journal of The Electrochemical Society,* **2006**, *153* (4), A787.

31. Zare, M.; Solaymani, S.; Shafiekhani, A.; Kulesza, S.; Ţălu, Ş.; Bramowicz, M., Evolution of rough-surface geometry and crystalline structures of aligned TiO_2 nanotubes for photoelectrochemical water splitting. *Scientific Reports,* **2018**, *8* (1), 1-11.

32. Rada, M.; Culea, E.; Rada, S.; Maties, V.; Pascuta, P., Novel structural properties of the lead-vanadate-tellurate glass ceramics. *Journal of Materials Science,* **2010**, *45* (6), 1487-1494.

33. Schubert, J. S.; Popovic, J.; Haselmann, G. M.; Nandan, S. P.; Wang, J.; Giesriegl, A.; Cherevan, A. S.; Eder, D., Immobilization of Co, Mn, Ni and Fe oxide co-catalysts on TiO_2 for photocatalytic water splitting reactions. *Journal of Materials Chemistry A,* **2019**, *7* (31), 18568-18579.

34. He, Q.; Shyam, B.; Macounová, K.; Krtil, P.; Ramaker, D.; Mukerjee, S., Dramatically enhanced cleavage of the C–C bond using an electrocatalytically coupled reaction. *Journal of the American Chemical Society,* **2012**, *134* (20), 8655-8661.

35. Santos, D. S.; Almeida, C. V. S.; Tremiliosi-Filho, G.; Eguiluz, K. I. B.; Salazar-Banda, G. R., Improved carbon dioxide selectivity during ethanol electrooxidation in acid media by

Pb@Pt/C and Pb@PtSn/C electrocatalysts. *Journal of Electroanalytical Chemistry,* **2020**, *879*, 114741.

36. De-los-Santos-Alvarez, N.; Alden, L.; Rus, E.; Wang, H.; DiSalvo, F.; Abruna, H., CO tolerance of ordered intermetallic phases. *Journal of Electroanalytical Chemistry,* **2009**, *626* (1-2), 14-22.

37. Chen, B.; Brueckner, T. M.; Altarawneh, R. M.; Pickup, P. G., Composition dependence of ethanol oxidation at ruthenium-tin oxide/carbon supported platinum catalysts. *Journal of The Electrochemical Society,* **2018**, *165* (15), J3019.

38. Kannan, P.; Akshaya, K.; Sudhakar, Y.; Vijayan, A.; Varghese, A., Amorphous Ru-Pi nanoclusters decorated on PEDOT modified carbon fibre paper as a highly efficient electrocatalyst for oxygen evolution reaction. *Materials Chemistry and Physics,* **2021**, *267*, 124650.

39. Gao, P.; Liu, Y.; Lv, W.; Zhang, R.; Liu, W.; Bu, X.; Li, G.; Lei, L., Methanothermal reduction of mixtures of $PbSO_4$ and PbO_2 to synthesize ultrafine α-PbO powders for lead acid batteries. *Journal of Power Sources,* **2014**, *265*, 192-200.

40. Duan, J.-J.; Feng, J.-J.; Zhang, L.; Yuan, J.; Zhang, Q.-L.; Wang, A.-J., Facile one-pot aqueous fabrication of interconnected ultrathin PtPbPd nanowires as advanced electrocatalysts for ethanol oxidation and oxygen reduction reactions. *International Journal of Hydrogen Energy,* **2019**, *44* (50), 27455-27464.

41. Rao, V.; Cremers, C.; Stimming, U.; Cao, L.; Sun, S.; Yan, S.; Sun, G.; Xin, Q., Electro-oxidation of ethanol at gas diffusion electrodes a DEMS study. *Journal of The Electrochemical Society,* **2007**, *154* (11), B1138.

42. Alvarenga, G.; Villullas, H., Transition metal oxides in the electrocatalytic oxidation of methanol and ethanol on noble metal nanoparticles. *Current Opinion in Electrochemistry,* **2017**, *4* (1), 39-44.

43. Wang, E.; Xu, J.; Zhao, T., Density functional theory studies of the structure sensitivity of ethanol oxidation on palladium surfaces. *The Journal of Physical Chemistry C,* **2010**, *114* (23), 10489-10497.

44. Zhang, B. W.; Yang, H. L.; Wang, Y. X.; Dou, S. X.; Liu, H. K., A comprehensive review on controlling surface composition of Pt ‐ based bimetallic electrocatalysts. *Advanced Energy Materials,* **2018**, *8* (20), 1703597.

45. Yoo, J. M.; Ahn, C.-Y.; Lee, J.; Sung, Y.-E., Effect of different surface functional groups on carbon supports toward methanol electro-oxidation of Pt nanoparticles. *Journal of Electroanalytical Chemistry,* **2020**, *875*, 113931.

46. Wakisaka, M.; Mitsui, S.; Hirose, Y.; Kawashima, K.; Uchida, H.; Watanabe, M., Electronic structures of Pt-Co and Pt-Ru alloys for CO-tolerant anode catalysts in polymer electrolyte fuel cells studied by EC-XPS. *The Journal of Physical Chemistry B,* **2006**, *110* (46), 23489-23496.

Chapter 6

Screening of Pt/metal oxide/Ti catalysts for ethanol and methanol oxidation

The introduction of this chapter has been published in the paper below:

P. G. Pickup; H. Hang, Pt/metal oxide/Ti and Pt/metal oxide/carbon composite films for ethanol oxidation. ECS Transactions, 2020, 97(7), 837.

The principal author (Hui Hang) as the main researcher contributed to all aspects of the project including: literature review, designing some of the experiments, performing all of the experiments, collecting, analyzing, and presenting the data. He wrote this chapter, except for the introduction.

The corresponding author (Prof. Peter G. Pickup) proposed the initial experiments, oversaw all aspects of the project, and contributed to several aspects of the project including: experimental design, data analysis, writing and revision of the published manuscript, submission to the journal, and supervision of the principal author (Hui Hang).

The raw data is provided in Appendix B.

6.1 Introduction

Direct alcohol fuel cells become attractive as an alternative power source, since the renewable fuels bioethanol and biomethanol have the advantages of high energy density and easy transportation, and can be produced from waste biomass.[1-2] Efficient electrochemical catalysts are a prerequisite for the development of direct alcohol fuel cells as a competitive technology for sustainable power generation.[3-4] In the past decade, a variety of binary and ternary electrocatalysts have been investigated to improve the current density and catalyst durability in ethanol electro-oxidation.[5-6] Metal oxide-supported Pt catalysts, with Mo, W, and Ti oxide supports have been widely explored for improving oxygen reduction, and Sn and Ni oxide supports have proved effective in the enhancement of electro-oxidation of ethanol and methanol.[7-8]

The co-catalytic effects of metal oxide (MO_x) supports promote oxidation of ethanol and methanol in a number of ways, as illustrated in Figure 6.1. These include changing the d-band level of the Pt via electron transfer (electronic effect) and providing surface -OH functionality for the oxidation of adsorbed CO (bifunctional effect).[9] For ethanol oxidation, it is important to induce these effects with minimal blocking of the ensembles of three Pt sites required for breaking the C-C bond,[10] and this can be achieved by using supports that incorporate metal oxides.[11-15] Sn oxide is one of the most studied metal oxide in previously reported research, and the addition of Ru oxide can provide further enhancement of ethanol oxidation.[16] Recently, it has been reported that carbon black (C) coated with a mixture of Ru and Sn oxides could increase the activity of Pt in ethanol oxidation without a significant loss of selectivity for its complete oxidation to CO_2.[17] This is important for the development of direct ethanol fuel cells, where the overall efficiency is strongly influenced by the yield of CO_2.[18-19]

Thermal decomposition of metal acetylacetonate complexes (M(acac)$_x$) has been widely developed for preparation of various metal oxides, such as RuO_2, TiO_2 and MnO_2.[20-22] The reaction products are mainly metal oxides and volatiles. Ti has become attractive as a type of electrode material due to its good conductivity, low cost, and stability in fuel cells arising from its compact and thin TiO_2 outer layer.[23-25] In terms of electrochemical properties, MO_x with crystalline structures have low reactivity due to the relatively unreactive M-O-M structure.[26] The higher activity of amorphous MO_x was attributed to the function of abundant M=O groups on the surface.[27] Here we report the use of various MO_x composites prepared by thermal decomposition of M(acac)$_x$ complexes on Ti. The aim of this work is to develop a methodology for preparing a wide range of MO_x supported Pt catalysts, and investigate their support effects on Pt catalyzed oxidation of ethanol and methanol. Various metal oxide layers were deposited onto Ti foil electrodes, then drop coated with preformed Pt nanoparticles, as illustrated in Figure 6.2. The co-catalytic effects of the oxide layers were studied through cyclic voltammetry in H_2SO_4(aq). A strong synergistic effect was observed on Mo, Mo+Sn, Ga, In, V and Ir oxide supports. The use of acetylacetonate precursors provided a versatile method for screening libraries of oxide supported catalysts, as well as the production and screening of electrodes for fuel cells.[28]

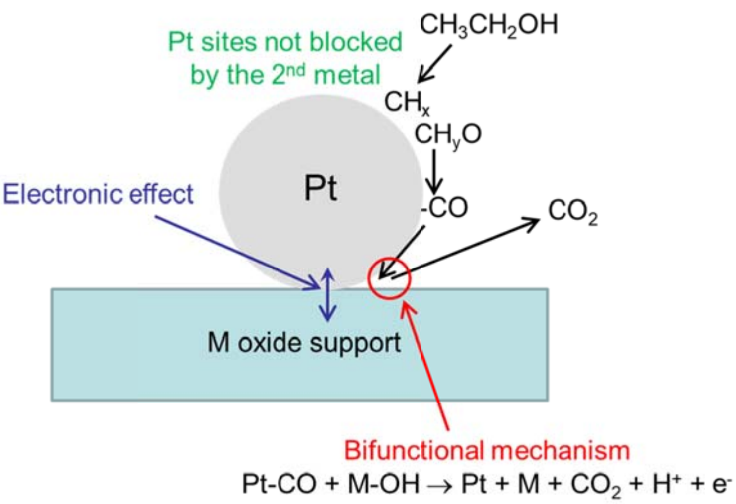

Figure 6.1. Schematic diagram of support effects on ethanol oxidation at a Pt nanoparticle.

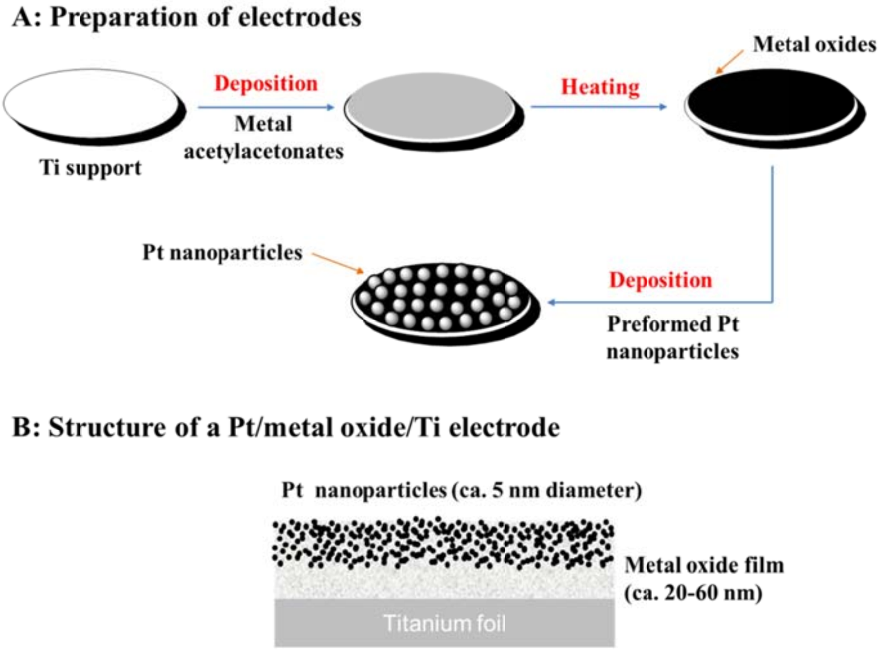

Figure 6.2. Schematic diagrams of the preparation and structures of the Pt/metal oxide/Ti electrodes employed in this work.

6.2 Experimental

Ti based working electrodes were prepared by synthesis of each catalyst on 5 × 5 mm area of a strip of Ti foil (250 μm thick), as illustrated in Figure 6.2. The metal oxide-coated Ti electrodes were prepared with a loading of ca. 2.5×10^{-5} mmol M(acac)$_x$ (using solutions of 0.02 M $MoO_2(acac)_2$, 0.02 M $VO(acac)_2$, 0.02 M $Zr(acac)_4$, 0.01 M $In(acac)_3$, 0.005 M $Ga(acac)_3$ in methanol, and 0.02 M $Sn(acac)_2$ in 2-propanol). After the solvent had evaporated, they were heated on a hot plate in air, at 150 °C for 1 h and then 180 °C for 1 h. After cooling to ambient temperature, the oxide deposits were washed with ethanol, 0.1 M H_2SO_4(aq) and deionized water, and then dried at 70 °C. A colloidal solution of 5 nm Pt nanoparticles (0.48 mg mL^{-1} Pt) was prepared as previously described.[16] Finally, 5.0 μL of the Pt nanoparticle solution (ca. 10 μg cm^{-2} Pt) was evenly drop-coated onto the oxide deposit and allowed to dry.

A Rigaku Ultima IV X-ray diffractometer (XRD) and a VG Microtech MultiLab ESCA 2000 X-ray Photoelectron Spectrometer (XPS, performed by Andrew George at Dalhousie University, Nova Scotia, Canada) were used to characterize the oxide layers. Electrochemical measurements in H_2SO_4(aq) at ambient temperature were carried out with a SP-50 Potentiostat operated with EC-Lab software. A saturated calomel electrode (SCE) and a platinum wire were used as the reference and counter electrode, respectively. All measurements were made under a nitrogen (N_2) atmosphere by purging N_2 for 15 min. Chronoamperometry (current *vs.* time) measurements were made consecutively over 100 s periods at each potential, after cleaning catalyst surface at 0.70 V for 5 s.

6.3 Results and discussion

6.3.1 XRD analysis of the metal oxide layers

Metal oxide layers were produced from thermal decomposition of M(acac)$_x$ (M = Mo, In, Ga, V and Zr) on Ti foils. To characterize the prepared metal oxide layers with XRD, the samples were prepared on thinner Ti foils (25 μm thick, 1 × 1 cm) with a higher loading of M(acac)$_x$ (2×10^{-6} mole cm^{-2}). The samples of Ti foils coated with M(acac)$_x$ were heated on a hot plate in air to 150 °C and then 180 °C, each for 1 h. As shown in Figure 6.3, the dominate peaks (35.2°, 38.5°, 40.3°, 52.9°, 63.0°, 70.7°, 76.3°, 77.4°, 82.3°, and 86.8°) were characteristics for the α-Ti substrate.[29] In comparison with unmodified Ti foil, the XRD patterns of metal oxide-modified Ti show no new sharp peaks attributable to crystalline metal oxides. The broad peaks in the range of 20°~30° indicate that the formed metal oxides (Mo, In, Ga, V and Zr) had amorphous structures.[30-36] This phenomenon was presumably due to a support effect of the thin layer of TiO_2 (see XPS data below) on the Ti surface. It was reported that a TiO_2 support greatly influenced the reaction temperature of thermal decomposition of M(acac)$_x$ and the structure of produced MO$_x$.[22] The TiO_2 support strongly bound M(acac)$_x$ by chemisorption, and lowered the temperature for their thermal decomposition relative to pure M(acac)$_x$. Rather than crystalline oxides (without TiO_2), amorphous MO$_x$ particles (1-5 nm) were formed and evenly distributed on the surface of TiO_2 resulting from the strong electronic communication between these two components. Furthermore, at a low loading of M(acac)$_x$, isolated monomeric metal oxide species were formed on TiO_2 supports due to suppression of crystal development by TiO_2.[37-38]

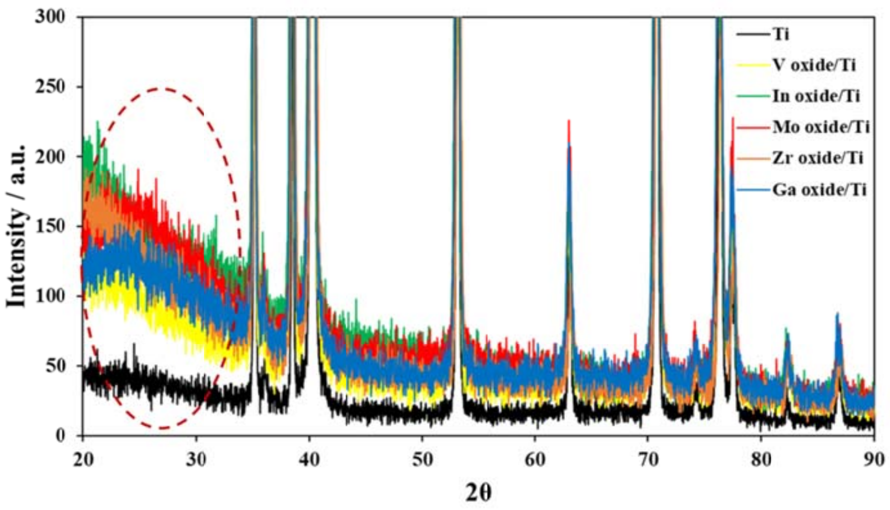

Figure 6.3. X-ray diffraction patterns for Ti foil, V oxide/Ti, In oxide/Ti, Mo oxide/Ti, Zr oxide and Ga oxide/Ti.

6.3.2 XPS analysis of the surface of the electrodes

XPS was applied to detect the components and oxidation states of the prepared MO_x layers. As shown in Figure 6.4, the XPS spectrum of Ti foil shows the peaks at binding energies of 464.3 eV and 458.6 eV, which is in agreement with Ti $2p_{1/2}$ (464.4 eV) and Ti $2p_{3/2}$ (458.6 eV) of TiO_2.[39] The signals at 232.8 eV and 235.9 eV of the Ti foil modified by $MoO_2(acac)_2$ thermal decomposition can be respectively assigned to Mo $3d_{3/2}$ and Mo $3d_{5/2}$ of MoO_3.[40] In the XPS spectrum of In_2O_3/Ti, the two peaks centered at binding energies of 444.6 eV and 452.1 eV are correspond to In $3d_{5/2}$ and In $3d_{3/2}$ of In_2O_3 with a slight positive shift (0.2 eV) due to TiO_2 support.[41-42] The two overlapping peaks (at 1117.3 eV and 1118.5 eV) of the Ti foil modified by $Ga(acac)_3$ thermal decomposition are attributed to Ga $2p_{3/2}$ of Ga_2O and Ga_2O_3, respectively.[43-45] The XPS spectrum of V_2O_5/Ti exhibits two peaks at 516.8 eV and 524.1 eV, which can be assigned to V $2p_{3/2}$ and V $2p_{1/2}$ of V_2O_5, respectively.[46] The XPS spectrum of the Ti foil modified by thermal decomposition of Zr(acac)$_4$ shows two peaks at 182.2 eV and 184.6 eV, which are attributed to Zr 3d$_{5/2}$ and Zr 3d$_{3/2}$ of ZrO$_2$, respectively.[47] The experimental binding energies are in agreement with literature values for MO$_x$ (M = Mo, In, Ga, V, Zr, and Ti), as listed in Table 6.1. Therefore, the results of XPS analysis imply that metal oxides were produced through thermal decomposition of M(acac)$_x$ on Ti foils.

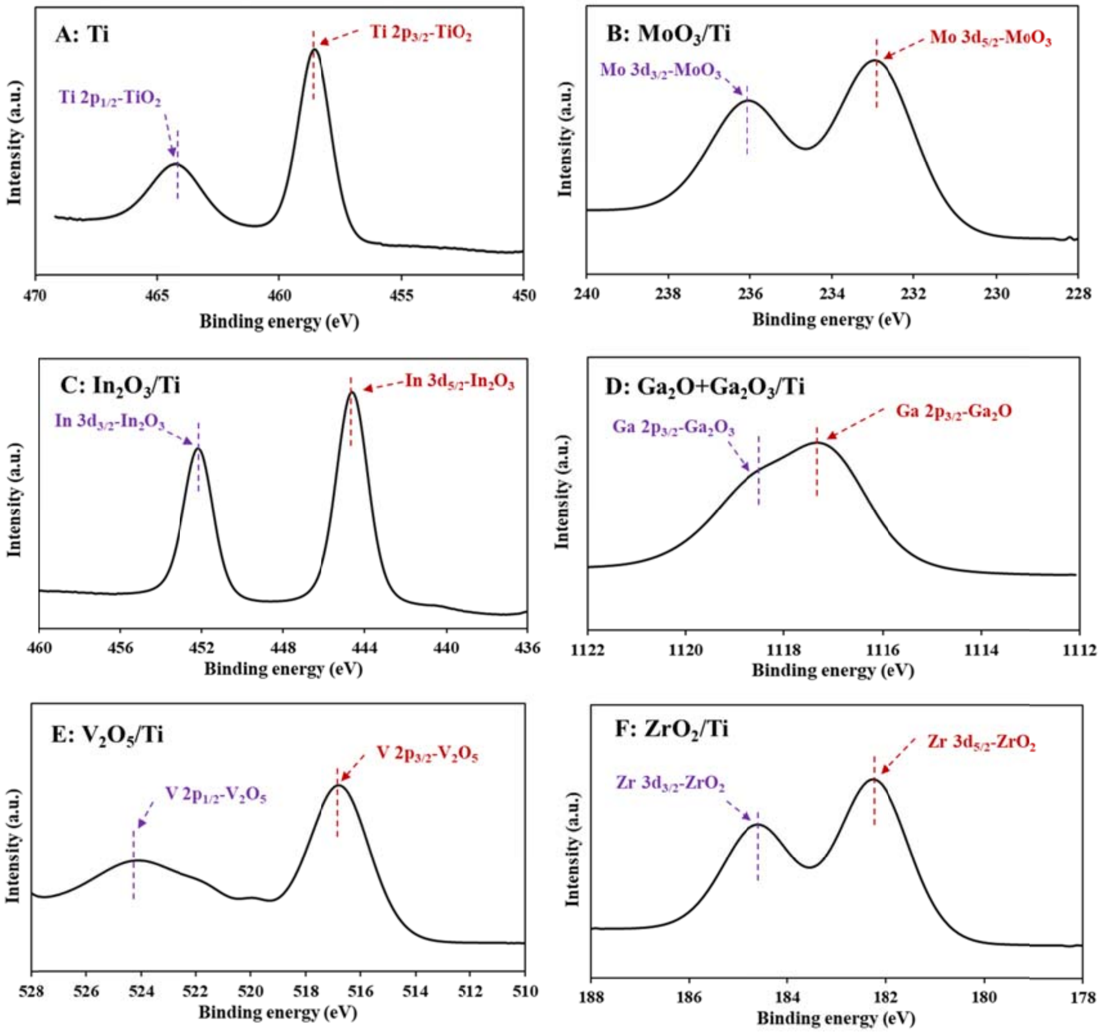

Figure 6.4. XPS spectra showing the metal oxide layers of Ti (A), MoO$_3$/Ti (B), In$_2$O$_3$/Ti (C), Ga$_2$O+Ga$_2$O$_3$/Ti (D), V$_2$O$_5$/Ti (E), and ZrO$_2$/Ti (F).

Table 6.1. Binding energies for metal oxides (M = Mo, Ga, In, V, Zr, and Ti) that were experimentally determined and from the literature.

Name	Peak	Experimental binding energy (eV)	Literature binding energy (eV)	Reference
MoO_3	Mo $3d_{3/2}$	232.8	232.8	40
	Mo $3d_{5/2}$	235.9	235.9	
In_2O_3	In $3d_{5/2}$	444.6	444.4	41, 42
	In $3d_{3/2}$	452.1	451.9	
Ga_2O	Ga $2p_{3/2}$	1117.3	1117.4	43
Ga_2O_3	Ga $2p_{3/2}$	1118.5	1118.5	44
V_2O_5	V $2p_{3/2}$	516.8	516.9	46
	V $2p_{1/2}$	524.1	524.0	
ZrO_2	Zr $3d_{5/2}$	182.2	182.2	47
	Zr $3d_{3/2}$	184.6	184.5	
TiO_2	Ti $2p_{1/2}$	464.3	464.4	39
	Ti $2p_{3/2}$	458.6	458.6	

The XPS high resolution spectra of O 1s region and corresponding fitting curves are presented in Figure 6.5. The deconvolution of the O 1s spectra indicates the existence of lattice oxygen (O^{2-}) and hydroxyl species (OH^-). Ti has two peaks at 529.9 eV and 531.0 eV, which are consistent with O^{2-} (529.9 eV) and OH^- (531.3 eV) of TiO_2.[39] In the spectrum of MoO_3/Ti, the peaks at 530.6 eV and 531.8 eV are well fitted with O^{2-} and OH^- of MoO_3.[40, 48] The fitting peaks of In_2O_3/Ti at 529.9 eV and 531.5 eV are attributed to O^{2-} and OH^- of In_2O_3.[42] In the spectrum of Ga_2O+ Ga_2O_3/Ti, the peak centered at 532.7 eV can be assigned to OH^- of Ga_2O_3,[49] and the peak at 529.7 eV is attributed to O^{2-} (530.0 eV) of Ga_2O_3.[50] The fitting curves of V_2O_5/Ti has two peaks at 530.0 eV and 531.7 eV, which can be assigned to O^{2-} and OH^{-} of vanadium oxide.[51] For ZrO_2/Ti, two signals at 529.8 eV and 531.3 eV is consistent with O^{2-} and OH^{-} of ZrO_2-TiO_2.[47] The experimental binding energies of O 1s for MO_x (M = Mo, In, Ga, V, Zr, and Ti) are in agreement with literature values listed in Table 6.2. The O^{2-} peak position of MoO_3/Ti is significantly different from TiO_2 on the Ti surface. The binding energies of OH^{-} for other MO_x (M = In, Ga, V, and Zr) are distinct from TiO_2. The results of O 1s spectra imply that other metal oxides were produced on the Ti surfaces. Among the metal oxide supports, MoO_3/Ti has the highest area ratio of OH^{-} to O^{2-} (1.83:1). Hydroxide species can play an important role in promoting ethanol oxidation, through the bifunctional mechanism as shown in Figure 6.1.

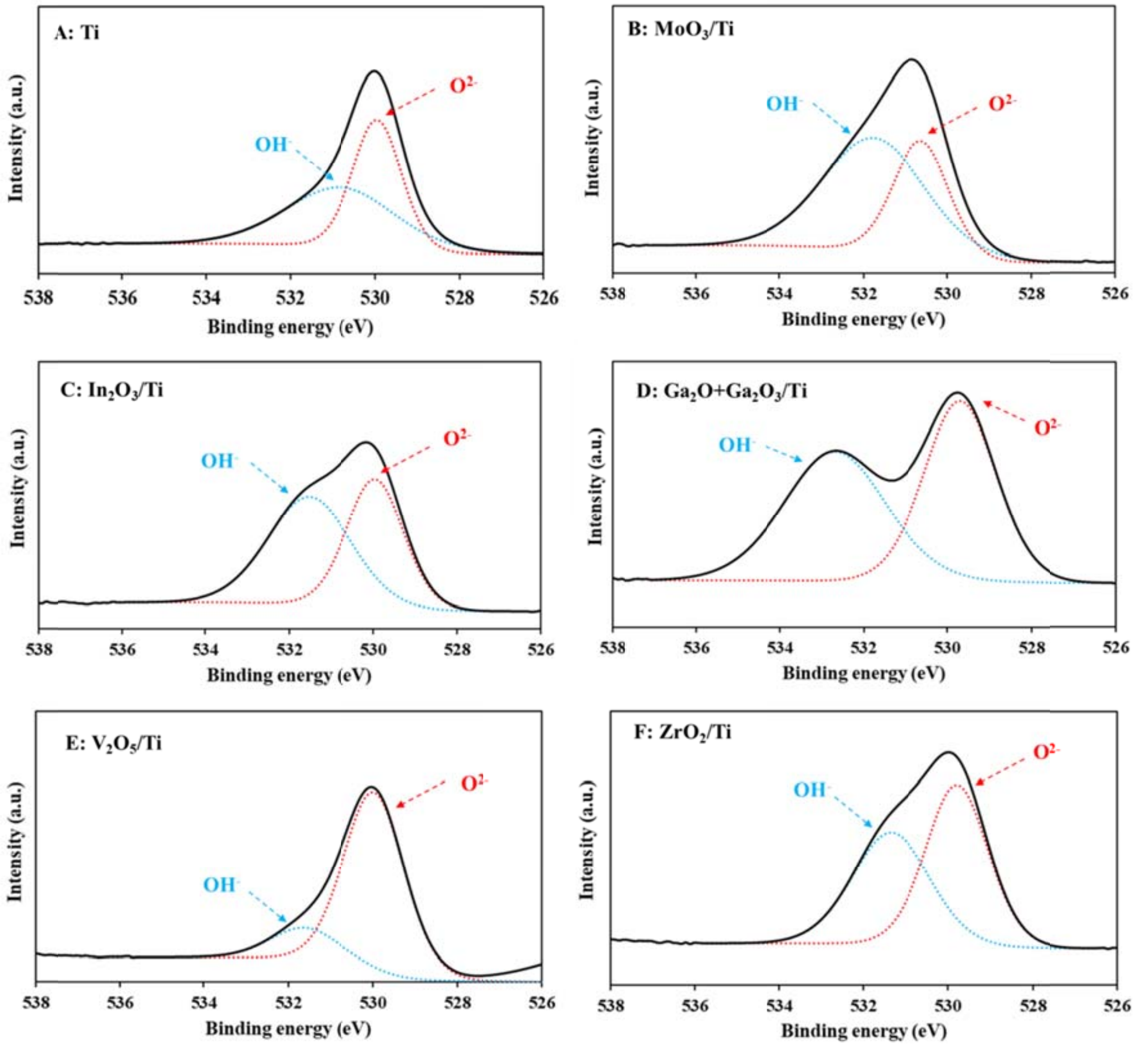

Figure 6.5. XPS spectra (O 1s) and fits for Ti (A), MoO_3/Ti (B), In_2O_3/Ti (C), Ga_2O+Ga_2O_3/Ti (D), V_2O_5/Ti (E), and ZrO_2/Ti (F).

Table 6.2. Binding energies of O 1s for metal oxides (M = Mo, Ga, In, V, Zr, and Ti) that were experimentally determined and from the literature.

Name	Oxygen species	Experimental binding energy (eV)	Literature binding energy (eV)	Reference
MoO_3	O^{2-}	530.6	530.6	40, 48
	OH^-	531.8	531.6	
In_2O_3	O^{2-}	529.9	530.0	42
	OH^-	531.5		
Ga_2O_3	O^{2-}	529.7	530.0	49, 50
	OH^-	532.7	532.7	
V_2O_5	O^{2-}	530.0	530.0	51
	OH^-	531.7		
ZrO_2	O^{2-}	529.8	529.8	47
	OH^-	531.3		
TiO_2	O^{2-}	529.9	529.9	39
	OH^-	531.0	531.3	

6.3.3 Electrochemical activity of the electrodes

The electrochemically active surface areas (EASA) of the Pt nanoparticles on the electrodes were determined by cyclic voltammetry in 0.1 M H_2SO_4(aq). As shown in Figure 6.6 and Figure 6.7, the peaks located between −0.20 V and 0.15 V are attributed to hydrogen adsorption and desorption at Pt, which can be used to calculate the electrochemically active surface area of Pt (Equation 6.1).[52]

$$EASA\ (cm^2) = \frac{Q_{H-adsorption}\ (\mu C)}{210\ (\mu C\ cm^{-2})} \qquad \text{(Equation 6.1)}$$

Where $Q_{H\text{−adsorption}}$ represents the hydrogen adsorption charge in μC, and Q_H (210 μC cm^{-2}) is the charge of full coverage for clean polycrystalline Pt. The calculated EASA and utilization are listed in Table 6.3. It shows that Pt/Ti, Pt/MoO_3/Ti, Pt/MoO_3+SnO_2/Ti, Pt/Ga_2O+Ga_2O_3/Ti, Pt/In_2O_3/Ti, Pt/V_2O_5/Ti and Pt/ZrO_2/Ti electrodes have a similar EASA and utilization rate of the Pt nanoparticles (ca. 60−66%).

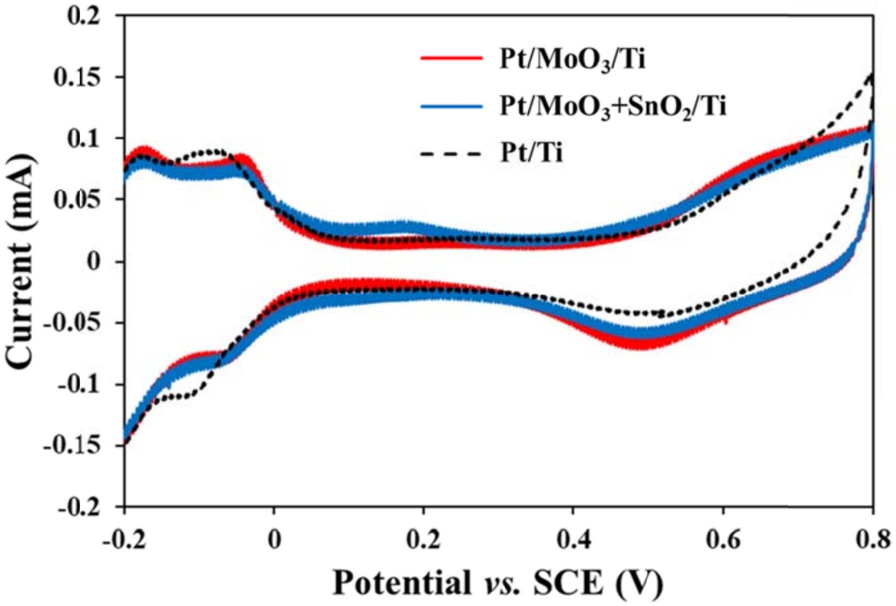

Figure 6.6. Cyclic voltammograms (100 mV s^{-1}) of Pt/Ti, Pt/MoO_3/Ti, and Pt/MoO_3+SnO_2/Ti electrodes in 0.1 M H_2SO_4(aq).

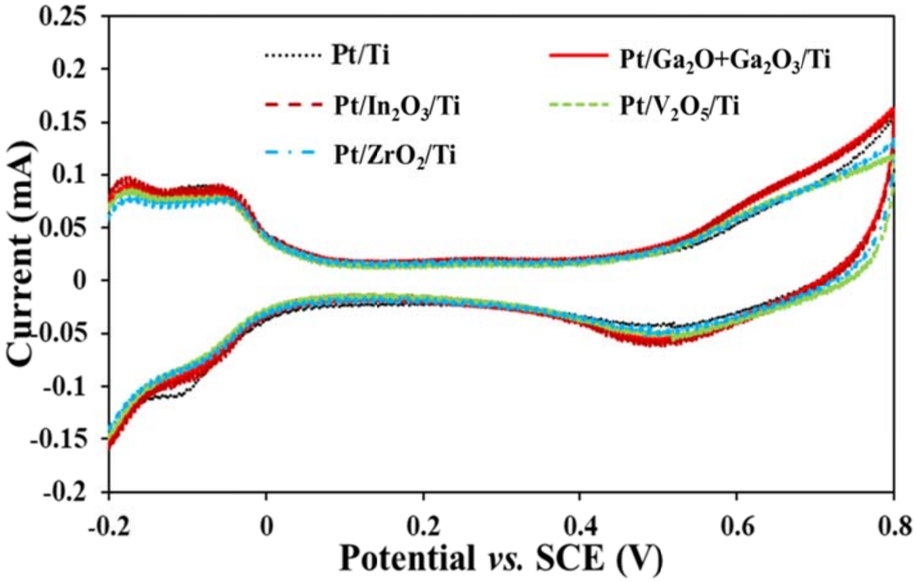

Figure 6.7. Cyclic voltammograms (100 mV s^{-1}) of Pt/Ti, Pt/Ga_2O+Ga_2O_3/Ti, Pt/In_2O_3/Ti, Pt/V_2O_5/Ti and Pt/ZrO_2/Ti electrodes in 0.1 M H_2SO_4(aq).

Table 6.3. The electrochemically active surface areas of Pt/metal oxide/Ti electrodes (M = Mo, Ga, In, V, Zr, and Sn). The average diameter (5 nm) of Pt nanoparticles was used for calculating utilization rate.

Name	EASA (cm^2)	Utilization rate
Pt/Ti	0.8467	62.58%
Pt/MoO_3/Ti	0.8636	63.83%
Pt/MoO_3+SnO_2/Ti	0.8181	60.46%
Pt/Ga_2O+ Ga_2O_3/Ti	0.8672	64.09%
Pt/In_2O_3/Ti	0.8949	66.14%
Pt/V_2O_5/Ti	0.8253	61.00%
Pt/ZrO_2/Ti	0.8117	60.00%

6.3.4 Ethanol oxidation

The electrodes were prepared by depositing preformed Pt nanoparticles on MO_x modified Ti foils. The same batch of pre-synthesized Pt nanoparticles was used for electrode preparation for control experiments with Pt drop coated on unmodified Ti foil, therefore the influence of strain effect (the significant effect of changing the Pt size) can be excluded. The effects of the oxide layers on Pt catalyzed ethanol electro-oxidation were preliminarily evaluated by linear sweep voltammetry. As shown in Figure 6.8, the MoO_3 support showed a large synergistic effect with Pt nanoparticles on ethanol oxidation. The peak current (at 0.56 V) of the Pt/MoO_3/Ti is around 1.8 times that of the Pt/Ti. The addition of MoO_3 lowers the onset potential for ethanol electro-oxidation from 0.25 V to 0.13 V. It was reported that MoO_3 promotes CO oxidation and the oxidation of the acetaldehyde intermediate to acetic acid (Equation 6.2 and 6.3).[53] The thermal decomposition method is also useful for preparing mixed metal oxides. The combination of SnO_2 with MoO_3 enhanced ethanol oxidation at low potential (0.10−0.30 V), but decreased the oxidation current above 0.33 V. This was probably caused by decrease of conductivity with the introduction of SnO_2 (Table 6.4).

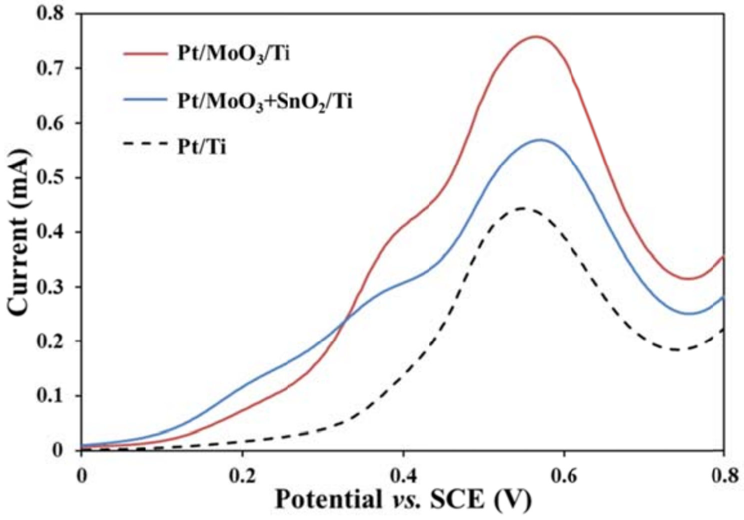

Figure 6.8. Linear sweep voltammograms (10 mV s^{-1}) for oxidation of 0.2 M ethanol + 0.1 M H_2SO_4 at Pt/Ti, Pt/MoO_3/Ti, and Pt/MoO_3+SnO_2/Ti electrodes.

$$\text{Pt-CHOCH}_3 + \text{MoO}_x(\text{OH})_{\text{ads}} \rightarrow \text{Pt} + \text{MoO}_x + \text{CH}_3\text{COOH} + \text{H}^+ + \text{e}^- \qquad \text{(Equation 6.2)}$$

$$\text{Pt-CO} + \text{MoO}_x(\text{OH})_{\text{ads}} \rightarrow \text{Pt} + \text{MoO}_x + \text{CO}_2 + \text{H}^+ + \text{e}^- \qquad \text{(Equation 6.3)}$$

Through chronoamperometry measurements, the currents (*vs.* time) for ethanol oxidation were investigated over a potential range of 0.10 to 0.50 V (each for 100 s), after applying 0.70 V for 5 s to clean the catalyst surface (Figure 6.9A). As shown in Figure 6.9B, Pt/MoO_3/Ti exhibited higher oxidation currents than Pt/Ti from 0.30 to 0.50 V, which is in good agreement with the result of cyclic voltammetry. However, enhancement by the MoO_3 support did not occur at 0.10 V and 0.20 V. In the process of ethanol electro-oxidation, breaking of the C-C bond of ethanol can occur at a low potential and generate adsorbed CO (CO_{ads}) at the Pt surface, but its further oxidation requires higher potentials.[54] The intermediate CO strongly binds to the Pt surface, which can impede the adsorption of ethanol and decrease its catalytic activity.[55] The introduction of SnO_2 can alter the linear bonding of CO_{ads} at Pt to bridge-bonding, which can be oxidized at a low potential.[56] Therefore, Pt/MoO_3+SnO_2/Ti had higher oxidation current at 0.1 and 0.2 V than Pt/Ti and Pt/MoO_3/Ti.

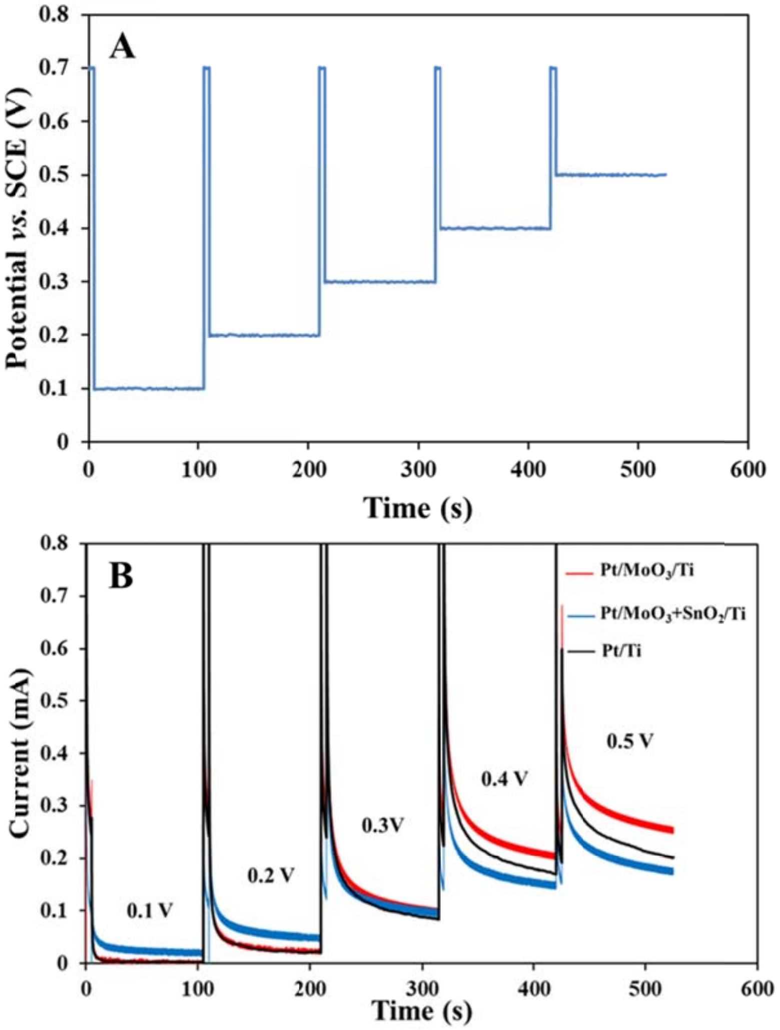

Figure 6.9. A: each potential from 0.10 to 0.50 V were maintained for 100 s, after applying 0.70 V for 5 s to clean the catalyst surface. B: current *vs*. time during a series of potential steps for oxidation of 0.2 M ethanol in 0.1 M H_2SO_4(aq) at Pt/Ti, Pt/MoO_3/Ti, and Pt/MoO_3+SnO_2/Ti electrodes.

The performances of some other metal oxides prepared by thermal decomposition of M(acac)$_x$ complexes (M = Ga, In, V, and Zr) were also investigated for catalyst screening. The linear sweep voltammograms (Figure 6.10) show that these metal oxides produce large enhancements in the activity of Pt for ethanol electro-oxidation. The peak currents of the MO$_x$ (M = Ga, In, and V) supported catalysts increase to approximately 0.7 mA, compared with 0.44 mA at Pt/Ti. The MO$_x$ modification introduces more OH species, which favors the oxidation of CO$_{ads}$ as illustrated in Figure 6.1. For Pt/ZrO$_2$/Ti, the slight enhancement in peak current probably resulted from hydroxide species provided by the ZrO$_2$ support, and positive shift of its peak potential were presumably due to significantly low conductivity of ZrO$_2$ (Table 6.4). The results of chronoamperometry measurements confirm the improvement on Pt-catalyzed ethanol electro-oxidation by the metal oxide supports. As shown in Figure 6.11, higher currents were maintained for Pt/MO$_x$/Ti (M = Ga, In, V, and Zr) at 0.30, 0.40 and 0.50 V, in contrast to Pt/Ti. In addition, the MO$_\mathrm{x}$ supports exhibit their improvement in catalyst durability, as less current decay was observed at the MO$_\mathrm{x}$ supported catalysts than Pt/Ti.

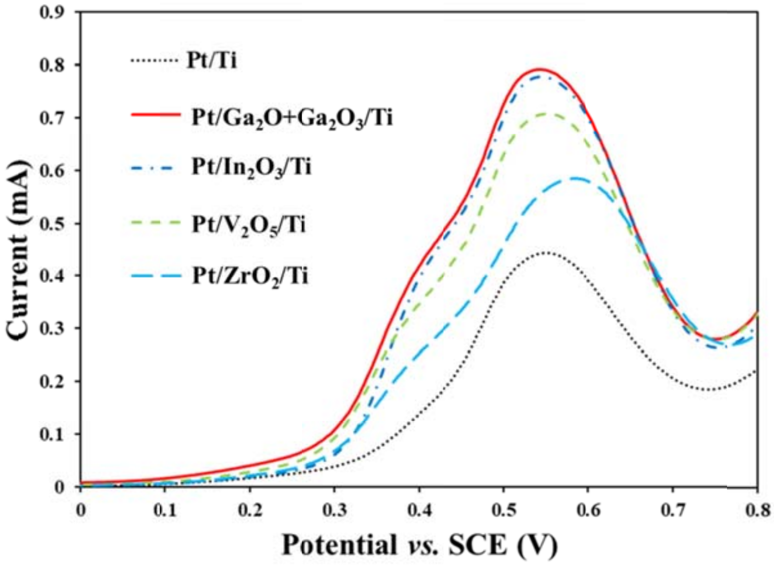

Figure 6.10. Linear sweep voltammograms (10 mV s^{-1}) for oxidation of 0.2 M ethanol + 0.1 M H_2SO_4 at Pt/Ti, Pt/Ga_2O+Ga_2O_3/Ti, Pt/In_2O_3/Ti, Pt/V_2O_5/Ti, and Pt/ZrO_2/Ti electrodes.

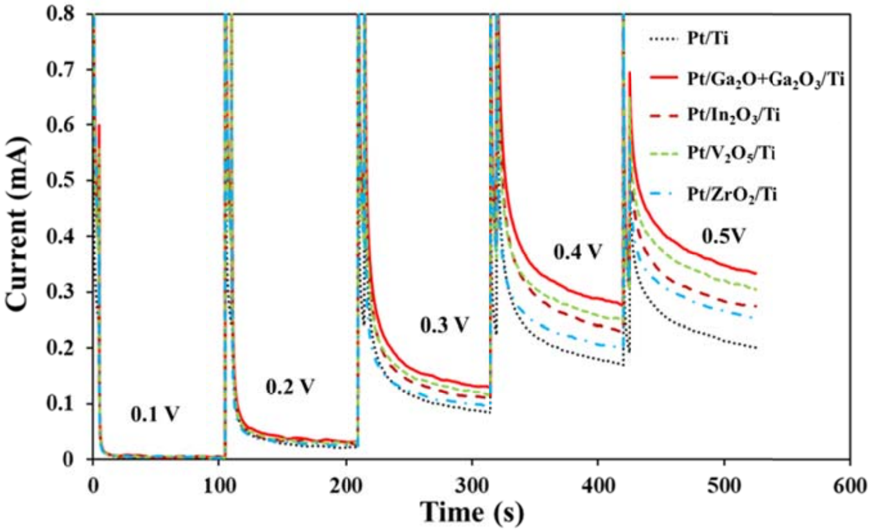

Figure 6.11. Current vs time during a series of potential steps for oxidation of 0.2 M ethanol in 0.1 M H_2SO_4(aq) at Pt/Ti, Pt/Ga_2O+Ga_2O_3/Ti, Pt/In_2O_3/Ti, Pt/V_2O_5/Ti, and Pt/ZrO_2/Ti electrodes.

Table 6.4. Electrical conductivities of MO_x (M = Mo, Ga, In, V, Zr, and Sn) from the selected literature.

Name	Electrical conductivity (Ω^{-1} cm^{-1})	Reference
MoO_3	1.0×10^3	57
Ga_2O_3	3.3×10	58
In_2O_3	5.6×10^2	59
V_2O_5	2.8×10^{-1}	60
ZrO_2	6.7×10^{-14}	61
SnO_2	3.6×10^{-6}	62
RuO_2	3.0×10^2	63

6.3.5 Methanol oxidation

The performances of electrodes modified by MO_x (M = Ga, In, V, and Zr) were investigated for methanol electro-oxidation. Several catalysts exhibited great potential as anode catalysts for direct methanol fuel cells. Linear sweep voltammograms (Figure 6.12) show that $Pt/Ga_2O+Ga_2O_3/Ti$, $Pt/In_2O_3/Ti$, and $Pt/V_2O_5/Ti$ have significantly higher peak currents than Pt/Ti. Different from ethanol oxidation, the process of methanol oxidation does not include C-C bond breaking. The oxidation of the CO_{ads} intermediates is the limiting step in the process of methanol oxidation. CO_{ads} at the Pt surface can migrate to the interface between Pt and MO_x support, and be oxidized with the assistance of abundant OH species provided by the MO_x support based on the Mars-van Krevelen model.[9] Charge transfer between Pt and MO_x support also plays an important role in promoting oxidation of CO_{ads}. It was reported that the interaction between Pt and Ga oxide positively shifted the peak positions of Pt 4f to higher binding energies.[64] The charge transfer from Pt to Ga oxide will result in weakening Pt-CO bond. The results of chronoamperometry measurements indicate Ga_2O+Ga_2O_3, In_2O_3, and V_2O_5 supports do have great improvement in the catalytic activity of Pt for methanol oxidation. As shown in Figure 6.13, the oxidation currents (at 0.30, 0.40, and 0.50 V) of catalysts supported by Ga_2O+Ga_2O_3, In_2O_3, and V_2O_5 are significantly higher than that of Pt/Ti. The results are consistent with that of linear sweep voltammetry.

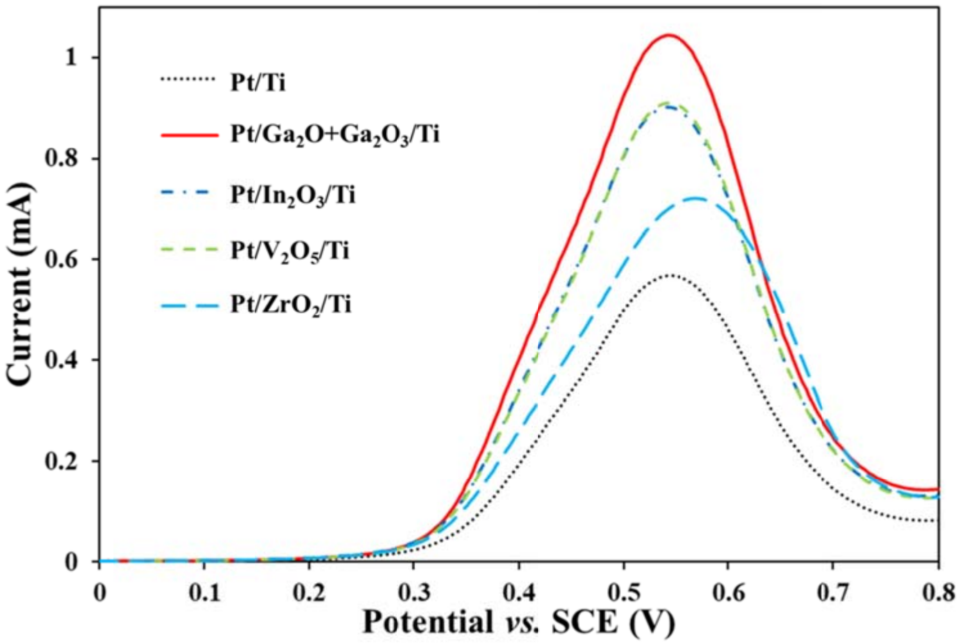

Figure 6.12. Linear sweep voltammograms (10 mV s^{-1}) of the 2nd cycle for oxidation of 0.2 M methanol + 0.1 M H_2SO_4 at Pt/Ti, Pt/Ga_2O+Ga_2O_3/Ti, Pt/In_2O_3/Ti, Pt/V_2O_5/Ti, and Pt/ZrO_2/Ti electrodes.

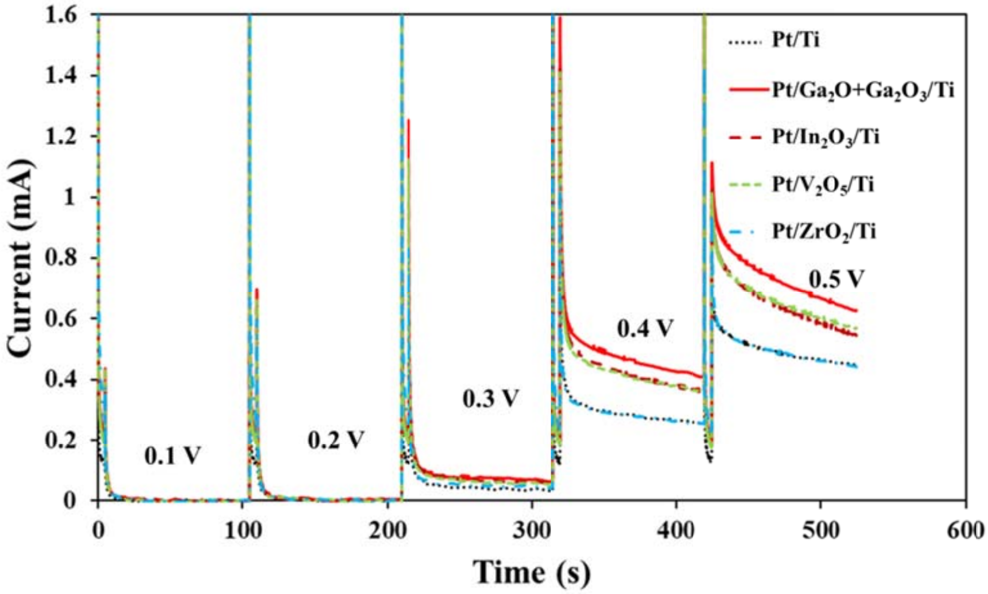

Figure 6.13. Current vs time during a series of potential steps for oxidation of 0.2 M methanol in 0.1 M H_2SO_4(aq) at Pt/Ti, Pt/Ga_2O+Ga_2O_3/Ti, Pt/In_2O_3/Ti, Pt/V_2O_5/Ti, and Pt/ZrO_2/Ti electrodes.

6.3.6 Mechanism

XPS analysis can be used to investigate occupied electronic states of an element. Charge transfer (in or out) leads to negative or positive shift of binding energies of its characteristic peaks. The XPS spectra of Pt 4d and Pt 4f regions of Pt/Ti and Pt/MoO_3/Ti are exhibited in Figure 6.14. In comparison with Pt/Ti, positive shift was observed in Pt 4d and 4f regions of Pt/MoO_3/Ti. For Pt/MoO_3/Ti, the binding energies of Pt $4d_{5/2}$ (317.0 eV) and Pt $4d_{3/2}$ (334.0 eV) are 2.0 eV higher than Pt/Ti (315.0 eV and 332.0 eV). In addition, the binding energies of Pt $4f_{7/2}$ (71.5 eV) and Pt $4f_{5/2}$ (74.7 eV) of Pt/MoO_3/Ti also have a positive shift in comparison with Pt $4f_{7/2}$ (71.1 eV) and Pt $4f_{5/2}$ (74.3 eV) of Pt/Ti, respectively. This suggests that charge transfer occurred from Pt to MoO_3 support, which can result in weakening of Pt-CO bond.[65-66] This can lead to faster rate of ethanol oxidation at Pt/MoO_3/Ti than Pt/Ti. In principle, the adsorption energies of other intermediates (e.g. CH_3CO and CH_x) and adsorbed OH species may also be affected by the variation of electronic properties of Pt, leading to changes of the reaction rates and barriers of intermediate oxidation and water dissociation.[67] It was mentioned that a positive charge shift could strengthen binding of H_2O to a Pt alloy catalyst, and ease water dissociation.

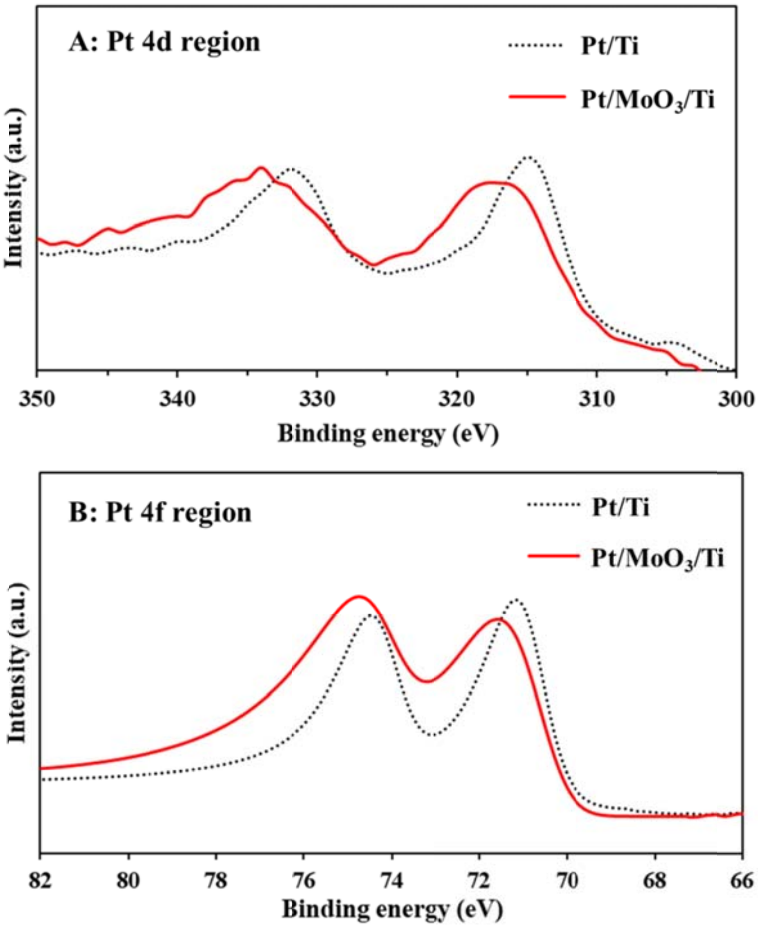

Figure 6.14. XPS spectra of Pt 4d (A) and Pt 4f (B) regions for Pt/Ti and Pt/MoO_3/Ti.

6.4 Conclusions

Thermal decomposition of M(acac)$_x$ complexes on Ti foil is a versatile method for rapidly preparing amorphous MO$_x$ supported catalysts, and suitable for catalyst screening. MO$_x$ supports exhibited significant enhancement in Pt catalyzed electro-oxidation of ethanol and methanol. According to preliminary investigation, the significant improvement was attributed to providing OH species and modifying electronic structure of Pt catalyst through introducing MO$_x$ supports. The bond strength of Pt-CO is susceptible to MO$_x$ support through charge transfer between Pt and MO$_x$. Weakening Pt-CO bond facilitates the oxidation of CO$_{ads}$. The abundance of OH species on MO$_x$ supports promotes oxidation of CO$_{ads}$ to CO$_2$ as bifunctional mechanism.

6.5 References

1. Badwal, S. P. S.; Giddey, S.; Kulkarni, A.; Goel, J.; Basu, S., Direct ethanol fuel cells for transport and stationary applications - A comprehensive review. *Applied Energy,* **2015**, *145*, 80-103.

2. Gautam, P.; Upadhyay, S. N.; Dubey, S. K., Bio-methanol as a renewable fuel from waste biomass: Current trends and future perspective. *Fuel,* **2020**, *273*, 117783.

3. An, L.; Zhao, T. S.; Li, Y. S., Carbon-neutral sustainable energy technology: Direct ethanol fuel cells. *Renewable and Sustainable Energy Reviews,* **2015**, *50*, 1462-1468.

4. Ong, B.; Kamarudin, S.; Basri, S., Direct liquid fuel cells: A review. *International Journal of Hydrogen Energy,* **2017**, *42* (15), 10142-10157.

5. Akhairi, M.; Kamarudin, S., Catalysts in direct ethanol fuel cell (DEFC): An overview. *International Journal of Hydrogen Energy,* **2016**, *41* (7), 4214-4228.

6. Antolini, E., Pt-Ni and Pt-M-Ni (M= Ru, Sn) anode catalysts for low-temperature acidic direct alcohol fuel cells: A review. *Energies,* **2017**, *10* (1), 42.

7. Elezovic, N.; Radmilovic, V.; Krstajic, N., Platinum nanocatalysts on metal oxide based supports for low temperature fuel cell applications. *Rsc Advances,* **2016**, *6* (8), 6788-6801.

8. Kuriganova, A. B.; Leontyeva, D. V.; Ivanov, S.; Bund, A.; Smirnova, N. V., Electrochemical dispersion technique for preparation of hybrid MO_x-C supports and Pt/MO_x-C electrocatalysts for low-temperature fuel cells. *Journal of Applied Electrochemistry,* **2016**, *46* (12), 1245-1260.

9. Alvarenga, G.; Villullas, H., Transition metal oxides in the electrocatalytic oxidation of methanol and ethanol on noble metal nanoparticles. *Current Opinion in Electrochemistry,* **2017**, *4* (1), 39-44.

10. Evarts, S. E.; Kendrick, I.; Wallstrom, B. L.; Mion, T.; Abedi, M.; Dimakis, N.; Smotkin, E. S., Ensemble site requirements for oxidative adsorption of methanol and ethanol on Pt membrane electrode assemblies. *ACS Catalysis,* **2012**, *2* (5), 701-707.

11. Kowal, A.; Gojković, S. L.; Lee, K.-S.; Olszewski, P.; Sung, Y.-E., Synthesis, characterization and electrocatalytic activity for ethanol oxidation of carbon supported Pt, Pt-Rh, Pt-SnO_2 and Pt-Rh-SnO_2 nanoclusters. *Electrochemistry Communications,* **2009**, *11* (4), 724-727.

12. Kowal, A.; Li, M.; Shao, M.; Sasaki, K.; Vukmirovic, M. B.; Zhang, J.; Marinkovic, N. S.; Liu, P.; Frenkel, A.; Adzic, R. R., Ternary Pt/Rh/SnO_2 electrocatalysts for oxidizing ethanol to CO_2. *Nature Materials,* **2009**, *8* (4), 325-330.

13. Li, M.; Zhou, W.-P.; Marinkovic, N. S.; Sasaki, K.; Adzic, R. R., The role of rhodium and tin oxide in the platinum-based electrocatalysts for ethanol oxidation to CO_2. *Electrochimica Acta,* **2013**, *104*, 454-461.

14. Castro, J. C.; Assumpção, M. H. M. T.; de Souza, R. F. B.; Spinacé, E. V.; Neto, A. O., Electro-oxidation of ethanol on PtSnRh/C-Sb_2O_5.SnO_2 electrocatalysts prepared by borohydride reduction. *Electrocatalysis,* **2013**, *4* (3), 159-166.

15. Yang, G.; Namin, L. M.; Deskins, N. A.; Teng, X., Influence of *OH adsorbates on the potentiodynamics of the CO_2 generation during the electro-oxidation of ethanol. *Journal of Catalysis,* **2017**, *353*, 335-348.

16. Moghaddam, R. B.; Pickup, P. G., Support effects on the oxidation of ethanol at Pt nanoparticles. *Electrochimica Acta,* **2012**, *65*, 210-215.

17. James, D. D.; Moghaddam, R. B.; Chen, B.; Pickup, P. G., Ruthenium-tin oxide/carbon supported platinum catalysts for electrochemical oxidation of ethanol in direct ethanol fuel cells. *Journal of The Electrochemical Society,* **2018**, *165* (3), F215.

18. Rousseau, S.; Coutanceau, C.; Lamy, C.; Léger, J.-M., Direct ethanol fuel cell (DEFC): Electrical performances and reaction products distribution under operating conditions with different platinum-based anodes. *Journal of Power Sources,* **2006**, *158* (1), 18-24.

19. Altarawneh, R. M.; Pickup, P. G., Product distributions and efficiencies for ethanol oxidation in a proton exchange membrane electrolysis cell. *Journal of The Electrochemical Society,* **2017**, *164* (7), F861.

20. Mahfouz, R. M.; Siddiqui, M. R. H.; Al-Ahmari, S. A.; Alkayali, W. Z., Kinetic analysis of thermal decomposition of unirradiated and γ-irradiated tris(acetylacetonato)-ruthenium(III) $[Ru(acac)_3]$. *Progress in Reaction Kinetics and Mechanism,* **2007**, *32* (1), 1-27.

21. Matsui, H.; Saito, Y.; Karuppuchamy, S.; Yoshihara, M., The electronic behaviors of TiO_2/MnO_2/carbon clusters composite materials obtained by the calcination of a $TiO(acac)_2/Mn(acac)_3$/epoxy resin complex. *Current Applied Physics,* **2009**, *9* (6), 1203-1209.

22. Schubert, J. S.; Popovic, J.; Haselmann, G. M.; Nandan, S. P.; Wang, J.; Giesriegl, A.; Cherevan, A. S.; Eder, D., Immobilization of Co, Mn, Ni and Fe oxide co-catalysts on TiO_2 for photocatalytic water splitting reactions. *Journal of Materials Chemistry A,* **2019**, *7* (31), 18568-18579.

23. Yi, Q.; Zhang, J.; Chen, A.; Liu, X.; Xu, G.; Zhou, Z., Activity of a novel titanium-supported bimetallic PtSn/Ti electrode for electrocatalytic oxidation of formic acid and methanol. *Journal of Applied Electrochemistry,* **2008**, *38* (5), 695-701.

24. Zulke, A. A.; Matos, R.; Pereira, E. C., Metallic multilayered films electrodeposited over titanium as catalysts for methanol electro-oxidation. *Electrochimica Acta,* **2013**, *105*, 578-583.

25. Yasutake, M.; Kawachino, D.; Noda, Z.; Matsuda, J.; Lyth, S. M.; Ito, K.; Hayashi, A.; Sasaki, K., Catalyst-integrated gas diffusion electrodes for polymer electrolyte membrane water electrolysis: Porous titanium sheets with nanostructured TiO_2 surfaces decorated with Ir electrocatalysts. *Journal of The Electrochemical Society,* **2020**, *167* (12), 124523.

26. Zhang, W.; Desikan, A.; Oyama, S. T., Effect of support in ethanol oxidation on molybdenum oxide. *The Journal of Physical Chemistry,* **1995**, *99* (39), 14468-14476.

27. Llordés, A.; Wang, Y.; Fernandez-Martinez, A.; Xiao, P.; Lee, T.; Poulain, A.; Zandi, O.; Cabezas, C. A. S.; Henkelman, G.; Milliron, D. J., Linear topology in amorphous metal oxide electrochromic networks obtained via low-temperature solution processing. *Nature Materials,* **2016**, *15* (12), 1267-1273.

28. Hang, H.; Altarawneh, R. M.; Brueckner, T. M.; Pickup, P. G., Pt/Ru-Sn oxide/carbon catalysts for ethanol oxidation. *Journal of The Electrochemical Society,* **2020**, *167* (5), 054518.

29. Zare, M.; Solaymani, S.; Shafiekhani, A.; Kulesza, S.; Ţălu, Ş.; Bramowicz, M., Evolution of rough-surface geometry and crystalline structures of aligned TiO_2 nanotubes for photoelectrochemical water splitting. *Scientific Reports,* **2018**, *8* (1), 1-11.

30. Li, Y.; Yu, H.; Huang, X.; Wu, Z.; Chen, M., A simple synthesis method to prepare a molybdenum oxide hole-transporting layer for efficient polymer solar cells. *Rsc Advances,* **2017**, *7* (13), 7890-7900.

31. Choi, C.-H.; Han, S.-Y.; Su, Y.-W.; Fang, Z.; Lin, L.-Y.; Cheng, C.-C.; Chang, C.-h., Fabrication of high-performance, low-temperature solution processed amorphous indium oxide thin-film transistors using a volatile nitrate precursor. *Journal of Materials Chemistry C,* **2015**, *3* (4), 854-860.

32. Rowe, M. C.; Brewer, B. J., AMORPH: A statistical program for characterizing amorphous materials by X-ray diffraction. *Computers & Geosciences,* **2018**, *120*, 21-31.

33. An, Q.; Wei, Q.; Mai, L.; Fei, J.; Xu, X.; Zhao, Y.; Yan, M.; Zhang, P.; Huang, S., Supercritically exfoliated ultrathin vanadium pentoxide nanosheets with high rate capability for lithium batteries. *Physical Chemistry Chemical Physics,* **2013**, *15* (39), 16828-16833.

34. Wood, S. R.; Woods, K. N.; Plassmeyer, P. N.; Marsh, D. A.; Johnson, D. W.; Page, C. J.; Jensen, K. M. Ø.; Johnson, D. C., Same Precursor, two different products: Comparing the structural evolution of In-Ga-O “gel-derived” powders and solution-cast films using pair

distribution function analysis. *Journal of the American Chemical Society,* **2017**, *139* (15), 5607-5613.

35. Pérez-Maqueda, L. A.; Matijević, E., Preparation and characterization of nanosized zirconium (hydrous) oxide particles. *Journal of Materials Research,* **1997**, *12* (12), 3286-3292.

36. Kokubun, Y.; Miura, K.; Endo, F.; Nakagomi, S., Sol-gel prepared β-Ga_2O_3 thin films for ultraviolet photodetectors. *Applied Physics Letters,* **2007**, *90* (3), 031912.

37. Wang, C.-B.; Cai, Y.; Wachs, I. E., Reaction-induced spreading of metal oxides onto surfaces of oxide supports during alcohol oxidation: Phenomenon, nature, and mechanisms. *Langmuir,* **1999**, *15* (4), 1223-1235.

38. Yun, D.; Wang, Y.; Herrera, J. E., Ethanol partial oxidation over VO_x/TiO_2 catalysts: The role of titania surface oxygen on vanadia reoxidation in the Mars–van Krevelen mechanism. *ACS Catalysis,* **2018**, *8* (5), 4681-4693.

39. Bharti, B.; Kumar, S.; Lee, H.-N.; Kumar, R., Formation of oxygen vacancies and Ti^{3+} state in TiO_2 thin film and enhanced optical properties by air plasma treatment. *Scientific Reports,* **2016**, *6* (1), 1-12.

40. Li, Z.; Gao, L.; Zheng, S., SEM, XPS, and FTIR studies of MoO_3 dispersion on mesoporous silicate MCM-41 by calcination. *Materials Letters,* **2003**, *57* (29), 4605-4610.

41. Wu, X. C.; Hong, J. M.; Han, Z. J.; Tao, Y. R., Fabrication and photoluminescence characteristics of single crystalline In_2O_3 nanowires. *Chemical Physics Letters,* **2003**, *373* (1-2), 28-32.

42. Reddy, B. M.; Chowdhury, B.; Smirniotis, P. G., An XPS study of La_2O_3 and In_2O_3 influence on the physicochemical properties of MoO_3/TiO_2 catalysts. *Applied Catalysis A: General,* **2001**, *219* (1-2), 53-60.

43. Milojevic, M.; Contreras-Guerrero, R.; O'Connor, E.; Brennan, B.; Hurley, P. K.; Kim, J.; Hinkle, C.; Wallace, R. M., In-situ characterization of Ga_2O passivation of $In_{0.53}Ga_{0.47}$ as prior to high-k dielectric atomic layer deposition. *Applied Physics Letters,* **2011**, *99* (4), 042904.

44. Cademartiri, L.; Thuo, M. M.; Nijhuis, C. A.; Reus, W. F.; Tricard, S.; Barber, J. R.; Sodhi, R. N. S.; Brodersen, P.; Kim, C.; Chiechi, R. C., Electrical resistance of Ag^{TS}-$S(CH_2)_{n-1}CH_3$//Ga_2O_3/EGaIn tunneling junctions. *The Journal of Physical Chemistry C,* **2012**, *116* (20), 10848-10860.

45. Sodhi, R. N.; Brodersen, P.; Cademartiri, L.; Thuo, M. M.; Nijhuis, C. A., Surface and buried interface layer studies on challenging structures as studied by ARXPS. *Surface and Interface Analysis,* **2017**, *49* (13), 1309-1315.

46. Reddy, B. M.; Ganesh, I.; Reddy, E. P., Study of dispersion and thermal stability of V_2O_5/TiO_2-SiO_2 catalysts by XPS and other techniques. *The Journal of Physical Chemistry B,* **1997**, *101* (10), 1769-1774.

47. Reddy, B. M.; Chowdhury, B.; Ganesh, I.; Reddy, E. P.; Rojas, T. C.; Fernandez, A., Characterization of V_2O_5/TiO_2-ZrO_2 catalysts by XPS and other techniques. *The Journal of Physical Chemistry B,* **1998**, *102* (50), 10176-10182.

48. Song, J.; Ni, X.; Zhang, D.; Zheng, H., Fabrication and photoluminescence properties of hexagonal MoO_3 rods. *Solid State Sciences,* **2006**, *8* (10), 1164-1167.

49. O'Donoghue, R.; Rechmann, J.; Aghaee, M.; Rogalla, D.; Becker, H.-W.; Creatore, M.; Wieck, A. D.; Devi, A., Low temperature growth of gallium oxide thin films via plasma enhanced atomic layer deposition. *Dalton Transactions,* **2017**, *46* (47), 16551-16561.

50. Xu, H.; Han, F.; Xia, C.; Wang, S.; Ramachandran, R. M.; Detavernier, C.; Wei, M.; Lin, L.; Zhuiykov, S., Wafer-scale fabrication of sub-10 nm $TiO_2-Ga_2O_3$ np heterojunctions with efficient photocatalytic activity by atomic layer deposition. *Nanoscale Research Letters,* **2019**, *14* (1), 1-10.

51. Biesinger, M. C.; Lau, L. W.; Gerson, A. R.; Smart, R. S. C., Resolving surface chemical states in XPS analysis of first row transition metals, oxides and hydroxides: Sc, Ti, V, Cu and Zn. *Applied Surface Science,* **2010**, *257* (3), 887-898.

52. Garsany, Y.; Baturina, O. A.; Swider-Lyons, K. E.; Kocha, S. S., Experimental methods for quantifying the activity of platinum electrocatalysts for the oxygen reduction reaction. *Analytical Chemistry,* **2010**, *82*, 6321-6328.

53. Dos Anjos, D.; Kokoh, K. B.; Léger, J.-M.; Andrade, A. D.; Olivi, P.; Tremiliosi-Filho, G., Electrocatalytic oxidation of ethanol on Pt–Mo bimetallic electrodes in acid medium. *Journal of Applied Electrochemistry,* **2006**, *36* (12), 1391-1397.

54. Magee, J. W.; Zhou, W.-P.; White, M. G., Promotion of Pt surfaces for ethanol electro-oxidation by the addition of small SnO_2 nanoparticles: Activity and mechanism. *Applied Catalysis B: Environmental,* **2014**, *152*, 397-402.

55. Chu, Y. H.; Shul, Y. G., Combinatorial investigation of Pt–Ru–Sn alloys as an anode electrocatalysts for direct alcohol fuel cells. *International Journal of Hydrogen Energy,* **2010**, *35* (20), 11261-11270.

56. Lim, D.-H.; Choi, D.-H.; Lee, W.-D.; Park, D.-R.; Lee, H.-I., The effect of Sn addition on a Pt/C electrocatalyst synthesized by borohydride reduction and hydrothermal treatment for a low-temperature fuel cell. *Electrochemical and Solid State Letters,* **2007**, *10* (5), B87.

57. Madhavi, V.; Kondaiah, P.; Rayudu, S. S.; Hussain, O. M.; Uthanna, S., Properties of MoO_3 films by thermal oxidation: Annealing induced phase transition. *Materials Express,* **2013**, *3* (2), 135-143.

58. Chikoidze, E.; Rogers, D. J.; Teherani, F. H.; Rubio, C.; Sauthier, G.; Von Bardeleben, H. J.; Tchelidze, T.; Ton-That, C.; Fellous, A.; Bove, P., Puzzling robust 2D metallic conductivity in undoped β-Ga_2O_3 thin films. *Materials Today Physics,* **2019**, *8*, 10-17.

59. Kaleemulla, S.; Reddy, A. S.; Uthanna, S.; Reddy, P. S., Physical properties of In_2O_3 thin films prepared at various oxygen partial pressures. *Journal of Alloys and Compounds,* **2009**, *479* (1-2), 589-593.

60. Kumar, A.; Singh, P.; Kulkarni, N.; Kaur, D., Structural and optical studies of nanocrystalline V_2O_5 thin films. *Thin Solid Films,* **2008**, *516* (6), 912-918.

61. Liu, D.-M.; Tuan, W. H., Microstructure and its influence on thermal and electrical conductivity of ZrO_2-Ag composites. *Materials Chemistry and Physics,* **1997**, *48* (3), 258-262.

62. Bahadur, J.; Ghahremani, A. H.; Martin, B.; Druffel, T.; Sunkara, M. K.; Pal, K., Solution processed Mo doped SnO_2 as an effective ETL in the fabrication of low temperature planer perovskite solar cell under ambient conditions. *Organic Electronics*, **2019**, 67, 159-167.

63. Ma, X.; Chen, Y.-A.; Zhou, K.; Wu, P.-C.; Hou, C.-H., Enhanced desalination performance via mixed capacitive-Faradaic ion storage using RuO_2-activated carbon composite electrodes. *Electrochimica Acta,* **2019**, *295*, 769-777.

64. Grabau, M.; Calderón, S. K.; Rietzler, F.; Niedermaier, I.; Taccardi, N.; Wasserscheid, P.; Maier, F.; Steinrück, H.-P.; Papp, C., Surface enrichment of Pt in Ga_2O_3 films grown on liquid Pt/Ga alloys. *Surface Science,* **2016**, *651*, 16-21.

65. Anniyev, T.; Ogasawara, H.; Ljungberg, M. P.; Wikfeldt, K. T.; MacNaughton, J. B.; Näslund, L.-Å.; Bergmann, U.; Koh, S.; Strasser, P.; Pettersson, L. G., Complementarity between high-energy photoelectron and L-edge spectroscopy for probing the electronic structure of 5d transition metal catalysts. *Physical Chemistry Chemical Physics,* **2010**, *12* (21), 5694-5700.

66. Wakisaka, M.; Mitsui, S.; Hirose, Y.; Kawashima, K.; Uchida, H.; Watanabe, M., Electronic structures of Pt-Co and Pt-Ru alloys for CO-tolerant anode catalysts in polymer electrolyte fuel cells studied by EC-XPS. *The Journal of Physical Chemistry B,* **2006**, *110* (46), 23489-23496.

67. Dai, L.-X.; Wang, X.-Y.; Yang, S.-S.; Zhang, T.; Ren, P.-J.; Ye, J.-Y.; Nan, B.; Wen, X.-D.; Zhou, Z.-Y.; Si, R., Intrinsic composition and electronic effects of multicomponent platinum nanocatalysts with high activity and selectivity for ethanol oxidation reaction. *Journal of Materials Chemistry A,* **2018**, *6* (24), 11270-11280.

Chapter 7

Summary and future work

7.1 Summary

Thermal decomposition of M(acac)$_x$ complexes on flat and high surface area electrode materials was developed as a versatile method for rapidly preparing metal oxide supported Pt catalysts for electrocatalysis. The performance of the prepared catalysts on oxidation of ethanol and methanol was investigated by cyclic voltammetry and chronoamperometry. Then, the optimized catalysts were applied in a PEM cell for ethanol oxidation. The faradaic CO_2 yields obtained at the prepared catalysts were determined online by a NDIR CO_2 detector.

In the first part of the study, metal oxide supported Pt catalysts on Ti electrodes were consistently and quickly prepared by the method of M(acac)$_x$ thermal decomposition for catalyst screening. A wide variety of metal oxides were successfully synthesized at a low temperature, and their support effects on Pt-catalyzed oxidation of ethanol and methanol were systematically studied. In cyclic voltammetry measurements for ethanol oxidation, the catalysts supported by Mo, Pb, Ru+Sn, In, V, Ga oxides exhibited outstanding performance. In comparison with the Pt catalyst, a large enhancement at low potentials was observed for the Ru+Sn oxide supported Pt catalyst. The Ru: Sn ratio had a significant effect on the performance of the catalyst, and the optimized Ru(acac)$_3$ to Sn(acac)$_2$ ratio was 2:1. Use of a PbO support shifted the oxidation peak of Pt-catalyzed ethanol oxidation to a lower potential relative to use of bare Ti. In addition, other metal oxide supports (e.g. Mo, In, Ga, and V oxides) greatly enhanced the oxidation current, especially at high potentials.

In order to better understand their support effects, the electronic effect between the metal oxide supports and Pt was investigated by XPS measurement. It was found that these metal oxides had distinct effects on the binding energies of Pt, which indicated that charge transfer occurred between metal oxide supports and Pt. This can affect the adsorption energy of poisoning species (e.g. CO) at Pt, resulting in easier CO removal. Moreover, metal oxides significantly promoted the catalytic activity of Pt in methanol oxidation.

In the second part of the study, the methodology of M(acac)$_x$ decomposition was successfully applied to a carbon black support for the preparation of anodes and investigation of their performance in a PEM cell for ethanol oxidation. Similar to Pt/Ru+Sn oxide/Ti, the prepared Pt/Ru+Sn oxide/C electrode also had a low onset potential in cyclic voltammetry measurements. In a PEM cell for ethanol oxidation, higher oxidation currents were obtained at Pt/Ru+Sn oxide/C electrodes than Pt/C electrodes in the region of low potentials. This suggested that the Pt/Ru+Sn oxide/C catalyst had the potential to be applied in DEFCs.

Modification of carbon black by Pb(acac)$_2$ thermal decomposition showed significant improvement on activities for ethanol oxidation at supported Pt catalysts. Different from the product of PbO on a Ti support, the thermal decomposition of Pb(acac)$_2$ produced BLC on carbon black. The presence of BLC significantly increased the activity and CO tolerance of Pt nanoparticles for ethanol oxidation in cyclic voltammetry measurements, and the oxidation current increased with the BLC percentage. In chronoamperometry measurements, the BLC support enhanced ethanol oxidation at 0.5 V, but had severe current decays at low potentials due to a change in the composition over time. However, the Pt/BLC(0.22)/C catalyst provided a stable performance for ethanol oxidation in a PEM cell. Compared with Pt/C, the lower CO_2 yield of Pt/BLC(0.22)/C indicated that providing OH species had no improvement on selectively breaking the C-C bond of ethanol. The increase of oxidation current might result from the promotion of the oxidation of acetaldehyde to acetic acid. Due to BLC reduction between 0 and 0.2 V, Pb deposition on the Pt surface led to a third body effect on the oxidation of formic acid, which selectively promoted direct oxidation of formic acid.

7.2 Future work

Through the method of M(acac)$_x$ thermal decomposition, only a small number of metal oxides have been prepared and investigated in this work, while a variety of mono metal oxides and complex metal oxides should be screened in the future.[1] Although charge transfer was found between metal oxide supports and Pt, its influence on reaction pathways and products need to be studied in detail. In order to specifically understand the mechanism of the improvement brought by metal oxide supports, a setup combining an infrared spectrometer with a spectroelectrochemical cell can be used to observe variations in intermediates and products with different catalysts. In this way, the relationship between charge transfer and product distribution could be developed.

M(acac)$_x$ complexes can also be reduced to synthesize binary or ternary alloy catalysts through co-deposition methods.[2-3] It is important for the systematic investigation of binary or ternary alloy catalysts to use the same synthetic method, as the particle size, composition, and morphology of the desired alloys can be well controlled.[4-7] Moreover, M(acac)$_x$ complexes can be used to prepare core-shell catalysts, by depositing a Pt shell on core-nanoparticles. In comparison with a supported Pt catalyst, a core-shell catalyst has a higher utilization rate of Pt atoms, and is more stable because of the inert Pt shell.[8]

Although metal oxide supported Pt catalysts significantly promote ethanol oxidation, their CO_2 selectivity is still low. In contrast to a Pt catalyst, several alloy catalysts (e.g. PtRh and PtNi) were found to have a higher selectivity for complete oxidation of ethanol to CO_2.[9-10] Fabrication of ternary catalysts such as PtRh/MO_x and PtNi/MO_x has the potential to address the problems of low catalytic activity and incomplete oxidation of ethanol.

Finally, metal oxide supported catalysts can also be applied in DMFCs, DFAFCs, and hydrogen-PEMFCs. Therefore, it is significant to evaluate the performance of metal oxide supported catalysts for the oxidation of methanol, formic acid, and hydrogen in a PEM cell.

7.3 References

1. Lu, H.; Wright, D. S.; Pike, S. D., The use of mixed-metal single source precursors for the synthesis of complex metal oxides. *Chemical Communications,* **2020**, *56* (6), 854-871.

2. Watanabe, M.; Takamura, H.; Sugai, H., Preparation of ultrafine Fe-Pt alloy and Au nanoparticle colloids by KrF excimer laser solution photolysis. *Nanoscale Research Letters,* **2009**, *4* (6), 565-573.

3. Liu, Z.; Guo, B.; Tay, S. W.; Hong, L.; Zhang, X., Physical and electrochemical characterizations of PtPb/C catalyst prepared by pyrolysis of platinum(II) and lead(II) acetylacetonate. *Journal of Power Sources,* **2008**, *184* (1), 16-22.

4. Kulbakov, A. A.; Allix, M.; Rakhmatullin, A.; Mikheykin, A. S.; Popov, Y. V.; Smirnova, N. V.; Maslova, O.; Leontyev, I. N., In situ investigation of non-isothermal decomposition of Pt acetylacetonate as one-step size-controlled synthesis of Pt nanoparticles. *Physica Status Solidi (A) Applications and Materials Science,* **2018**, *215* (23), 1800488.

5. Womes, M.; Cholley, T.; Le Peltier, F.; Morin, S.; Didillon, B.; Szydlowski-Schildknecht, N., Study of the reaction mechanisms between Pt (acac)$_2$ and alumina surface sites: Application to a new refilling technique for the controlled variation of the particle size of Pt/Al$_2$O$_3$ catalysts. *Applied Catalysis A: General,* **2005**, *283* (1-2), 9-22.

6. Varanda, L. C.; Souza, C. G. S.; Moraes, D. A.; Neves, H. R.; Souza, J. B.; Silva, M. F.; Bini, R. A.; Albers, R. F.; Silva, T. L.; Beck, W., Size and shape-controlled nanomaterials based on modified polyol and thermal decomposition approaches. A brief review. *Anais da Academia Brasileira de Ciências,* **2019**, *91.*

7. Sodhi, R. K.; Paul, S., An overview of metal acetylacetonates: Developing areas/routes to new materials and applications in organic syntheses. *Catalysis surveys from Asia,* **2018**, *22* (1), 31-62.

8. Li, G.; Tang, Z., Noble metal nanoparticle@metal oxide core/yolk-shell nanostructures as catalysts: Recent progress and perspective. *Nanoscale,* **2014**, *6* (8), 3995-4011.

9. Zhu, Y.; Bu, L.; Shao, Q.; Huang, X., Subnanometer PtRh nanowire with alleviated poisoning effect and enhanced C–C bond cleavage for ethanol oxidation electrocatalysis. *ACS Catalysis,* **2019**, *9* (8), 6607-6612.

10. Altarawneh, R. M.; Brueckner, T. M.; Chen, B.; Pickup, P. G., Product distributions and efficiencies for ethanol oxidation at PtNi octahedra. *Journal of Power Sources,* **2018**, *400*, 369-376.

Appendix A

Modification of carbon black and titanium by thermal decomposition of lead acetylacetonate to improve activities for ethanol and formic oxidation at supported Pt catalysts

XRD patterns for the calculation of average Pt particle sizes in the catalysts

In the XRD patterns (Figure A.1, Figure A.2, Figure A.3 and Figure A.4), the peaks of Pt (111) at 40.0° were used to calculate average Pt particle sizes of the catalysts. No characteristic peak of BLC was observed in the XRD patterns of Pt/BLC(0.14)/C and Pt/BLC(0.22)/C, except Pt/BLC(0.80)/C. The calculated detection limit of BLC was Pb:Pt ratio (ca. 0.6) to form a monolayer of BLC crystal particles (ca. 1.3 nm thick) on the carbon support. Only Pt/BLC(0.80)/C fitted the requirement. For Pt/BLC(0.14)/C and Pt/BLC(0.22)/C), their low loadings of $Pb(acac)_2$ could not support the formation of BLC crystals. This implies that the BLC is evenly coated over the carbon support.

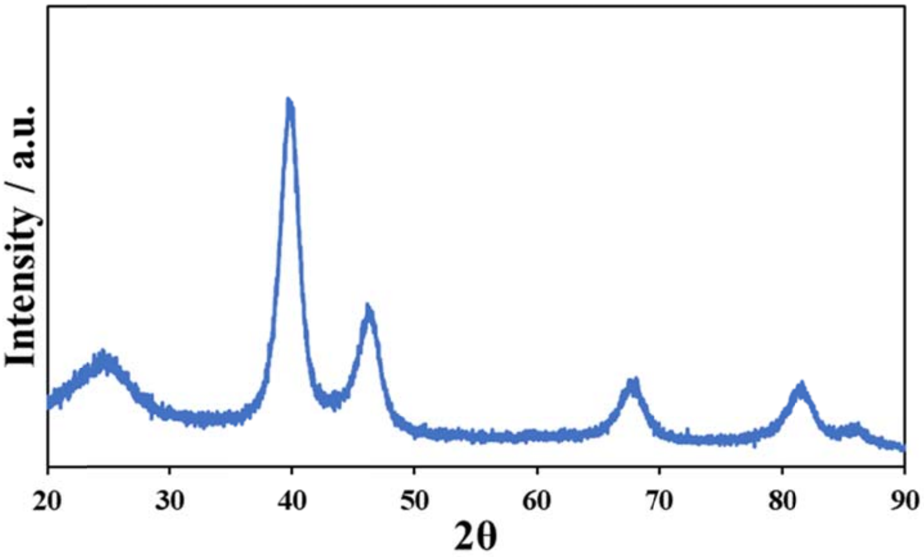

Figure A.1. XRD pattern of Pt/C used for particle size calculation in Table 5.2.

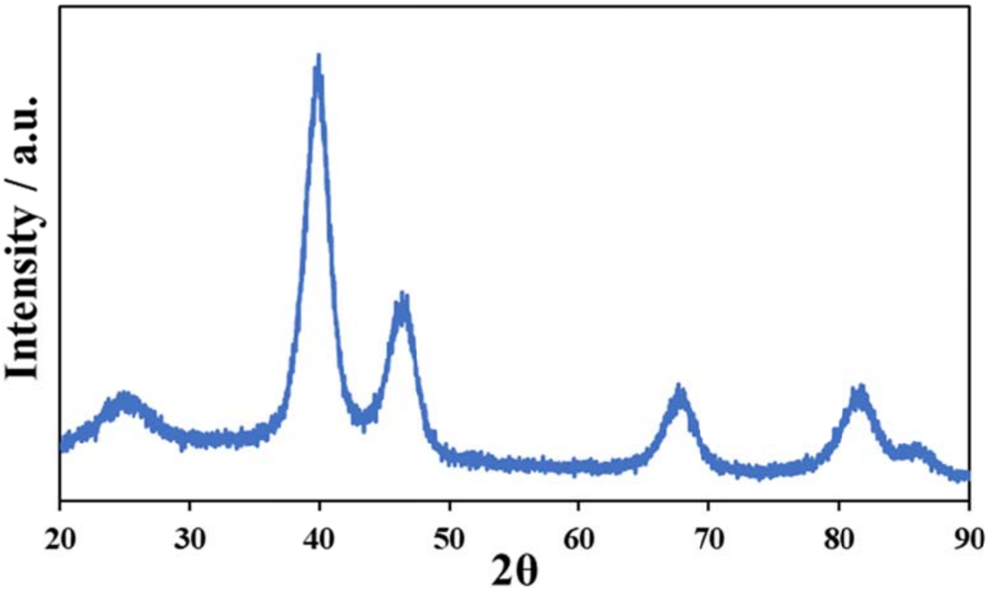

Figure A.2. XRD pattern of Pt/BLC(0.14)/C used for particle size calculation in Table 5.2.

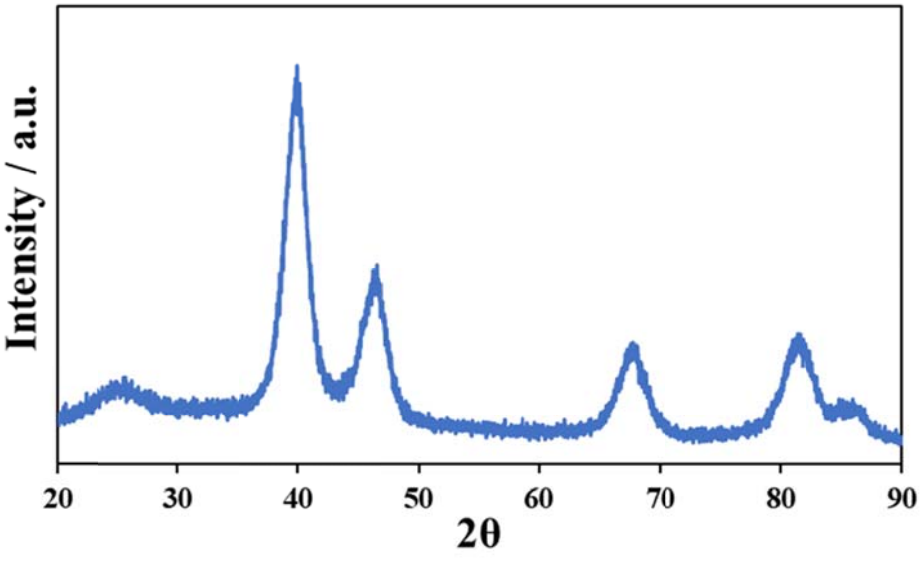

Figure A.3. XRD pattern of Pt/BLC(0.22)/C used for particle size calculation in Table 5.2.

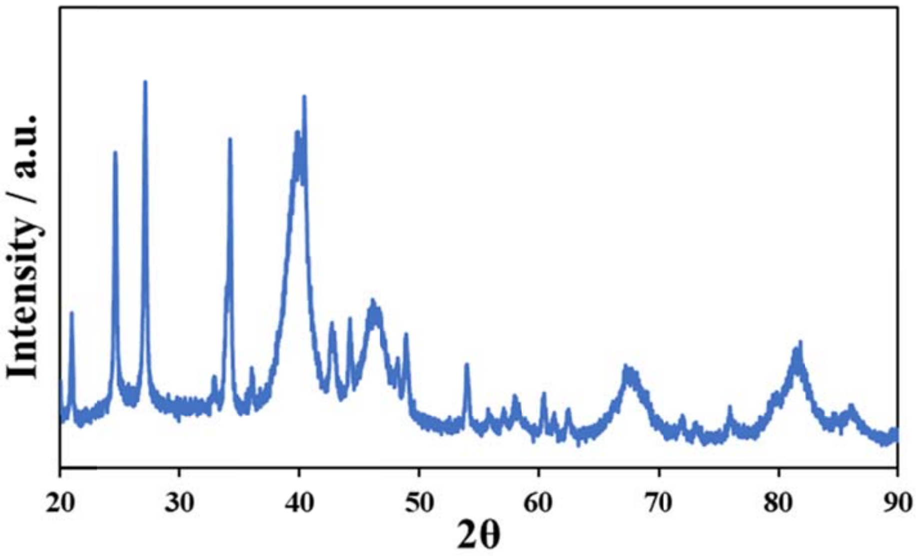

Figure A.4. XRD pattern of Pt/BLC(0.80)/C used for particle size calculation in Table 5.2.

Appendix B

Screening of Pt/metal oxide/Ti catalysts for ethanol and methanol oxidation

Charge calculation for electrochemically active surface area of the electrodes

To estimate the electrochemically active surface areas of the electrodes, the charge for hydrogen adsorption (Figure B.1) was used for the calculation.

$$Q = \int I \, dt$$

Where Q is charge in μC, I represents current in mA, and t is time in s.

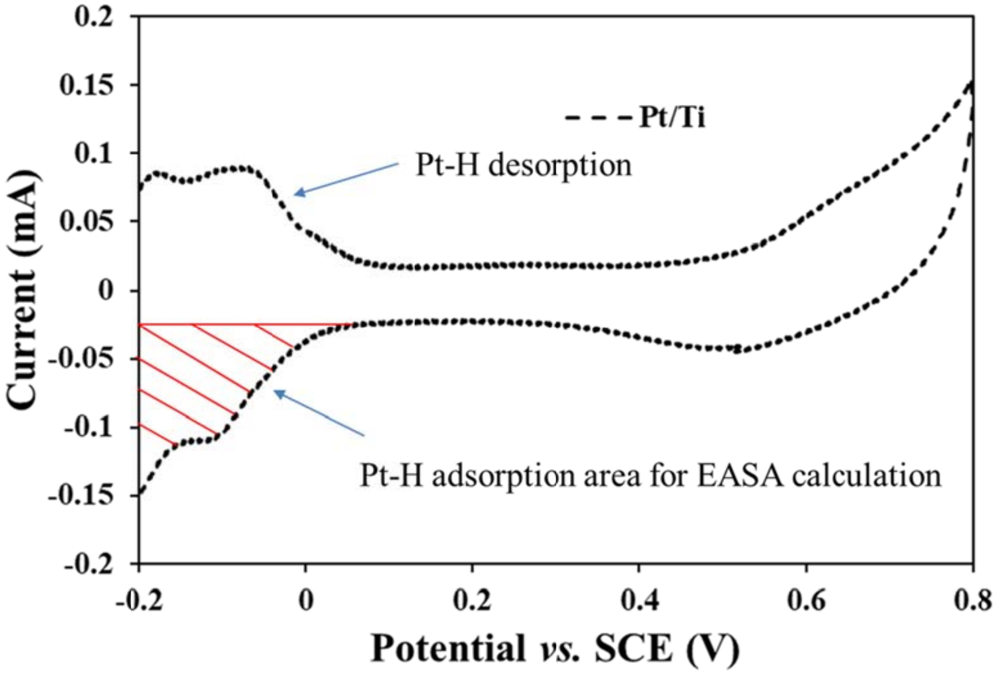

Figure B.1. Cyclic voltammogram (100 mV s^{-1}) of Pt/Ti (as an example from Figure 6.6 and Figure 6.7) with labeled Pt-H adsorption area used for calculation of electrochemically active surface area in Table 6.3.